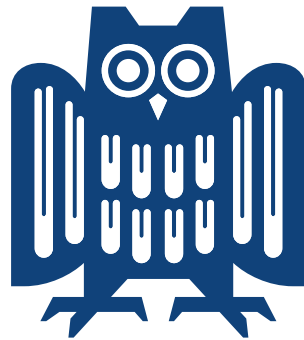


Universität des Saarlandes



Fachrichtung Physik

# Nonlinear Rheology of Granular Matter

---

Dissertation  
zur Erlangung des Grades  
des Doktors der Naturwissenschaften  
der Naturwissenschaftlich-Technischen Fakultät  
der Universität des Saarlandes  
von

**Rishab Handa**

---

Saarbrücken

2022



Tag des Kolloquiums: 06.05.2022

Dekan: Univ.-Prof. Dr. Jörn Erik Walter

Berichterstatter: Univ.-Prof. Dr. Christian Wagner  
Univ.-Prof. Dr. Rolf Pelster

Vorsitz: Univ.-Prof. Dr. Jochen Hub

Akad. Mitarbeiter: Dr. Stephan Kucera



## Abstract

A tremendous amount of upheaval and rethinking of "free-volume" theories to describe granular systems has made staggering progress. However, owing to a plethora of macroscopically equivalent yet microscopically distinct metastable states, the average free volume density (a single macroscopic degree of freedom) does not fully describe the complex dynamics of granular systems. Nonlinear rheology of grains and powders are filled with an assortment of such micro-macro processes interrupted by shear bands or decorated with filamentary force chain networks, preventing the homogeneous response, challenging to predict its physical interpretation. In this regard, FT-rheology combined with Chebyshev polynomial representation allowed us to efficiently quantify the nonlinear behaviour of grains and powders where the nonlinear viscoelastic moduli were found to scale with the characteristic energy by a Boltzmann factor, invoking a temperate-like parameter. Therefore, to account for both, the spatial heterogeneity and the intermittent dynamics, we referred to a generalised version of the "trap" model, the *Soft Glassy Rheology* (SGR) model. Although intentionally adopted to study glass formers, the crucial ingredient here is the "noise temperature" accounting for the configurational state of a system, recognizing glass transition, ageing, rejuvenation and nonlinear rheology. Hence, to systematically study this special class of athermal materials that fall within the purview of this constitutive model, we varied confinement, the surface tension of the wetting fluid and frequency with respect to the stress-strain response. Our experimental study recognises the crucial physical processes underlying rapid granular flows, and characterizes the significance of nonlinearities in the rheology of granular materials.

## Zusammenfassung

Die Theorien des "freien Volumens" zur Beschreibung granularer Systeme haben einen enormen Umbruch und ein Umdenken bewirkt. Aufgrund einer Fülle makroskopisch gleichwertiger, aber mikroskopisch unterschiedlicher metastabiler Zustände wird die durchschnittliche Dichte des freien Volumens (ein einziger makroskopischer Freiheitsgrad) der komplexen Dynamik granularer Systeme jedoch nicht gerecht. Die nichtlineare Rheologie von Körnern und Pulvern ist mit einer Vielzahl solcher Mikro-Makro-Prozesse gefüllt, die durch Scherbänder unterbrochen oder mit filamentären Kraftkettennetzwerken ausgestattet sind, was eine homogene Reaktion verhindert und damit die Vorhersage ihrer physikalischen Interpretation erschwert. Das Modell, das sowohl die räumliche Heterogenität als auch die intermittierende Dynamik berücksichtigt, ist eine verallgemeinerte Version des "Fallen"-Modells, das Modell der weichen glasartigen Rheologie (engl. *soft glassy rheology*, SGR). Obwohl es absichtlich zur Untersuchung von Glasbildnern eingesetzt wird, ist der entscheidende Bestandteil hier die "Rauschtemperatur", die den Konfigurationszustand eines Systems berücksichtigt und Glasübergang, Alterung, Verjüngung und nichtlineare Rheologie berücksichtigt. In dieser Arbeit untersuchen wir eine spezielle Klasse von athermischen Materialien, die in den Anwendungsbereich dieses konstitutiven Modells fallen.

## Eidesstattliche Erklärung

Hiermit versichere ich an Eides statt, dass ich die vorliegende Arbeit selbstständig und ohne Benutzung anderer als der angegebenen Hilfsmittel angefertigt habe. Die aus anderen Quellen oder indirekt übernommenen Daten und Konzepte sind unter Angabe der Quelle gekennzeichnet. Die Arbeit wurde bisher weder im In- noch im Ausland in gleicher oder ähnlicher Form in einem Verfahren zur Erlangung eines akademischen Grades vorgelegt.

\_\_\_\_\_  
Ort, Datum

\_\_\_\_\_  
Rishab Handa

To all the readers of this thesis and to those  
who never stop searching for the ultimate truth in Hilbert spaces.

# Contents

<b>Introduction</b>	<b>1</b>
<b>1 Theoretical Background</b>	<b>7</b>
1.1 Non-linear Contact Mechanics . . . . .	7
1.1.1 Hertzian Contacts and Cluster Linearity . . . . .	7
1.2 Soft Glasses in a Viscoelastic Stress Landscape . . . . .	10
1.2.1 Mean Field Theory, Topology Conservation and Quenched Disorder . . . . .	11
1.3 Non-linear Rheology . . . . .	13
1.3.1 Large Amplitude Oscillatory Shear (LAOS) Rheometry . . . . .	14
1.3.2 MITlaos: Characterizing Non-linearities . . . . .	17
1.3.3 Chebyshev Polynomial and FT-rheology: Illustration of Higher Harmonics . . . . .	18
1.4 Differential Rheology: Proof of Stress-Strain Symmetry . . . . .	21
1.5 Summary . . . . .	23
<b>2 Experimental Methods and Challenges</b>	<b>25</b>
2.1 Rheometry . . . . .	25
2.1.1 On choosing the right setup for confined granular flows . . . . .	27
2.1.2 Computing viscoelastic measures via rheometer . . . . .	28
2.1.3 Where lies the effective shearing zone? or How to be sure if the response is homogeneous? . . . . .	33
2.1.4 How to avoid bad data in rheology of granular materials? . . . . .	34
2.2 Bright Field Microscopy . . . . .	36
2.3 Pendant Drop Tensiometry . . . . .	37
<b>3 Non-linear Granular Flows from a Soft Glassy Perspective</b>	<b>41</b>
3.1 Non-linear Rheology of Granular Materials . . . . .	41
3.1.1 Characteristic Degree of Nonlinearity . . . . .	49
3.2 Soft Glassy Rheology of Confined Granular Flows . . . . .	54
3.3 Discussions and General Remarks . . . . .	67
3.4 Summary . . . . .	72
<b>4 Role of Cohesion in Wet Granular Matter</b>	<b>75</b>
4.1 Non-linear Viscoelasticity in Wet Granular Matter . . . . .	76
4.2 Rearrangement Dynamics of Wet Grains and Powders . . . . .	80
4.3 Discussions and General Remarks . . . . .	83
<b>5 Conclusions and Outlook</b>	<b>87</b>

<b>Bibliography</b>	<b>91</b>
<b>Appendix</b>	<b>103</b>
A    Supplementary Figures: LAOS and Soft Glassy Rheology . . . . .	103
B    Powder Formulation for Glass Particles . . . . .	117
B.1    Hydrophilic and Hydrophobic Functionalization . . . . .	117
<b>Acknowledgements</b>	<b>119</b>

# Introduction

*Matter and energy seem granular in structure, and so does "life", but not so mind.*

– Erwin Schrödinger, *WHAT IS LIFE? The Physical Aspect of the Living Cell*

Amongst athermal materials, granular matter classifies as a system of particles typically of  $\geq 1 \mu\text{m}$  size, characterized by their slow relaxation, which upon perturbation continuously solidifies under the action of static friction [1–3]. If smaller than a micron, Brownian motions begin to determine their natural dynamics as thermal fluctuations become apparent [4–6]. At long times, aforesaid dynamics are often recognized as a reminiscence of structural rearrangements, frustration disorder, or frozen state in systems such as supercooled liquids (structural glasses) [7, 8], flocculated nanoparticles [9, 10], polymers [11, 12], concentrated colloids [13, 14] and vortices in superconductors [10]. Although, most physical systems age when disrupted, the Universe itself at the largest scale is in ever-ageing state to reach equilibrium and so does the plasmonic and magnetic patterns in solar flares, convection cells, supergranules, and sunspots [15–18].

Until recently, when the theory of self-organized criticality was introduced [19–21], the general view of how simple the sand or a sandpile is, changed to the very antithesis of it. Unlike materials that are governed by thermodynamics, an intuitive picture of the granular matter remains a major challenge among complex systems. Favourably, the salient features of thermal (glasses, colloids, emulsions, and polymers) and athermal (grains, non-Brownian colloids and powders) materials exhibit striking similarities, such as they flow under specific deformation or form disordered solid (jamming) under other disruptions. To illustrate this, Cates [22–24] in the late '90s, showed that shear driven jammed systems were acknowledged as a class of "fragile matter", clearly captured by the jamming phase diagram, which hereafter became a standard reference. A thermodynamic view of jamming is demonstrated in Fig. 0.1 as a concave surface illustration of jamming-transition based on the equation of state, where jamming is a path-dependent state defined by pressure, shear, and the density [2, 22, 25]. Ageing temperature  $\Theta$  is used to identify the metastable packing arrangement density. A granular system unjams as the jamming point supersede  $J > 1$  and ceases to compact or age when  $J = 1$  [25]. The images ascribed to the diagram illustrate the significance of the jamming-unjamming phenomenon in everyday commodities. An emerging application of such force chains and jammed granular networks has been used as an inspiration to model multifaceted webs of global structures and solve complex network science problems [26]. Note: the readers who wish to go deeper in details are encouraged to study [27].

A granular solid will fluidize and exhibit anomalous rheological response with decreasing density, increasing stress, and increasing pressure, analogously due to temperature in the case of thermal glasses and owing to confinement or some other form of perturbation in the case of granular materials. Another hallmark of the granular matter is the formation of force

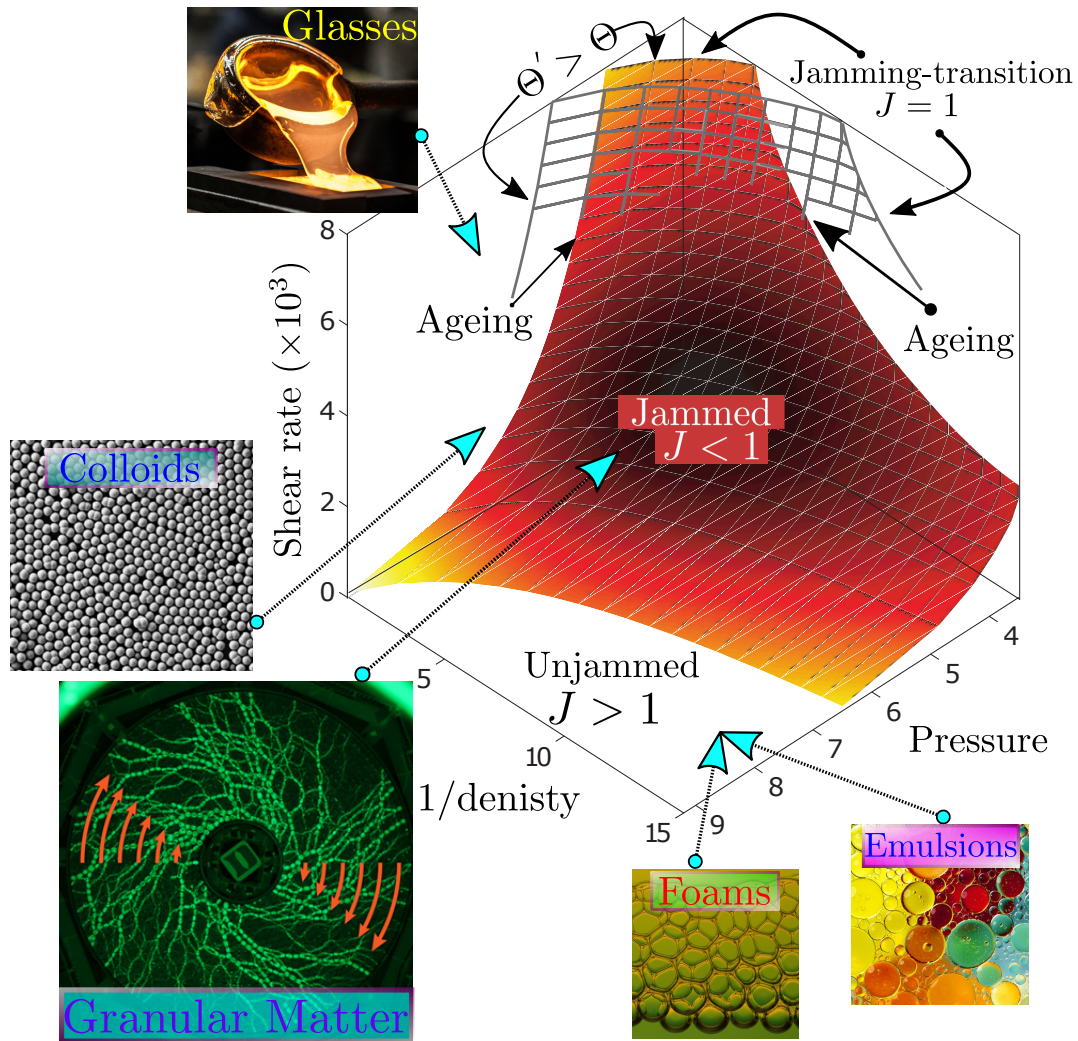


**Figure 0.1:** Jamming phases were first introduced by Liu and Nagel. The modified diagram is redesigned based on the work [28].

chain networks, defined as the inhomogeneous distribution of linear filament-like structures bifurcating with short-ranged spatial correlation function of stress under isotropic compression and long-ranged, under shear [1, 2, 8, 9]. Besides, due to absent tensile stresses in dry grains, inaccessible forces at microscopic scales driven by friction and disorder exhibiting dissipation, classical fluid dynamics, or elasticity theory are rendered inefficient in describing the complete mechanical response of sheared granular systems [9, 22, 29]. In this regard, a statistical framework on how to incorporate structural disorder to elucidate the atypical rheology of soft glasses, Sollich, Hebraud, and Cates ([30, 31]) proposed a model by introducing an additional degree of freedom to the Bouchaud's trap model [7, 32] entitled "Soft Glassy Rheology" model. On further exploration by Fielding, Sollich, and Cates, the model has been widely acknowledged by [2, 8, 9, 12, 23, 29, 33, 34] in studying the complex dynamics of foams, polymers, colloids, and grains.

Experimental issues, that most likely stem from inhomogeneous flow, grain anisotropy, force networks, and those particularly important in rheology, have been broadly studied

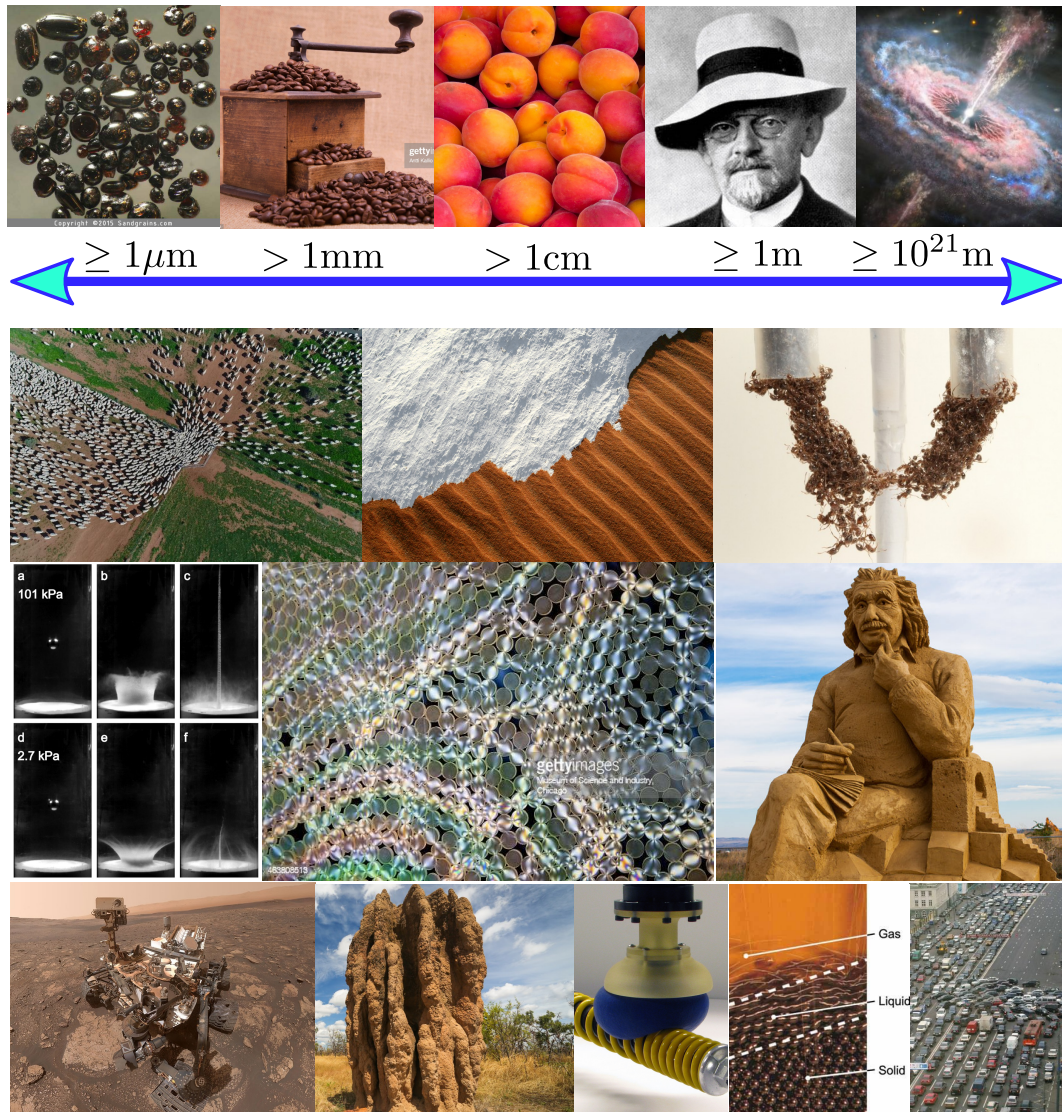


**Figure 0.2:** Granular Matter and its panoramic existence. Top: Size spanned by granular media, from volcanic sand (micron) to quasars (light-years). Bottom: Mother Nature and research competence: from robotic hand using jamming phenomena in picking a heavy spring to the landing of rovers on Mars, sheep herding, ants (active or granular?), granular jets, and photoelastic illustration of force chain networks, snow on Saharan dunes, traffic jams, termite colonies, and the three states of granular matter. All of the images shown here are obtained from google images with suitable keywords.

by Lu, Brodsky, and Kavehpour [25, 35]. The study correlates granular flow regimes: grain-inertial, translational, and quasi-static to common industrial and natural processes; avalanches, landslides, dredging, segregation, and compaction [35]. Moreover, by minimizing the effects of avalanches and shear bands, granular flows in a tube (Poiseuille-like) and steady-state rheology revealed wet grains flow faster than dry [36]. Nevertheless, despite the attempts [9, 33, 35, 37–41], a long-standing problem of providing a coarse-grained description of sheared granular matter, lies the accurate quantification of grain-level structures projected on the macroscopic behaviour, as the associated non-linear contributions

are often overlooked. Non-equilibrium thermodynamics have made staggering progress in the light of developing a statistical framework for complex materials. Despite their vast differences, glasses and grains share a multitude of attributes, much deeper than we may conjecture. The underlying physical processes governing their dynamics seem similar but the reality might be surprising. Albeit the ongoing studies, theory of shear transformation zones (STZs), and the concept of complexity has been a success in understanding the role of effective disorder (temperature) and entropy in glass formers [42]. As proposed, this temperature might just be the tipping point to describe the phenomenological processes of soft condensed matter. Whether manipulated by Nature or industry, the vast majority of materials are in non-equilibrium, and disruption or rapid change in a physical variable (quenching) pushes them into a state of disorder. Consequently, the system begins to relax to attain a new equilibrium state. How fast or slow? hinges upon its plastic response to applied stresses and the dynamics of "effective" temperature.

Owing to the ubiquity of granular matter and its broad application span (see Fig. 0.2), the primary motivation of this thesis is to study the nonlinear rheology of granular matter and powder (relatively more cohesive) systems at large deformation scales, collecting data bodies to develop a soft glassy perspective and provide valuable insights on rapid granular flows. Confined systems under deformation such as kinetically constrained grains, show a "yield stress", or "freeze" into the arrested states of non-zero stress. By gently shearing, from quasi-static to near-inertial regime (0.1 Hz to 10 Hz; large amplitude oscillatory shear, LAOS), granular matter relaxes and stiffens over time exhibiting a plethora of nonlinear events in their rheological response. We demonstrate this by exploiting the analytical and qualitative features of the rheology via Soft Glassy Rheology (SGR) model and FT-rheology combined with Chebyshev Polynomials, the non-linear dynamics of dry and wet granular matter.

*Inertial granular rheology* is recognized for its effectiveness in steady simple shear experiments that allows a direct scaling between the ratio of stress to normal pressure and the inertial number (which non-dimensionalizes the shear rate by mean particle size, normal pressure, and solid density), but in common practice, granular media strongly deviates from inertial rheology [43, 44]. For example, if we look at inclined plane flows, their spatially homogeneous stress fields are described by a tilt angle, however, the angle at which the flowing layer ceases to flow would depend explicitly on the pile thickness [45, 46]. Whereas in the case of standard rheology measurements, the non-uniform flow profiles begin to grow in zones such as shear banding, and the direct scaling to exploit inertial rheology is no longer valid [47, 48]. Inspired by emulsions, the works of Kamrin et. al. [43, 44, 49] provide a constitutive model for size-dependent *nonlocal* rheology, where the flow at any point is influenced by local stress and the flow of neighbouring points. Although the microscopic basis of this nonlocal rheology model stems from the SGR formalism, the focus is on the macroscopic flows of dense granular media. Nevertheless, an opposite approach would entail viewing microscopic processes governed by nonlinear events at mesoscopic scales by virtue of granular rearrangements, which can be too rich in dynamics for the standard rheology to capture. FT-Rheology and other linear algebraic approaches have been previously adopted to describe the sinusoidal input to non-sinusoidal output (nonlinear regime) involving models as Bingham and Giesekus [50], nonetheless, due to overexploitation of assuming a large or infinite number of basis states in the viscoelastic description, render these techniques inefficient [50–55]. Soft glassy rheology perspective however provides a constitutive means to break and solve the nonlinear stress-strain response of a material to

describe its yield events by a single parameter "the noise temperature" as we will study in this thesis.

A brief outline of this thesis is as follows, chapter 1 gives a brief overview of the theories and source models in the vicinity of granular materials. In chapter 2, common difficulties in granular rheology and how to resolve them are presented. Chapter 3 deals with the identification of dynamical regimes in dry and wet grains, namely linear, nonlinear and slip, recognized by an onset strain at which, the characteristic degree of nonlinearity turns intermittently anomalous. By scaling the dissipated energy and viscoelastic moduli via Boltzmann-like constant, rearrangement dynamics of grains are explored where force chains were found to govern dry granular flows, but contrarily, breaking and regeneration of capillary bridges were most pronounced in wet granular systems. Thereupon, by breaking the stress-strain waveforms via symmetry arguments, we argue that the solutions to the SGR model resemble a periodic sequence corroborated by computing the same noise temperature as standard rheological measures, which were all found to increase logarithmically with the applied confinement. The packing dynamics of granular assembly under rheometer is also investigated that provided valuable insights on the failure of percolating force chain networks due to epitaxial arrest of quasilinear clusters of dry grains ascribed to the jamming transition while wet grains expanded as dilatant. Chapter 4 is dedicated to the cohesive granular flows, ergo examines the wet grains and powders, whereby the noise temperature was found to decay asymptotically with increasing surface tension of the wetting fluid, strongly indicating transient caging effects. Besides, we found evidence that suggests a strong coupling between elasticity and viscosity of a granular sample, scalable by a factor that is exactly equal to the applied frequency.



# 1

## Theoretical Background

This chapter is a brief introduction to the theoretical frameworks and formal definitions of the source models required for the remaining part of the thesis. In particular, the topics of contact physics and soft glassy rheology.

### 1.1 Non-linear Contact Mechanics

Bringing two macroscopic solids together, although visibly flat or smooth, the real area at which the contact takes place is in between the tiny fraction of microscopically rough asperities with a plethora of adhesive sites (the birth of a solid-solid *multi-contact* interface). For about 250 years, Coulomb conjectured the universal *coarse-grained* description of granular material, exclusively to link their mechanical response and the morphological features (shape, size and topology) which is still not clear [2]. The key to unravelling the mechanisms behind the exchange of energies at the inter-granular contacts upon perturbation lies in the foreground of solutions to the constraint satisfaction problem. Granular materials being athermal adopt mechanically stable packing, as the force and torque constraint is balanced for all grains. Frictional contacts being the reminiscence of dry granular packings are established by virtue of satisfying Coulomb criterion, an additional constraint,  $f_t \leq \mu f_n$ , where  $\mu$  is the coefficient of friction and  $f_{t(n)}$  is the (normal) tangential contact force [56]. When modelling these systems, the forces are often decomposed into elastic deformation (accounts for repulsion) and dissipative energy loss (momentum transfer and degrees of freedom) [9, 56]. To describe such complex contacts controlling a material's behaviour upon deformation, the stress tensor requires force balance, torque and constitutive equation of stress-strain relation to be satisfied.

#### 1.1.1 Hertzian Contacts and Cluster Linearity

For a couple of overlapping viscoelastic grains ( $i$  and  $j$ ) with radius  $R_i$  and  $R_j$  as shown in Fig. 1.2, a hard-core interactive contact force (see [57]) is given by,

$$F_h(\xi) = \begin{cases} 1 & \text{for } \xi < 0 \\ \infty & \text{for } \xi \geq 0. \end{cases} \quad (1.1)$$

where  $\zeta = R_i + R_j - |\mathbf{r}_{ij}|$  defines the overlap surface of pressure upon hard contact, with  $\mathbf{r}_{ij}$  being the distance between grain centres. Such that the transferred momentum between grains  $i$  and  $j$  with velocity  $\mathbf{v}_i^*, \mathbf{v}_j^*$  (before contact) and  $\mathbf{v}_i, \mathbf{v}_j$  (after contact) is illustrated in the Fig. 1.1 below.

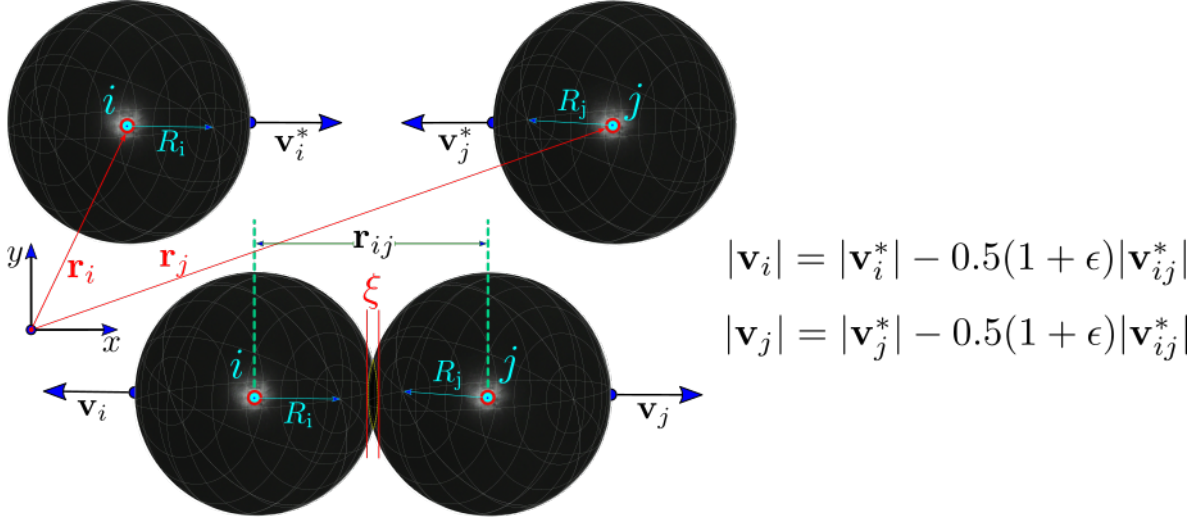


**Figure 1.1:** Schematics of an elastic collision before and after contact between two hard viscoelastic particles  $i$  and  $j$  of radii  $R_i$  and  $R_j$  with corresponding position vectors as  $\mathbf{r}_i$  and  $\mathbf{r}_j$ , respectively. Where  $\mathbf{v}_{ij}^*$  is the velocity of particle  $i$  with respect to the particle  $j$  before contact [57],  $\mathbf{r}_{ij}$  is the distance between grain centres, and  $\zeta$  is the overlap surface upon contact.

Thenceforth, the dissipation can be defined in terms of the restitution coefficient  $\epsilon$  as  $\epsilon \equiv \frac{p_f}{p_i}$  [58], with  $p_i$  and  $p_f$  being the initial and final momenta, respectively, and the dissipated energy is  $\Delta E_d = E_i(1 - \epsilon^2)$ , with  $E_i$  being the kinetic energy before the contact. To apply this formalism in reality, it is often reported analytically rigorous and sometimes impossible to solve for soft grains, as the time-dependence does not fit to the infinite force systems [57, 58]. Therefore, incorporating the Hertzian contact force is preferred in order to mutually link simulations and experiments. For a typical granular system, the Hertzian contact force  $F_{\text{Hertz}}$  combines the elastic repulsion (as  $\zeta$ ) and dissipative damping (as  $A_d$ ) and is given as,

$$F_{\text{Hertz}}(\zeta) = \frac{2Y_m\sqrt{R_{\text{eff}}}}{3(1 - \nu^2)} \left( \zeta^2 + A_d\sqrt{\zeta}\frac{d\zeta}{dt} \right) \quad (1.2)$$

where  $Y_m$  is the Young modulus,  $R_{\text{eff}} \equiv \frac{R_i + R_j}{R_i R_j}$  is the effective radii,  $\nu$  is the Poisson ratio, and  $A_d$  is the dissipative constant, can be defined as a function of viscous constants  $\eta_1$  and  $\eta_2$  [57, 58],

$$A_d = \frac{1}{3} \frac{(3\eta_1 - \eta_2)^2}{3\eta_1 + \eta_2} \frac{(1 - \nu)(1 - 2\nu)}{Y_m\nu^2} \quad (1.3)$$

The idea here is that, if we assume a system  $S$  we know the dynamics of and rescale for example all its sizes  $R'_i$  by a constant factor  $\alpha$ , such that  $R'_i = \alpha R_i$  then how would this new system  $S'$  change? or for both  $S$  and  $S'$  to behave identically, then how the material also has to be changed? In this regard, the table below provides some valuable information on the elastic and dissipative properties of a material when comparing scaled and original [57]. This can be taken into account when comparing numerical simulations and experiments where the system is usually scaled for mathematical convenience.

Parameters	Original System	Scaled System
All Lengths	$x$	$\alpha x$
Time	$t$	$\sqrt{\alpha} t$
Elastic Constant	$\frac{\gamma_m}{\phi(1-\nu^2)}$	$\alpha \frac{\gamma_m}{\phi(1-\nu^2)}$
Dissipative Constant	$A_d$	$\sqrt{\alpha} A_d$

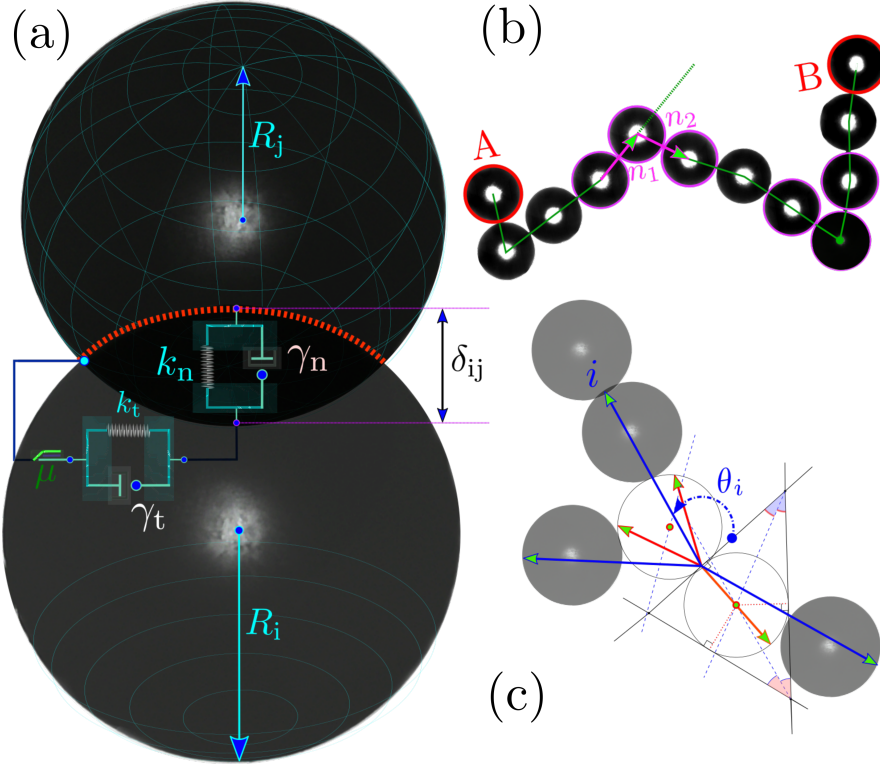


**Figure 1.2:** (a) Schematics of the soft particle interaction model between spheres  $i$  and  $j$  employed for modelling clusters with (b) triplets (encircled in magenta) as shown here, being the smallest cluster in a directed map, here from  $A$  to  $B$  or  $B$  to  $A$  in conjunction with neighbouring contacts that when assigned with a unique identification serves as a graph representation of particle packing. (c) A sketch to illustrate cluster orientation  $\theta_i$  estimation, where the orientation of the vectors forming a new contact (circles) are measured over an arbitrary coordinate axis, where its weighted average computes the probability distribution. The figure is redesigned to briefly summarize the work [59, 60].

Furthermore, when the stress is transmitted through an array of inter-granular contacts, it gives rise to the networks of percolating filamentary force chains [2, 59, 60]. A recent

approach [59, 60] comes to light as one attempts to understand this percolation behaviour of force chains, where these networks are classified by virtue of linear connectivity determined by the critical transition from 1 – *dimensional* systems to silo and hopper flows. Introducing a rate-independent frictional force in the spring-dashpot model by adding a Coulomb slider simplifies the overlap contact between grains  $i$  and  $j$  [59], as shown in Fig. 1.2, where  $k_t$  and  $k_n$  are the tangential and normal coefficients of spring stiffness, and similarly  $\gamma_t$  and  $\gamma_n$  are the damping factors and  $\mu$  is the friction due to the Coulomb slider.

The smallest network of connected particles can be described as a product of unit normals at two contacts ( $\mathbf{n}_1$  and  $\mathbf{n}_2$ ) as  $\mathbf{n}_1 \cdot \mathbf{n}_2 \equiv r_t$ , allowing us to define the linearity of a contact network as  $r = \min(r_t | r_t > 0)$  [59]. Where this minimum triplet linearity  $r$  is intuitively viewed as the "weakest link" due to the fact that as  $r_t \rightarrow 0$ , the fraction of normal force to be transmitted to the subsequent grain decays gradually.

## 1.2 Soft Glasses in a Viscoelastic Stress Landscape

Glasses, as ubiquitous as it may sound, are still among the most sought after topic of condensed matter physics. The conjecture lies in dramatic shifts in the equilibration ("ergodic time",  $\tau_{\text{erg}}(T)$ ) of a glass upon cooling, characterized by the myriad relaxation timescales, where the longest timescale  $\tau_e$  diverges at the experimental glass transition temperature  $T_{g,e}$  by several orders of magnitude with an exponential tail ( $T^{-1}$ ) [2, 7, 12]. Although this glass transition is defined as analogous to supercooled liquids, in nature however the process of supercooling has been vastly exploited by winter flounder (marine life form) and plants (such as lignin, suberin) to survive in harsh weather [61]. Nevertheless, soft glasses constitute smooth and soft interactions, characterized by a growing coherence length between its constituents, similarly diverges at  $T_g$  [12, 31] (see Fig. 1.3). Besides, due to assorted metastable states and unrecognizable order in a given configuration of glass as  $T < T_{g,e}$ , the underlying physics continues to puzzle. Granular solids, unlike soft glasses, adopts isostatic states by satisfying the number of degrees of freedom to the number of constraints [9, 12, 31].

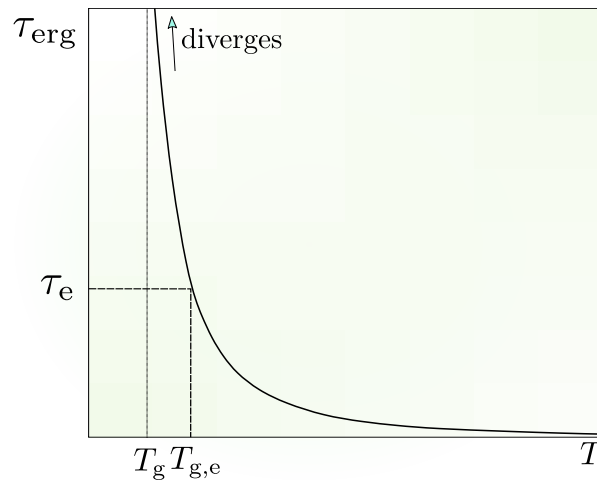


**Figure 1.3:** A sketch to illustrate ergodic time dependence on the temperature, revealing divergence at the experimental glass transition temperature [12].

For a constitutive framework of the Soft Glassy Rheology model to work on soft glasses, the structural disorder is separately introduced by incorporating the strain degree of freedom in trap model formalism. Analogous to Bouchaud's trap models, the sample material is divided into mesoscopic elements, where each individual element is identified by its local shear strain  $l$  ( $l \propto \gamma$ ). Although strain rate  $\dot{\gamma}$  is assumed uniform in the system,  $l$  and stress vary. Hence, the strain energy  $\equiv \frac{1}{2}kl^2$  ascend to reach yield energy  $E$ , allowing an element to yield while resetting  $l = 0$ , where  $k$  is the local shear modulus. Intriguingly, fixing  $E$  and  $k$  same for all the elements in the landscape, the SGR model would manifest a non-glassy model for the ideal case of 2D foam (uniform distribution of hexagonal cells) developed by Princen in the late '70s [62]. Consequently, the disorder is conceptualised by picturing the individual elements in association with their  $E$ , whose initial distribution through mesoscopic elements is determined by the sample preparation. Upon yielding, a mesoscopic element thereupon rearranges in a local equilibrium structure, where a new yield energy  $E$  is then allocated by a history-independent distribution  $\rho(E) \propto e^{-E/\bar{E}}$ . Wherefore, such interactions between elements are described by a scalar variable that accounts for yielding events, termed as noise temperature  $k_B\Theta$  where ( $\bar{E} \gg k_B T$ ). Eventually, the probability  $P(E, l, t)$  of an element with yield energy  $E$  and local strain  $l$  at time  $t$  can be defined in terms of an attempt frequency  $\Gamma_0$  as,

$$\dot{P}(E, l, t) = -\dot{\gamma} \frac{\partial P}{\partial l} - \Gamma_0 e^{-(E - \frac{1}{2}kl^2)/(k_B\Theta)} P + \Gamma(t) \rho(E) \delta(l) \quad (1.4)$$

where  $\Gamma$  is the ensemble average yielding rate  $\Gamma = \Gamma_0 \langle e^{-(E - \frac{1}{2}kl^2)/(k_B\Theta)} \rangle$ . The first term on RHS accounts for convection of  $l$  second describes the yielding of a mesoscopic element and third ensure the rebirth of elements subsequent to yielding (rearrangement or hopping). Such that, the macroscopic stress becomes  $\sigma(t) = k \langle l \rangle$ , and can be calculated when ascribed to the initial condition  $P(E, l, 0)$  and the corresponding strain history (as input signal). Clearly, by setting  $E, l, t$  to output  $\bar{E} = \Gamma_0 = k = 1$ , gives typical yield strain of 1. Besides,  $l = 0$  when the flow is absent so that,  $\dot{P}(E, t) = -e^{(-E/(k_B\Theta))} P + \Gamma(t) \rho(E)$ . On equilibration at long  $t$ ,  $P_{\text{eq}} \propto \exp\{E/(k_B\Theta)\} \rho(E)$  is analogous to the Boltzmann distribution, allows to estimate glass transition if and only if,  $\rho(E)$  is assumed to have an exponential tail, as shown in figure 1.4.

The viscoelastic response of a material in such a stress ensemble can therefore be described by a spatial scalar function  $k_B\Theta$ . For sufficiently small  $k_B\Theta < 1$ , the system is a glass and refrain from equilibration as  $P_{\text{eq}}(E)$  is not normalised, hence the glass transition occurs at  $k_B\Theta = 1 \forall \rho(E) = e^{-E}$ . This ageing thereafter continuously evolve into deeper traps.

### 1.2.1 Mean Field Theory, Topology Conservation and Quenched Disorder

A stress landscape can be constructed for mechanically stable granular systems approaching jamming (point J) by deriving the conservation principles for 1.) force ensemble where stress replaces the role of energy, such that the ensemble basis is analogous to the thermodynamic referential frame, and 2.) the force-moment tensor (volume integral of the stress tensor), which provides a basis to define stress ensemble, computing tensorial analogue of thermodynamic temperature, the noise temperature  $k_B\Theta$  as acknowledged by the works

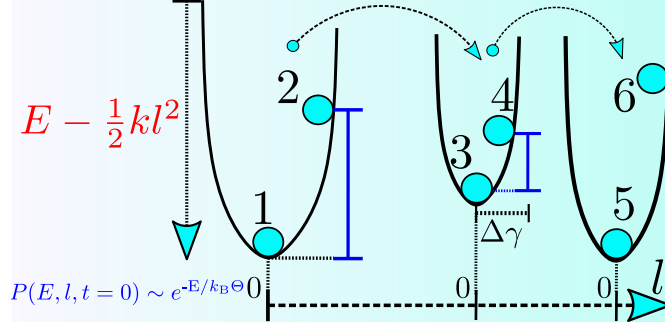


**Figure 1.4:** Schematics showing dynamics of mesoscopic regions (cyan circles, 1-6) at the different local strain in a quadratic potential well, where each trap is given by its depth  $E - \frac{1}{2}kl^2$ , where  $E$  scales as  $\langle E \rangle \propto k_B \Theta \ln(t)$ . The blue vertical bars indicate the energy dissipated by a mesoscopic region while yielding and falling in a less deformed state. The horizontal displacement is arbitrary, each having its own independent zero for the scale of the local strain  $l$ , thus, any trap can be accessed from every other trap and there is no specific connectivity. The figure is inspired by the works [12, 30, 31].

of Henekes, Chakraborty and Behringer [2, 8, 34] on developing the Ginzburg-Landau description of jammed granular systems. The activated yielding events in a viscoelastic stress landscape is modelled by the interactions between mesoscopic elements. Thermodynamic description of such an ageing system is assumed quenched in an energy field, initially at high temperature  $T_i \gg T_{g,e}$  and evolving to a low temperature  $T < T_{g,e}$  for the waiting time  $t_w$ , measures the total relaxation [7, 12]. Hereof, one might ask, what does a plethora of yielding events and structural disorder have in common? or can a typical rheological response of material provide a crucial path that connects microscopic processes to macroscopic?

The answer lies in the conception of "complexity", and more precisely, defining a naturally conserved variable that can quantify the collection of metastable states. Mean field theory (MFT) allows us to establish a constitutive relationship between stress and the microscopic geometry of the packed granular matter. Assuming that the granular packing is mechanically stable, in the mean field spirit, a path integral is then performed over all the configurational states of packing and coarse-grained variables to provide a continuous field as a collection of microscopic descriptors of the packing, such as the *force – moment* tensor (a measure of the noise temperature). In MFT of granular packings, a field comprising all the possible constraints is defined in terms of the *Airy stress function* that accounts for force and torque balance constraints and by incorporating symmetry arguments and stress fluctuations, a statistical framework for jammed granular packing was proposed [34]. To this end, such form of complexity to describe disordered systems such as spin glasses, was previously reported successful, in understanding the free energy minima of metastable states [7, 32]. However, despite their similarities, weak thermal motions in the granular matter make it really challenging to adopt a similar basis for complexity akin to spin glasses. Notwithstanding, the mean field theory picture these states in an energy potential well diverging in the thermodynamic limit [2, 7, 9]. To lay a similar ground for granular materials, their topology is assumed conserved, providing an analogous means to define complexity [9, 34]. The primary notion to demonstrate this stems from drawing a comparison with Boltzmann's *Stosszahlansatz*, first demonstrated by Boltzmann in formulating his conjecture for dilute

gases, where the distribution of momenta would evolve as a function of translation in time, resulting in precisely tracking the growth of single-particle distribution in time [63]. Nevertheless, the statistics involved in static granular packings must be defined in space and not time [9, 63]. In other words, the time dimension from kinetic theory is replaced by a spatial translation motion, such that the sum of momentum vectors implicated in the action of a particle colliding is conserved, as shown by Fig. 1.5. Favourably, this theoretical framework allows defining a rank-2 tensor "temperature", provided that at maximum entropy the intergranular contact forces in equilibrium are conserved in all the directions. Consequently, the partition of stress and fabric fluctuations (joint contact angle distribution) together satisfy all the possible force-torque constraints. To illustrate this, let's imagine a dashed line as shown in Fig. 1.5, passing horizontally and perpendicularly through grains highlighted in green, exploring the phase space in a packed granular assembly with force contact points shown as blue dots. Now, if we attempt to calculate the amount of force along horizontal line, the result will be identical to the perpendicular line, as this sheet of force *translate* through a 2D granular packing, hence proving that the contact forces are conserved.

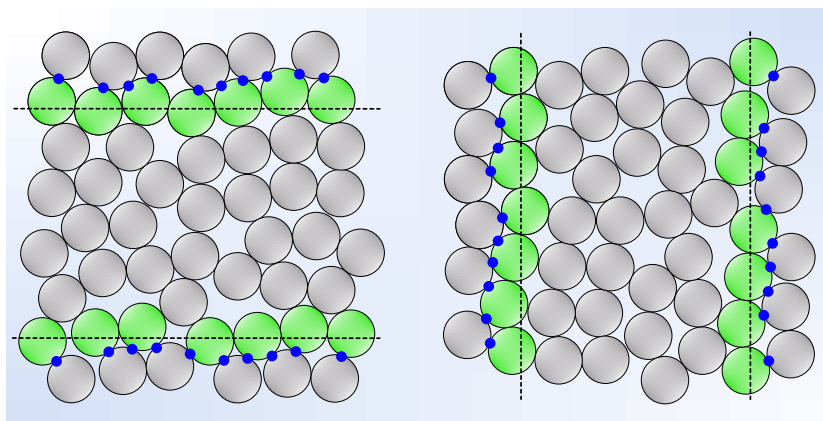


**Figure 1.5:** Conservation of contact forces in granular packing, in order to introduce an additional degree of freedom to describe granular packings and their evolution in space and not time. The figure is inspired from the work [63].

As a final remark, a system in a state of equilibrium by virtue of its internal interactions (which are self-enforced) would be classified under a statistical framework similar to what encompasses the ergodic theorem for kinetic systems, where all conserved-energy states are equally probable, thereby justifying the hallmark entitled for granular packings that evolve as "self-ergodic" systems. This analogy with Boltzmann-like distribution, allows us to predict the probability of a microscopic state in an equilibrated packed granular assembly existing at a certain noise level as the well known Kramers rate [34, 63, 64].

### 1.3 Non-linear Rheology

Rheology is the study of deformation and flow of matter [65]. As defined, the topic studies the vast majority of condensed matter, with its prime motivation to explain the unusual mechanical behaviour (storage and loss moduli) of matter, otherwise rendered inexplicable via classical models of elasticity and Newtonian fluid dynamics. The objective is to identify

the underlying mechanism as the matter deforms, expands in two branches; 1) macroscopic (characterize a material at scales larger than its microstructures) and 2) microscopic (combination of statistical physics and defect mechanics). Being the fundamental concept of continuum mechanics, the stress-strain relationship is thus the most important one to establish [65].

The mechanical response of a material to oscillatory shear results in either elastic properties or viscous properties, or viscoelastic properties. A purely elastic material outputs the stress response as a function of the applied strain and viscous with respect to strain rate. The shear modulus  $G$  (intrinsic property) can be calculated by a ratio of stress  $\sigma$  to the applied strain  $\gamma$ , as  $G = \sigma/\gamma$  [65, 66]. Linear response of material would typically output  $G$  as a constant slope over strain amplitude. Nevertheless, for a nonlinear response,  $G$  has a strong dependence on the strain amplitude,  $G = G(\gamma)$ . A convenient alternative to describe mechanical response is by the use of tangent modulus  $G_\kappa$ , which would diverge from  $G$  as the response becomes non-linear. Similarly, by applying a constant shear rate, a purely viscous material can be characterized accredited by the resulting shear stress as  $\eta = \sigma/\dot{\gamma}$ , with a nonlinear viscosity  $\eta(\dot{\gamma})$  and the velocity gradient as  $\dot{\gamma} = v/d$  where  $v$  is the velocity and  $d$  is the fluid layer's thickness (Newton's law) [65, 66]. Consequently, a tangent viscosity is therefore defined as,  $\eta_\kappa = d\sigma/d\dot{\gamma}$  [65]. Common protocols to study and obtain rheological data, complex behaviour, in particular, involve small amplitude oscillatory shear (SAOS), large amplitude oscillatory shear (LAOS), stress relaxation on sudden shearing displacement, and creep recovery. Readers, who wish to go deeper in details, are encouraged to study the following books [51, 65–73].

A nonlinear viscoelastic response however not only depends on the deformation timescale but also the amplitude of deformation and due to which, many test protocols fails to systematically provide the full spectrum of important timescales and the respective strain dependence. Alternative to oscillatory deformation to examine nonlinear rheology is the step-strain or step-rate tests, but neither takes into account, both, linear viscoelasticity and steady flow [54, 74]. Besides, thixotropic tests are also used typically to probe time-dependent nonlinearities in the viscous response, for example, by setting the shear-rate up to a certain value over a fixed time followed by successively reverse ramping the shear-rate. Dynamic viscosity is then depicted by a hysteresis-like loop as  $\sigma(\dot{\gamma}, t)$ , but the linear response of the ramps often mismatch to the shear-rate and therefore under-perform to characterize a genuine viscoelastic response [75].

### 1.3.1 Large Amplitude Oscillatory Shear (LAOS) Rheometry

The most common dynamic oscillatory shear test entails a sinusoidal deformation is applied on the material and its mechanical response is measured in time [52, 53]. The test regime that reveals a linear viscoelastic response is termed as small amplitude oscillatory shear (SAOS), where LAOS would evoke a nonlinear response [54, 74]. As we increase the amplitude of strain or stress in the test protocol at a fixed frequency, the linear to nonlinear transition in the material response can be identified [51, 76]. As the strain amplitude in SAOS is small ( $\gamma \sim 10^{-2} - 10^{-1}$  for polymers while  $\gamma < 10^{-2}$  for dispersions and emulsions), the viscoelastic moduli are found independent of the strain and the stress response

results as a sinusoidal output [74]. Note: within the resolution limit of the rheometer, a SAOS test generally depicts the material in a linear regime to describe its complete rheological response in terms of the viscoelastic moduli. Albeit the relevance of SAOS in capturing a thorough view of microstructure and the respective rheology of a material, the picture is still limited to the linear viscoelastic regime only (i.e. small deformation). Nevertheless, in industries, the situation is quite nonlinear, as the material is processed rapidly and at large deformation scales, wherein SAOS fails to provide any relevant information to put into practice. Thenceforth, for better quality control and deeper characterization of the undergoing processes when a material is processed, LAOS offers a broader scale to study the nonlinear response of the material. In LAOS, to simultaneously determine the elastic and viscous response, the material is subjected to oscillatory deformation that acknowledges the nonlinear viscoelastic response pertaining to the steady flow and linear viscoelasticity in a 2D space  $\{\omega, \gamma_0\}$  [69]. Shear deformation depicts the input strain in the form of  $\gamma(t) = \gamma_0 \sin(\omega t)$ , where  $\gamma_0$  is the strain amplitude and  $\omega$  is the frequency of deformation. As a response, an oscillatory strain-rate  $\dot{\gamma}(t) = \dot{\gamma}_0 \cos(\omega t)$  with  $\dot{\gamma}_0$  as the strain-rate amplitude, is imposed, the stress becomes oscillatory with a component in phase with the strain i.e. elastic stress as  $\sigma' = f'(\gamma)$  and a component in phase with the strain-rate i.e. viscous stress as  $\sigma'' = f''(\dot{\gamma})$ , provided that the strain and strain-rate inputs are 90 deg out of phase as acknowledged by the phase quadrature [54, 72]. This enables us to decompose viscoelastic stresses as elastic stress, a function of strain  $\sigma \sim G\gamma$  and viscous stress, a function of strain-rate  $\sigma \sim \eta\dot{\gamma}$ . The stress response in the linear regime thus reads,[71],

$$\sigma(t) = \gamma_0(G' \sin(\omega t) + G'' \cos(\omega t)) \quad (1.5)$$

with  $G'$  as the elastic modulus and  $G''$  as the viscous modulus [77, 78]. LAOS approach requires two input parameters, frequency  $\omega$  (with Deborah number as  $De = \lambda\omega$ , where  $\lambda$  is a relaxation time) and strain amplitude  $\gamma_0$  that forms a 2D parameter space, the well known Pipkin space (see Fig. 1.6) which maps the important response boundaries of viscoelastic materials [72].

The low frequency limit in vanishing strain-amplitude,  $\gamma_0 \rightarrow 0$ , integrate the material properties only as a function of the loading timescale, where  $\omega \rightarrow 0$ , represents the quasi-static response in a steady flow test. At the third limit of high frequency,  $\omega \rightarrow \infty$ , the response is purely elastic. Nevertheless, the region of our interest (questioned in Fig. 1.6) belongs to an intermediate frequency and large amplitudes, where most materials are often processed and used (the nonlinear viscoelastic region)[53, 54, 72]. It has been since a challenge to provide complete rheology of material bridging micro-macro processes, ergo answering the question posed here. By systematically ramping up the strain amplitude  $\gamma_0$ , the nonlinear viscoelastic regime is eventually reached. This approach is entitled the large amplitude oscillatory shear (LAOS) test. Works of Harris [77], Philippoff [78] and Onogi et al. [79] in mid '60s-late '70s introduced FT-rheology and the basis for LAOS rheology. In a nonlinear viscoelastic response, the stress is no longer defined by Newton's law and the viscoelastic moduli,  $G'$  and  $G''$  possesses what's called "non-linearities". As challenging as it may sound to separate and describe these non-linearities from a material's response, two analytical concepts are generally used. 1) The time-series response  $\sigma(\omega t)$  or 2) the parametric representation as waveforms of stress vs. strain or stress vs. strain-rate (given the stress is a

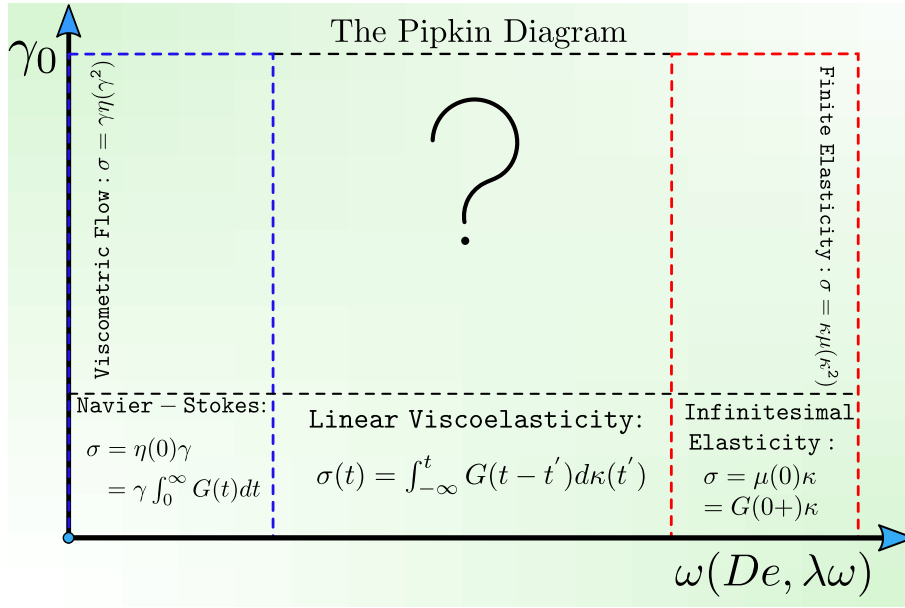


**Figure 1.6:** Pipkin diagram sourced from the works of A. C. Pipkin [72] on fluids flow regimes. The viscoelastic flow falls in low frequency regime for viscous behaviour and high frequency for elastic properties. Linear viscoelasticity is observed at small strain amplitude  $\gamma_0$ . The question mark though, conjecture the region of large strains and frequencies, at which vast majority of materials are processed and applied.

function of the orthogonal inputs). Owing to its relatively simple transformation, delicately distinguishing the inherent periodic signals holding within the nonlinearities into a series of orthogonal trigonometric functions, Fourier Transform (FT-) Rheology, offers a rather tailored approach that suits the time-dependent oscillatory stress to give the periodic response as [51, 77, 78, 80],

$$\sigma(t; \omega, \gamma_0) = \gamma_0 \sum_n \{G'_n(\omega, \gamma_0) \sin(n\omega t) + G''_n(\omega, \gamma_0) \cos(n\omega t)\}. \quad (1.6)$$

Although mathematically strong and most convenient at small strains, FT-Rheology face two major challenges when applied to LAOS data. 1) Lacks physical definitions of detected nonlinearities in accordance with Total Harmonic Distortion (T.H.D.), which is known as a global indicator of nonlinear response [54, 70, 80, 81]. Albeit the typical outcome of commercial rheometers is the first-harmonic viscoelastic moduli ( $G'_1$  and  $G''_1$ ), the stress response is no longer a single-harmonic sinusoid. 2) Even though the use of strain rate superposition provide sufficient information pertaining to LAOS data, still fails to acknowledge a significant amount of nonlinearities. Alternatively, the time-series stress signal for LAOS [53, 82] analysis can be used to decompose the response into viscoelastic functions by sets of sinusoidal, square and triangular wave formalism [54, 83, 84] to have a clearer picture of nonlinearities in the raw data signals. Nevertheless, unlike the harmonic series basis functions in FT-rheology, the aforesaid functions are not mutually orthogonal, are thus reported obscure [52, 54, 74, 82]. Moreover, Tee and Dealy [54, 70] proposed another viable approach that quantifies non-linear viscous Lissajous-Bowditch curves but without any physical de-

scription, hence akin to the earlier demonstration by Philippoff [78]. Eventually, the works of Cho [52] on the geometrical decomposition of Lissajous-Bowditch loops into a superposition of elastic and viscous response via symmetry arguments offered a unique distinction but due to the non-orthogonality and a user dependent choice of polynomial order for regression analysis, rendered pragmatic in quantifying nonlinearity. Taking into consideration the aforementioned successes and drawbacks, a relatively refined approach was proposed as an analytical framework, developed by Ewoldt and Mckinley [54, 82, 85].

### 1.3.2 MITlaos: Characterizing Non-linearities

Decades of studies and efforts have been dedicated to investigating the yield and rheology of granular matter, with an aim to predict and fine-tune its flow behaviour for industrial and geological benefits. However, one of the major drawback in predicting granular flows with basic rheological means, is that the presence of non-linearities in their raw signal, prevent us from obtaining valuable information [35, 43, 86]. This issue was recently resolved for gels and polymers by applying an analytical framework termed "MITlaos" developed for the MATLAB platform by Ewoldt and Mckinley [54, 74, 76]. Hence, with this motivation, we employ this analytical method to precisely characterize the nonlinearities in granular flows. MITlaos is an open-source licenced tool and the code can be obtained upon a formal request to the authors. As explained above, MITlaos uses the time-series signals of raw stress-strain data with options to set user-specified parameters for the analysis (frequency, strain, stress and time). The code output includes processed data files (in ASCII format) and analysed datasets in image format. The data file outputs can be used for further analysis, as it already calculates the viscoelastic moduli and the corresponding time-series signals as,  $\sigma'(\gamma(t))$  and  $\sigma''(\dot{\gamma}(t))$ , respectively [54]. Typically, one applies an oscillatory shear strain,  $\gamma(t) = \gamma_0 \sin(\omega t)$  and so the orthogonal strain-rate  $\dot{\gamma} = \gamma_0 \omega \cos(\omega t)$ . Linear response of a material is often obtained at small strain amplitudes and can be determined by the viscoelastic moduli  $G'$  and  $G''$  obtained from the stress in phase with  $\gamma(t)$  and  $\dot{\gamma}(t)$ , respectively. Increasing strain amplitude  $\gamma_0$  leads to the nonlinear viscoelastic properties, hence classifies the large amplitude oscillatory shear (LAOS) test. A complete representation of stress (caused by a sinusoidal input strain  $\gamma(t) = \gamma_0 \sin(\omega t)$ ) can be written in the following forms of Fourier series, corresponding to either the elastic or the viscous response,

$$\sigma(t; \omega, \gamma_0) = \gamma_0 \sum_{n, \text{odd}} G'_n(\omega, \gamma_0) \sin n\omega t + G''_n(\omega, \gamma_0) \cos n\omega t \quad (1.7)$$

$$\sigma(t; \omega, \gamma_0) = \dot{\gamma}_0 \sum_{n, \text{odd}} \eta''_n(\omega, \gamma_0) \sin n\omega t + \eta'_n(\omega, \gamma_0) \cos n\omega t \quad (1.8)$$

Assuming that the stress response is in an odd symmetry to the axial direction of shear strain, therefore only the odd-harmonics are represented by the Fourier transform [67]. The presence of even-harmonic would imply that the stress response stemmed from the transient flows, such as secondary flows [87], or the dynamic wall slip [88]. Although this FT-rheology gives a robust interpretation of linear viscoelastic measures in the small strain limit, but is still inefficient to satisfy the T.H.D. [89] or the normalized intensity of the 3rd harmonic [90]. Furthermore, Lissajous-Bowditch (LB) loops representation of the raw

LAOS stress-strain data offers rich analytical features to describe nonlinear properties like strain-stiffening or shear thickening [37, 52, 54, 74, 82]. The data corresponding to  $\sigma(t)$  vs.  $\gamma(t)$  refers to the elastic Lissajous-Bowditch loop and similarly,  $\sigma(t)$  vs.  $\dot{\gamma}(t)$  to the viscous Lissajous-Bowditch loop [54]. Despite the attempts to build on the FT rheology, several approaches have been put forward for quantifying the nonlinear viscoelasticity in LAOS [52, 70, 82]. Nonetheless, the methods do not provide sufficient information do not account for all the viscoelastic materials.

### 1.3.3 Chebyshev Polynomial and FT-rheology: Illustration of Higher Harmonics

The physical significance of LAOS data lies in the extension of orthogonally decomposed stress into an elastic stress as  $\sigma'(x)$ , with  $x = \gamma/\gamma_0 = \sin \omega t$  and the viscous stress as  $\sigma''(y)$  with  $y = \dot{\gamma}/\dot{\gamma}_0 = \cos \omega t$  by exploiting the symmetry arguments [52-54]. Thus, the total oscillatory stress can be written as a sum of the superposed stresses,  $\sigma(t) = \sigma'(t) + \sigma''(t)$ . Here, the assumption is that the elastic stress  $\sigma'$  is in the odd-symmetry with respect to  $x$ , and even-symmetry to  $y$ , and vice versa for viscous stress  $\sigma''$ . A direct correlation of  $\sigma'$  and  $\sigma''$  to the Fourier decomposition ([52, 74, 82]) then reads,

$$\sigma' \equiv \frac{\sigma(\gamma, \dot{\gamma}) - \sigma(-\gamma, \dot{\gamma})}{2} = \gamma_0 \sum_{n, \text{odd}} G'_n(\omega, \gamma_0) \sin(n\omega t), \quad (1.9)$$

$$\sigma'' \equiv \frac{\sigma(\gamma, \dot{\gamma}) - \sigma(\gamma, -\dot{\gamma})}{2} = \gamma_0 \sum_{n, \text{odd}} G''_n(\omega, \gamma_0) \cos(n\omega t). \quad (1.10)$$

Many choices of basis functions have been applied and studied in their quest to simplify the time-series functions of the stress response, such as polynomial regression fit [52, 85], in addition to other proposed sets of orthogonal polynomial basis functions as Laguerre, Hermite, Jacobi, Ultraspherical (Gegenbauer), Legendre, and Chebyshev polynomials of the first and second kind [53, 54, 91]. In this regard, the choice of "efficient" polynomials is Chebyshev polynomials, as it describes  $\sigma'$  and  $\sigma''$  over a specified range  $[-1, +1]$ , keeping odd symmetry at  $x = 0$  with access to an additional range of higher-order harmonic contributions. Hence building on the chosen basis set, we can reformulate the elastic and viscous contributions to the total stress response as

$$\sigma'(x) = \gamma_0 \sum_{n: \text{odd}} e_n(\omega, \gamma_0) T_n(x) \quad (1.11)$$

$$\sigma''(y) = \gamma_0 \sum_{n: \text{odd}} v_n(\omega, \gamma_0) T_n(y) \quad (1.12)$$

where  $T_n(x)$  is the  $n$ th-order Chebyshev polynomial of the first kind, with  $x$  and  $y$  being  $\gamma/\gamma_0$  and  $\dot{\gamma}/\dot{\gamma}_0$ , respectively, that lies in  $[-1, +1]$  domain to allow orthogonality. Due to the orthonormal nature of the functions for all orders, the Chebyshev coefficients  $e_n$  and  $v_n$  are independent of each other. Henceforth,  $e_n(\omega, \gamma_0)$  represents elastic Chebyshev coefficients and  $v_n(\omega, \gamma_0)$  represents the viscous Chebyshev coefficients. For a linear regime  $e_3/e_1 \ll 1$

and  $v_3/v_1 \ll 1$  such that the linear viscoelasticity can be determined as  $e_1 \rightarrow G'$  and  $v_1 \rightarrow \eta' = G''/\omega$  [76]. Positive contribution of the third-harmonic, i.e. at  $n = 3$  implies higher elastic stress at maximum strain, and  $e_3 > 0$  would be interpreted as an intra-cycle strain-stiffening of the elastic response, and  $e_3 < 0$  would points to the strain-softening. Likewise, positive values of  $v_3$  would corresponds to intra-cycle shear thickening and  $v_3 < 0$ , shear-thinning [52, 54]. Favourably, the Chebyshev coefficients  $e_n$  and  $v_n$  in the strain or strain-rate test, can be recast in Fourier coefficients (in time domain) as follows,

$$e_n = G'_n (-1)^{\frac{n-1}{2}} \quad n : \text{odd} \quad (1.13)$$

$$v_n = \frac{G''_n}{\omega} = \eta'_n \quad n : \text{odd} \quad (1.14)$$

We exploit this compatibility clause with FT-rheology to deduce the noise temperature of grains from their non-linear viscoelastic response, in Chapter 4. Thus, the third-order Chebyshev coefficients exhibit deviation from linear viscoelasticity however only provide a rough physical interpretation given that the Fourier coefficients are used as a meaningful measures of the nonlinearity [82, 85]. Some reports in FT rheology are presented by utilizing the amplitude and phase [92], in which the above equations can be formulated as,

$$\sigma = \gamma_0 \sum_{n:\text{odd}} |G_n^*| \sin(n\omega t + \delta_n) \quad (1.15)$$

where  $|G_n^*| = \sqrt{G_n'^2 + G_n''^2}$  is the scaled stress magnitude and  $\delta_n$  is the phase angle of the applied strain,  $\gamma(t) = \gamma_0 \sin \omega t$ . Hereby, we only take the signs of third harmonic Chebyshev coefficients into consideration to reveal the elastic and viscous nonlinearities. A set of equations is shown below as a reference adopted from the works [54, 85], to signify the nature of elastic and viscous Chebyshev coefficients and their underlying physical description, as illustrated later in Fig. 1.7.

$$2e_3 = -|G_3^*| \cos \delta_3 \begin{cases} > 0, \text{ strain-stiffening} & \text{for } \pi/2 < \delta_3 < 3\pi/2 \\ = 0, \text{ linear elastic} & \text{for } \delta_3 = 0, \pi \\ < 0, \text{ strain-softening} & \text{for } -\pi/2 < \delta_3 < \pi/2 \end{cases} \quad (1.16)$$

$$v_3 = \frac{|G_3^*|}{\omega} \sin \delta_3 \begin{cases} > 0 \text{ Shear-thickening} & \text{for } 0 < \delta_3 < \pi \\ = 0 \text{ linear viscous} & \text{for } \delta_3 = 0, \pi \\ < 0 \text{ shear-thinning} & \text{for } \pi < \delta_3 < 2\pi \end{cases} \quad (1.17)$$

Where sine transform of the first-harmonic is defined as  $G_1' = \omega/(\pi\gamma_0^2) \oint \sigma(t)\gamma(t)dt$  to account for the average elasticity in LAOS coordinate space  $(\omega, \gamma_0)$ . Herein, the set of elastic moduli can be given in relation to the conventional FT-rheology and the Chebyshev polynomial decomposition as [80, 85],

$$G'_M \equiv \left. \frac{d\sigma}{d\gamma} \right|_{\gamma=0} = \sum_{n \text{ odd}} n G'_n = e_1 - 3e_3 + \dots \quad (1.18)$$

$$G'_L \equiv \left. \frac{\sigma}{\gamma} \right|_{\gamma=\gamma_0} = \sum_{n \text{ odd}} G'_n (-1)^{\frac{n-1}{2}} = e_1 + e_3 + \dots \quad (1.19)$$

with a quoted description as " $G'_M$  is the *minimum-strain modulus* or tangent modulus at  $\gamma = 0$  and  $G'_L$  is the *large-strain modulus* or secant modulus at  $\gamma_{\max}$ " [52, 54, 82]. The graphical definitions of these non-linear viscoelastic measures are alternatively illustrated for a typical Lissajous-Bowditch loop in Chapter 4. Furthermore, since the elasticity can converge to the linear elastic modulus in small strain limit, entailing, that at  $e_3/e_1 \ll 1$ ,  $G'_L = G'_M = G'_1 = G'(\omega)$  are equivalent to the linear viscoelastic moduli in the linear regime and different otherwise in the nonlinear regime. The respective Lissajous-Bowditch loop with a tangent at  $\gamma = 0$  and a secant at  $\gamma/\gamma_0 = x = 1$ . In addition, the value of elastic stress taken at  $\gamma_{\max}$  as  $G'_k \equiv d\sigma'/d\gamma|_{\gamma=\gamma_0}$  results in the differential modulus. A natural approximation of elastic modulus can be given by measuring the minimum-strain modulus  $G'_M$  at zero instantaneous strain. Because for oscillatory measurements where  $\gamma(t) = \gamma_0 \sin(\omega t)$  at  $\gamma = 0$ , the strain rate is at a local maximum,  $d\dot{\gamma}/dt = 0$ , due to which the viscosity measures are locally constant. Alternatively,  $G'_L$ , the secant modulus at maximum strain also results in elastic modulus, given that for  $\dot{\gamma} = 0$  at  $\gamma = \gamma_0$ , indicating zero viscosity [54, 82, 85].

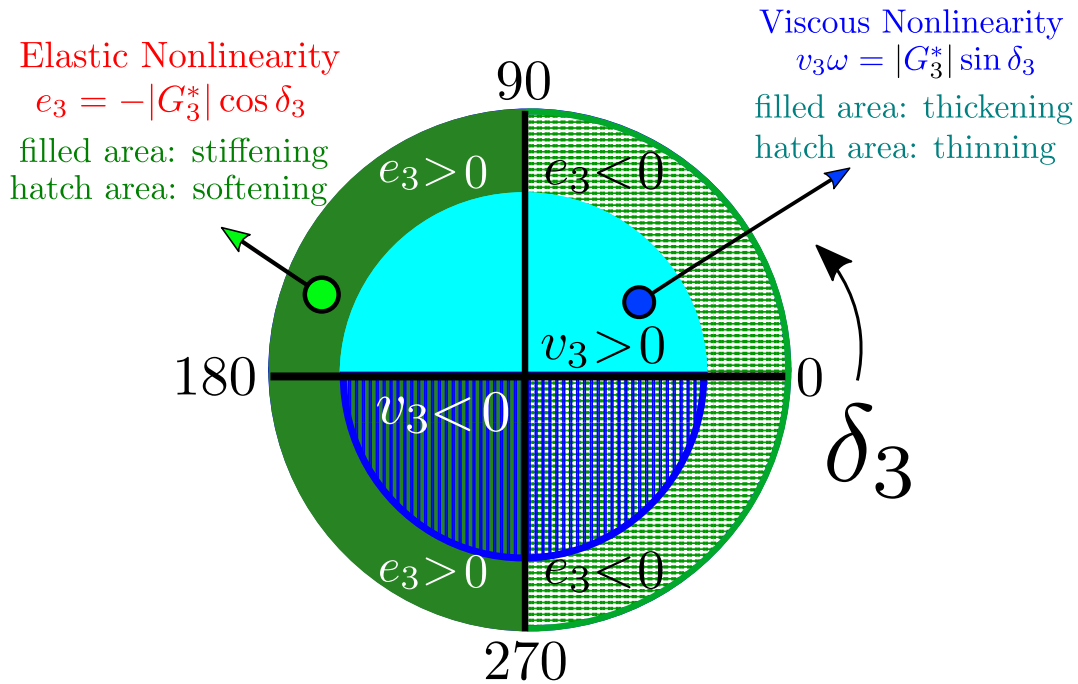


**Figure 1.7:** Diagram adapted from the study [54, 85] to capture the physical significance of the third-harmonic phase angle  $\delta_3$  pertaining to Chebyshev coefficients, via quadrant picture.

Many have reported [79, 81, 83, 84] that the first-harmonic loss modulus  $G''_1$  determines the total energy dissipated by the material under oscillatory shear deformation. Therefore, the

energy dissipated per unit volume can be written as  $\pi\gamma_0^2 G_1''$ , with the average coefficient of dissipation per cycle being,  $G_1'' = \eta_1' \omega$ . Furthermore, a similar set of measures relative to elastic response can be defined as below, to capture the viscous contribution in the present nonlinearities,

$$\eta_M' \equiv \left. \frac{d\sigma}{d\dot{\gamma}} \right|_{\dot{\gamma}=0} = \frac{1}{\omega} \sum_{n:\text{odd}} n G_n'' (-1)^{(n-1)/2} = v_1 - 3v_3 + \dots, \quad (1.20)$$

$$\eta_L' \equiv \left. \frac{d\sigma}{d\dot{\gamma}} \right|_{\dot{\gamma}=\pm\gamma_0\omega} = \frac{1}{\omega} \sum_{n:\text{odd}} G_n'' = v_1 + v_3 + \dots \quad (1.21)$$

Where  $\eta_M'$  is the minimum-rate dynamic viscosity at  $\dot{\gamma} = 0$  and  $\eta_L'$  is the large-rate dynamic viscosity at  $\dot{\gamma} = \gamma_0\omega$ .  $G_1'$  is the first harmonic (linear) elastic modulus and  $\eta_1'$  is the corresponding dynamic viscosity.

## 1.4 Differential Rheology: Proof of Stress-Strain Symmetry

Thus defined, the stress under LAOS is depicted in the following form, with proof expressed in axioms as; (1) Stress under LAOS is a continuous and differentiable function of  $x$  and  $y$ , and (2) The dependence of stress on the strain amplitude, frequency and time is implicit through  $x(t)$  and  $y(t)$  [52]:

$$\sigma(\omega, \gamma_0, t) = \sigma(x, y) \quad (1.22)$$

(3) By changing the sign of the strain, it follows:

$$\sigma(-x, -y) = -\sigma(x, y) \quad (1.23)$$

The stress in the case of arbitrary deformation is a form of nonlinear differential or integral equation, however, for a steady oscillatory shear can be represented in a nonlinear algebraic function of the strain, strain rate and its higher time derivatives [52, 93, 94]. Although these derivative of the strain are independent, they are directly scalable with the strain or strain rate, validating the use of algebraic form. This further ensures that the LB-loops are true "loops" and not open or "broken" (so implies the axiom (1)). Consequently, the second axiom is satisfied when the direction of flow is reversed. Lastly, the third axiom then proves, that the stress is in odd symmetry for both  $x$  and  $y$  [52, 95], thenceforth can be decomposed as:

$$\sigma(x, y) = \frac{\sigma(x, y) - \sigma(-x, y)}{2} + \frac{\sigma(x, y) - \sigma(x, -y)}{2} \quad (1.24)$$

such that,

$$\sigma(-x, y) = -\sigma(x, -y) \quad (1.25)$$

where the first term on the rhs is odd for  $x$  and even for  $y$ , and the second term is even for  $x$  and odd for  $y$  [93, 94, 96]. This mathematically acknowledge the symmetry of stress-strain relationship [52, 97, 98] (that we ought to invoke to reveal symmetry lines of viscoelastic stress-strain waveforms in correspondence with the SGR model in Chapter 4). This equality or stress-strain symmetry can be described as:

$$\sigma_{\text{Elastic}} = \frac{\sigma(x, y) - \sigma(-x, y)}{2}, \sigma_{\text{Viscous}} = \frac{\sigma(x, y) - \sigma(x, -y)}{2}, \quad (1.26)$$

As defined previously, the stress  $\sigma_{\text{Elastic}}$ , is odd for  $x$  and even for  $y$  (vice-versa for viscosity), therefore

$$\oint \sigma_{\text{Elastic}} dx = 0; \quad \text{and} \quad \oint \sigma_{\text{Viscous}} dy = 0 \quad (1.27)$$

so that,

$$\oint \sigma dx = \oint \sigma_{\text{Elastic}} dx, \quad \oint \sigma dy = \oint \sigma_{\text{Viscous}} dy. \quad (1.28)$$

As we recall the symmetry breaking equations first defined in 1.11 and 1.12, and here in 1.26, it satisfies equations 1.29 and 1.30 and eventually shows that  $\sigma' = \sigma_{\text{Elastic}}$  the elastic stress, and  $\sigma'' = \sigma_{\text{Viscous}}$  the viscous stress. To prove this, we take the loop integral of a function  $f$  of  $x$  and  $y$  and  $g$  of  $x$  and  $y$ , and separately show that with respect to  $x$  or  $y$ , the integral outputs zero provided that the odd-even symmetrical basis is not violated [52, 94, 95], we thus write,

$$\begin{aligned} \oint f(x, y) dx &= \int_{-\gamma_0}^{\gamma_0} f(x, \sqrt{\gamma_0^2 - x^2}) dx + \int_{\gamma_0}^{-\gamma_0} f(x, -\sqrt{\gamma_0^2 - x^2}) dx = 0, \\ \oint g(x, y) dy &= \int_{-\gamma_0}^{\gamma_0} g(\sqrt{\gamma_0^2 - y^2}, y) dy + \int_{\gamma_0}^{-\gamma_0} g(-\sqrt{\gamma_0^2 - x^2}, y) dy = 0. \end{aligned} \quad (1.29)$$

Solving for  $x$  and  $y$  being zero  $\forall \gamma_0$ , we get even  $f$  and  $g \forall x$  and  $\forall y$  respectively,

$$\begin{aligned} f(x, y) - f(x, -y) &= 0, \\ g(x, y) - g(-x, y) &= 0 \end{aligned} \tag{1.30}$$

Similarly, satisfying the fundamental symmetry of stress-strain would result in odd functions of  $x$  and  $y$  [52]. Additionally, for elastic stress to depend implicitly on  $y$  and viscous on  $x$  happens by strain amplitude dependence of the form  $\gamma_0 = \sqrt{x^2 + y^2}$  [52]. Thenceforth, a central point between linear and non-linear viscoelasticity reads as,

$$\sigma'(x, y) = \sigma'(x, \gamma_0), \sigma''(x, y) = \sigma''(x, \gamma_0) \tag{1.31}$$

and so does the elastic and viscous stress,

$$\sigma' = \Gamma'(x, \gamma_0)x, \sigma'' = \Gamma''(y, \gamma_0)y, \tag{1.32}$$

where  $\Gamma'$  and  $\Gamma''$  represents dynamic moduli, which in the linear viscoelastic limit reads,

$$\lim_{\gamma_0 \rightarrow 0} \Gamma'(x, \gamma_0) = G'(\omega), \lim_{\gamma_0 \rightarrow 0} \Gamma''(y, \gamma_0) = G''(\omega). \tag{1.33}$$

## 1.5 Summary

This chapter briefly summarises some important theoretical concepts and recent developments in contact mechanics, soft glassy rheology and FT-rheology, relevant for this thesis. Section 1.1 highlights previous works where the nonlinear contacts were defined by adding a Coulomb friction slider to the conventional Hertzian contact theory and its significance in cluster linearity. These concepts will aid us in drawing conclusions and inferences in chapter 3 and chapter 4 regarding force chain percolation failure and structural arrest of quasilinear clusters as the granular system approaches jamming. Section 1.2 describes the key components required to develop the SGR model and how it can be applied to study the dynamics of granular matter analogous to soft glasses. The definitions and explanation provided in this section will be extensively used in chapter 3 and chapter 4 in order to invoke characteristic energy scaling, validating and verifying our estimations of the noise temperature and draw analogies. Section 1.3 is dedicated to the rheophysics with emphasis on the applications of MITlaos to analyse rheological measurements, FT-rheology and the differential rheology. This section provides an extensive analytical and technical foreground, which serves as the basis to qualitatively demonstrate the experiments carried out in this work.



## 2

# Experimental Methods and Challenges

This chapter briefly discusses the experimental and analytical procedures employed in this work. From an experimentalist standpoint, much attention is given to the major challenges and how to avoid or solve them, that one might face when studying granular matter via rheometer.

## 2.1 Rheometry

All the rheological measurements were made on HAAKE MARS II rheometer (Thermo Fisher Scientific, Karlsruhe, Germany; see Fig. 2.1(a)). The machine is operated by a RheoWin software that offers to operate both, controlled deformation (CD) or controlled shear (CS) tests. In a CD test, a torque is applied to obtain the angular displacement, while in the CS test, the torque is measured on application of rotational motion.

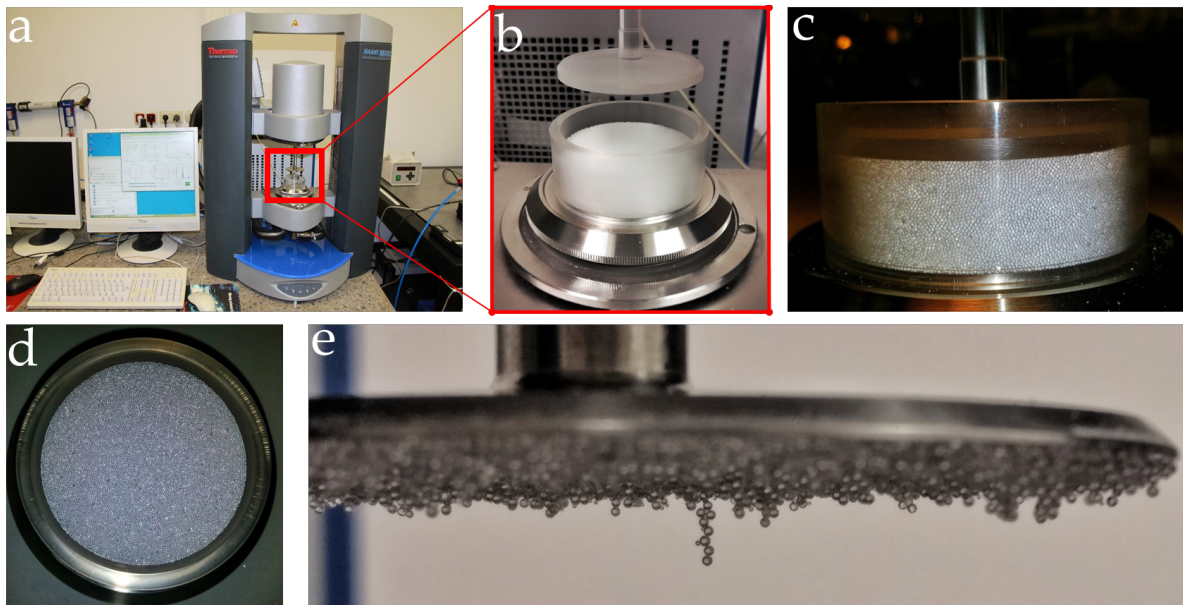


**Figure 2.1:** (a) HAAKE MARS II Rheometer (b) Plexiglass cup-plate geometry before test. (c) Dynoseeds of 500  $\mu\text{m}$  diameter being sheared between cup-plate setup. (d) A view of Dynoseeds from top after the test is performed. (e) A retracted glass-blasted plate with a chain of wet grains.

In a standard protocol, a granular sample was added to the cup-plate shear cell (as shown in Fig. 2.1 (b), (c) and (d)) and the upper plate is axially rotated with a steady angular frequency. As an experimentalist, the prime task is usually to optimize and carefully calibrate the operating system and its constituents we ought to study, thereby avoiding any peculiar artefacts or even prevent from damaging the machine. In our attempt to begin rheological operations on granular materials, we came across some noteworthy anomalies, as illustrated in Fig. 2.2.

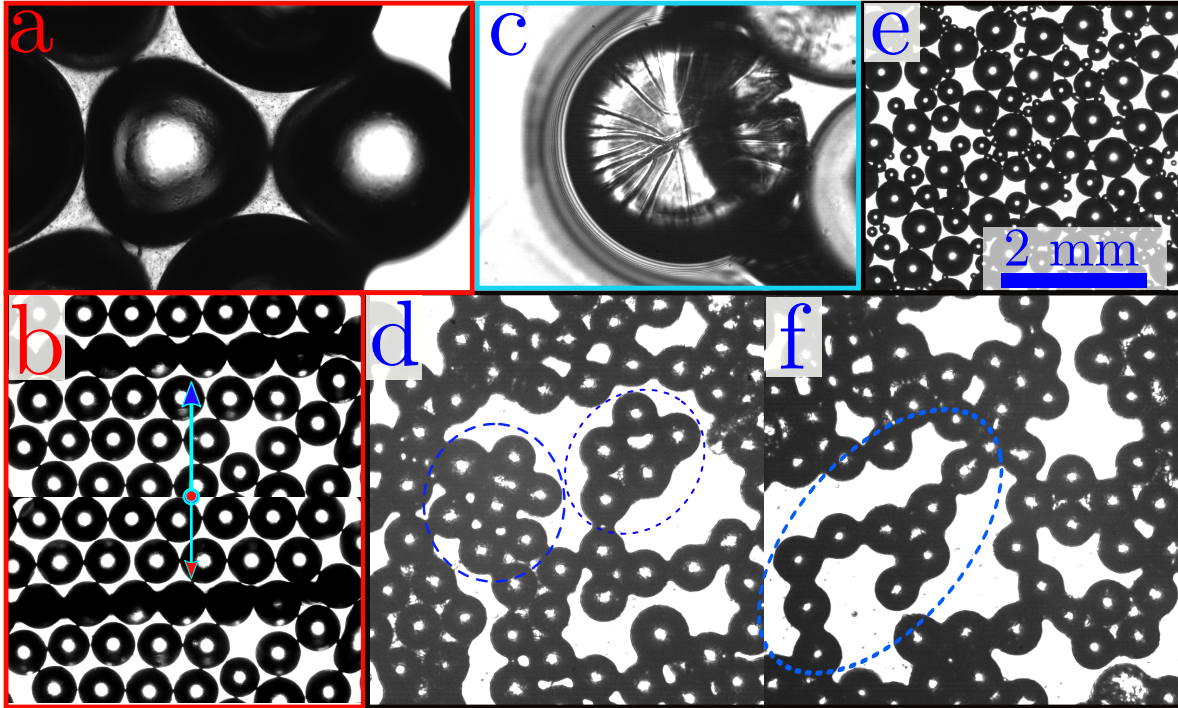


**Figure 2.2:** Micrographical illustration of artefacts or anomalous phenomenon captured for shear rheology of granular samples confined between parallel plates of plexiglass ( $5\text{ cm} \times 5\text{ cm}$ ), posing data risks and the credibility of experiments as they also occurred in a cup-plate, although mostly at the interface between the shear plate and the sample. Images in (a) and (b) shows morphological deformation and irregular contact with the shearing plate, caused by granular jamming. In (c) rectangle, a fractured grain after 5 repetitions of the same granular sample at  $\gamma_0 \sim 0.1$ ,  $f = 1\text{ Hz}$ . From (d) to (f) the aggregation/percolation behaviour (marked in blue ellipses) in wet grains due to improper mixing when preparing the sample, and dilution due to high void density in a polydisperse granular sample (unfiltered grains). The size of one grain shown in (a) to (d) and (f) are  $500\text{ }\mu\text{m}$ .

The images in red are a result of premature jamming (causing plastic deformation of grain and bulging as a convex-concave sample-air interface). To avoid this, pre-shearing a granular sample before one begins the test protocol can be taken into consideration, ensuring a flat interface and uniform distribution. Pre-shearing not only prevents bulging but also minimizes the non-uniform distribution of granular clusters as marked in blue, exhibiting percolation/ aggregation and premature jamming, as shown in Fig. 2.2. Furthermore, the image in cyan answers of why only a fresh granular sample should be used for each stress-strain cycle, because the grains wear off upon repetitive use, hence break or fracture. All the tests were carried out in a plexiglass cup (height  $h$ :  $30\text{ mm}$ )-sandblasted plate (diameter  $d$ :  $50\text{ mm}$ ) geometry (Fig. 2.2 (b)). Where the bottom plate is fixed, the angular motion

$\omega$  of the plate is regulated by a DC motor mounted on a vertical positioning stage. The current applied by the motor is translated to the torque  $\vec{M}$  while the moment of inertia  $I$  of the geometry and load bearing forces are optimized as we set the rheometer while calibration. The resolution limit of the rheometer required to obtain reliable data lies at the torque of  $\vec{M}_{\min} = 2 \mu\text{N}\cdot\text{m}$ . Where the axial force  $F_z$  measures a strain gauge up to the values of 10 mN. The shear component of the rate-of-strain tensor in cylindrical coordinates ( $R$ : radius,  $\varphi$ : azimuth angle and  $h$ : height of cylinder) can be written as [73, 99, 100],

$$\dot{\gamma}_{\theta h}(R) = \frac{\sin \varphi}{R} \frac{\partial}{\partial \varphi} \left( \frac{v_h}{\sin \varphi} \right) = \frac{v}{h} = \dot{\gamma} \quad (2.1)$$

where,  $v_h$  is velocity of the shear plate. Thus the strain can be calculated as  $\gamma = \Delta\ell(\varphi)/h$ , with  $\ell$  being the distance spanned by the moving plate in radians as  $\varphi$ .

### 2.1.1 On choosing the right setup for confined granular flows

This is important when deciding between cup-plate or parallel plate geometries. In a parallel-plate or a cup-plate, the biggest disadvantage is that, at a constant rotational speed of the rheometer, shear rate  $\dot{\gamma}$  is not constant throughout the sample and depends on the distance  $x$  from the rotational axis as  $0 \leq x \leq R$ . For that reason, cone-plate or *conicylinder* geometries are highly preferred among rheologists for polymer melts or emulsions [65, 66] as it facilitates the homogeneous shear flow, however for a granular sample it is more sophisticated than a parallel plate as the particulate features become critical. For example, by sandblasting the cone to shear grains in a cylinder seems plausible however in reality the first compromise will be on the exact dimension of the cone such as its surface, cone angle and cone centre. Not only that, for samples described by their limited maximum particle size, such as pastes, granulates, gels, powders [100], a number of inhomogeneities most likely at the cone edge might occur, that includes: turbulent flow, inertial effects, migration or discharge off the gap, premature jamming, skin formation and surface fracture due to concave-convex contact with cone [65, 66, 70, 100]. Nevertheless, the shear flow gradient is still a disadvantage in cup-plate geometry however ensuring constant contact between shearing plate and the granular sample with additional normal force control outweighs the cone-cylinder for this particular case. Not to mention, that the shear rate range can be controlled by changing  $h$ . Although, typical rheological calculations and analysis for polymers or suspensions in parallel-plate setup are obtained from the region with maximum shear rate i.e.  $\dot{\gamma}_{\max}$  (typically at the edge boundaries), the granular sample on the other hand is relatively sensitive as the rearrangements begin to define its response to shear. Such that, the shear rate varies linearly as  $\dot{\gamma} = 0|_{x=0}$  to  $\dot{\gamma} = \dot{\gamma}_{\max}|_{x=R}$ , where for large  $h$  at same rotational speed or  $\varphi$ , a low shear rate  $\dot{\gamma}$  or deformation will occur, that encourages the growth of shear bands and other inhomogeneities [65, 70, 100]. Hereof, we first set the standard reference to support our identification of strain amplitude  $\gamma_0$  as an indicator of nonlinear response (invoked later in the next chapters) in terms of displacing a grain by its size when the shear plate moves  $\varphi$  radians. For example, if we attempt to displace a grain of diameter  $d = 500 \mu\text{m}$  by its own size in a cup-plate setup ( $R = 25 \text{ mm}$ ) with a gap of  $h = 10 \text{ mm}$  i.e.

20 monolayers of grains, what shear strain we must apply? To estimate this, we incorporate the distance spanned by  $\varphi$  over the gap  $h$  from  $\angle = 0$  to  $\angle = \varphi$  and radially integrate the strain  $\gamma$  from  $x = 0$  to  $x = R$ ,

$$\gamma = \frac{1}{hR} \left( \int_0^R R dR + \int_0^\varphi \varphi d\varphi \right) \quad (2.2)$$

Using the aforementioned values, we find that for one grain to move by its own  $d$ , i.e. total length span is  $2d = 1$  mm in a cup-plate gap of 10 mm, a shear strain of  $\gamma \approx 0.1$  is required, such that,

$$\gamma = \frac{\Delta\ell(\varphi)}{h} = \frac{1 \times 10^{-3} \text{m}}{10 \times 10^{-3} \text{m}} = 0.1 \quad (2.3)$$

where the plate has moved by  $\varphi \approx 0.04$  rad with plate velocity in the range  $v_h \approx 10^{-3} \text{m s}^{-1}$ .

### 2.1.2 Computing viscoelastic measures via rheometer

For a standard rotational rheometer, the constant shear component ( $\sigma$ ) and rate for a cup-plate geometry is calculated by the integral torque at a constant rate of rotation [65, 73, 100],

$$\dot{\gamma} = \frac{\omega R}{h}; \quad \sigma = \frac{2\overset{\ominus}{M}}{\pi R^3 h} \quad (2.4)$$

where  $\omega$  is the angular frequency,  $h$  the height of the cup,  $\overset{\ominus}{M} = \int_0^h 2\pi\sigma(R)R^2 dR$  the torque and  $R$  is the radius of the plate. In addition, the normal force  $N$  for a cup-plate setup can be obtained by translating the axial normal force  $F_z$  as [99],

$$F_N = \frac{2(F_z - F_z^{initial})}{\pi R^2 h} \quad (2.5)$$

Since the shear plate and cup radii are equal, the viscosity then reads for a large cylinder gap, [100],

$$\eta = \frac{\overset{\ominus}{M}(R)}{\dot{\gamma}(R)} = \frac{2b\overset{\ominus}{M}}{\pi\omega R^4} \quad (2.6)$$

Furthermore, a standard shear rate sweep test entails a stepwise increment of shear rate at some frequency in a shear cell with a fixed gap (initially set during calibration), with several other options of parameters, that are otherwise important to run specific tasks. The operation mode applied, for example, control of angular velocity (constant rate, CR) or torque (constant stress, CS), decides the representation of storage modulus  $G'$  and the loss modulus  $G''$  as a function of dissipation per cycle of deformation [101, 102]. Consider an imposed strain  $\gamma$  of the form  $\gamma = \gamma_0 \cos \omega t$  with the amplitude  $\gamma_0$ , the angular frequency  $\omega$  and the sinusoidal strain rate  $\dot{\gamma} = -\omega \gamma_0 \sin(\omega t)$ , while stress and strain are 90 deg out of phase. In such a scenario, the total torque measured  $\overset{\leftrightarrow}{M}$  would then be computed partially in  $\overset{\leftrightarrow}{M}'$  and  $\overset{\leftrightarrow}{M}''$ , lagged in phase and out of phase  $\delta$  with excitation, respectively and is given as [65, 99],

$$\overset{\leftrightarrow}{M} = \overset{\leftrightarrow}{M}' \cos \omega t - \overset{\leftrightarrow}{M}'' \sin \omega t \quad (2.7)$$

Alternatively, in its complex form [65, 103],

$$\overset{\leftrightarrow}{M} = \frac{\pi h^4}{2b} \eta^* \omega_0 i \omega e^{i\omega t} \quad (2.8)$$

with viscosity being,  $\eta^* = G^*/i\omega = (G' \cos \omega t + iG'' \sin \omega t)$ .

Comparing above equations, we get,

$$G' = \frac{2b}{\pi h^4 \omega_0} \overset{\leftrightarrow}{M}', G'' = \frac{2b}{\pi h^4 \omega_0} \overset{\leftrightarrow}{M}'' \quad (2.9)$$

where the shear stress  $\sigma(t)$  directly scales with  $\gamma$  by a phase difference [66]:

$$\sigma(t) = \sigma_0 \sin(\omega t + \delta) = \gamma_0 [G'(\omega) \sin(\omega t) + G''(\omega) \cos(\omega t)]. \quad (2.10)$$

Where the phase difference is given as  $\tan \delta = \frac{G''}{G'}$ . For a purely elastic material,  $G'' = 0$  and  $\delta = 0$ , but contrarily, for a purely viscous materials  $G' = 0$  and  $\delta = 90$  deg. Nevertheless, for yield-stress fluids, both  $G'$  and  $G''$ , are non-zero. The storage modulus  $G' = \frac{\sigma_0}{\gamma_0} \cos \delta$  measures the in-phase elasticity, the loss modulus  $G'' = \frac{\sigma_0}{\gamma_0} \sin \delta$  measures the out-of-phase viscosity and as a result, complex modulus  $G^* = \frac{\sigma_0}{\gamma_0} = \sqrt{G'^2 + G''^2}$  measures the total strength of a material. See chapter 1 for a detailed explanation of how nonlinear rheology data is evaluated.

Additional parameters of interest for non-linear rheology have been thoroughly covered in the theoretical works of Baravian-Quemada [94], emphasizing Kelvin-Voigt mechanical model to elucidate instrumental inertia and viscoelasticity [93–97]. Note that this section below was used for cross-identifying critical or transition points in the rheological data and thus serves as an alternative approach to check for nonlinearity in the data for rheologists. The critical parameters defined here have been helpful in confirming the robustness of the experiments presented in this thesis, as the critical elasticity and differential modulus served as the initial reference map to check whether the rheological data corresponds to creep [51, 94, 97] and as if it truly lies in the linear or non-linear regime [57, 79, 89].

We begin with the equation of motion for a moving apparatus,

$$I \frac{\partial \Omega_w}{\partial t} = \overset{\oplus}{M}_{\text{applied}} - \overset{\oplus}{M}_{\text{wall}} \quad (2.11)$$

where  $\overset{\oplus}{M}_{\text{applied}}$  is the imposed torque and  $\overset{\oplus}{M}_{\text{wall}}$  is the resistant torque at the moving wall,  $I$  is the momentum of inertia for the non-stationary part of the setup and  $\Omega_w$  is the angular velocity. Furthermore, space and time variables are partitioned by default in a constitutive equation, connoting the parallel attributes between shear rate and angular velocity scaled by a factor of  $F_{\dot{\gamma}}$  where shear stress and the torque are scaled with  $F_{\sigma}$  [94, 95]. Thus, we can rewrite the equation of motion as,

$$a \ddot{\gamma}_w = \sigma_{\text{applied}} - \sigma_{\text{wall}}, \quad \text{where} \quad a = I \frac{F_{\sigma}}{F_{\dot{\gamma}}}. \quad (2.12)$$

Upon conjugation with Maxwell-Jeffreys model and coupling  $(\eta_1 + \eta_2)\dot{\sigma} + G\sigma = \eta_2 G \dot{\gamma} + \eta_1 \eta_2 \ddot{\gamma}$  with equation of motion, the applied shear with step amplitude  $\sigma_0$  is can be expressed as following,

$$(\eta_1 + \eta_2)\dot{\sigma} + \left(G + \frac{\eta_1 \eta_2}{a}\right) \sigma = \frac{G \eta_2}{a} \sigma_0 h(t) + \frac{\eta_1 \eta_2}{a} \sigma_0 \delta(t) \quad (2.13)$$

where  $h(t)$  is the Heaviside distribution function and  $\delta(t)$  is the Dirac delta impulsion. The implication here being, that any elastic material coupled to this equation 17 provide an oscillating solution, where purely viscous materials are incapable of exhibiting any oscillations. Therefore, the analytical solution of this equation can be further divided in oscillating and non-oscillating parts, thereby the critical elasticity  $G_{\text{critical}}$  can be defined in accordance with Maxwell-Jeffery model as,

$$\frac{\eta_2 G}{a(\eta_1 + \eta_2)} - A^2 \geq 0 \quad (2.14)$$

with  $A = \frac{aG + \eta_1\eta_2}{2a(\eta_1\eta_2)}$ , such that,

$$G \geq G_{\text{critical}} = \frac{2\eta_2^2}{a} \left( 1 + \frac{\eta_1}{2\eta_2} + \sqrt{1 + \frac{\eta_1}{\eta_2}} \right) \quad (2.15)$$

For  $G \geq G_{\text{critical}}$ :

$$\sigma_{\text{wall}}(t) = \sigma_0 \left\{ 1 - e^{-At} \left[ \cos(\omega t) + \frac{aG - \eta_1\eta_2}{2a\omega(\eta_1\eta_2)} \sin(\omega t) \right] \right\} \quad (2.16)$$

with  $\omega = \sqrt{\frac{\eta_2 G}{a(\eta_1 + \eta_2)} - A^2}$  and integrating this computes the shear rate at the wall,

$$\dot{\gamma}_{\text{wall}}(t) = \frac{\sigma_0}{\eta_2} \left\{ 1 - 1 - e^{-At} \left[ \cos(\omega t) + \frac{1}{a\omega} (\alpha A - \eta_2) \sin(\omega t) \right] \right\} \quad (2.17)$$

and correspondingly the strain at the wall as,

$$\gamma_{\text{wall}}(t) = \sigma_0 \left\{ \frac{t}{\eta_2} - B + e^{-At} \left[ B \cos(\omega t) + \frac{A}{\omega} \left( B - \frac{1}{A\eta_2} \right) \sin(\omega t) \right] \right\} \quad (2.18)$$

with  $B = \frac{a(\eta_1 + \eta_2)}{\eta_2 G} \left( \frac{2A}{\eta_2} - \frac{1}{a} \right)$  and  $\gamma(0) = 0$ . Since  $\eta_1 \xrightarrow{0}$  (Maxwell model) critical elasticity then reduce to:  $G_{\text{critical}} = \frac{4\eta_2^2}{a}$  and the shear stress, shear rate and strain then simplifies as,

$$\sigma_{\text{wall}} = \sigma_0 \left\{ 1 - e^{-\frac{G}{2\eta_2} t} \left[ \cos(\omega t) + \frac{G}{2\eta_2\omega} \sin(\omega t) \right] \right\} \quad (2.19)$$

$$\dot{\gamma}_{\text{wall}} = \frac{\sigma_0}{\eta} \left\{ 1 - e^{-\frac{G}{2\eta_2} t} \left[ \cos(\omega t) + \frac{1}{\omega} \left( \frac{1}{2\eta_2} - \frac{\eta_2}{a} \right) \sin(\omega t) \right] \right\} \quad (2.20)$$

and

$$\gamma_{\text{wall}} = \frac{\sigma_0}{\eta_2} \left\{ t - \frac{a}{G} \left( \frac{G}{\eta_2} - \frac{\eta_2}{a} \right) \left[ 1 - e^{-\frac{G}{2\eta_2} t} \left( \cos(\omega t) + \frac{G}{2\eta_2\omega} \frac{G/\eta_2 - 3\eta_2/a}{G/\eta_2 - \eta_2/a} \sin(\omega t) \right) \right] \right\} \quad (2.21)$$

with  $\omega = \sqrt{\frac{G^2}{4\eta_1^2} - \frac{G}{a}}$ . Whereas according to Kelvin-Voigt model,  $\eta_2 \rightarrow \infty$ , similarly the  $G_{\text{critical}}$  evolves to  $G_{\text{critical}} = \frac{\eta_1^2}{4a}$ , with shear stress, shear rate and strain as following,

$$\sigma_{\text{wall}} = \sigma_0 \left\{ 1 - e^{-\frac{\eta_1}{2a}t} \left[ \cos(\omega t) + \frac{\eta_1}{2a\omega} \sin(\omega t) \right] \right\} \quad (2.22)$$

$$\dot{\gamma}_{\text{wall}} = \frac{\sigma_0}{a\omega} e^{-\frac{\eta_1}{2a}t} \sin(\omega t) \quad (2.23)$$

and

$$\gamma_{\text{wall}}(t) = \frac{\sigma_0}{G} \left\{ 1 - e^{-\frac{\eta_1}{2a}t} \left[ \cos(\omega t) + \frac{\eta_1}{2a\omega} \sin(\omega t) \right] \right\} \quad (2.24)$$

where  $\omega = \sqrt{\frac{G}{a} + \left(\frac{\eta_1}{2a}\right)^2}$ . As defined previously, that stress is determined by superposing on strain via symmetry arguments, also can be used to derive the differential modulus and can be used to answer how dominantly the material is driven by elasticity or favourably in case of granular materials, might provide an alternative indication of filamentary force chain networks in granular packings upon shear stress. However this modulus might not be the best choice when viscous dissipation equally governs the material response (such as for wet granular systems) [94, 95, 97], hence it was only used as partial fulfilment to acknowledge the presence of force chain networks. Following works [93, 94, 96, 97, 104, 105] gives a general description of differential stress modulus. In a typical rheometry, the elastic and loss modulus are usually derived as previously  $I(F_\sigma/F_\gamma)(d^2\gamma/dt^2) = \sigma_A - \sigma_S$ , where  $I$  is the moment of inertia of the rheometer,  $F_\sigma$  here relates to the stress and torque, with  $\sigma_A = F_\sigma\tau$ , as  $F_\gamma$  relates to strain and the angular displacement, lastly,  $\gamma = F_\gamma\theta$  with  $\sigma_A$  being the applied stress and  $\sigma_S$ , the resistant stress of the sample [94]. As defined above in Kelvin-Voigt model,  $\sigma_S$  can be determined as in  $\sigma_S = E\gamma + \eta(d\gamma/dt)$  and so the  $G_{\text{critical}}$ , by combining the constitutive law and the equation of motion [94, 95, 105]. A threshold for the onset of oscillation must be defined as  $E > \eta^2/4a$  so the oscillations can occur where  $a = I(F_\sigma/F_\gamma)$  and  $\eta$  is the viscosity. We can now solve the coupled differential equations under critical shear stress  $\sigma_c$  [52, 93, 94, 96, 105] and obtain the analytical solution,

$$\sigma_S = \sigma_c \left[ 1 - e^{-\beta t} \left( \cos(\omega t) - \frac{\beta}{\omega} \sin(\omega t) \right) \right] \quad (2.25)$$

and

$$\frac{d\gamma}{d\gamma} = \frac{\sigma_c}{a\omega} e^{-\beta t} \sin(\omega t), \quad (2.26)$$

where  $\beta = \eta/2a$  and  $\omega = \sqrt{E/a - \beta^2}$ . Integrating this at  $\gamma(0) = 0$ , yields the value of  $\gamma$  as,

$$\gamma = \frac{\sigma_c}{E} \left[ 1 - e^{-\beta t} \left( \cos(\omega t) + \frac{\beta}{\omega} \sin(\omega t) \right) \right] \quad (2.27)$$

where the complex dynamic modulus  $G^*$  and the elastic modulus  $K'$  can be expressed as:  $G^* = E + i\eta\omega$  yielding  $K'_c(\sigma_c) = E = a(\omega^2 + \beta^2)$ , respectively.

### 2.1.3 Where lies the effective shearing zone? or How to be sure if the response is homogeneous?

An important characteristic of grains, that can easily be overlooked, is their notorious inhomogeneous flow that often leads to the formation of shear band(s) [2, 36, 38, 43, 44, 106]. For a cup-plate shear cell, we find that the number of layers of grains that make up the test sample can affect the rheology by a considerable number. To demonstrate this for a broader scope, different granular materials (including powders) were deformed at large strains at  $f = 1$  Hz as their number of monolayers  $n_m$  were allowed to vary subsequent to each stress-strain cycle until a homogeneous-like flow was achieved. Since we are taking into account the presence of one shear band, the energy that will be dissipated by the system, in this case, should potentially be affected by the sample size [65, 107, 108]. To illustrate this point, let's assume a fluid is subjected to permanent deformation, where the mechanical energy that is spent to work on the fluid is dissipated as heat in response, and especially granular matter as a fluid system can "heat" up to a Terakelvin range [65, 109]. As the fluid begins to evolve upon deformation (from a stationary state) for infinite time  $t \rightarrow \infty$ , the stress  $\sigma_{\text{Applied}}(t \rightarrow \infty)$  is measured at a shear rate  $\dot{\gamma}$ . Hence, to find out how much heat is dissipated per unit volume, we calculate the work done per unit time by the applied stress on the fluid, that is the dissipated power per unit volume of the fluid  $P(\dot{\gamma}) = \sigma_{\text{Applied}}\dot{\gamma}$  [65]. And since the viscosity  $\eta(\dot{\gamma})$  plays the role of dissipating heat, the dissipated power can therefore be written as  $P(\dot{\gamma}) = \eta(\dot{\gamma})\dot{\gamma}^2$ . Nevertheless, in reality, the experiments are performed at finite amplitude  $\gamma$ , henceforth the total dissipated energy  $E_d(\gamma) \equiv \oint P(\dot{\gamma})d\gamma$  would provide a rather realistic measure which can be defined as [65],

$$E_d(\gamma) = \oint P(\dot{\gamma})d\gamma = \sigma_{\text{Applied}}\gamma = \eta(\dot{\gamma})\dot{\gamma}\gamma. \quad (2.28)$$

where  $\oint \Rightarrow$  is a loop integral to quantify the area of stress-strain loop in  $E_d$ . This implies that for a quasi-static case,  $E_d$  vanishes as  $\dot{\gamma} \rightarrow 0$ , wherefore,  $\sigma_{\text{Applied}}$  becomes the total stress  $\sigma$  [65] and the dissipated energy can be calculated as [36, 65, 76],

$$E_d(\gamma) = \oint \sigma d\gamma \quad (2.29)$$

One might here ask, how come strain rate replaced the strain to compute the dissipation energy as the fluid is deformed in time? It is interesting to know that albeit the validity of Boltzmann's *Stosszahlansatz* in thermal fluids, meaning that the fluid in "quasi-static limit"

(in its ergodic state) exist at a finite temperature ( $k_B T$ , thermal motions) where  $E_d \rightarrow 0$  at  $\dot{\gamma} \rightarrow 0$ . Contrarily, for granular materials (athermal),  $E_d$  does not vanish and is relatively finite for a quasi-static deformation [65], thus ruling out the strain rate  $\dot{\gamma}$ , and is instead defined by a strain  $\gamma$ . Coming back to the problem at hand, on how to identify the "effective shear zone" to ensure that the rheological response of granular assemblies remains uniform (homogeneous-like) in a cup-plate geometry. We solve this by depicting the total dissipated energy  $E_d$  of granular materials as a function of the number of monolayers  $n_m$  of grains, as shown in Fig. 2.3. Since a LAOS test typically outputs stress-strain loops (LB Loops), wherein by integrating the area enclosed by these loops of  $\sigma$  vs.  $\gamma$  reveals the energy dissipated by the sample [36, 76].

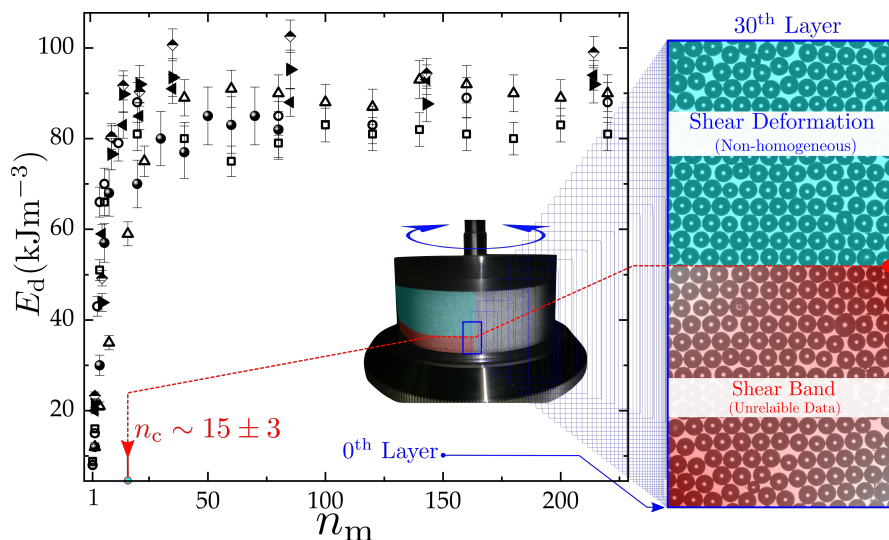


**Figure 2.3:** Dissipated energy as a function of number of monolayers, for different types of powders in a plexiglass cup-plate geometry. Legends  $\square$ : Dynoseeds: square, 140  $\mu\text{m}$ ; circle, 250  $\mu\text{m}$ ; and triangle, 500  $\mu\text{m}$ ; diamond: glass (140  $\mu\text{m}$ ), half filled diamond: Lactose monohydrate (140  $\mu\text{m}$ ) and sphere: glass (1.5 mm). The sketch of rheometer cup-plate cell with a zoomed-in image of 500  $\mu\text{m}$  Dynoseeds represents the threshold ( $n_c \sim 15 - 20$ ) of monolayers forming a shear band, and for  $n_m \geq n_c$ , begins the "true" deformation of a granular sample.

This also let us define a critical number of monolayers  $n_c \sim 15 - 20$  (grain diameters) (when  $E_d \rightarrow \text{constant}$ ), required to reach the "true shearing zone" as previously predicted by [107] ( $n_c \sim 5 - 15$  grain diameters) for a vane-in-cup geometries. A slightly higher threshold of  $n_c$  obtained for cup-plate than vane-in-cup can be attributed to low or no confinement in the latter geometry than the former. Note: the number of monolayers ( $n_m \geq n_c$ ) that contribute to the non-homogeneous response begins at the shearing plate as the shear band forms at the bottom, and the image above (Fig. 2.3) only captures a rough boundary where the non-homogeneous shear zone comes into effect.

### 2.1.4 How to avoid bad data in rheology of granular materials?

Additionally, in our attempt to cover the generic aspects and issues related to the standard data resolution for the rheometry of granular flows, we reviewed the recent work of Ewoldt [55] on How to avoid bad data in shear rheology? Although the relevance of their study

revolves around soft materials, the viewpoint is general and raise critical concerns about the measuring instrument used [55]. Therefore, to test and find the resolution limit of the HAAKE Mars II rheometer, we provide a data window to identify where lies the bad data (outliers or artefacts) and where lies the meaningful response. Fig. 2.4 summarizes several steady shear experiments made with different materials; Glycerol, Milli-Q Water, Glycerol-Water Mixture, Polyacrylamide, Blood, Lactose Powder, and Glass Particles.

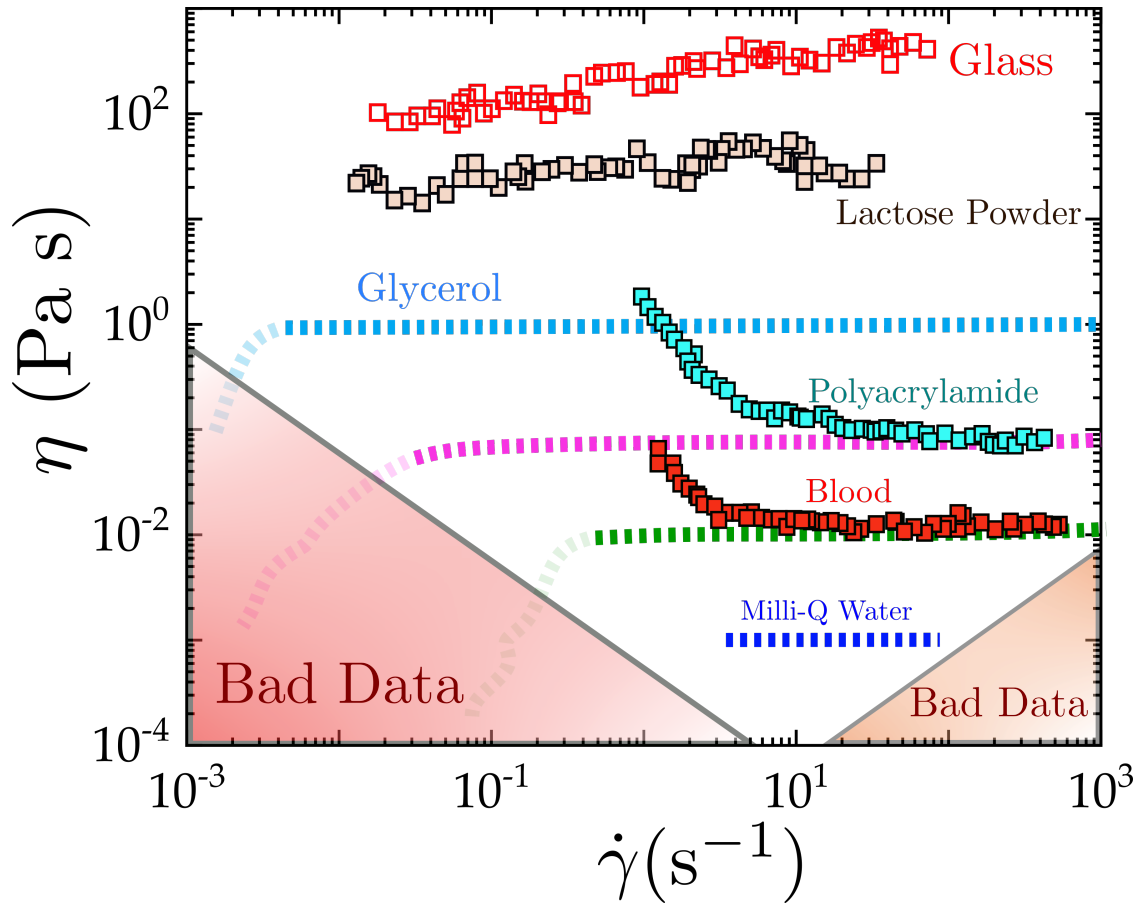


**Figure 2.4:** Summary of steady shear rheology of different classes of materials, providing a rheological map to distinguish between good and bad data regions. Legend: water-glycerol 70:30 (magenta) and water-glycerol 50:50 (green), other legends can be directly referred on the figure. The region of interest, where the data is mostly unreliable has been shaded for quick reference. The samples were used following standard preparation protocols and pre-treatments.

Furthermore, we highlight the slipping of a shearing plate on a granular sample. Unlike fluids such as polymer solutions or liquids, granular sample on the other hand does not really stick to the shearing plate (smooth surface, partially in contact), hence the plate slips over the sample surface. This slipping can cause the rheological data to deviate from standard references, and by a considerable amount. To illustrate this and how to avoid slip when performing a rheological test on granular samples, we compare three different cases; 1) Glass-blasted shear plate (80  $\mu\text{m}$  size particles), 2) Sandpaper attached shear plate (200 grit), 3) Standard shear plate (smooth surface). Keeping frequency  $f = 1$  Hz and volume of the granular sample (20 layers of 500  $\mu\text{m}$  size Dynoseeds i.e. the gap  $h = 10$  mm) constant,

we depict the viscosity in Fig. 2.5. Clearly, the standard shear plate with a smooth surface caused a significant deviation in the viscosity, as corroborated by the square symbols (closed red: first attempt, black: second attempt and open red: final attempt). Whereas, the viscosity calculated for Dynoseeds sheared by sandpaper attached or glass-blasted shear plate, showed a relatively cleaner response (blue symbols; circles: glass-blasted, cross: sandpaper).

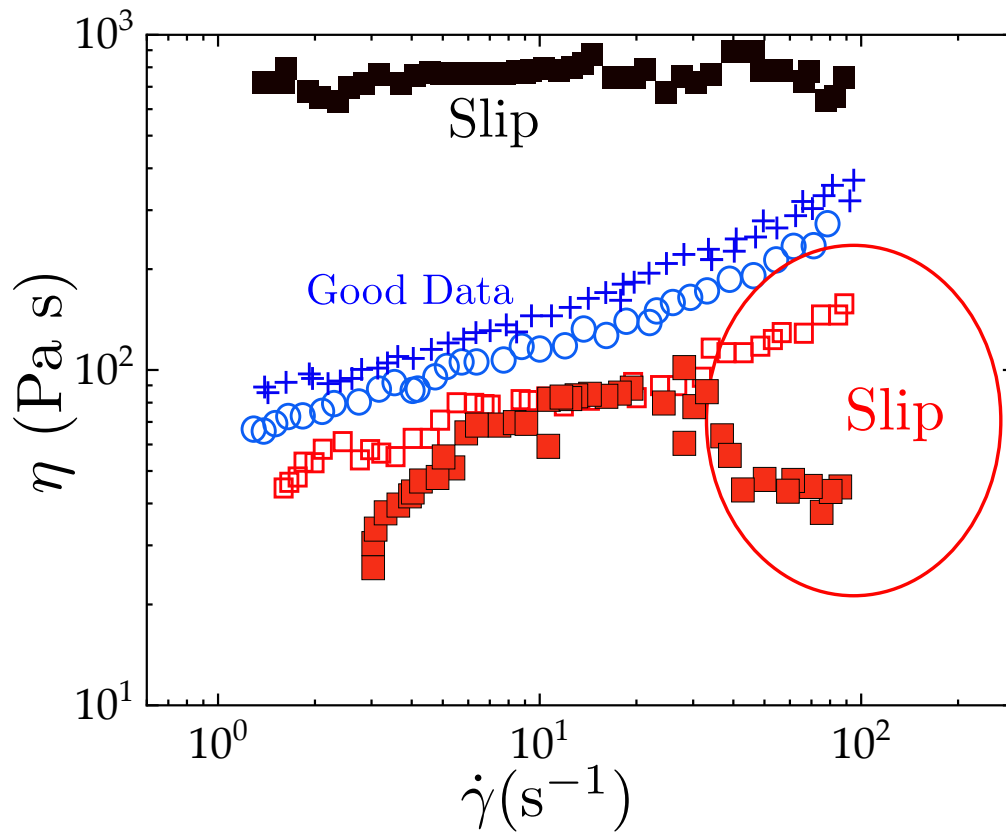


**Figure 2.5:** Comparison of shear plate surface and its effect on the rheology of granular materials. The anomalous behaviour of Dynoseeds sheared by standard rheometer plate is clearly visible in contrast to roughened shear plate. The data shown by the square symbols (closed red: first attempt, black: second attempt and open red: final attempt) belongs to the standard shear plate, while data in blue are an average of 5 attempts each with sandpaper attached (cross symbols) and glassblasted (circles) shear plates, respectively.

Hereof, the use of sandpaper (preferred due to longer life) or glass particles (effective but can erode or wear due to highly abrasive contacts, usually after 15-20 times of application) can efficiently prevent the inconsistencies in rheological data, obtained for granular materials in particular.

## 2.2 Bright Field Microscopy

To capture and demonstrate the differences between dry and wet grains, granular contacts and capillary bridges, in particular, we used a bright field microscope (Nikon Eclipse TE2000-s), shown in Fig. 2.6. A uniform projection is ensured by an illuminating hollow

cylinder of light coming from an incandescent source triggered by a beam halter subsequent to the condenser lens setting a bright field for the objective. Advantageously, this allows to cover the oblique angles (including all azimuths) and only filtering the first-order waveforms through the objective lens. Consequently, high contrast and bright appearance of the test sample is facilitated by such attenuation of light. All micrographs shown in this thesis have been obtained with the aforesaid settings.

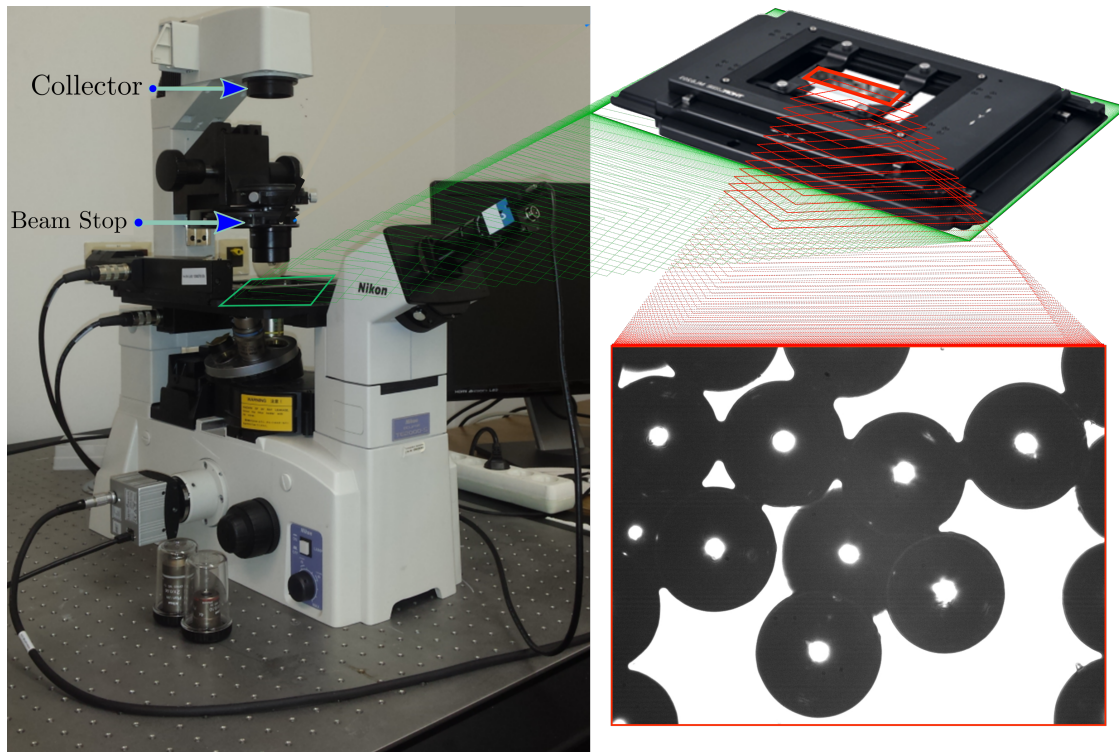


**Figure 2.6:** Nikon Eclipse TE2000-s Microscope with a horizontal moveable stage, controlled by a switch, precisely calibrated to the distance spanned and an image of a 3D granular cluster (a pentamer in the pendular state) of 500  $\mu\text{m}$  Dynoseeds.

In contrast to dry grains, the capillary bridges in wet granular materials are dynamically rich when examined under a microscope, and upon a thorough study, can provide valuable insights on how these bridges break, rearrange and regenerate. We, therefore, mounted a 2D moving stage (shown in green, Fig. 2.6) that allows us to apply unidirectional strain  $\gamma_0^e$  to shear a monolayer of wet grains in a parallel plate geometry. For further details, chapter 4 covers the physical aspects of capillary bridges relevant to the compaction and dilatant behaviour of granular matter.

## 2.3 Pendant Drop Tensiometry

As pointed out, the significance of capillary bridges in governing the rheology of wet granular materials is crucial. In Chapter 5, we will study the role of physical properties (such as surface tension) of the wetting fluid giving rise to slow compaction flows of grains. A straightforward approach to systematically vary the cohesivity of wet granular materials

is by changing the surface tension of the interstitial fluid wetting the grains. We thus employed a pendant drop method, DataPhysics OCA 20 with the attached CCD camera, as shown in Fig. 2.7, offering a maximum resolution of 768pixels  $\times$  576pixels (which can be enhanced by magnification objective of: 0.7 $\times$  to 4.5 $\times$ , in special cases), to calculate the surface tensions and fluid densities of liquids we chose to wet the grains.

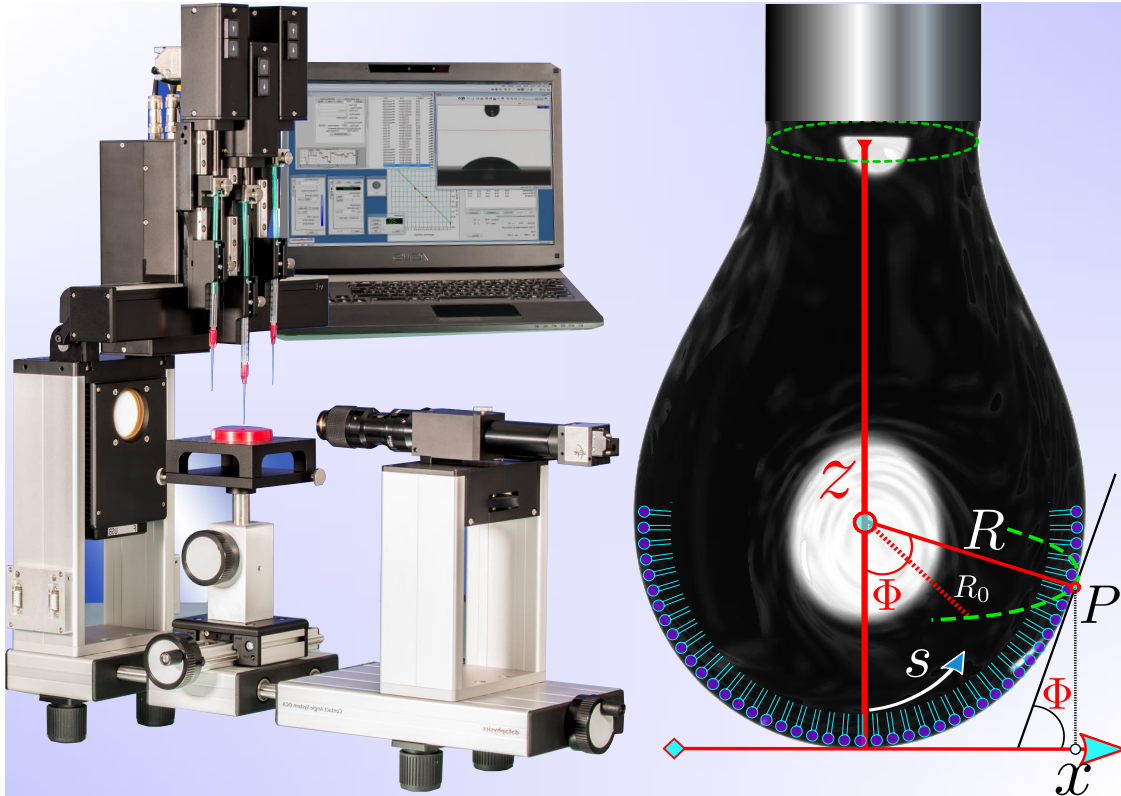


**Figure 2.7:** (a) DataPhysics OCA 20: for the pendant-drop method to measure surface tension of a fluid, equipped with a CCD-camera (max resolution: 768pixels  $\times$  576pixels) operated by an embedded software to analyse real-time information as shown on the monitor screen (b), an image to highlight the contour and positioning of a drop at the end of a needle. (c) A typical experimental state of pendant drop tensiometry; where the drop hangs on a needle, the annotations illustrate the important variables (as described in the text below) necessary for numerical analysis to approximate the surface tension.

In a typical apparatus, a liquid drop is deposited on the tip of a needle (the absolute bottom of the needle, as shown in Fig. 2.7(a)). The contour of a droplet is then analysed from an optical image to compute the surface tension [110, 111]. The shape and contour of the droplet are estimated by the surface tension and gravity [112]. The shape of a droplet is the result of surface tension competing with gravity to achieve minimum surface area, therefore, the drop appears spherical as it simultaneously gets pulled by the gravity. Consequently, the droplet adopts a pear-like pendant shape, hence the name of this method. For systems in equilibrium, the surface tension  $\mu$  can be approximated by balancing the Laplace pressure  $P_L$  and the hydrostatic contribution ( $\rho gh$ ) as  $P_L = \rho gh$  [113], where  $P_L$  is the curvature of the droplet surface,  $\rho$  the density of the liquid and  $g$  the acceleration due to gravity [112]. In a cylindrical coordinate system (see Fig. 2.2(c)), the curvature can be defined by assuming

a symmetrical drop in the  $z$ -axis, with  $z$  being the direction of gravity,  $R$  is the radius of curvature at the point with coordinates  $(x, z)$  with azimuth angle  $\Phi$ , given as [112, 113],

$$R = \frac{ds}{d\Phi} = \frac{[1 + (\frac{dz}{dx})^2]^{3/2}}{\frac{d^2z}{dx^2}}, \quad \sin \Phi = \frac{\frac{dz}{dx}}{\sqrt{1 + (\frac{dz}{dx})^2}}. \quad (2.30)$$

This numerical approximation process is based on the model of Bashforth and Adams as described in [98, 114, 115], a straightforward derivation of Laplace's equation that ascribes the state of the drop to the interfacial tension via nonlinear differential equation as  $\mu = \frac{gD_e^2\Delta\rho}{H}$ . Where  $\mu$  is the interfacial tension,  $D_e$  is the equatorial diameter of the drop,  $H$  is a shape  $s$  dependent parameter, defined as,  $s = \frac{D_s}{D_e}$ , where  $D_s$  is the horizontal diameter of the drop at  $D_e$ , away from the apex of the drop. Nevertheless, these methods are relatively difficult to fully implement as software to characterize the shape of the drop in real-time. Recent work by [98, 114] on [115], provides an improved methodology to measure the surface tension, summarised in four steps as demonstrated in Fig. 2.8 (a)-(d): (a) capture and digitization of the pendant drop to an image; (b) estimation of the radius of curvature at the apex and drop contour; (c) polynomial regression fit on the contour for smoothing; (d) use of the reference scale to compare the shape and approximate the surface tension.

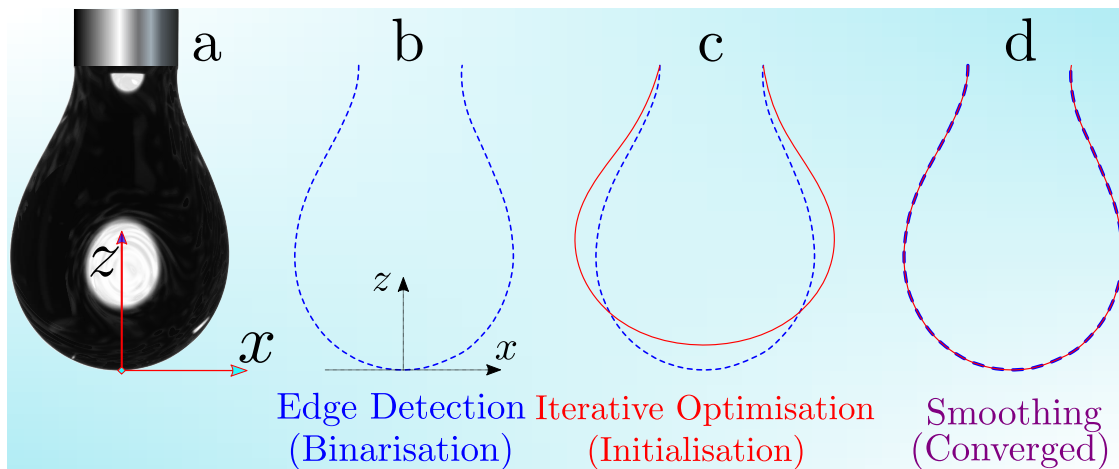


**Figure 2.8:** Schematic illustration to estimate surface tension  $\mu$  by polynomial regression fitting (in red, (d)) of the raw experimental image (a) via pendant drop tensiometry process.

Subsequent to the smoothing of a pendant drop, the shape is then compared to a theoretical and an experimental reference, to fit with the fourth-order Runge-Kutta method to precisely calculate the surface tension [98, 115]. We henceforth, provide a table of physical constants obtained by aforesaid methods, for interstitial fluids, applied to wet the grains to varying their *cohesiveness*. These values will be used later to calculate capillary forces and rupture energies of liquid bridges in chapter 3.

**Table 2.1:** Physical constants of fluids calculated by the methods as shown heretofore

Fluid	Property			Grade
	$\mu$ Nm <sup>-1</sup>	$\eta$ Pas	$\rho$ kgm <sup>-3</sup>	
Silicon Oil	0.021	0.18	1070	<i>KF – 6011</i>
Triton <sup>®</sup>	0.033	0.24	1061	<i>X – 100</i>
Polysorbat <sup>®</sup>	0.043	0.44	1076	<i>PS – 80</i>
Polyethylene oxide	0.055	0.75	1045	<i>N750</i>
Optiprep <sup>®</sup>	0.079	0.9	1032	<i>V35</i>

# 3

## Non-linear Granular Flows from a Soft Glassy Perspective

In this chapter, we experimentally study what has been extensively researched and yet an obscure topic: the nonlinear rheology of granular matter at large deformations near jamming. The mechanical stress in such dynamic granular matter system, is governed by the ensemble of strain fluctuations by the virtue of active rearrangements of inter-granular contacts (translation motion) causing force chain network at mesoscopic scale to percolate [59, 60, 63, 116]. Consequently, granular materials begin to yield once the applied deformation exceeds the stored elastic energy, which otherwise acts as a barrier against structural rearrangement [8, 9, 30, 34, 117]. As a result, we observe that the rheological response of dry and wet granular matter at large deformations is greatly affected by nonlinearities [35, 37]. The first section of this chapter addresses the significance of nonlinearities by introducing a characteristic degree of nonlinearity  $\zeta$  analogous to Q-parameter in FT-rheology for LAOS rheometry [80, 82]. In addition, by scaling the nonlinear viscoelastic moduli with strain amplitude, characteristic energy is invoked, previously shown to measure a non-thermal temperature (the noise temperature) via a Boltzmann-like parameter [36]. In addition, a good fit of  $\zeta$  for elastic and viscous nonlinearities with a stretched exponential function revealed a strong coupling between elasticity and viscosity by a scaling margin of the applied frequency  $\omega$ . Wherein, the aforesaid dynamics were recognised to roughly match the description of the SGR model [9, 23, 30, 33, 34]. Therefore, in the next section, we adopt this constitutive model and study the stress-strain behaviour of granular materials, in the hope to provide a complete rheological picture.

### 3.1 Non-linear Rheology of Granular Materials

To tentatively demonstrate the fundamental differences between dry and wet grains, we first investigate a monolayer of Dynoseeds with and without the addition of Silicon oil (2 wt. %) confined between parallel plexiglass plates (5 cm  $\times$  5 cm) under the microscope in bright field settings. Fig. 3.1 illustrates via optical micrographs, the significance of contacts in dry (high Coulomb's friction [35, 56, 118]) and wet granular materials [109, 119, 120] as shown by the rearrangement dynamics of a triplet of beads (encircled in red) from (a) to (c) compared to the triplet in case of wet beads from (d) to (g). These capillary bridges as captured in a pendular wetting regime in (d) has been previously shown to provide a spring-like action upon breaking or regenerating in [86, 119, 120], resulting in a higher yield

strength and cohesivity [119–122].

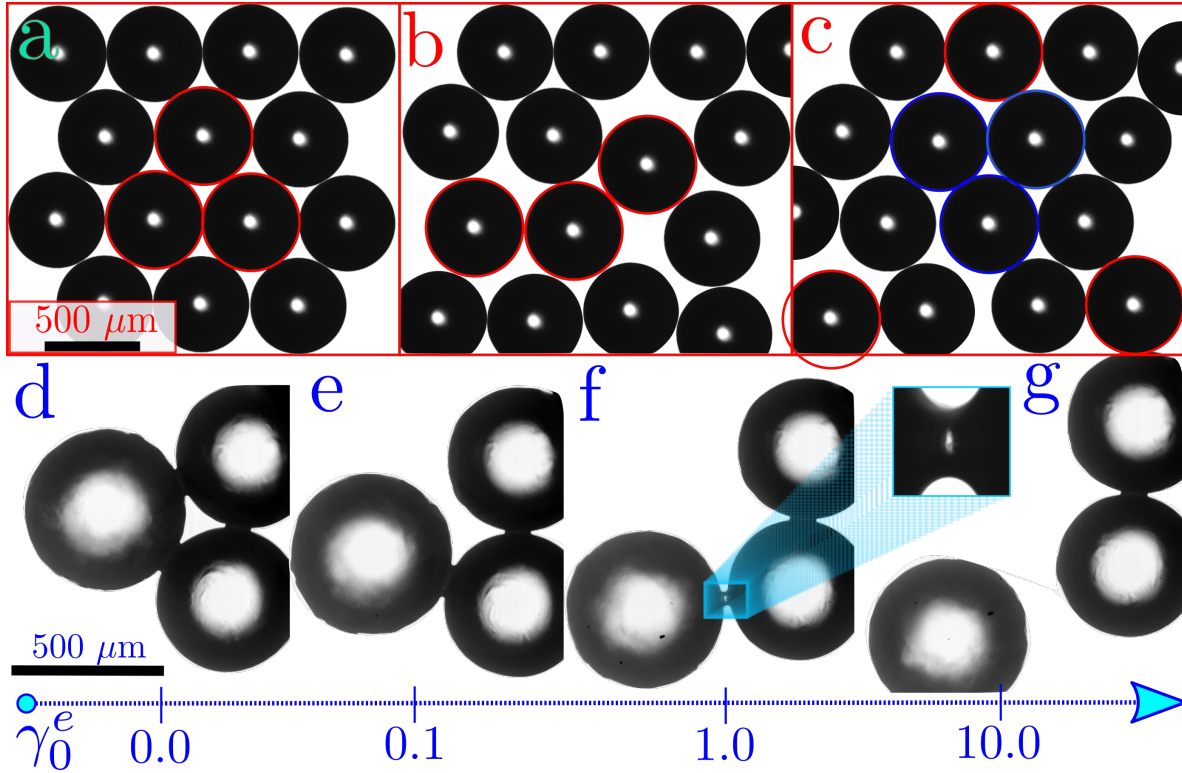


**Figure 3.1:** (a) to (c) Micrographical illustration of a monolayer of Dynoseeds to capture their dry contact dynamics as the granular layer is allowed to deform between parallel plates of plexiglass. Note that the strain applied here via moving stage is unidirectional  $\gamma_0^e$ , and should not be confused with  $\gamma_0$  for rheometer. Beads encircled in red demonstrate the maximum contact state, as the assembly evolves with the deformation, the beads begin to rearrange, which in the next scenario is displaced with the other set of beads (encircled in blue). (d) to (g) Dynoseeds with capillary bridges in pendular regime at same strain deformation as dry, illustrating the process of rupture of a liquid bridge and separation.

Nevertheless, whether dry or wet, grains under shear in a cup-plate geometry tends to adopt inhomogeneous flow profiles with a random distribution of shear bands as confinement effects emerge [35, 37, 43, 106, 123]. Recently, the work [106] on the numerical approximation of a linear force model to predict the correlation between friction, inertia, and cohesion in granular flows finds that the inhomogeneity results from the geometrical and local constraints at the grain scale. These constraints in dry granular materials are primarily the result of varying time scales of local interaction in contrast to the invariant global timescales associated with particle size and its density. Moreover, in wet granular materials, cohesive time scales are shown to dominate as global constraints, which although weakly depends on the volume of a capillary bridge, is defined by the surface tension instead and determines the maximum cohesion [106]. In addition, a recent study [124] proposed a general model to determine the additive rheology by a dimensionless number (a further generalization of  $\mu(I)$ -rheology) however still lacks to connect inherent dynamics of grains (microscopic processes) to their macroscopic properties.

In our attempt to systematically study and develop an experimental strategy to understand the nonlinear rheology of granular materials, we shear grains with and without a small addition of wetting fluid (Silicon oil) in a rotational rheometer under LAOS mode. We used Polystyrene beads (Dynoseeds<sup>®</sup>) of 80  $\mu\text{m}$ , 140  $\mu\text{m}$ , 250  $\mu\text{m}$  and 500  $\mu\text{m}$  diameter, purchased from Microbeads, USA. All the measurements were made at 23  $^{\circ}\text{C}$  coupled with a plexiglass cup-plate geometry (diameter  $d = 50$  mm). We sheared dry and wet (2 vol.% silicon oil- Shin Etsu SE KF-6011 with viscosity  $\eta = 0.18$  Pa s, surface tension  $\mu_{\text{oil}} = 21$  mN m<sup>-1</sup> and density  $\rho = 1,070$  kg m<sup>-3</sup>) Dynoseeds with these physical constants. The global packing fraction was kept at  $\phi_i^{\text{dry}} \sim 0.611$  and  $\phi_i^{\text{wet}} \sim 0.612$  (to ensure a liquid bridge network formation [36]) and subsequently, it was measured later as ( $\phi_f \equiv$  change in the total volume of a granular sample) after every LAOS test. The values for the packing fractions were found consistent in all the experiments: wet grains  $\mapsto \phi_i = 0.612 \pm 0.01$  and  $\phi_f = 0.619 \pm 0.03$ ; and dry grains  $\mapsto \phi_i = 0.611 \pm 0.02$  and  $\phi_f = 0.620 \pm 0.05$ . Note that these values are obtained for experiments made at a constant normal force of  $N = 1$  N and a frequency of 1.5 Hz. A strain range of  $10^{-3} \leq \gamma_0 \leq 500$  was chosen to cover the significant regions of LAOS rheometry. In a good agreement to [36], the Lissajous-Bowditch (LB) loops were found reproducible and stable for at least 10 cycles. Estimating the Savage number to be  $Sa = \rho(\omega d/3)^2/(F/(\pi d^2/2)) \sim 0.05$  confirms that the granular sample is in the *quasi-static* regime [35]. As described previously in Chapter 3, the stress response for a temporal sinusoidal strain input can be written as  $\gamma(t) = \gamma_0 \sin(\omega t)$ , with  $\omega$  the imposed oscillation frequency,  $t$  time and  $\gamma_0$  the strain amplitude [68, 74, 125]. Where the rate of deformation  $\dot{\gamma} = \gamma_0 \omega \cos(\omega t)$ , determines the viscous and elastic moduli  $G'(\omega)$  and  $G''(\omega)$  respectively. The linear viscoelastic response however can be reformulated by eliminating the time  $t$ , for which the LB curve becomes an ellipse, as sketched here in Fig. 3.1,

$$\gamma(t) = \gamma_0 \sin(\omega t) \quad \text{and} \quad \dot{\gamma}(t) = (\gamma_0 \omega) \cos \omega t \quad (3.1)$$

$$\sigma(t) = \gamma_0 [G' \sin(\omega t) + G'' \cos(\omega t)]. \quad (3.2)$$

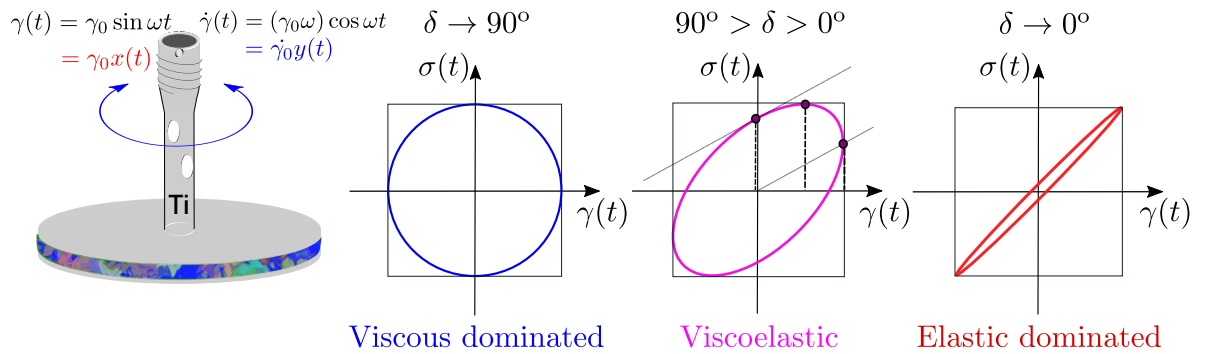


**Figure 3.2:** Basic definitions of viscoelastic moduli.

A general overview of MITlaos approach combining FT-rheology with Chebyshev polynomials is therefore delineated in Fig. 3.3 (a)-(g).

The analytical benefit of using Chebyshev polynomials is due to their orthonormality and near-optimal polynomial interpolation, offering reproducible physical interpretation even when the response is temporal, further allowing to write the elastic  $\sigma'$  and viscous stresses

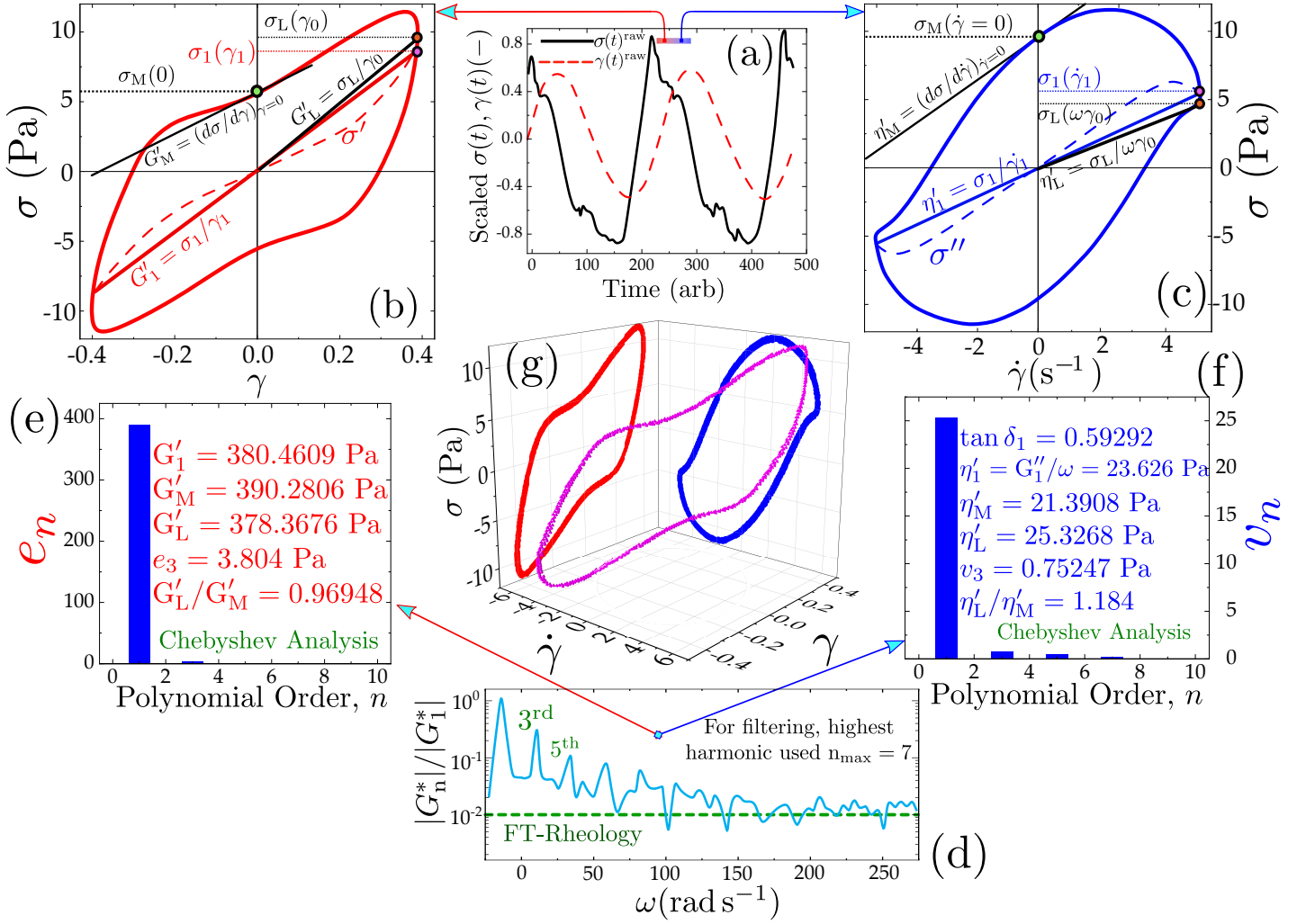


**Figure 3.3:** A schematic illustration of MITlaos analysis. (a) Typical raw data obtained from LAOS rheometry, as marked by sinusoidal input strain (dashed line in red) and distorted (non-sinusoidal) stress output (solid line in black). (b) LB loop representation of the elastic response as a function of strain, to extract linear and nonlinear elastic moduli:  $G'_1$  as the first harmonic,  $G'_M$  is measured at minimum strain and  $G'_L$  is measured at large strain. Similarly, (c) describes the LB loop for a viscous response as a function of strain-rate, with definitions for dynamic viscosities:  $\eta'_1$  as the first harmonic,  $\eta'_M$  at minimum strain-rate and  $\eta'_L$  at maximum strain-rate. (d) FT response generated via MITlaos for the depicted stress-strain data marked with the harmonics as  $n = 3, 5, 7$  accounting for the contribution of nonlinearities in descending order, thus  $n = 7$  is chosen as the terminal harmonic as the response saturates, subsequently admissible for further analysis with Chebyshev polynomials. Consequently, (e) and (f) depicts the elastic and viscous nonlinear measures, characterized by Chebyshev polynomials  $e_n$  and  $v_n$ , respectively. (g) A 3D illustration of nonlinear stress-strain LB loops.

$\sigma''$  by Fourier decomposition as shown in Chapter 2. Following are the formal definitions of nonlinear viscoelastic moduli (as defined in Chapter 2 and 3), which otherwise are briefly previewed in Fig. 3.3 (b) and (c) as an extrapolation of the corresponding slopes of elastic and viscous stress-strain loops.

$$G'_M \equiv \left. \frac{d\sigma}{d\gamma} \right|_{\gamma=0} = \frac{1}{\gamma_0} \sum_{n:\text{odd}} n\sigma_n \cos(\delta_n) = \sum_{n:\text{odd}} nG'_n = e_1 - 3e_3 + \dots, \quad (3.3)$$

$$G'_L \equiv \left. \frac{\sigma}{\gamma} \right|_{\gamma=\pm\gamma_0} = \frac{1}{\gamma_0} \sum_{n:\text{odd}} (-1)^{(n-1)/2} \sigma_n \cos(\delta_n) = \sum_{n:\text{odd}} G'_n (-1)^{(n-1)/2} = e_1 + e_3 + \dots, \quad (3.4)$$

$$\eta'_M \equiv \left. \frac{d\sigma}{d\dot{\gamma}} \right|_{\dot{\gamma}=0} = \frac{1}{\omega} \sum_{n:\text{odd}} nG''_n (-1)^{(n-1)/2} = v_1 - 3v_3 + \dots, \quad (3.5)$$

$$\eta'_L \equiv \left. \frac{d\sigma}{d\dot{\gamma}} \right|_{\dot{\gamma}=\pm\gamma_0\omega} = \frac{1}{\omega} \sum_{n:\text{odd}} G''_n = v_1 + v_3 + \dots, \quad (3.6)$$

The viscoelastic response of granular materials obtained by the methods shown heretofore, is first categorised in three characteristic regimes; linear regime I, nonlinear regime II and slip regime III, as depicted in Fig. 3.4.

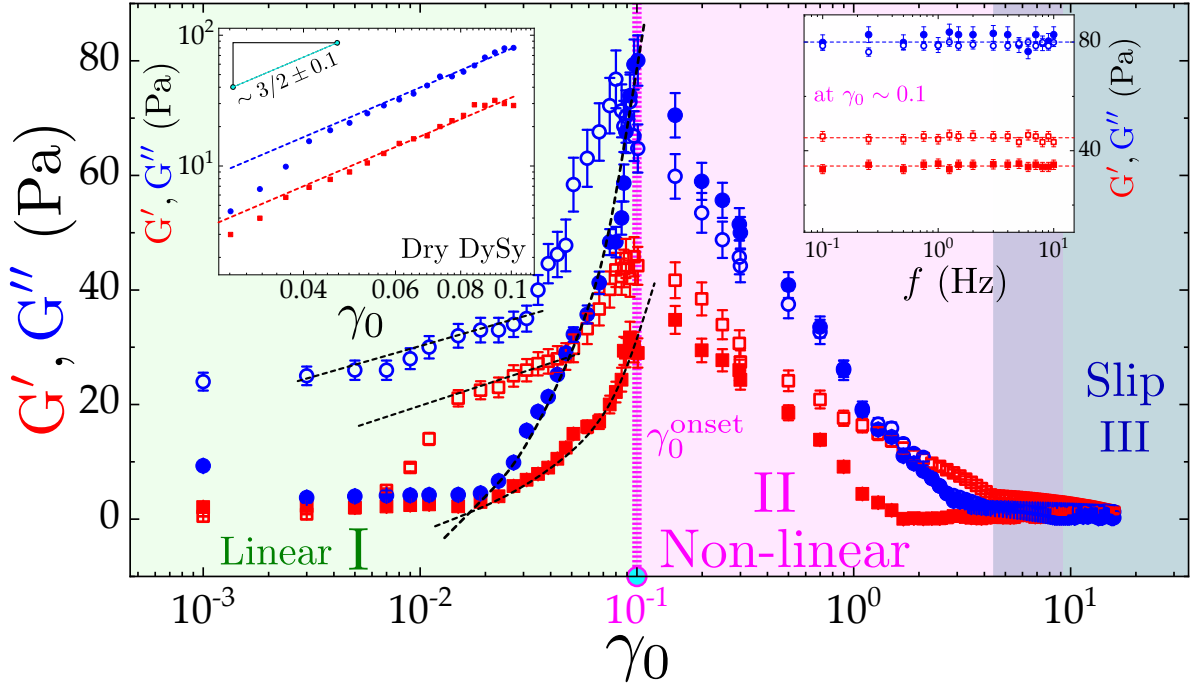


**Figure 3.4:** A semi-logarithmic plot of the amplitude sweep experiments with dry (closed symbols) and wet (open symbols) Dynoseeds. Squares represent  $G'$  and circles  $G''$ . The normal force was fixed to  $N = 1$  N and frequency to  $f = 1.5$  Hz. Fitting wet grains in regime I by equation  $G^j = G_0^j \ln(\frac{\gamma_0}{0.1}) + G^j|_{\gamma_0=0.1}$ ;  $j = ', ''$  with  $G^j|_{\gamma_0=0.1} \sim 33.3$  Pa and  $G''|_{\gamma_0=0.1} \sim 41.44$  Pa, the characteristic moduli revealed the slopes to be  $G_0^j \sim G'_0 \sim G''_0 \sim 0.2 \pm 0.2$  nJ/grain. The onset of nonlinearity in regime II is denoted by  $\gamma_0^{\text{onset}} \sim 0.1$ . The inset of  $G''(\gamma_0)$  is a zoomed-in part of the dry Dynoseeds data in a log-log scale with a slope of  $\sim 3/2$ . The second inset shows the frequency dependence of the viscoelastic moduli measured at  $\gamma_0 \sim 0.1$ . The shaded area marks the onset strain for the corresponding flow regime.

In amplitude sweep protocol,  $\gamma_0$  was increased successively after 10 complete oscillations. In regime I as entailed in SAOS [85],  $G'$  and  $G''$  are found independent of strain amplitude

(in the range,  $10^{-3} \leq \gamma_0 \leq 10^{-2}$ ) confirming the linear viscoelastic response for grains. As the strain increases  $10^{-2} < \gamma_0 < 10^{-1}$ ,  $G'$  and  $G''$  begins to follow a power-law behaviour (dashed fits in black) for dry grains, which we relate with the formation of force chain networks [59, 118, 126], whereas for wet grains, logarithmic growth is followed that can be alluded to the oscillating capillary bridges, provided that the applied strain does not exceed the energy required to rupture a capillary bridge [40, 86]. Nonlinear regime II comes into effect as the strain amplitude, in our case is larger than  $\gamma_0 \geq 10^{-1} \equiv \gamma_0^{\text{onset}}$ , as corroborated by the onset strain wherein the slope of  $G'$  and  $G''$  decays for both dry and wet grains. The slip regime III then follows as the material response flattens. Note: although SAOS test assumes that the material is in the linear regime I until  $\gamma_0 \approx 10^{-1}$  within the resolution limits of the rheometer, the response becomes nonlinear as the inter-granular contact dynamics (such as force chains for dry and capillary bridges for wet grains) begins to contribute before LAOS even starts. In the inset of Fig. 3.4,  $G'$  and  $G''$  for both dry and wet grains were found independent over the applied frequency measured at  $\gamma_0 \sim 1$ . Comparing our values of  $G'$  and  $G''$  of wet grains to the results of [127], we find  $G' < G''$ , implying viscous flow for liquid bridge network under confinement and not purely elastic. Since in the aforesaid study a vane-in-cup geometry (low or no confinements) was employed to shear  $100 \mu\text{m}$  beads at relatively (to our) small strain amplitude ( $\gamma_0 \sim 10^{-6}$  to  $10^{-2}$ ) finds  $G' > G''$ . Therefore to understand this contribution of viscous effects arising from a network of capillary bridges in  $G'$  and  $G''$ , we estimate the energy released in rupturing a standard capillary bridge in a pendular regime as previously proposed in the works [36, 109]. By following the study of [128] a schematic approach was adopted, as illustrated in Fig. 3.5.

This method allowed us to calculate the dynamic forces between two grains, capillary and viscous  $F_c$  and  $F_v$ , respectively, which can be further integrated to estimate the rupture energy required to form or break a capillary bridge. Forces describing the capillary (source: Young-Laplace equation) and viscous (source: Lubrication approximation and Reynold's equation) action of the liquid bridge reads as,

$$F_c = \pi\mu R_{\text{meridian}} \left[ 1 + \frac{R_{\text{meridian}}}{R_{\text{neck}}} \right] \quad (3.7)$$

$$R_{\text{neck}} = \frac{(H/2) + R(1 - \cos \alpha)}{\cos(\theta_p + \alpha)}, \quad R_{\text{meridian}} = R \sin \alpha - [1 - \sin(\theta_p + \alpha)] \times R_{\text{neck}} \quad (3.8)$$

$$F_v = \frac{3}{2} \pi \frac{Ca}{H} \times 1 - \left( 1 + \frac{2x^2 H}{R^3 \tilde{H}^2} \right)^{-1} \quad (3.9)$$

where  $H$  is the distance between the surface of the two beads,  $x$  is the azimuthal radius of the liquid bridge at its contact line,  $R$  is the radius of the particle,  $d$  is the distance between the surface of the bead at the centre of the capillary bridge and the line that connects the two opposite points of the contact line,  $\theta_p$  is the contact angle between liquid-particle,  $\mu$  is the surface tension,  $Ca \equiv \frac{\eta \dot{\gamma}}{\mu}$  is the capillary number [128] with  $\eta$  the viscosity and  $\alpha$  is the embracing angle. For analytical precision, we divide  $F_c$  and  $F_v$  by the liquid volume  $\mu R$  and then integrate them with respect to the distance between two grains  $H$ , from zero to *quasi-static* rupture distance  $\tilde{H}$  for  $F_c$  and from characteristic surface roughness length

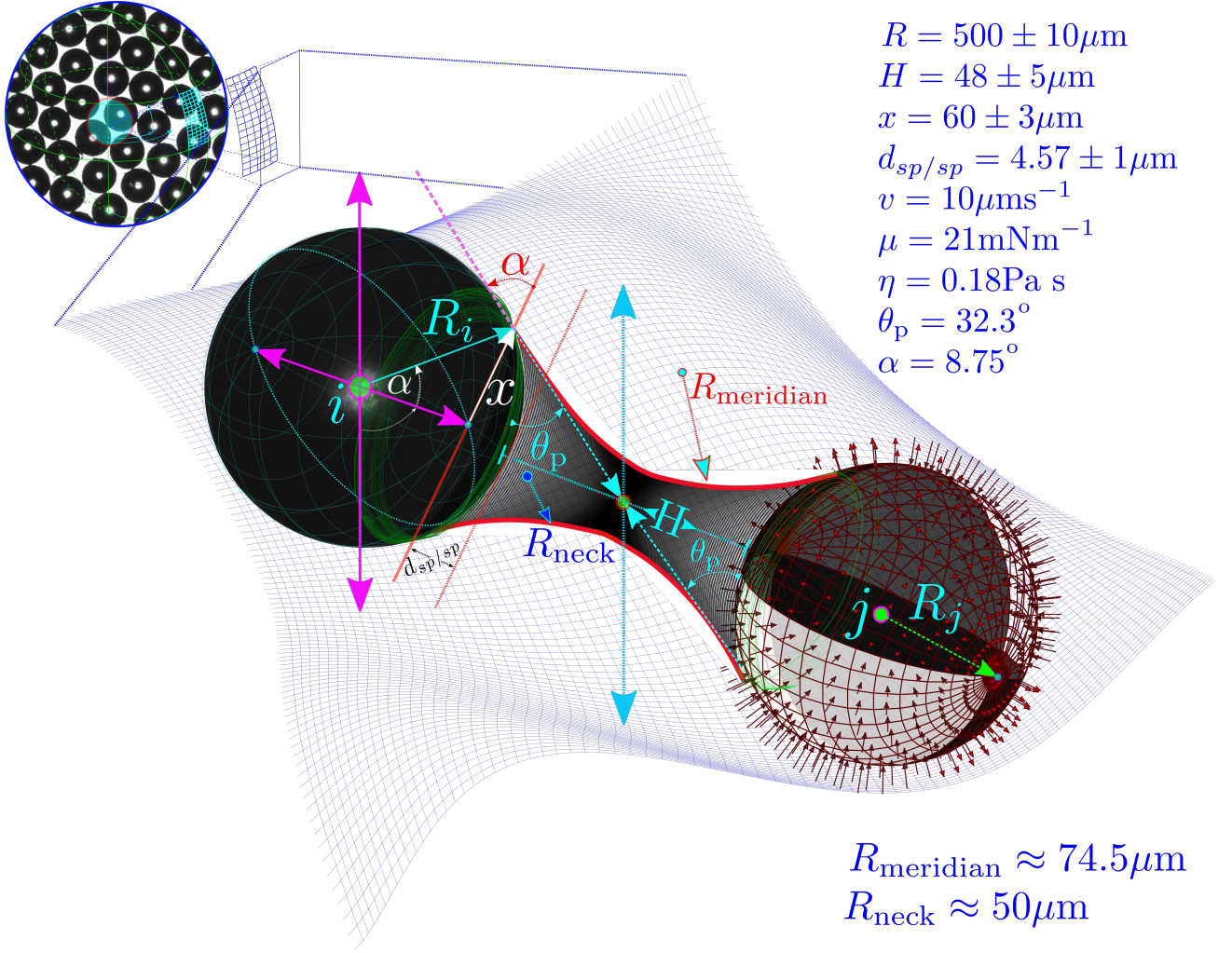


**Figure 3.5:** A schematic illustration of a capillary bridge between two Dynoseeds ( $i$  and  $j$ ) inspired by the works of [128, 129]. All the parameters displayed here describes the state of a capillary bridge as formally defined in the text below, with the respective values used in calculating how much energy is required to break such a capillary bridge. The encircled image in blue is a plexiglass cup-plate geometry employed for rheological measurements.

[109, 128]  $\tilde{d}$  to  $\tilde{H}$ , such that the rupture energies associated with capillary and viscous forces,  $\tilde{W}_c$  and  $\tilde{W}_v$  respectively, yields

$$\tilde{W}_c = \int_0^{\tilde{H}} \frac{F_c}{\mu R} dH \approx 2\pi \cos \theta_p \left\{ (1 + \theta_p/2)(1 - A)\pi^{1/3} \frac{x + H}{2R} + \sqrt{\frac{2x^2 H}{R^3}} \right\}, \quad (3.10)$$

$$\begin{aligned} \tilde{W}_v = \int_{\tilde{d}}^{\tilde{H}} \frac{F_v}{\mu R} dH = \frac{3}{2} \pi Ca \left[ \ln \left( \frac{A\sqrt{\pi}}{(1+A)^2} \right) - \ln \tilde{d} - 2 \ln \left( \tilde{d} + \sqrt{\tilde{d}^2 + \frac{2x^2 H}{R^3}} \right) \right. \\ \left. + \frac{1}{2} \ln \left( \pi \tilde{d}^2 + 2 \frac{\pi x^2 H}{R^3} \right) \right]. \end{aligned} \quad (3.11)$$

where  $A = (1 + 2\pi^{1/3} \frac{x+H}{2R} / \pi(1 + \theta_p/2)^{1/2})^{1/2}$  and rupture distance is  $\tilde{H} \simeq (1 + \frac{\theta_p}{2})\pi^{1/3} \frac{x+H}{2R}$ . Therefore the total rupture energy,  $\tilde{W}_{\text{tot}} = \tilde{W}_c + \tilde{W}_v$  can be estimated for a capillary bridge between two grains. The dynamic forces for a liquid bridge (used in this study) between grains at  $\gamma \approx 0.1$  as described with following constants;  $\mu \approx 21 \text{ mN m}^{-1}$ ,  $\eta = 0.18 \text{ Pa s}$ ,  $H \approx 50 \text{ }\mu\text{m}$ ,  $R \approx 250 \text{ }\mu\text{m}$ ,  $x \approx 60 \text{ }\mu\text{m}$ ,  $\alpha \approx 8.75 \text{ deg}$ ,  $\theta_p \approx 32.3 \text{ deg}$  and  $d_{sp/sp} \approx 4.57 \text{ }\mu\text{m}$ , reads  $F_c \approx 7.64 \pm 0.02 \text{ }\mu\text{N}$  and  $F_v \approx 6.24 \pm 0.02 \text{ }\mu\text{N}$ . Adding both contributions gives a total force as  $F_{\text{tot}} = (F_c + F_v) \approx 13.88 \pm 0.15 \text{ }\mu\text{N}$ , with  $R_{\text{meridian}} \approx -74 \pm 5 \text{ }\mu\text{m}$  and  $R_{\text{neck}} \approx -48 \pm 5 \text{ }\mu\text{m}$ . With a large capillary number  $Ca \approx 0.85$  at high velocity  $v \approx 10.5 \text{ }\mu\text{m s}^{-1}$ , gives the approximate rupture distance as  $\tilde{H} \simeq 5.525 \pm 0.035 \text{ }\mu\text{m}$  and the characteristic surface roughness length, assuming minimum roughness and uniform distribution of adhesive asperities [109, 128–131] gives  $\tilde{d} \sim 0.05 \pm 0.02 \text{ }\mu\text{m}$ . Henceforth, with  $A \approx 1.36$  and the dimensionless capillary bridge volume  $\tilde{V} = (x^2\pi H) \times R^{-3} \approx 0.001152$ , we calculate the total rupture energy of a capillary bride as described here, by using a relation of the following form,

$$\begin{aligned} \tilde{W}_{\text{tot}} = & 2\pi \cos \theta_p \left\{ (1 + \theta_p/2)(1 - A)\pi^{1/3} \frac{x + H}{2R} + \sqrt{2\tilde{V}} \right\} \\ & + \frac{3}{2} \pi Ca \left[ \ln \left( \frac{A\sqrt{\pi}}{(1 + A)^2} \right) - \ln \tilde{d} - 2 \ln \left( \tilde{d} + \sqrt{\tilde{d}^2 + 2\tilde{V}} \right) + \frac{1}{2} \ln(\pi\tilde{d}^2 + 2\pi\tilde{V}) \right] \end{aligned} \quad (3.12)$$

yielding,

$$\tilde{W}_{\text{tot}} \approx \tilde{W}_c + \tilde{W}_v \approx 8.4 \pm 0.5 \text{ nJ/bridge}. \quad (3.13)$$

Although, the significance of this estimation corresponds to grains sheared in I and require a reference scale to make a comparison, to reveal the threshold of  $\tilde{W}$  when oscillating capillary bridges begin to break. Since the average loss modulus accounts for the energy dissipated while a capillary bridge breaks, has to balance the rupture energy  $\tilde{W}_{\text{tot}}$ . Thus, on the basis of regime I, terminating at  $\gamma_0 = 0.1$  estimates an average loss modulus of  $\langle G'' \rangle = 25 \pm 5 \text{ Pa} \approx 1.6 \pm 0.3 \text{ nJ/grain}$ , a volume unit in terms of 'grain' can be defined for a grain of diameter  $500 \text{ }\mu\text{m}$ .

Non-linear regime II typically begins at strain amplitudes larger than the grain diameter ( $\gamma_0 > 500 \text{ }\mu\text{m}$ ) in our case with the range  $10^{-1} \leq \gamma_0 \leq 10$ , clearly indicated by the differences between  $G'$  and  $G''$  for wet and dry grains. Albeit an order of magnitude difference found for  $\tilde{W}_{\text{tot}} \approx 8.4 \pm 0.5 \text{ nJ/bridge} > 0.26 \pm 0.02 \text{ nJ/grain}$  (see fits in Fig. 3.4) and the identification of dynamical regimes via  $G'$  and  $G''$ , for nonlinear flow aspects to be quantified a rigorous analytical approach with a strong mathematical foundation is therefore required.

Fig. 3.6 (a) and (b) summarizes the LB-loops for wet and dry granular matter, respectively, with arrows showing their clockwise rotation (i.e. strain stiffening). In (c) a clear transition from linear (ellipse) to non-linear (distorted ellipse) viscoelastic response is shown at  $\gamma < \gamma_0^{\text{onset}}$  in green and  $\gamma > \gamma_0^{\text{onset}}$  in magenta, respectively. Fig. 3.6 (d) shows the stored elastic energy per unit cycle  $\tau_a$  depicted for dry (open circles in red) and wet (open squares in blue) granular matter. The slopes  $\tau_0^{\text{onset}}$  and  $\tau_0^{\text{offset}}$  were measured at the onset of nonlinearity and

the offset to slip regime III, respectively, in correspondence to the scaling relation  $\frac{\gamma_0}{\gamma_{\text{onset}}} = \exp\left(\frac{\tau_a}{\tau_0}\right)$ , as previously proposed for tube rheometer in [36, 120, 132] and later demonstrated by [36] to estimate a non-thermal temperature. Therefore, the slopes of  $\tau_0^{\text{onset}}$  and  $\tau_0^{\text{offset}}$  will be invoked in the next section for a comparison with other similar scaling relations.

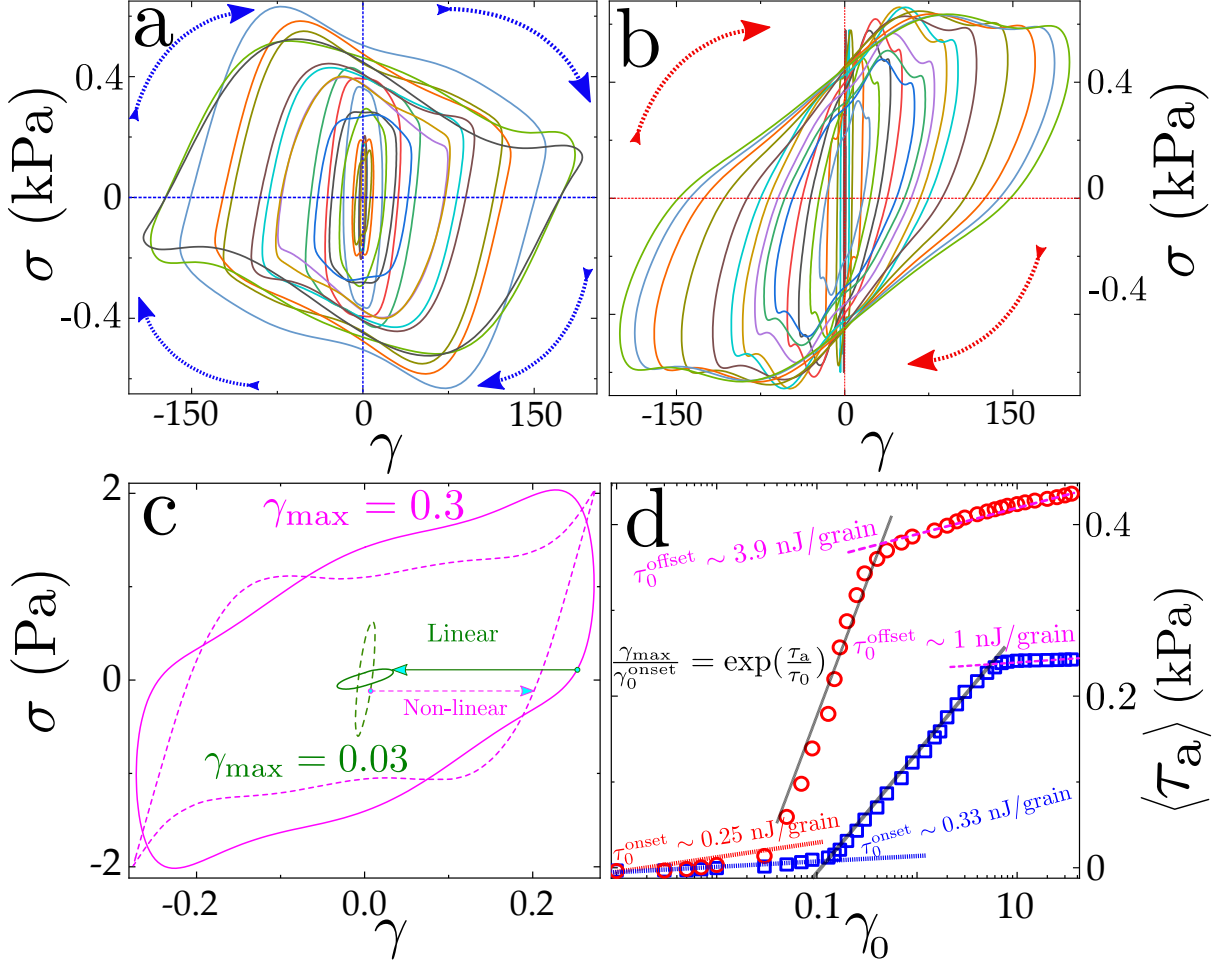


**Figure 3.6:** A summarised overview of LB loops for (a) wet and (b) dry Dynoseeds of 500  $\mu\text{m}$  as a function of  $\gamma$ . (c) Illustrates a linear to nonlinear transition of the viscoelastic response, as the LB ellipse clearly distorts at large  $\gamma$  for dry (solid line) and wet (dashed line) grains. (d) Stored elastic energy per unit cycle as a function of strain amplitude with slopes corresponding to a non-thermal temperature, corroborated by the fits to the equation shown here, where circles represent wet grains and squares, dry grains.

### 3.1.1 Characteristic Degree of Nonlinearity

By applying FT-rheology with Chebyshev polynomials as shown before in Fig. 3.3, we present the first harmonic viscoelastic moduli  $G_1'$  and  $G_1''$  in Fig. 3.7 as a function of  $\gamma_0$  and  $\omega\gamma_0$ . Fig. 3.7 (c) depicts the non-linear elastic moduli and (d) the dynamic viscosities, obtained by MITlaos analysis and subsequently verified from the representative LB loops.

Furthermore, building on the characteristic moduli scaling described in equation 14 for linear viscoelastic response and at  $\gamma_0^{\text{onset}}$ , we, therefore, rewrite the scaling relation explicitly

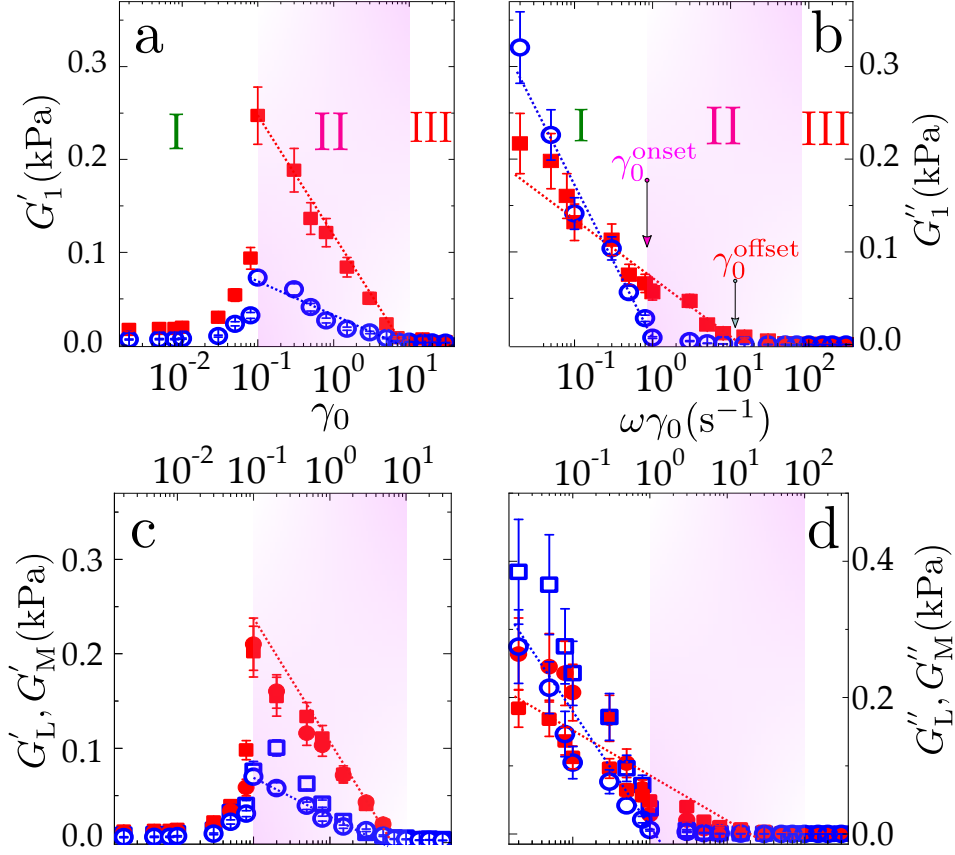


**Figure 3.7:** Semi-logarithmic representation of viscoelastic moduli corresponding to the linear and nonlinear stress-strain response. In (a) the first harmonic elastic modulus  $G'_1$  as a Chebyshev polynomial  $e_1$  and (b) the first harmonic dynamic viscosity  $G''_1$  as  $\omega v_1$  is presented for dry (closed squares) and wet (open circles) Dynoseeds, respectively. Similarly, (c) represents the non-linear elastic moduli as a function of strain amplitude with squares as large strain elastic modulus  $G_L$ , and circles, the minimum strain elastic modulus  $G_M$ , and (d) highlights the non-linear dynamic viscosity as a function of the evaluated (by MITlaos) strain rate  $\omega\gamma_0$ , with fixed  $\omega = 9.42 \text{ rad s}^{-1}$ . Squares represent large strain rate viscosity  $\eta_L$ , and circles correspond to the minimum strain rate viscosity,  $\eta_M$ . Dashed lines are fits of the equation 3.14.

for the non-linear regime. Hereof characterized in the strain limit  $\gamma_0^{\text{onset}} \leq \gamma_0 \leq \gamma_0^{\text{offset}}$  and estimate the characteristic energy associated with nonlinear response, and since the representative slope values (including  $\tau_0^{\text{onset}}$  and  $\tau_0^{\text{offset}}$ ) are found similar, strongly indicate a correlation with structural rearrangements.

$$\frac{\gamma_0}{\gamma_0^{\text{offset}}} = \exp\left(\frac{-G'_1}{G'_0}\right); \quad \gamma_0^{\text{onset}} \leq \gamma_0 \leq \gamma_0^{\text{offset}} \quad (3.14)$$

Upon fitting,  $G_{0j} \sim 1.3 \text{ nJ/grain}$  is found for the wet grains and  $G_{0j} \sim 3.4 \text{ nJ/grain}$  for the dry grains. Comparing to what we obtained in Fig. 3.4 and the experimental conclusions of [36], the values are in good agreement to support the characteristic moduli scaling for shear-cell geometry. By ruling out the first harmonic, the moduli collapsed in the vanishing strain

limit, and revealed a clean non-linear response calculated for wet grains in  $\gamma_0 \leq \gamma_0^{\text{onset}}$ , and dry in  $\gamma_0 \leq \gamma_0^{\text{offset}}$  as:

$$\frac{\omega\gamma_0}{\omega\gamma_0^j} = \exp\left(-\frac{G_1''}{G_1''^0}\right) \quad \gamma_0 \leq \gamma_0^j \quad j = \gamma_0^{\text{onset}}, \gamma_0^{\text{offset}}, \quad (3.15)$$

evaluating  $\gamma_0^{\text{onset}} = 0.11 \pm 0.02$  and  $G_1''^0 = 4.9 \pm 0.3 \text{ nJ/grain}$  for wet grains and  $\gamma_0^{\text{offset}} = 1.5 \pm 0.5$  and  $G_1''^0 = 1.9 \pm 0.2 \text{ nJ/grain}$  for dry grains. As indicated earlier in Fig. 3.4, these values strongly indicate  $\gamma_0^{\text{offset}} \sim 2$  being the offset for the force branching out, such that at  $\gamma_0 < \gamma_0^{\text{offset}}$ , the network of force chains acts as the reinforcement and strengthen the contacts between grains, as additionally evidenced by high Coulomb friction of  $\mu_f = 0.33 \pm 0.2$ , explaining the strain stiffening behaviour. However, the viscous first harmonic for the wet grains captured a contrasting image than elastic moduli, in revealing a pre-yielding range  $\gamma_0 \leq \gamma_0^{\text{onset}}$  (Fig. 3.7 (b)). This allowed us to express pure non-linear viscoelastic response via third harmonic only  $e_3$  and  $v_3$ , respectively:

$$e_3 \sim \frac{(G_M' - G_L')}{3} \quad v_3 \sim \frac{(\eta_L' - \eta_M')}{3} \quad (3.16)$$

Correspondingly, these nonlinear measures (including the higher odd harmonics) can be integrated into a single Q-parameter-like (FT-rheology [51, 52, 82]) variable, the characteristic degree of nonlinearity  $\zeta$ . In Fig. 3.8 we depict elastic  $\zeta_e$  and viscous  $\zeta_v$  degree of nonlinearity, which are found consistent with the linear regime I, as  $\zeta_e \sim \zeta_v \approx 0$ . Furthermore, positive values of  $\zeta_e$  are attributed to strain stiffening among dry and wet granules, as we find  $\zeta_e^{\text{dry}} > \zeta_e^{\text{wet}}$ . However, in the non-linear regime II,  $\zeta_e$  gradually increased until saturation with  $\zeta_v$  exhibiting a peak behaviour at  $\gamma_0^{\text{onset}} \approx 0.1$  suggesting a relation between elastic and viscous non-linearities  $\zeta_e$  and  $\zeta_v$ , respectively. To understand the physical significance of  $\zeta$ , defined as,

$$\zeta_e = \sqrt{\frac{e_3^2 + e_5^2 + e_7^2}{e_1^2}}, \quad \text{and} \quad \zeta_v = \sqrt{\frac{v_3^2 + v_5^2 + v_7^2}{v_1^2}} \quad (3.17)$$

we intuitively draw an analogy with a study on compaction experiments [133] and fit  $\zeta$  with a stretched exponential equation [25, 133, 134]. Although the fits corroborates the compaction-like dynamics due to applied normal force, an accurate demonstration to invoke Kohlrausch-William-Watts law (as shown in the referred studies) requires a clear relaxation in  $\zeta$ . Besides, at large strain amplitudes the granular system may exhibit accelerated rejuvenation as found previously for glasses and colloids [33, 41], also known as *overageing*, wherefore the time frame to capture such accelerated relaxation processes is too small. Nevertheless, we assume that the underlying physics in compaction study and the steady-state rheology of granular matter is inherently similar however the rapid deformation or large strain amplitudes, can also suppress the relaxation mechanisms as grains begin to slip or

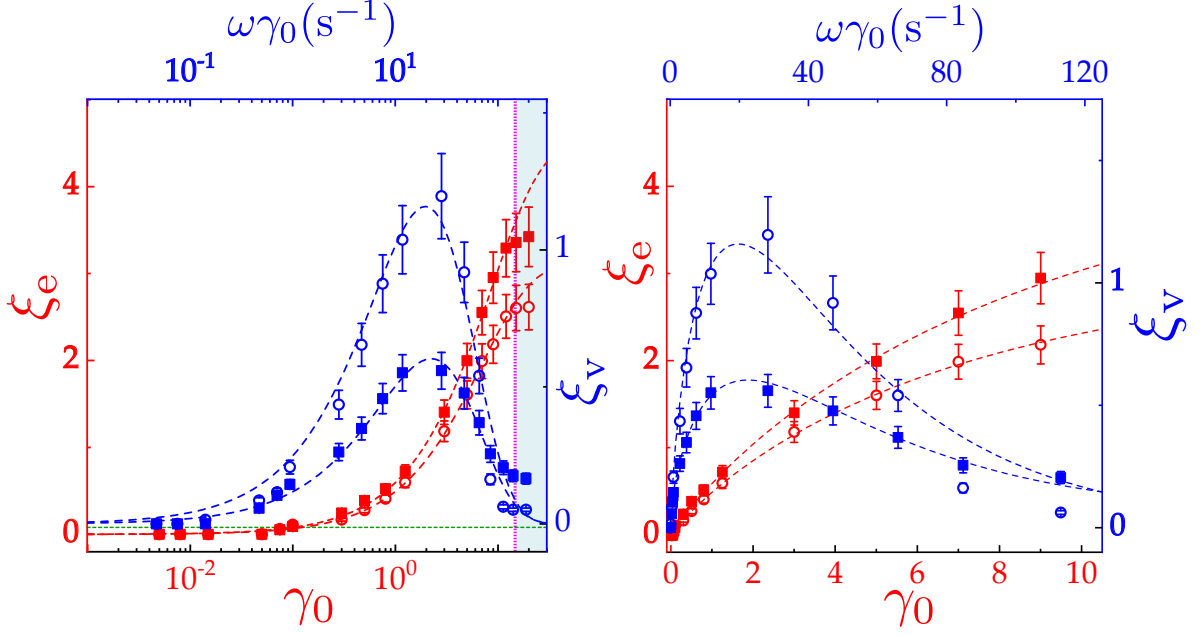


**Figure 3.8:** (a) Semi-logarithmic and (b) linear representation of elastic and viscous nonlinearity:  $\zeta_e$  and  $\zeta_v$ , quantified with equations 3.1.1 by the Chebyshev polynomials of higher order as a function of the strain amplitude  $\gamma_0$  and the evaluated strain rate  $\omega\gamma_0$ , respectively. Open symbols: wet dynoseeds, closed symbols: dry dynoseeds, colour code: red represents elastic non-linearities and blue, viscous non-linearities. The red lines are the corresponding fits for  $\zeta_e$  curves according to equation 3.1.1 reveal a relation with the adjustment of the blue lines representing  $\zeta_v$  peak curves following the equation 3.1.1 (see text). The shaded area corresponds to the slip regime III

stick as shear banding dominates (jammed-like). Furthermore, this suggests that the viscous non-linearities  $\zeta_v$  can be ascribed to the rearrangement of mesoscopic domains caused by external shear forces, implying that the undulations of elastic non-linearities  $\zeta_e$  until saturation is governed by the growth and coalescence of mesoscopic domains (as we interpret from Fig. 3.8). Thereupon,  $\zeta_e$  should be scalable with viscous non-linearity analogous to the scaling of macroscopic packing fraction  $\bar{\rho}$  demonstrated in [133, 134], thence follows,

$$y = \frac{\zeta_e}{\zeta_e^\infty} = 1 - \exp\left(-\frac{\gamma_0}{\gamma_0^\infty}\right)^\delta \quad (3.18)$$

$$\frac{\zeta_v}{\zeta_v^\infty} \sim \frac{dy^2}{dx^2}\bigg|_{kx}; \quad \text{where } kx = \frac{\omega\gamma_0}{(\omega/k)\gamma_0^\infty}. \quad (3.19)$$

By fitting the data in Fig. 3.8 with these equations, we obtain the stretched exponent and the elastic range for the dry grains as,  $\delta = 0.9 \pm 0.1$  and  $\gamma_0^\infty = 8.7 \pm 0.6$ ; and for the wet grains,  $\delta = 0.9 \pm 0.2$  and  $\gamma_0^\infty = 7 \pm 3$ . The undulations in the data were tweaked in accordance with values of  $\delta$  and  $\gamma_0^\infty$  to adjust the error margins for more accurate approximations. Consequently, a relation between the elastic and viscous non-linearities based on the fits of  $\zeta_v$  with respect to  $\omega\gamma_0$  defines a  $k$ -parameter to adjust the position of the data curves, where

$k \approx 1.5$  indicate that there exist a coupling between elastic and viscous nonlinearities where  $\zeta_e$  and  $\zeta_v$  can be consistently scaled by a factor  $\omega$ . Taking into account an existence of at least one shear band, where the deformation gradient hinders the granular rearrangements, this coupling can thus be attributed to the phase lag between shearing plate and the granular sample in a cup-plate geometry. On a side note: it would appear as if  $\zeta$  is allowed to evolve only in the nonlinear regime II as the  $\delta$  is directing the corresponding stretched exponential fit, Kohlrausch-William-Watts law can thus be invoked, and we thenceforth leave it as a partial outlook of this thesis, because further in-depth investigation on this matter, is required.

On these grounds, we propose that the characteristic scaling ( $\tau_0, G_{0,j}$ , and  $G_1^{0''}$ ) as demonstrated above, invokes a proportionality constant similar to the Boltzmann-like parameter hitherto adopted in [36] to estimate a non-thermal variable, the mean-field noise temperature for tube rheometer. Moreover, the values of  $\zeta_e$  and  $\zeta_v$  can be attributed to the phenomenon that the ensemble of elastic structures undergoing rearrangements at  $\gamma_0^{\text{onset}} \geq \gamma_0 \leq \gamma_0^{\text{offset}}$  seems to be governed by the mesoscopic flows. Finding that the rearrangement dynamics or the competition between microstructural relaxation and macroscopic elasticity, although from different origins in dry and wet grains, begins at  $\gamma_0 \geq \gamma_0^{\text{onset}}$ , strongly implies yield-like events similar to thermal glasses. We, therefore, draw an analogy with glasses to study and view the dynamics of these mesoscopic elements with the *Soft Glassy Rheology* (SGR) model [12, 30, 135], heretofore acknowledged by [2, 8, 9, 33] for slow granular flows. It is in light of these aforesaid studies, the next section is concerned, focusing on the inherent dynamics of granular materials from a standpoint of the SGR model.

### 3.2 Soft Glassy Rheology of Confined Granular Flows

In this section, we introduce two additional parameters, constant confinement with pressure and the size of granulates to study the physical significance of nonlinearities via the SGR model on the accounts of the rheology of granular matter at large strains. Henceforth, we study the stress-strain behaviour of confined granular matter with a constitutive approach to approximate the noise temperature via decomposition of LB loops in elastic and viscous symmetry lines using the equations in 1.3.3. To ensure that the structural rearrangements are maintained near jamming while the granular sample stays confined, a normal force  $N$  was applied to the shear cell without violating the strain cycle malfunction. This allowed estimating the noise temperature of a quenched granular sample at a fixed normal force, as additionally corroborated by its strong dependence on the packing fraction  $\phi$ . Furthermore, upon scaling  $\phi$  with  $P$  identified a jamming confinement pressure ( $P_j$  at  $\phi_j$ ) in a good agreement with the studies [2, 9, 59, 60] that associated this pressure to the force chain percolation failure [59, 60], by demonstrating that the force chains and the linearity percolation stem from the topological constraints of the granular contact networks and not the friction and force-torque balance [56, 59, 60], hence serving as a relevant statistical feature. In Fig. 3.9 below, a typical decomposition process of LB loops is shown for dry (solid lines) and wet (dashed lines) Dynoseeds of 80  $\mu\text{m}$  diameter, obtained from the LAOS rheometry experiments made at  $N = 1 \text{ N}$  and  $f = 1.5 \text{ Hz}$ . An LB loop at  $\gamma \approx 3$  is then chosen (Fig. 3.9 (b)) to illustrate the decomposition via symmetry arguments (as shown by the  $\sigma - \gamma$  relation) and later summarised in (c) for all the loops shown in (a).

This process is hereafter repeated for all the experiments made in the nonlinear regime  $\gamma_0^{\text{onset}} \geq \gamma_0 \leq \gamma_0^{\text{offset}}$  at different  $N \approx 0.5 \text{ N} - 12 \text{ N}$  and at constant frequency  $f = 1.5 \text{ Hz}$  for dry (solid lines) and wet (dashed lines) grains.

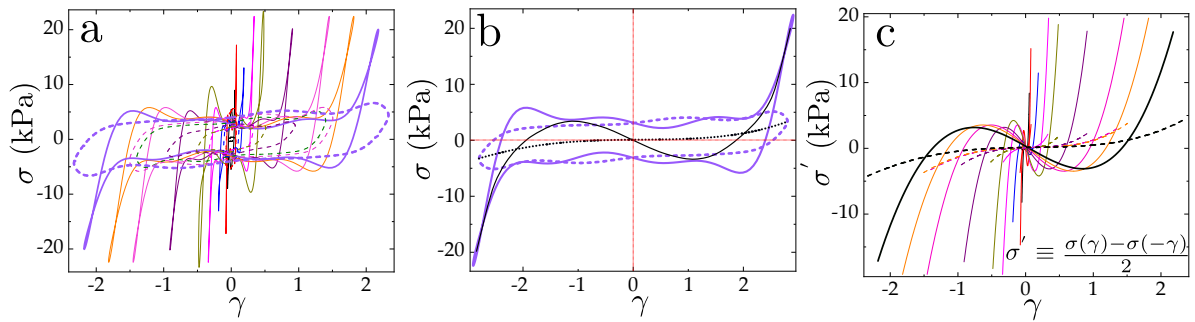


**Figure 3.9:** (a) Lissajous-Bowditch loops as obtained from a LAOS experiment on Dynoseeds beads of 80  $\mu\text{m}$  diameter with (dashed lines) and without (solid lines) small additions of Silicon oil. (b) Decomposition of a selected LB loop (at  $\gamma \approx 3$ ) via stress-strain symmetry arguments. (c) Elastic symmetry lines summarised correspondingly to the LB loops shown in (a).

Fig. 3.10 and 3.11 gives a general overview of the representative LB loops and elastic symmetry lines, respectively, summarised for 80  $\mu\text{m}$  Dynoseeds with (dashed lines) and without (solid lines) the addition of Silicon oil.

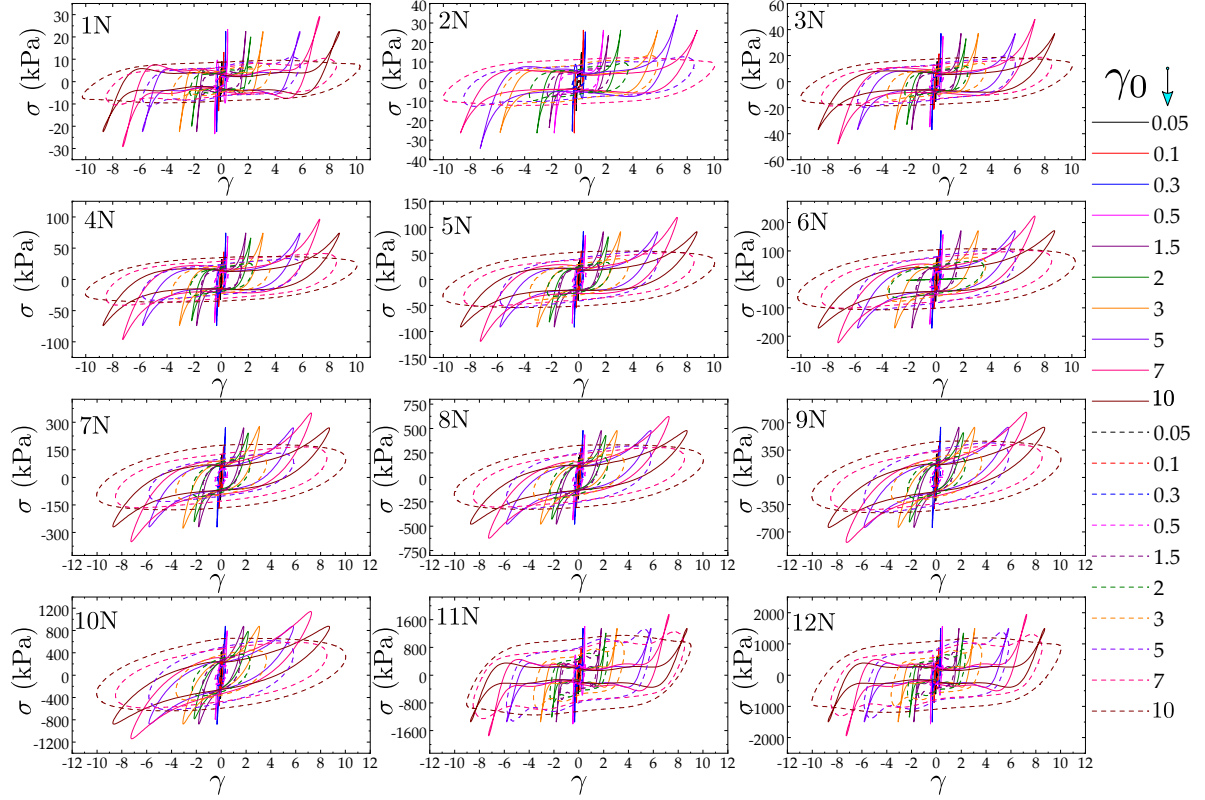


**Figure 3.10:** LB loops summarised for Dynoseeds beads of 80  $\mu\text{m}$  diameter with (dashed lines) and without (solid lines) small additions of Silicon oil as a function of strain  $\gamma$  for each normal force as  $N = 1\text{ N} - 12\text{ N}$ , respectively.

The additional data summary for other sizes ( $d : 140\ \mu\text{m} - 500\ \mu\text{m}$ ) is given in Appendix A. The strain at which  $G'_L$  and  $G'_M$  diverges, fixes an onset strain  $\gamma_0^{\text{onset}}$ , separating linear viscoelastic (LVE) regime and non-linear viscoelastic regime (NLVE).

In Fig. 3.12 (a) and (b), a series of LB loops and the corresponding elastic symmetry lines chosen at ( $\gamma \sim 2$ ) are shown for increasing  $N$  for dry and wet grains represented by solid and dashed lines, respectively. As demonstrated previously, the LB loops were additionally processed via Fourier transform and Chebyshev polynomial interpolation, to extract the associated non-linear viscoelastic measures. The slope extrapolation to obtain  $G'_L$ ,  $G'_M$  and the basic definition of auxiliary rheological measures ( $E_d$ ,  $\tau_a$ ) is still shown in Fig. 3.12 (a) (for further details, see chapter 2 and 3). Although clearly visible, the evolution of LB loops with increasing  $N$ , as  $G'_L$ ,  $G'_M$ ,  $E_d$  and  $\tau_a$  vary along, the idea here is to define a single variable that is deeply ingrained in aforesaid variables. In connection with this comes the consideration of the constitutive model (SGR), where the complete viscoelastic response of a system can be expressed via noise temperature alone, and thus must be true contrariwise,

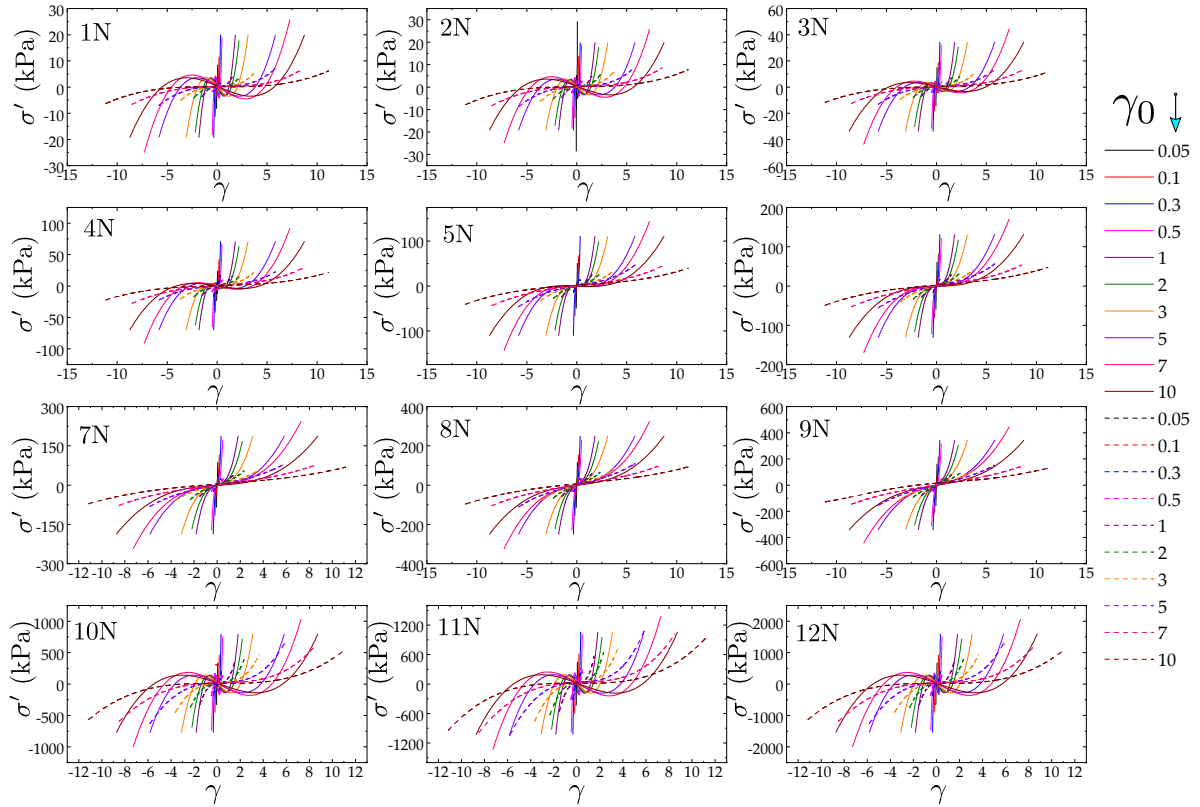


**Figure 3.11:** Corresponding elastic symmetry lines summarised for Dynoseeds beads of  $80\ \mu\text{m}$  diameter with (dashed lines) and without (solid lines) small additions of Silicon oil as a function of strain  $\gamma$  for each normal force as  $N = 1\ \text{N} - 12\ \text{N}$ , respectively.

i.e. definable by virtue of basic viscoelasticity measures.

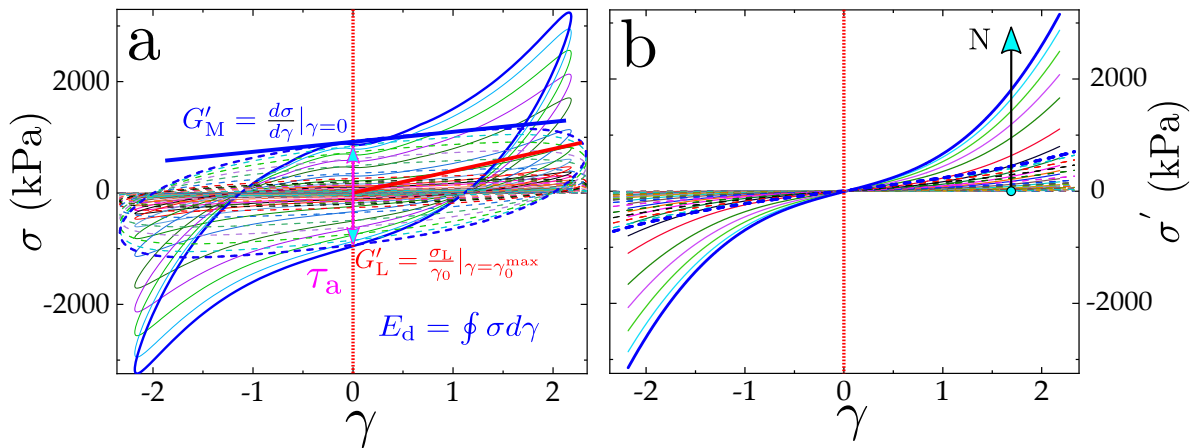


**Figure 3.12:** (a) Lissajous-Bowditch loop from a LAOS experiment on Dynoseeds beads of  $80\ \mu\text{m}$  diameter with (dashed lines) and without (solid lines) small additions of Silicon oil. (b) Elastic symmetry lines corresponding to the LB loops. The data is chosen at  $\gamma_0 \approx 2 > \gamma_0^{\text{onset}}$  for normal force  $N (= 0.5\ \text{N} - 12\ \text{N})$

We begin this verification by first analysing the elastic symmetry lines as an alternative

approach, which upon fitting with a periodic function of the following form computes solutions resembling the constitutive formalism of SGR model,

$$\sigma' = \sigma'_0 + A\gamma - B \sin\left(\frac{\gamma}{\gamma_0}\right); \quad B = \ln\left(\frac{\gamma_0}{\gamma_0^{\text{onset}}}\right) k_B \Theta \quad (3.20)$$

where  $\sigma'$  on lhs is the elastic response the system, first two terms on rhs accounts for stored energy in the system, and the third term on rhs describes the dissipation. Besides,  $B$  either represents the noise temperature or proportionality to it. Fig. 3.13 (a)-(c), compares the similarity between the first harmonic elastic moduli  $G'_1$ , non-linear elastic moduli  $G'_M$  and  $B$ , respectively calculated for dry (closed symbols, black) and wet (open symbols, blue) grains.

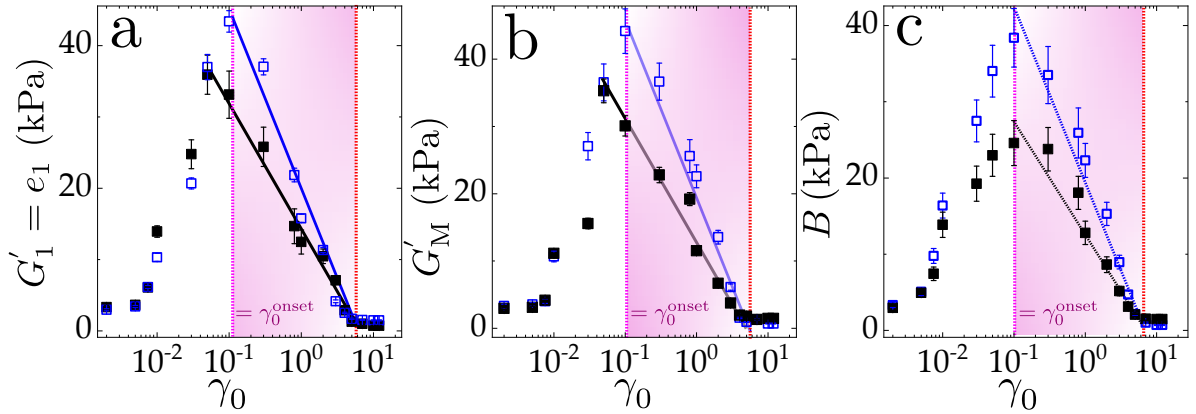


**Figure 3.13:** Comparison of non-linear elastic modulus ( $G'_1$ (a),  $G'_M$ (b)) and the amplitude  $B$  (Symmetry Line) in (c); for dry (black) and wet (blue) grains of  $80 \mu\text{m}$  diameter, the fittings shown here acknowledges the ubiquitous presence of noise temperature.

Since the SGR model takes only the elastic stress landscape into consideration to describe glassy materials via constitutive laws, we will therefore aim to address this with elastic stresses and demonstrate viscous profile, briefly in the discussion section at the end of this chapter. Note: even though the SGR model only considers elastic contributions, in this study viscous symmetry lines are taken into consideration, however only up to the pre-yielding range. To further support this analysis, we calculated (as shown in Fig. 3.12 (a)) the dissipated energy  $E_d$  and the stress amplitude of the LB loop  $\tau_a \propto$  stored elastic energy [109, 132], as a function of strain exclusively in the nonlinear regime  $\gamma_0^{\text{onset}} \geq \gamma_0 \leq \gamma_0^{\text{offset}}$ .

Note that the supporting data of  $E_d$  and  $\tau_a$  is presented below in Fig. 3.16 and Fig. 3.17, respectively, for increasing strain amplitude with the corresponding data fits that are obtained from the fitting functions of the following form,

$$\ln\left(\frac{\gamma_0}{\gamma_0^{\text{onset}}}\right) \times (\gamma_0^{\text{offset}}) = \frac{E_d}{E_0}, \quad \gamma_0^{\text{onset}} \leq \gamma_0 \leq \gamma_0^{\text{offset}} \quad (3.21)$$

$$\ln\left(\frac{(\gamma_0 + \tau_0^\infty)}{\gamma_0^{\text{onset}} \tau_0}\right) \times (\gamma_0^{\text{offset}}) = \frac{\tau_a}{\tau_0}, \quad \gamma_0^{\text{onset}} \leq \gamma_0 \leq \gamma_0^{\text{offset}}. \quad (3.22)$$

where  $\tau_\infty$  and has been introduced to obtain the meaningful slopes in the nonlinear regime II, because upon comparison to the other rheological measures, the data for  $E_d$  and  $\tau_a$  shows logarithmic increase for all  $\gamma_0$  with  $\gamma_0^{\text{onset}}$  and  $\gamma_0^{\text{offset}}$  being non-zero. To fit the linear regime I of  $E_d$  and  $\tau_a$ , following equations can be followed instead:  $\ln\left(\frac{\gamma_0}{\gamma_0^\infty}\right) = \frac{E_d}{E_0}$  and  $\ln\left(\frac{\gamma_0}{\gamma_0^\infty}\right) = \frac{\tau_a}{\tau_0}$ .

Finding consistency in the values of  $G'_M \equiv G'_1 \equiv B$  at  $\gamma_0^{\text{onset}} = 0.12 \pm 0.01$  for varying normal force, support the calculations made for the noise temperature, as the minimum and maximum values of the fittings are shown below in the captions of each figure from Fig. 3.14 to Fig. 3.18.

It is with these proofs, we present a summarized representation of the following measures at constant  $N$  over  $\gamma_0$ : the  $B$ -parameter (Fig. 3.14),  $G'_1$  (Fig. 3.15),  $G'_M$  (Fig. 3.16),  $E_d$  (Fig. 3.17) and  $\tau_a$  (Fig. 3.18) as a function of strain amplitude ( $\gamma_0$ ). The figures represent grains of  $d : 80 \mu\text{m} - 500 \mu\text{m}$  with (open symbols, blue) and without (closed symbols, black) a small addition of Silicon oil. The fittings are according to the corresponding equations, as described above. All these statistics is thence applied to approximate the noise temperature for all confinement pressures  $k_B \Theta(N)$ . The region highlighted in light magenta is ascribed to the nonlinear regime II.

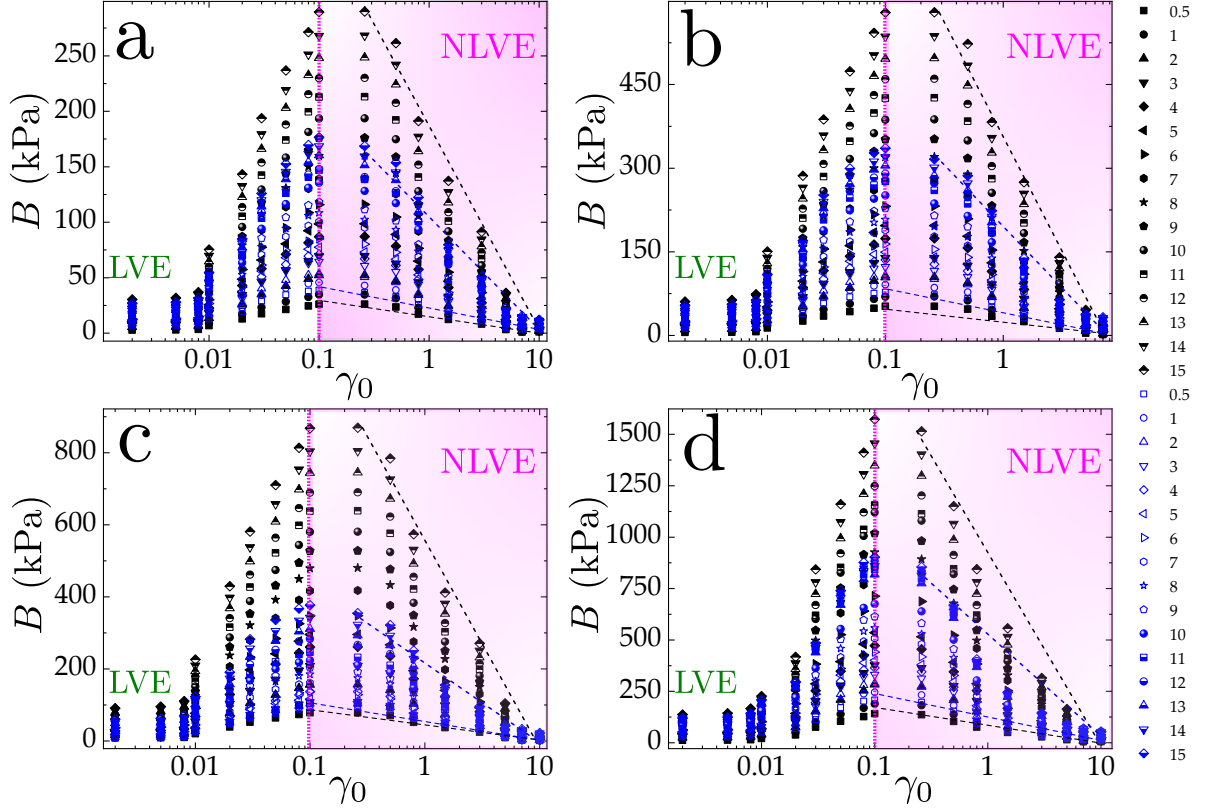


**Figure 3.14:** Summary of the proposed parameter  $B$  to approximate the noise temperature of dry (solid black) and wet (open blue) granular matter as a function of strain amplitude for (a)  $500\ \mu\text{m}$  with  $|B_{\min}^{\text{dry}}| \approx 4\ \text{nJ}/\text{grain}$ ,  $|B_{\min}^{\text{wet}}| \approx 9\ \text{nJ}/\text{grain}$ ,  $|B_{\max}^{\text{dry}}| \approx 48\ \text{nJ}/\text{grain}$ ,  $|B_{\max}^{\text{wet}}| \approx 49\ \text{nJ}/\text{grain}$ , (b)  $250\ \mu\text{m}$  with  $|B_{\min}^{\text{dry}}| \approx 8\ \text{nJ}/\text{grain}$ ,  $|B_{\min}^{\text{wet}}| \approx 13\ \text{nJ}/\text{grain}$ ,  $|B_{\max}^{\text{dry}}| \approx 94\ \text{nJ}/\text{grain}$ ,  $|B_{\max}^{\text{wet}}| \approx 61\ \text{nJ}/\text{grain}$ , (c)  $140\ \mu\text{m}$  with  $|B_{\min}^{\text{dry}}| \approx 12\ \text{nJ}/\text{grain}$ ,  $|B_{\min}^{\text{wet}}| \approx 18\ \text{nJ}/\text{grain}$ ,  $|B_{\max}^{\text{dry}}| \approx 118\ \text{nJ}/\text{grain}$ ,  $|B_{\max}^{\text{wet}}| \approx 65\ \text{nJ}/\text{grain}$ , and (d)  $80\ \mu\text{m}$  with  $|B_{\min}^{\text{dry}}| \approx 16\ \text{nJ}/\text{grain}$ ,  $|B_{\min}^{\text{wet}}| \approx 21\ \text{nJ}/\text{grain}$ ,  $|B_{\max}^{\text{dry}}| \approx 140\ \text{nJ}/\text{grain}$ ,  $|B_{\max}^{\text{wet}}| \approx 95\ \text{nJ}/\text{grain}$ , respectively. The dashed lines are the fits of the characteristic scaling law described in 3.2 with minimum and maximum values presented here. The legend on the right side corresponds to the applied confinement  $N$  for each experimental set. Thus defined, the exact legend henceforth applies to the following figures: Fig. 3.15 to Fig. 3.18.

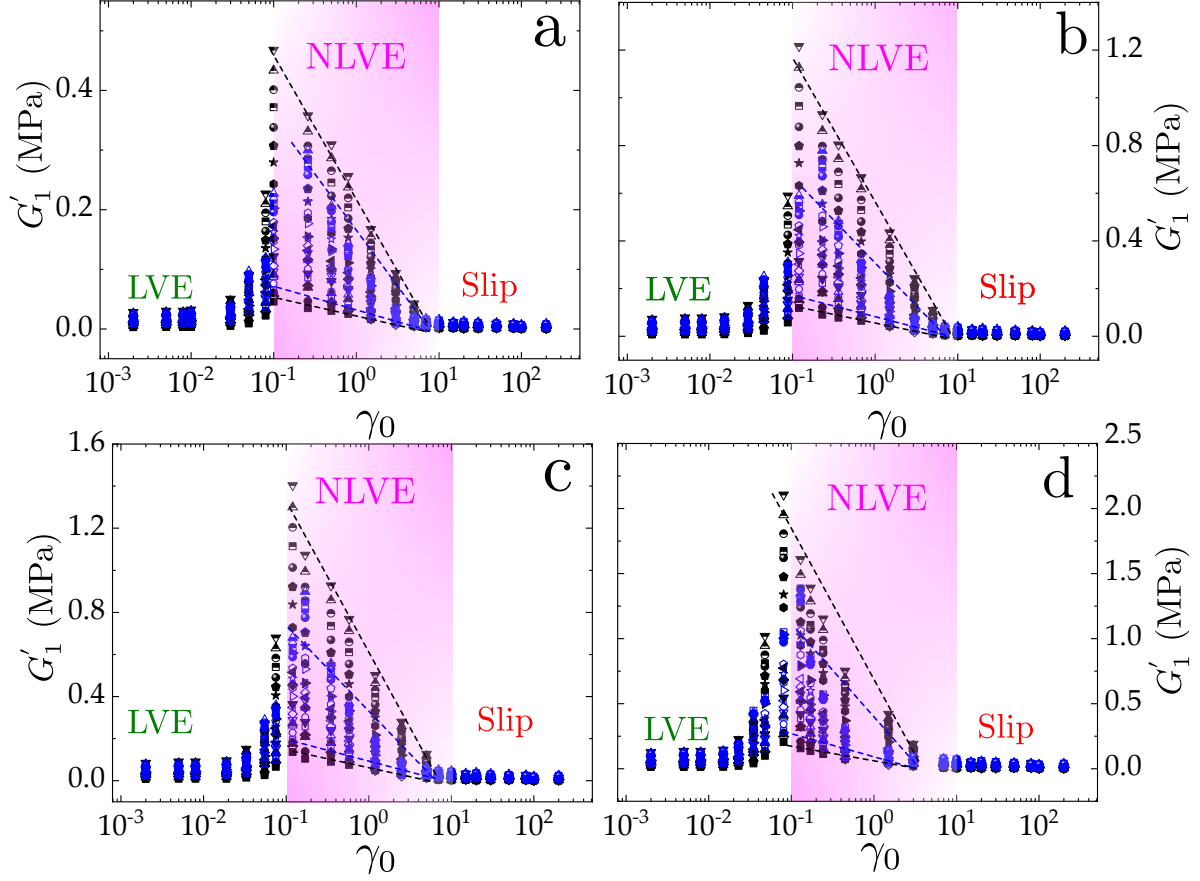


**Figure 3.15:** Summary of the elastic moduli  $G'_1$  in support to approximate the non-thermal motions of dry (solid black) and wet (open blue) granular matter as a function of strain amplitude for (a)  $500\ \mu\text{m}$  with  $|G'_{1,\text{min}}|^{\text{dry}}| \approx 3.5\ \text{nJ}/\text{grain}$ ,  $|G'_{1,\text{min}}|^{\text{wet}}| \approx 7\ \text{nJ}/\text{grain}$ ,  $|G'_{1,\text{max}}|^{\text{dry}}| \approx 49\ \text{nJ}/\text{grain}$ ,  $|G'_{1,\text{max}}|^{\text{wet}}| \approx 47\ \text{nJ}/\text{grain}$ , (b)  $250\ \mu\text{m}$  with  $|G'_{1,\text{min}}|^{\text{dry}}| \approx 10\ \text{nJ}/\text{grain}$ ,  $|G'_{1,\text{min}}|^{\text{wet}}| \approx 14\ \text{nJ}/\text{grain}$ ,  $|G'_{1,\text{max}}|^{\text{dry}}| \approx 97\ \text{nJ}/\text{grain}$ ,  $|G'_{1,\text{max}}|^{\text{wet}}| \approx 63\ \text{nJ}/\text{grain}$ , (c)  $140\ \mu\text{m}$  with  $|G'_{1,\text{min}}|^{\text{dry}}| \approx 15\ \text{nJ}/\text{grain}$ ,  $|G'_{1,\text{min}}|^{\text{wet}}| \approx 21\ \text{nJ}/\text{grain}$ ,  $|G'_{1,\text{max}}|^{\text{dry}}| \approx 120\ \text{nJ}/\text{grain}$ ,  $|G'_{1,\text{max}}|^{\text{wet}}| \approx 68\ \text{nJ}/\text{grain}$ , and (d)  $80\ \mu\text{m}$  with  $|G'_{1,\text{min}}|^{\text{dry}}| \approx 19\ \text{nJ}/\text{grain}$ ,  $|G'_{1,\text{min}}|^{\text{wet}}| \approx 24\ \text{nJ}/\text{grain}$ ,  $|G'_{1,\text{max}}|^{\text{dry}}| \approx 143\ \text{nJ}/\text{grain}$ ,  $|G'_{1,\text{max}}|^{\text{wet}}| \approx 93\ \text{nJ}/\text{grain}$ . The dashed lines are the fits of the characteristic scaling law described in 3.14 with minimum and maximum values presented here. The legend follows up with Fig. 3.14 for the applied  $N$  for each experiment.

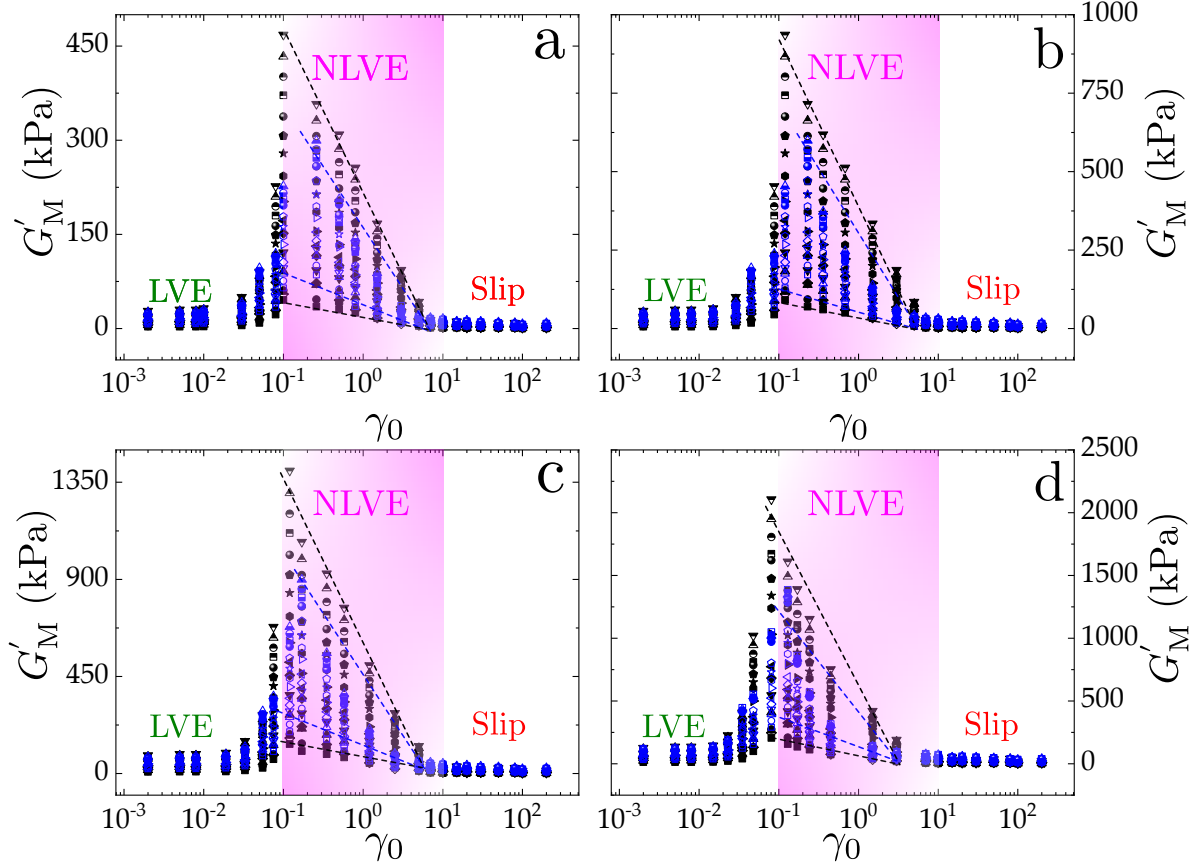


**Figure 3.16:** Summary of the nonlinear elastic moduli  $G'_M$  in support to approximate the non-thermal motions of dry (solid black) and wet (open blue) granular matter as a function of strain amplitude for (a)  $500\ \mu\text{m}$  with  $|G'_{M,\text{min}}{}^{\text{dry}}| \approx 4.2\ \text{nJ}/\text{grain}$ ,  $|G'_{M,\text{min}}{}^{\text{wet}}| \approx 8.5\ \text{nJ}/\text{grain}$ ,  $|G'_{M,\text{max}}{}^{\text{dry}}| \approx 51\ \text{nJ}/\text{grain}$ ,  $|G'_{M,\text{max}}{}^{\text{wet}}| \approx 49\ \text{nJ}/\text{grain}$ , (b)  $250\ \mu\text{m}$  with  $|G'_{M,\text{min}}{}^{\text{dry}}| \approx 11\ \text{nJ}/\text{grain}$ ,  $|G'_{M,\text{min}}{}^{\text{wet}}| \approx 13\ \text{nJ}/\text{grain}$ ,  $|G'_{M,\text{max}}{}^{\text{dry}}| \approx 98\ \text{nJ}/\text{grain}$ ,  $|G'_{M,\text{max}}{}^{\text{wet}}| \approx 62\ \text{nJ}/\text{grain}$ , (c)  $140\ \mu\text{m}$  with  $|G'_{M,\text{min}}{}^{\text{dry}}| \approx 16\ \text{nJ}/\text{grain}$ ,  $|G'_{M,\text{min}}{}^{\text{wet}}| \approx 19\ \text{nJ}/\text{grain}$ ,  $|G'_{M,\text{max}}{}^{\text{dry}}| \approx 117\ \text{nJ}/\text{grain}$ ,  $|G'_{M,\text{max}}{}^{\text{wet}}| \approx 64\ \text{nJ}/\text{grain}$ , and (d)  $80\ \mu\text{m}$  with  $|G'_{M,\text{min}}{}^{\text{dry}}| \approx 20\ \text{nJ}/\text{grain}$ ,  $|G'_{M,\text{min}}{}^{\text{wet}}| \approx 27\ \text{nJ}/\text{grain}$ ,  $|G'_{M,\text{max}}{}^{\text{dry}}| \approx 144\ \text{nJ}/\text{grain}$ ,  $|G'_{M,\text{max}}{}^{\text{wet}}| \approx 98\ \text{nJ}/\text{grain}$ . The dashed lines are the fits of the characteristic scaling law described in 3.14 with minimum and maximum values presented here. The legend follows up with Fig. 3.14 for the applied  $N$  for each experiment.

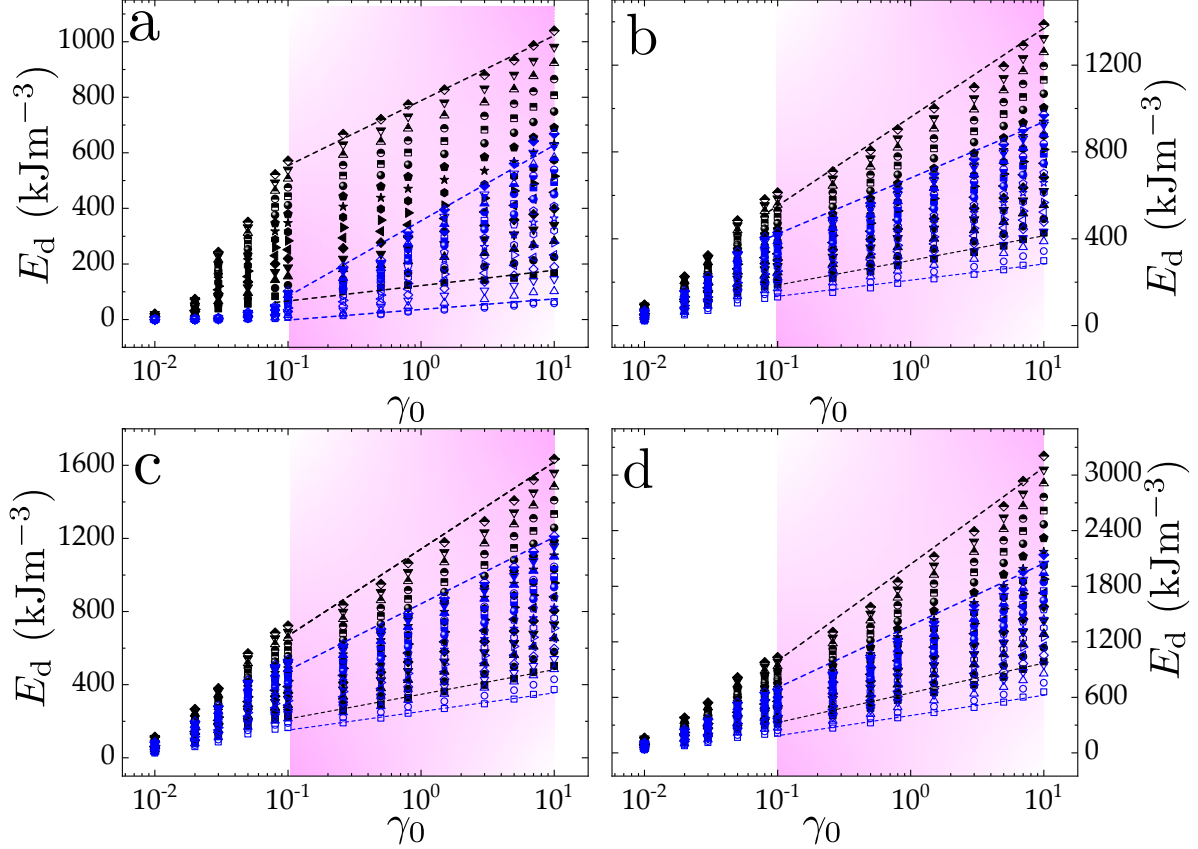


**Figure 3.17:** Summary of the dissipated energy  $E_d$  in support to approximate the non-thermal motions of dry (solid black) and wet (open blue) granular matter as a function of strain amplitude for (a)  $500\ \mu\text{m}$  with  $|E_{d,\min}^{\text{dry}}| \approx 3.5\ \text{nJ}/\text{grain}$ ,  $|E_{d,\min}^{\text{wet}}| \approx 7\ \text{nJ}/\text{grain}$ ,  $|E_{d,\max}^{\text{dry}}| \approx 49\ \text{nJ}/\text{grain}$ ,  $|E_{d,\max}^{\text{wet}}| \approx 47\ \text{nJ}/\text{grain}$ , (b)  $250\ \mu\text{m}$  with  $|G_{d,\min}^{\text{dry}}| \approx 10\ \text{nJ}/\text{grain}$ ,  $|E_{d,\min}^{\text{wet}}| \approx 14\ \text{nJ}/\text{grain}$ ,  $|E_{d,\max}^{\text{dry}}| \approx 97\ \text{nJ}/\text{grain}$ ,  $|E_{d,\max}^{\text{wet}}| \approx 63\ \text{nJ}/\text{grain}$ , (c)  $140\ \mu\text{m}$  with  $|E_{d,\min}^{\text{dry}}| \approx 15\ \text{nJ}/\text{grain}$ ,  $|E_{d,\min}^{\text{wet}}| \approx 21\ \text{nJ}/\text{grain}$ ,  $|E_{d,\max}^{\text{dry}}| \approx 120\ \text{nJ}/\text{grain}$ ,  $|E_{d,\max}^{\text{wet}}| \approx 68\ \text{nJ}/\text{grain}$ , and (d)  $80\ \mu\text{m}$  with  $|E_{d,\min}^{\text{dry}}| \approx 19\ \text{nJ}/\text{grain}$ ,  $|E_{d,\min}^{\text{wet}}| \approx 24\ \text{nJ}/\text{grain}$ ,  $|E_{d,\max}^{\text{dry}}| \approx 143\ \text{nJ}/\text{grain}$ ,  $|E_{d,\max}^{\text{wet}}| \approx 93\ \text{nJ}/\text{grain}$ . The dashed lines are the fits of the characteristic scaling law described in 3.21 with minimum and maximum values presented here. The legend follows up with Fig. 3.14 for the applied  $N$  for each experiment.

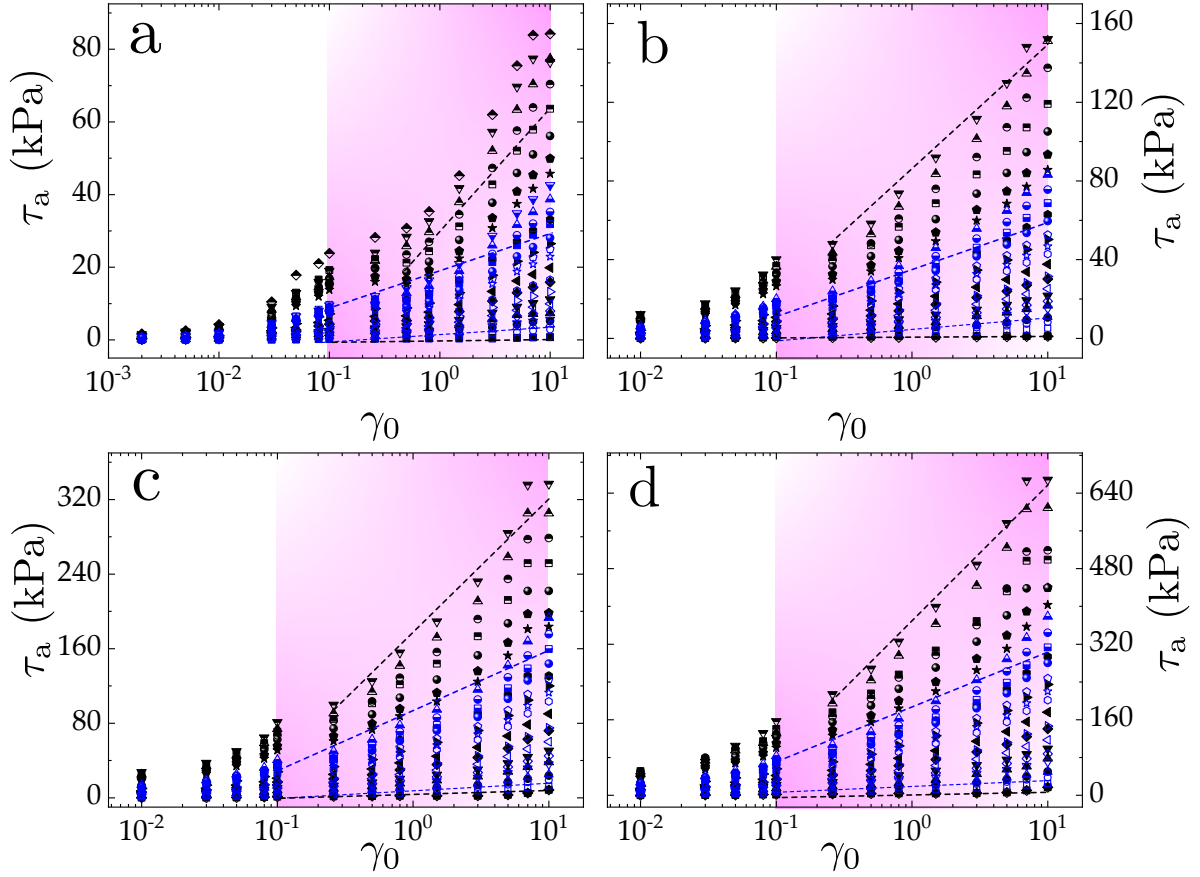


**Figure 3.18:** Summary of the stress amplitude  $\tau_a$  in support to approximate the non-thermal motions of dry (solid black) and wet (open blue) granular matter as a function of strain amplitude for (a)  $500\ \mu\text{m}$  with  $|\tau_{a,\text{min}}^{\text{dry}}| \approx 3.5\ \text{nJ/grain}$ ,  $|\tau_{a,\text{min}}^{\text{wet}}| \approx 8\ \text{nJ/grain}$ ,  $|\tau_{a,\text{max}}^{\text{dry}}| \approx 46\ \text{nJ/grain}$ ,  $|\tau_{a,\text{max}}^{\text{wet}}| \approx 40\ \text{nJ/grain}$ , (b)  $250\ \mu\text{m}$  with  $|\tau_{a,\text{min}}^{\text{dry}}| \approx 11\ \text{nJ/grain}$ ,  $|\tau_{a,\text{min}}^{\text{wet}}| \approx 15\ \text{nJ/grain}$ ,  $|\tau_{a,\text{max}}^{\text{dry}}| \approx 93\ \text{nJ/grain}$ ,  $|\tau_{a,\text{max}}^{\text{wet}}| \approx 60\ \text{nJ/grain}$ , (c)  $140\ \mu\text{m}$  with  $|\tau_{a,\text{min}}^{\text{dry}}| \approx 13\ \text{nJ/grain}$ ,  $|\tau_{a,\text{min}}^{\text{wet}}| \approx 17\ \text{nJ/grain}$ ,  $|\tau_{a,\text{max}}^{\text{dry}}| \approx 123\ \text{nJ/grain}$ ,  $|\tau_{a,\text{max}}^{\text{wet}}| \approx 66\ \text{nJ/grain}$ , and (d)  $80\ \mu\text{m}$  with  $|\tau_{a,\text{min}}^{\text{dry}}| \approx 22\ \text{nJ/grain}$ ,  $|\tau_{a,\text{min}}^{\text{wet}}| \approx 29\ \text{nJ/grain}$ ,  $|\tau_{a,\text{max}}^{\text{dry}}| \approx 146\ \text{nJ/grain}$ ,  $|\tau_{a,\text{max}}^{\text{wet}}| \approx 98\ \text{nJ/grain}$ . The dashed lines are the fits of the characteristic law described in 3.21 with minimum and maximum values presented here. The legend follows up with Fig. 3.14 for the applied  $N$  for each experiment.

Albeit the significance of applied frequency in soft glasses has been well demonstrated in the following reports [9, 33, 136], the granular matter is found to have relatively monotonous noise temperature, as clearly depicted in Fig. 3.19. Nonetheless, the parameter  $A$  (Fig. 3.19 (e)) that was used for adjusting the fitting margins of the elastic symmetry lines (see Fig. 3.19 (c)) followed a Carreau-Yasuda-like scaling, whose implications are discussed in the next section with a supporting Fig. 3.22. The noise temperature  $k_B\Theta$ , hitherto defined in the unit of Joule per grain for dry (closed symbols, black) and wet (open symbols, blue) grains at different  $P$ , is presented in Fig. 3.20.

The inset revealing the particle size dependence of noise temperature  $d(k_B\Theta)$  is found in a good agreement with propositions raised in [109, 132]. We find that the noise temperature  $k_B\Theta$  followed a decay of  $d^{-1}$  for dry and  $d^{-\frac{1}{2}}$  for wet grains until arrest wherefrom the

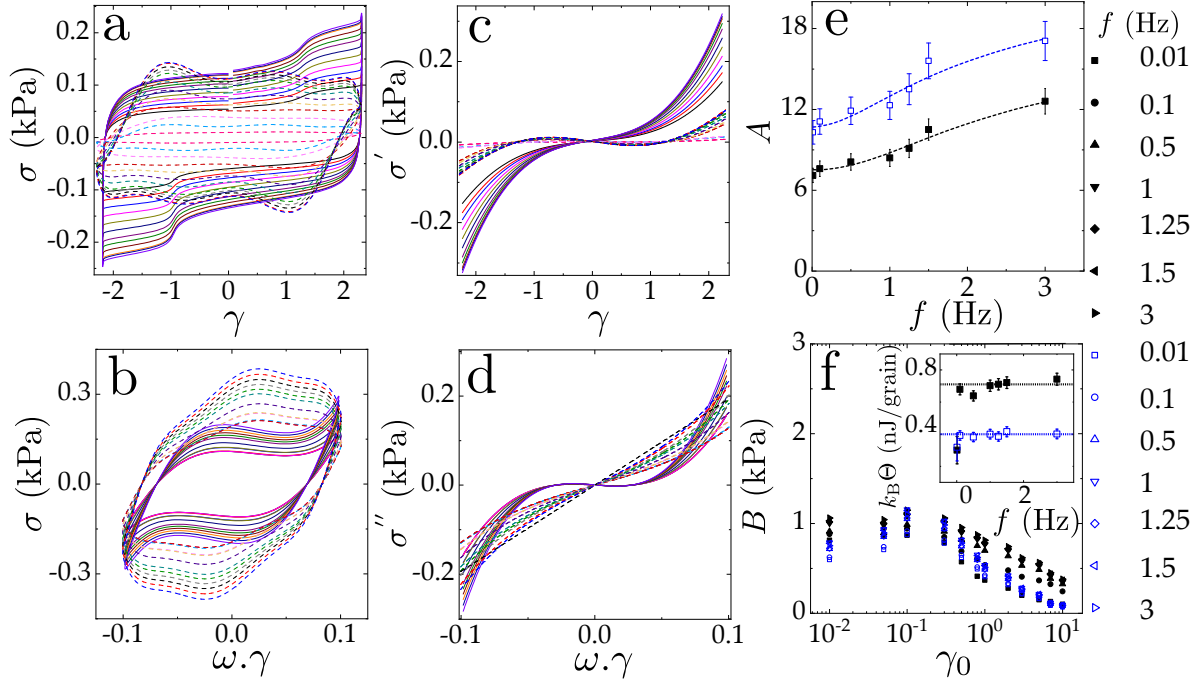


**Figure 3.19:** Frequency dependence of the noise temperature. (a), (b), (c) and (d) summarizes the elastic and viscous LB loops and symmetry lines, respectively for dry (solid lines) and wet (dashed lines) granular matter of  $500\ \mu\text{m}$  size. (e) As defined in 3.2, the parameter  $A$  is depicted as a function of  $f$  averaged for the corresponding symmetry lines in (c) and (d), where open circles represent wet grains and solid squares, dry grains. (f) represents the parameter  $B$  (3.2) as a function of strain amplitude for varying  $f$  (see legends), with inset showing a monotonous response of the noise temperature obtained from  $B$  over frequency for dry (solid symbols) and wet (open symbols) grains.

granular matter begins to jam (slip regime III), as identified at a jamming pressure  $P_j \approx 20\ \text{kPa}$ .

Consequently, for high  $P$ , the percolative quasi-linear clusters of force chains are expected to drive the arrested granular system to relax faster [59, 60]. Thus, to investigate the similarities or phase transition and the compaction behaviour in non-linear confined granular flows, we measured the variation in the packing fraction for each experimental run as  $\phi^* = \frac{(\phi_f - \phi_i)}{\phi_i}$ . Where  $\phi_f$  is the final packing fraction calculated at the end of every LAOS cycle at constant  $P$  (while the shearing plate is still intact, and the system is allowed to anneal at  $\gamma = 0$ ),  $\phi_i$  is the initial packing fraction measured after pre-shearing of grains and kept constant to minimize the error in the measurements. Packing dynamics are hereby shown as a function of confinement  $P$  in figure 3.21.

The next section will provide a tentative view on these experimental findings presented here, with a general commentary, drawing analogies and future outlook of the current work.

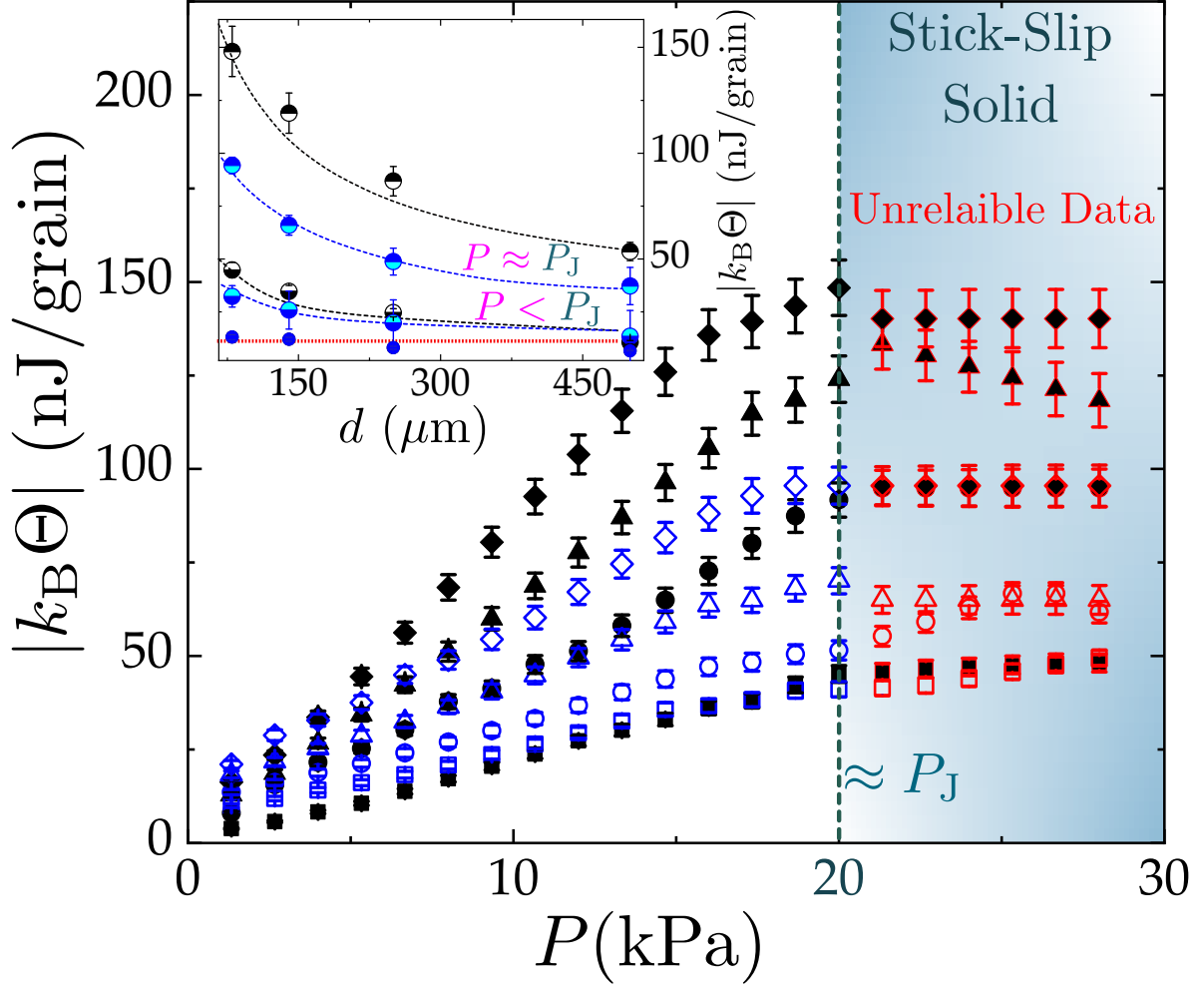


**Figure 3.20:** Noise temperature as estimated in accordance to 3.2 as a function of confinement pressure for dry (solid symbols) and wet (open symbols) grains. Squares: 500  $\mu\text{m}$ , circles: 250  $\mu\text{m}$ , triangles: 140  $\mu\text{m}$  and diamonds: 80  $\mu\text{m}$ . The inset shows a size dependence of noise temperature for dry (black-white) and wet (blue-cyan) grains. Note that the noise temperature estimated in accordance to 3.2 is negative, however, presenting (as here) in its magnitude facilitate a thorough interpretation. Henceforth, the higher is the magnitude of the noise temperature for a corresponding data set, the lesser are the granular rearrangements. For instance, 80  $\mu\text{m}$  grains will jam significantly faster than 500  $\mu\text{m}$  grains.

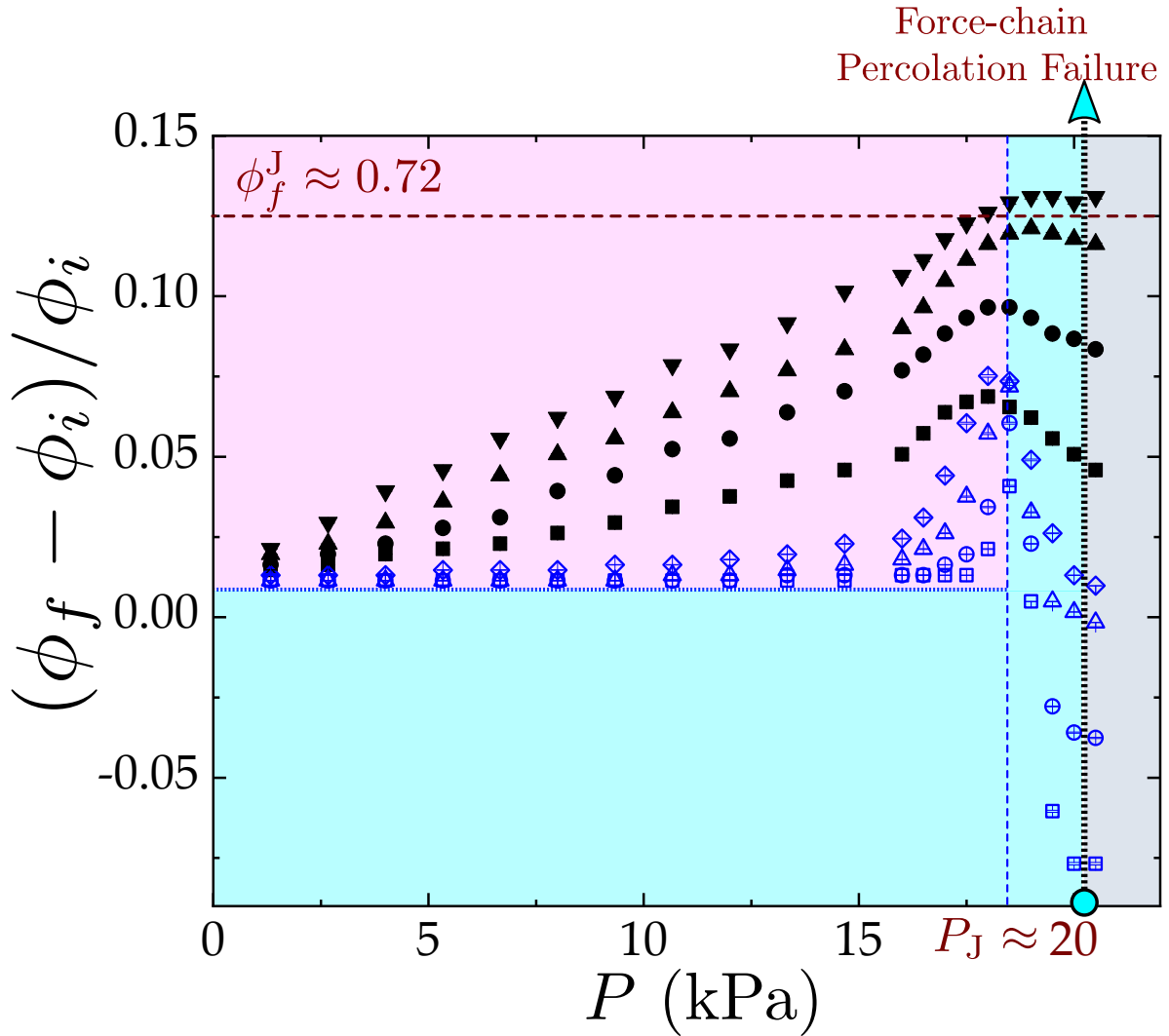


**Figure 3.21:** Variation in the packing fraction per experiment depicted as a function of confinement pressure for dry (solid symbols) and wet (open symbols) grains. Squares: 500  $\mu\text{m}$ , circles: 250  $\mu\text{m}$ , triangles: 140  $\mu\text{m}$  and diamonds: 80  $\mu\text{m}$ . The variable  $\phi_f^J$  is the maximum packing fraction observed for the experiments shown here, at which the granular sample jams.

### 3.3 Discussions and General Remarks

In the first section of this chapter 3.1, we identified the dynamical regimes (linear, nonlinear and slip) of granular flows in a shear cell under SAOS to LAOS rheology. The rheological response of grains was found nonlinear upon increasing strain, while the sample is still under SAOS, as shown in Fig. 3.4 for  $G'$  and  $G''$ . The differences found in  $G'$  and  $G''$  for dry and wet grains indicated the importance of their respective contact dynamics. A prevalent phenomenon yet an outstanding feature of granular matter is the sudden change of physical attributes upon introducing a small amount of interstitial fluid (such as water in sand) [86, 109, 137]. Unlike dry (Fig. 3.1 (a)), the wet granular matter is driven by *cohesive* bonds between adjacent grains as shown in Fig. 3.1(b), a characteristic of well-defined energy scale and strong dissipation [138–140]. At large deformation, dry grains in the non-linear regime, exhibit filamentary force-chain networks due to friction-driven elasticity [3, 35, 44, 118]. Whereas, the logarithmic dependence of the wet grains on strain in SAOS regime, suggested the oscillation of capillary bridges [36, 119, 127]. As the wet granular sample was subjected to LAOS scales, breaking and regeneration of capillary bridges began to control the rheological response. To address the role of capillary bridges in wet granular matter flows, we followed the works [119, 128, 129] to estimate the rupture energy  $\tilde{W}_{\text{tot}}$ , which turns out to be  $8.4 \pm 0.5 \text{ nJ/bridge}$  for a standard bridge of pendular regime in our case. As described, the experimental conditions for a capillary bridge in this study and the typical state of the capillary breakup extensional rheometer (CaBER) with silicon oil are similar, implying that the filament thinning of oil is found to be independent of the piston speed for a considerable range. Therefore,  $v$  under capillary pressure scales as  $v \sim \sqrt{2\mu H/\rho}$  with  $\rho$  being the drop density, and unless the system is static,  $v$  will correspond as a velocity gradient ( $\nabla v(x, H)$ ) to the profile of a capillary bridge, which in our case estimated a capillary number  $Ca < 1$ . As studied in [128], one finds that due to small rupture lengths ( $\tilde{H}$ ) and surface asperities ( $\tilde{d}$ ), viscous effects tend to participate while capillary forces still dominate during rupture process, which is also corroborated by the respective values we obtained. Moreover, the time scale for the contacts resisting tangential forces is found at least 10 times smaller, thence neglected. Thus, with an optimal coordination number of  $C_N = 6$  [109, 117], and provided that the granular sample is confined within all the boundaries of a shear cell and does not have any convex-concave contact with parallel plates forming the cylinder, the total rupture energy of maximum capillary contacts on one grain then reads  $\tilde{W}_{\text{tot}} \approx 50 \pm 5 \text{ nJ/grain}$ . In light of our earlier remarks, the inhomogeneous shear flows and assuming at least one shear band in our cup-plate geometry in the linear regime, the viscous dissipation was found to be caused by small oscillations (insufficient to break the bridge) around the length of the liquid bridge.

In SAOS regime, obtaining a logarithmic dependence of  $G''$  at  $\gamma_0 \geq \gamma_0^{\text{onset}}$  [35, 44, 119] with slope values corresponding to the rupture energy  $\tilde{W}_{\text{tot}}$ , implies that the nonlinear viscoelastic response of wet grains explicitly depends on linear to non-linear transition as the breaking and regeneration of capillary bridges begins. Thus described, wet grains in the linear viscoelastic state (I) are under the action of capillary bridges being deformed by small oscillations and only begin to break and rearrange as  $\gamma_0^{\text{onset}} \sim 0.1$  is reached (II). At  $\gamma_0 > 10$ , grains slip past each other (III) and the response is relatively arbitrary or trivial. Furthermore, slope values obtained for dry grains in regime I,  $G'$  and  $G''$  indicated the formation of filamentary force-chain networks spreading in branch-like fashion over the strain direc-

tion as the friction continues to increase the elasticity until the granular sample begins to "yield". Whereas for wet grains, the slope values corresponded to the oscillating capillary bridges, which eventually begins to yield at  $\gamma_0 \approx \gamma_0^{\text{onset}}$ . Nevertheless, to account for the nonlinearities present in the viscoelastic response via  $G'$  and  $G''$  alone, is still insufficient, as the further breakdown of higher harmonics becomes necessary.

The entire spectrum of chosen harmonics showed a weak dependence on strain at small deformations (regime I). The onset of non-linearity at  $\gamma_0 \sim 0.1$  can also be recognized as the large and minimum strain elastic moduli diverges with a non-linear slope. At large deformations as in LAOS, grains begins to transmit stresses through successive granular contacts, causing total stress to be out of phase with applied shear. A sudden acceleration in elastic moduli, therefore, indicate the hardening of grains (strain stiffening), followed by the softening at large deformations (see Fig. 3.7). Elastic moduli were decreased gradually for dry than wet, indicating microstructural rearrangements with shear fields [35, 44, 117]. In this state, due to anisotropic forces, grains begin to dissipate energy due to non-affine motions [106, 118, 126]. However, the relaxation dynamics continues to vary [37, 106]. Similarly, the non-linear viscosities were found decreasing (Fig. 3.7), though pronounced in the case of dry grains, was caused by the compression at large deformation, where capillary bridges between grains squeeze out to the bottom due to compressive stresses, resulting in the partial saturation of the liquid bridge network into pendular and capillary regimes [109, 119, 132]. Hence, dry and wet granular matter behaves as a quasi-Newtonian solid in slip regime III. Taking into account the correlation between raw LAOS data and the processed one with non-linear measurements, we compared the characteristic elastic energy to the capillary energy of  $\sim 8.4 \text{ nJ/bridge}$ , which in reference to [36], we find that smaller characteristic energy  $G_{0j}$  for the wet granulate alludes to better *flowability* than dry grains, which can be ascribed to the extension and contraction of capillary bridges. Furthermore, the viscous dissipation state drops to zero at the onset of breaking and regeneration dynamics  $\gamma_0^{\text{onset}}$ . However, in the case of dry grains, the range  $\gamma_0 \leq \gamma_0^{\text{offset}}$  corresponds to the viscous dissipation driven by friction between grains, which not only include the pre-yielding range of small movements around the contacts between particles but also from the onset of particle rearrangements.

Upon comparing all these remarks and inferences drawn from all the statistics shown here, with the previous studies on the rheology of dense granular matter [36, 38, 86], a clear distinction between its dry and wet state thus follows as, that dry grains rearrange under the action of dissipative friction of filamentary force chain branches, whereas wet grains dissipate capillary energy due to breaking and regeneration of liquid bridges. Therefore, to describe the viscous non-linearity, we draw analogies between steady state rheology and compaction experiments [133, 134], assuming both studies share the same origin for nonlinearities, i.e. rearrangements of the grains, described as non-linear events. In retrospect of these experimental findings, the compaction dynamics are characterized by three different spatial and temporal scales: (1) evolution of the packing fraction to its saturation value fitted by the stretched exponential function  $\tilde{\rho} = 1 - \exp -(t/\tau)^\beta$ , where  $\tau$  is the relaxation time and  $\beta$  is the stretched exponent; (2) diffusion-controlled growth of mesoscopic domains determined by scaling the mesoscopic packing fraction  $\tilde{\phi}$  with the macroscopic packing fraction  $\tilde{\rho}$  via power function as  $\tilde{\phi} = \tilde{\rho}^2$ ; and (3) the mobility of grains directly

scales with packing fraction variable provoked by an external force,  $\mu \sim d\bar{\rho}/dt$ . Contrarily, the peak functions for the viscous non-linearities  $\zeta_v^{\text{dry}} < \zeta_v^{\text{wet}}$  were found to characterize the rearrangements at the mesoscopic scale that is proportional to the elastic nonlinearity by a factor equivalent to the applied frequency  $\omega \approx 9.42 \text{ rad s}^{-1}$ . This implies that there exist an autocorrelation between viscoelastic nonlinearities at mesoscopic and macroscopic scale.

Before we proceed to discuss on SGR model, let's have a brief recall from Chapter 2, where the rearrangements of grains are viewed as a set of mesoscopic elements, and each individual element is identified by its local shear strain  $l$  ( $l \propto \gamma$ ). These elements are assumed to be in a quenched-in distribution of energy barriers which interacts by escaping and hopping out (yielding) of the potential well once they cross an energy barrier of  $E - \frac{1}{2}kl^2$ . This process is sketched in Fig. 1.6 to illustrate how circle number 1 (mesoscopic region) hops to the subsequent trap ("favourable" metastable state, at number 2) [7, 31, 116], where  $k$  is an elastic constant (shear modulus) and  $l$  is a local strain variable. The mesoscopic element, subsequent to yielding becomes unstrained and deforms at  $l = 0$ , hence resetting  $l$  to zero. Regardless of the yielding event, caused by either the noise or strain or both, SGR model view these events as an activated process such that the average lifetime of a mesoscopic element undergoing rearrangement follows  $\Gamma = \Gamma_0 \langle e^{-(E - \frac{1}{2}kl^2)/(k_B\Theta)} \rangle$ , where  $\Gamma_0$  is an inverse of attempt frequency for yielding. Analogous to Bouchaud's trap model retrospective [7, 22, 32], the SGR model develops on the same ground assuming a similar energy barrier distribution  $\rho(E) = \exp(-E/(k_B\Theta_g)) / (k_B\Theta_g)$ , where  $(k_B\Theta_g) = \langle E \rangle$  is the average trap depth. Thereby, supporting the analogue of Boltzmann (

Stosszahlansatz) probability distribution ( $P_{\text{eq}}(E)$ ) which for a given  $(k_B\Theta)$  scales as  $P_{\text{eq}}(E) \propto \Gamma(E)\rho(E) = \exp(-E/(k_B\Theta)) \exp(-E/(k_B\Theta_g))$ , redefines the average lifetime of an element hopping as  $\langle \Gamma \rangle_E = \int_0^\infty dE \Gamma(E)\rho(E)$ . This Arrhenius form of an average lifetime leads to the glass transition at  $k_B\Theta = k_B\Theta_g$ . Therefore, at  $k_B\Theta < k_B\Theta_g$ , the soft glassy material ages and undergo ergodicity breaking [2, 9, 30, 31, 34, 63, 135]. The overall yielding rate can thus be given as,  $Y(t) = \int_0^\infty dE \int_0^\infty dl \Gamma(E, l) P(E, l, t)$ , where  $\Gamma(E, l)$  is the local yielding rate [30, 33]. Thus, the solution to the equation of motion [30, 31] for  $k_B\Theta < k_B\Theta_g$  reads,

$$P(E, t) = P_0(E) \exp \left[ - \frac{Z(t, 0)}{\exp(E/(k_B\Theta))} \right] + \rho(E) \int_0^t Y(t') \exp \left[ - \frac{Z(t, t')}{\exp(E/(k_B\Theta))} \right] dt' \quad (3.23)$$

where  $P_0(E, l)$  is initial probability and  $Z(t, t')$  is the effective time of survival probability [31, 33]. The overall yielding rate  $Y(t)$  can be obtained by differentiating further with respect to  $t$  [12],

$$0 = \frac{dG_0(Z(t, 0))}{dt} + Y(t) + \int_0^t Y(t') \frac{dG_\rho(Z(t, t'))}{dt} dt' \quad (3.24)$$

To solve this numerically, we can follow the study [33], where the assumption is that the time is discretized,  $t_0(= 0), t_1, t_2, \dots, t_{n-1}, t_n, t_{n+1}$ , such that for any  $t_{n-1} < t' \leq t_n$ , the linear interpolation of  $Y(t')$  would result in [12, 30, 33],

$$0 = \frac{dG_0(Z(t,0))}{dt} + Y(t_n) + \int_0^{t_{n-1}} Y(t') \frac{dG_\rho(Z(t_n, t'))}{dt_n} + Y(t_n) \int_{t_{n-1}}^{t_n} \frac{dG_\rho(Z(t_n, t'))}{dt_n} dt' - \left( \frac{Y(t_n) - Y(t_{n-1})}{t_n - t_{n-1}} \right) \int_{t_{n-1}}^{t_n} (t_n - t') \frac{dG_\rho(Z(t_n, t'))}{dt_n} dt' \quad (3.25)$$

Note: the numerical solution provided here is not used in this study and therefore, it only serves as an alternative extension of the SGR model to soft materials, however the intuitive picture can still be drawn for athermal materials. Since the initial conditions are of the form  $Y(t_0) = (k_B\Theta)/(1 + k_B\Theta), Y(t_i)$ , we can use forward differentiation method to solve the above differential terms, and trapezoidal method to solve the integral terms [33] leading to a constitutive equation,

$$\sigma(t) = \gamma(t)G_0(Z(t,0)) + \int_0^t dt' \Gamma(t') [\gamma(t) - \gamma(t')] G_\rho(Z(t, t')) \quad (3.26)$$

where, the functions  $G_0$  and  $G_\rho$ , that purely describes the stress decay due to noise are shown to be governed by an "effective time interval"  $z = Z(t, t')$  which are defined as [31],

$$G_0(z) = G_0(z) = \int dE P_0(E) \exp\left(-ze^{-E/(k_B\Theta)}\right) \\ G_\rho(z) = \int dE \rho(E) \exp\left(-ze^{-E/(k_B\Theta)}\right) \quad (3.27)$$

This section then builds on the following fundamental differences found between dry and wet granular matter in a shear cell; (1) the presence of filamentary force chain networks [35, 59] branching out at  $\gamma_0 \rightarrow \gamma_0^{\text{offset}}$ , comprising percolating quasilinear clusters of grains [59, 60] and (2) the breaking and regeneration of capillary bridges, as the variation in the packing fraction per experiment  $\phi^*$  competes with the jamming point  $\phi^* < \phi_f^J$ . Therefore, to understand these differences between long-range force structures originating from the non-linear flow fluctuations of dry and wet granular assemblies, we employ the SGR model and estimate the noise temperature under the assumption that it holds the complete viscoelastic description of a material [9, 30, 33, 41]. Moreover, the values of noise temperature at  $\gamma_0^{\text{onset}}$  and the approximate amount of work required to cause one rearrangement of a grain by its diameter ( $d = 500 \mu\text{m}$ ) at given conditions is  $G_1''^0 = 3.5 \pm 0.3 \text{ nJ/grain}$  for dry and  $G_1''^0 = 7.0 \pm 0.5 \text{ nJ/grain}$  for wet. Additionally, based on the analytical approaches, as shown in Fig. 3.6, 3.7 and 3.8, we obtained relatively congruent values between the characteristic measures of linear and nonlinear variables. This strongly supports the idea that noise temperature might just be the key parameter to unlock the mechanism of: how the mesoscopic scale

viscosity govern the macroscopic elasticity? Therefore, we argue that the solutions to the fits of stress symmetry lines with a periodic function can be interpreted in light of the solution to the constitutive equations of the SGR model, i.e. the complete viscoelastic response of a material inherently caused by its constitutional rearrangements. Furthermore, in Fig. 3.22 (b) and (c), a typical comparison is depicted between  $B_{\text{elastic|viscous}}$  and  $G_M''$  as a function of strain and strain-rate amplitude, respectively, estimated from the corresponding LB loops of elastic (a) and viscous stress (b) shown in Fig. 3.12. Note that, SGR model does not take into account the viscous effects however the formalism for the dynamic viscosity can still be written as  $\eta_1'$  and  $\eta_1''$  as  $\omega\gamma_0/\omega\gamma_0^j = \exp(-\eta_1'/\eta_1'^0) \in \gamma_0 \leq \gamma_0^j; j = \gamma_0^{\text{onset}}, \gamma_0^{\text{offset}}$ . Although we find this valid up to the pre-yielding range, therefore relevant to describe the percolation dynamics of force chain networks.

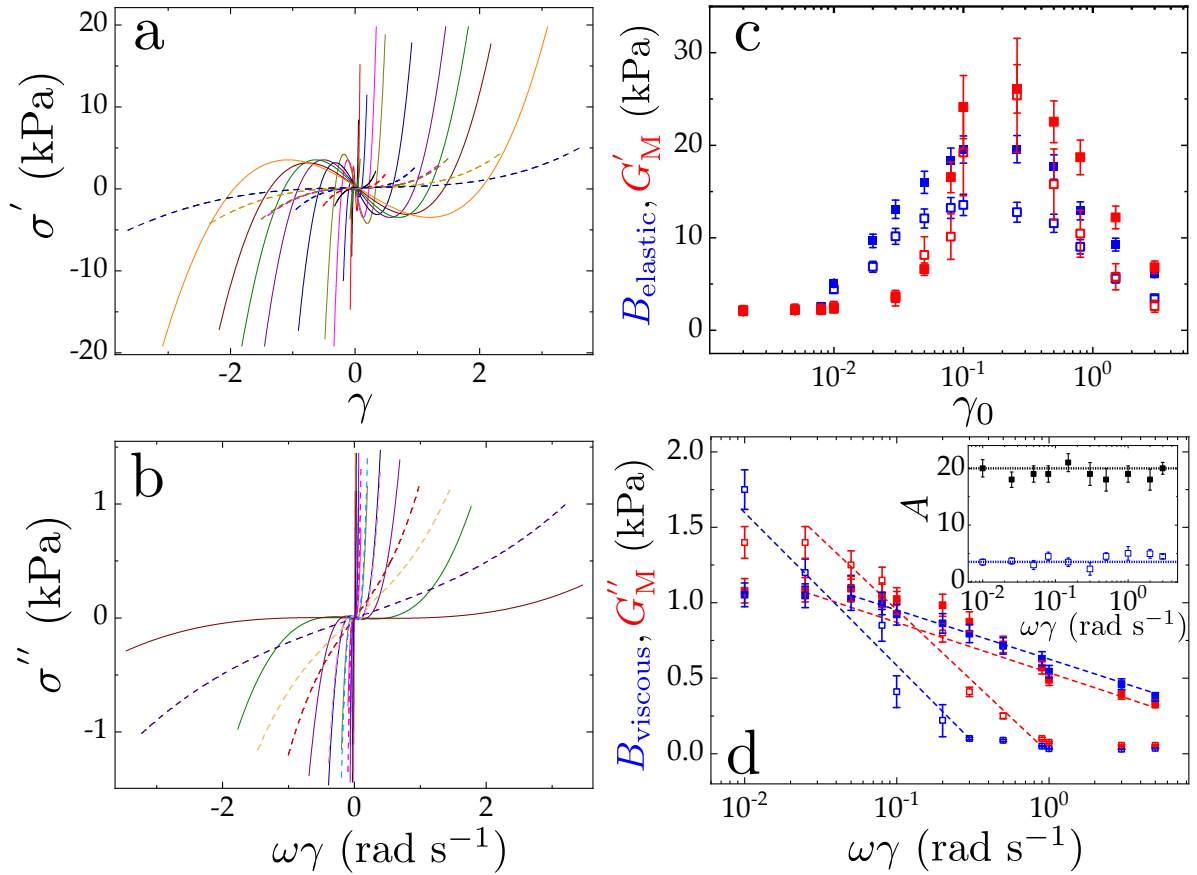


**Figure 3.22:** A typical comparison of elastic (a) and viscous (b) symmetry lines for dry (solid lines) and wet (dashed lines) grains of  $d \approx 500 \mu\text{m}$ . Hereof, (c) and (d) acknowledges the close similarities between dry (squares, red) and wet (circles, blue) grains, hence the entailed deductions between nonlinear elastic moduli with  $B_{\text{elastic}}$  and dynamic viscosity with  $B_{\text{viscous}}$ , respectively. The inset of (f) depicts the adjustment parameter  $A$  illustrating the strain-rate independence, however, followed a Carreau-Yasuda scaling upon varying frequency  $f$ .

Since  $B$  is numerically accurate and assuming that it takes the mesoscopic and macroscopic variables into consideration, our findings therefore compliment the constitutive laws of the SGR model in application to granular matter. Nevertheless, the Carreau-Yasuda like scal-

ing as  $\left( A = A_\infty + \frac{A_0 - A_\infty^v}{[1 + (\tau\omega\gamma_0)^a]^{\frac{1-v}{a}}} \right)$ , obtained for  $\langle A \rangle$  as a function of frequency  $f$  in Fig. 3.22 might just be an indication of pseudoplastic-like response stemming from the transition of strain-stiffening to quasi-Newtonian behaviour as the granular assembly is close to jamming. Where  $a$  is the transition control factor,  $n$  is the power index and  $\tau$  is the time constant. As a topic of our ongoing investigation, we are currently studying the physical significance of these properties, relating pseudoplasticity and compactivity to the confined granular flows.

Intriguingly, comparing the noise temperature of dry to wet grains suggested a possible transition from high mesoscopic flow fluctuations to the low density arrested states of grains as  $k_B\Theta_{\text{dry}} < k_B\Theta_{\text{wet}}$  for  $d_{\text{dry}} \sim (k_B\Theta_{\text{dry}})^{-1 \pm 0.1}$  and  $d_{\text{wet}} \sim (k_B\Theta_{\text{wet}})^{-1/2 \pm 0.1}$ . This might support our aforesaid arguments, that for decreasing grain size, dry grains exhibit structural arrest driven by Coulomb friction coefficient maximizing the Hertzian force contacts, which rapidly decays with grain size, and contrarily, for wet grains, the breaking and regeneration of liquid bridges decays with rearrangements approaching a jamming point. However, this transition for wet grains would not hold for high  $P \approx P_j$  as compressive stresses would prevent wet grains from readjusting to the adjacent neighbouring locations due to reduced activity of breaking and regeneration of capillary bridges, causing low meta-stability and consequently high  $k_B\Theta$ . Such a non-uniform spatial ordering of dry and wet grains driven by a combination of confinement and packing fraction ( $P; \phi$ ), also indicate the similarities with the compaction dynamics of grains, as illustrated in Fig. 3.21.

Clearly, the system gradually packs at increasing  $P$ , which, near jamming  $P_j \sim 20$  kPa, follow a bifurcation-like transition. The dry granular system followed saturation and evolved to a deeper state of arrest while decreasing rapidly with  $d$  toward dilation (Fig. 3.20). Contrastingly, wet grains showed strong dilatant behaviour. This outcome has strong implications, as the faster grains are packed, the higher is the probability of dilation, and vice versa to attain jamming or arrest at slow packing. Noise temperature and the energy required for force-chains to percolate is found to scale with the size and packing fraction, accounting for the epitaxial coalescence of rattlers and non-rattlers, attributed to the volume expansion at  $\phi^* < \phi_f^J$ . The accelerated fall of  $\phi_{\text{wet}}^*$  in contrast to dry grains indicate that the wet grains expand in volume 50 times faster than dry at large deformation under confinement. Furthermore, the crossover at which, wet grains dilate and dry grains arrests by epitaxial jamming of quasilinear clusters, the percolating force-chain networks therefore must fail to allow this dilation-arrest transition. This decay of elastic fluctuations controlling the spatial and structural rearrangements ("attraction and repulsion")  $\phi^*(P) \sim ?' \phi^*(k_B\Theta)$ , poses an important proposition (?), whether this is a point of Singularity or a first order phase transition in granular matter near or at jamming?

### 3.4 Summary

This chapter systematically studied the non-linear dynamics of dry and wet granular matter at large deformations. By employing a standard rotational rheometer in LAOS mode with confinement at constant pressure to trigger a non-linear material response, we present

a descriptive picture of nonlinear viscoelasticity in granular materials and the characteristic degree of non-linearity via FT-rheology and Chebyshev Polynomials. The degree of non-linearity identified the dynamical regimes of granular flows in a shear cell; linear, non-linear and stick-slip. On finding that the deformation larger than the size of grain set the divergence from the linear response (at  $\gamma_0^{\text{onset}}$ ), confirmed that the nonlinear events are the reminiscence of rearrangements. In addition, logarithmic dependence for  $G'$  and  $G''$  for wet Dynoseeds strongly indicated the breaking and regeneration of capillary bridges between grains. Contrarily, for dry grains,  $G'$  and  $G''$  scaled as  $\sim \gamma^{3/2}$ , acknowledged the presence of filamentary force-chain networks of polycrystalline quasilinear clusters driven by friction, within the SAOS limits. Wherein, the viscoelastic non-linearities were quantified by the virtue of higher order harmonics revealing timescales corresponding to the compaction-like dynamics. Supporting analysis of nonlinear viscoelastic moduli ( $G'_M$  and  $G'_L$ ) as a function of strain amplitude was found scalable with the characteristic energy via a Boltzmann-like factor, in reference to the study [36]. Consequently, the slope values of characteristic moduli ( $\tau_0, G_{0,j}$  and  $G_1^{0''}$ ) implied that the wet granular system can be assumed to be driven by a network of damped elastic oscillators, fluctuating around this characteristic energy while friction governed force chain networks in dry grains are the origin of their elasticity. This allowed us to invoke the non-thermal temperature to provide a general view of these complex dynamics of grains.

Based on these experimental findings, the granular dynamics were recognized to follow the concepts of the SGR model. Thenceforth we followed the works [7, 12, 30–32] to extend our understanding of this non-thermal temperature ( $\equiv$  noise temperature), in the vicinity of granular matter rheology. Thereon, in pursuant to the lemmas of SGR formalism, the granular assembly is assumed a quenched-in distribution of mesoscopic regions in an elastic stress landscape. We first confirmed the strain onset of non-linearity, a transition point of oscillating grains to the yielding of mesoscopic regions. Intriguingly, in our study we find that the viscous flow at mesoscopic scale controls the macroscopic elastic response, thereby complimenting, that the mesoscopic flow affects the macroscopic attributes in a more complicated manner than previously assumed. Since the constitutive description of noise temperature involves the contribution of viscoelastic moduli, we, therefore, provide an experimental approach using basic measures of viscoelasticity to study the inherent dynamics (e.g. fluctuations, rearrangements and caging) of dry and wet grains, exhibiting shear induced compaction-like flows, dilatant-like expansion and the jamming. This analytical strategy entailing the decomposition of stress-strain signal via its symmetry arguments reveal the noise temperature as a periodic solution in a close resemblance to the constitutive equations of the SGR model. The ubiquity of noise temperature in defining a complete rheological response of granular matter was supported by different flow aspects ( $\gamma_0^{\text{onset}}, \tau, E_d, G'_1, G'_M, B$ ) computing approximately the same noise temperature. Upon scaling with packing fraction, the noise temperature of different sized grains at constant confinement identified a sub-transition point, where percolation of filamentary force chains fails and grains solidifies by the epitaxial arrest of quasilinear clusters. Additionally, this jamming pressure was found in good agreement with the Jamming point as defined in standard literature [2, 25, 35, 60] which demonstrated the phase change from compaction to solidification for dry grains and dilatancy for wet grains. Obtaining such an accelerated volume expansion in wet grains under LAOS with constant confinement raised concerns about its significance in the complex flow behaviour of cohesive powders under such con-

ditions. Thenceforth, to illuminate the interplay between cohesivity (dynamic contact and capillary forces) and non-thermal motions, we made an extensive study on wet granular systems that the next chapter will demonstrate. The prime motivation for this study stems from the phenomenological inferences conjectured on using surface tension to control the noise temperature, in [30, 135, 136].

## 4

# Role of Cohesion in Wet Granular Matter

At some point in our life, we have all witnessed how dramatically a small amount of water can transform sand. From dust to a complicated termite mound with an extensive architecture of tunnels and conduits is nothing but pure inspiration. Not only prevalent in nature, granular matter owing to their complex dynamics: agglomeration, cement binding, segregation, compaction, colloidal flocculation, contact fusion of metal particles in sintering, capillary adhesion, solute recrystallization, and dilatancy, has accumulated industrial grandeur over the past decades. Understanding their deformation dynamics by means of disruption and predict the mechanical failure or the point of critical instability is crucial for geophysical and industrial benefits [21, 117, 124, 141]. Myriad studies are filled with an assortment of various flow aspects of granular matter [40, 133, 134, 142–148]. It has been shown that dissipative contacts (force chain networks) and structural rearrangements are what determines if a granular assembly will compact, jam or dilate [2, 3, 25, 35, 44, 86, 122]. Nevertheless, often-times homogeneous shear flow fields are assumed [106, 109, 120, 132, 149] however, in reality, the flow is particularly affected by inhomogeneities, shear banding and nonlinearity as the material approaches rigidity transition (jamming) [56] and the respective models/ theories are rendered inconsistent to account for the *flowability* [119, 127] or cohesive behaviour subsequent to yielding [123]. The underlying physics of cohesive granular flows is much more complicated than it is generally assumed. Although, despite the attempts to address the aforesaid concepts, the role of the compaction mechanism in wet granular matter is still unclear. Whether grains really diffuse under the action of transient caging effects analogous to thermal glasses or if it is due to the critical slowdown of fluidization in granular matter leading to a glassy state, and how the interstitial fluid affect its structural rearrangements, it is still unclear.

As we found in the preceding chapter, the interplay of breaking and regeneration of capillary bridges (elasticity) and the dissipation (viscous) are both inherently linked to a single parameter, the noise temperature should thus elucidate the importance of caging driven cohesive granular flows. Therefore we apply the constitutive formalism of the SGR model on wet granular media at large deformations under constant confinement. Furthermore, the primary motivation for this work stems from the following studies [30, 36, 136] that have previously argued that the noise temperature can be manipulated by varying the surface tension of the wetting fluid.

## 4.1 Non-linear Viscoelasticity in Wet Granular Matter

For oscillations with strain amplitude larger than  $\gamma_0 \geq \gamma_0^{\text{onset}}$  in the non-linear regime, wet granular assembly begins structural rearrangements under the action of breaking and regeneration of capillary bridges as illustrated in Fig. 4.1 (a)-(h). The micrographic simulation to demonstrate this breaking and regenerating action is captured for a monolayer of wet grains confined between parallel plates of plexiglass (5 cm  $\times$  5 cm) (for experimental details, see Chapter 3).

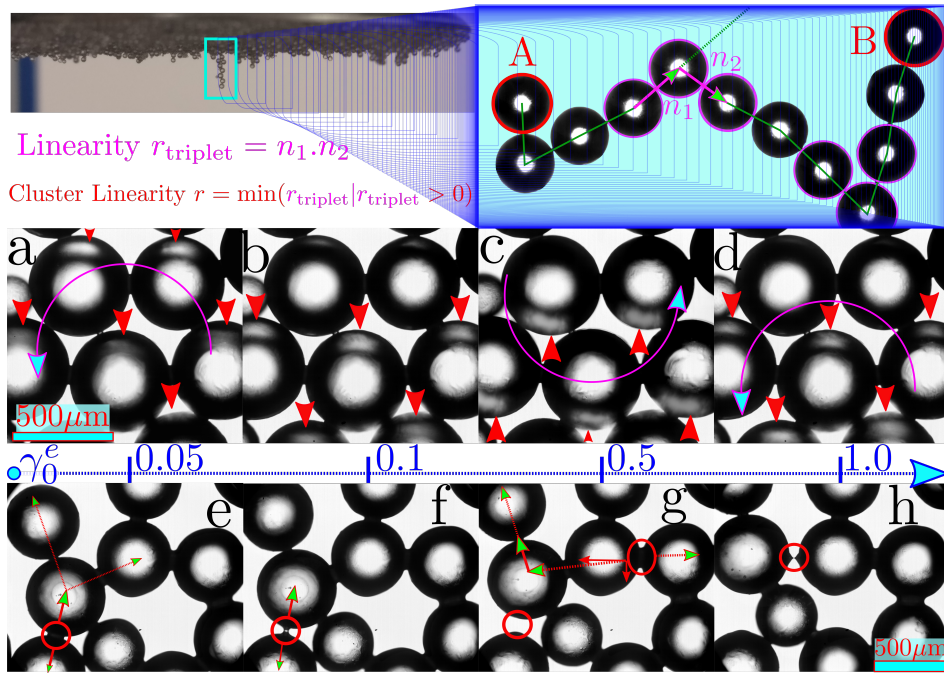


**Figure 4.1:** (a) to (d) demonstrate the cyclic stress-strain contact points captured on the grain surface in a monolayer of wet grains confined between the plexiglass plates, as pointed out by the red arrowheads. (e) to (f) rearrangement of grains wet with Silicon oil (2 wt. %) by the action of breaking and regeneration of capillary bridges. In (e) red arrows represents the force chain direction as the capillary bridge (encircled in red) undergoes elastic stretching, and continues to stretch in (f) and break in (g) while grains rearrange. As this process continues (followed on the scalebar of  $\gamma_0$ ), another bridge begins to stretch in (g) and thins in (h). Top: illustration of a granular chain attached to a sand-blasted shear-plate upon retraction from a granular assembly in a cup-plate setup used for rheometry. The linearity concept is merely to show the significance of the granular clustering process.

The markings (red arrowheads) in (a) to (d) point out the area of contact between applied shear and granular sample. Fig. 4.1 (e) to (g) with guiding arrows and circles highlights the elastic stretching of a liquid bridge (e)-(f), followed by breaking while the stretching begins elsewhere (g) and finally capillary thinning is shown in (h). The top part of the Fig. 4.1 serves as an observation, complimentary to the practical importance of triplet in the clustering of wet grains, displayed by a carefully retracted chain of grains from its sample. The surface tension of the fluids is determined in accordance with [150], using a pendant drop method as sketched in Fig. 4.2 (b) (see Chapter 3 for details) with measurements depicted in Fig. 4.2 (a).

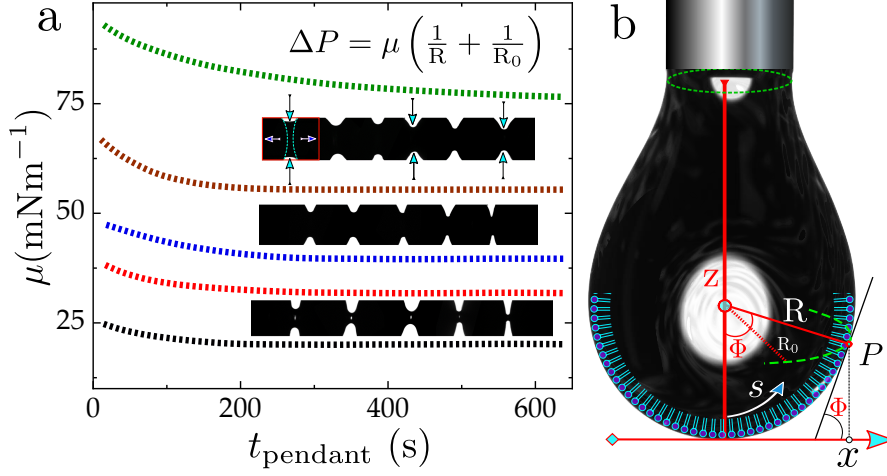


**Figure 4.2:** The surface tension of fluids applied to wet the grains from highest to lowest surface tension as Optiprep<sup>®</sup> (green), PEO (brown), Polysorbital 80 (blue), Triton X (red), Silicon oil (black). (b) A standard analytical sketch to measure the surface tension by the pendant drop method. The image strips in (a) depict a size span of pendular capillary bridges (thick at high surface tension  $\mu$  and gets thinner at low  $\mu$ ), with arrows illustrating extensional and compressive stresses.

In Fig. 4.1 (a), the nonlinear rheology of granular assemblies wet with different fluids is shown by the first harmonic (a) elasticity ( $G'_1$ ) and (b) viscosity ( $G''_1$ ) as a function of strain and strain-rate amplitude, respectively. In (c), the noise temperature  $k_B\Theta$  is depicted by fitting the nonlinear viscoelastic moduli for different cases of wet grains, as shown previously in Chapter 4.

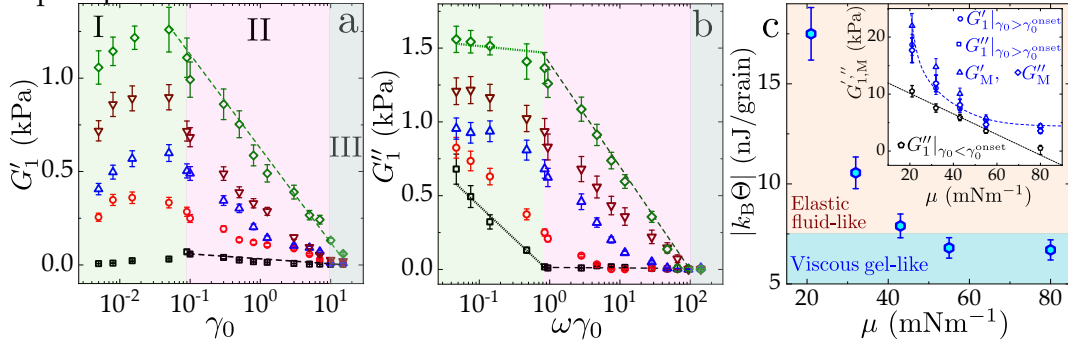


**Figure 4.3:** Nonlinear rheology overview of the wet granular matter: (a) First harmonic elastic modulus ( $G'_1 = e_1$ ) as a function of strain amplitude, (b) first harmonic viscous modulus ( $G''_1 = \omega v_1$ ) as a function of strain rate and (c) the estimated noise temperature ( $k_B\Theta$ ) obtained by fitting  $G'_1$  with  $\frac{\gamma_0}{\gamma_0^{\text{offset}}} = \exp\left(\frac{-G'_1}{G'_1{}^0}\right)$  and  $G''_1$  with  $\frac{\omega\gamma_0}{\omega\gamma_0^{\text{offset}}} = \exp\left(\frac{-G''_1}{G''_1{}^0}\right)$  in regime II (where  $\gamma_0^{\text{onset}} \geq \gamma_0 \leq \gamma_0^{\text{offset}}$ ), for Dynoseeds ( $d = 500 \mu\text{m}$ ) wet by; Optiprep<sup>®</sup> (diamond); Polyethylene oxide (downward triangle); Polysorbital 80 (upward triangle); Triton X (circle) and Silicon oil (square), respectively. The dotted lines in regime I of (b) are fits obtained by adjusting  $G''_1{}^0$ , to compare Dynoseeds wet with different surface tensions. Inset: slope values of  $G'_1|_{\gamma_0 > \gamma_0^{\text{onset}}}$ ,  $G''_1|_{\gamma_0 < \gamma_0^{\text{onset}}}$ ,  $G'_1|_{\gamma_0 > \gamma_0^{\text{onset}}}$ ,  $G''_1|_{\gamma_0 > \gamma_0^{\text{onset}}}$  and  $G''_1|_{\gamma_0 > \gamma_0^{\text{onset}}}$  as a function of  $\mu$ .

The corresponding LB loops are summarized below in Fig. 4.4 (a)-(d), (excluding the case of Silicon oil, as it can be referred in chapter 3). The loops were further analysed to obtain the characteristic degree of elastic  $\zeta_e$  and viscous  $\zeta_v$  nonlinearity in accordance with our approach as shown in chapter 3. The characteristic degree of viscoelastic nonlinearity is illustrated here in Fig. 4.1 (a) to (b), and as a support, the frequency dependence for one such case of Silicon oil in (c) and (d), respectively.

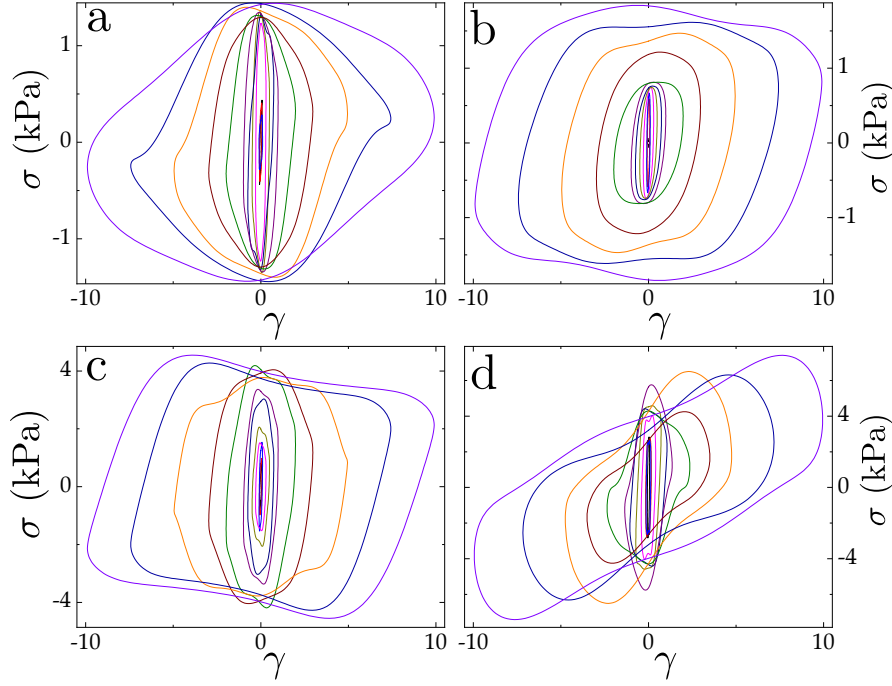


**Figure 4.4:** LB loops summarised for grains wet with (a) Optiprep<sup>®</sup>, (b) Polyethylene oxide, (c) Polysorbitol 80 and (d) Triton X. Note: the LB loops regarding Silicon oil can be referred in Chapter 4.

We fit  $\zeta_e$  and  $\zeta_v$  with a stretched exponential function, given as  $y = \frac{\zeta_e}{\zeta_e^\infty} = 1 - \exp\left(-\left(\frac{\gamma_0}{\gamma_0^\infty}\right)^\delta\right)$  for elastic nonlinearities and  $\frac{\zeta_v}{\zeta_v^\infty} \sim \frac{dy^2}{dx} |_{kx}$  for viscous nonlinearities, where  $kx = \frac{\omega\gamma_0}{(\omega/k)\gamma_0^\infty}$ . The dashed lines shown in Fig. 4.1 are the representative fits to the aforesaid relations where the corresponding values of the parameters involved for different surface tension and frequencies are given in table 4.1 and 4.2, respectively. The data shown in black (Fig. 4.1 (c) and (d)) belongs to the case of Silicon oil, with inset depicting monotonous behaviour of  $k$ -parameter while  $\gamma_0^\infty$  was found to show strong dependence on the applied frequency  $f$ . Nevertheless, the successful working of the stretched exponential model can be pointed out by the fact that for all the values of  $\gamma_0^\infty$  obtained for  $\zeta_e$  was found consistently scalable to compute all the values of  $\gamma_0^\infty$  for  $\zeta_v$  by  $\omega$ , which for our case is  $= 9.42 \text{ rad s}^{-1}$ , such that  $\gamma_{0,\text{viscous}}^\infty \approx \gamma_{0,\text{elastic}}^\infty \times \omega$ . In other words, at low  $\mu$ , the frequency at which the material response is measured, differs from the input or applied frequency, for example in case of Silicon oil by a factor of 0.69, which gets closer to the input frequency as  $\mu$  is increased. Therefore, the significance of  $\gamma_0^\infty$  lies in the frequency range  $f = 1 \text{ Hz}$  to  $f = 3 \text{ Hz}$ , where the material responds to the input frequency.

Therefore, to understand the relevance of viscoelasticity in wet granular material at a meso-

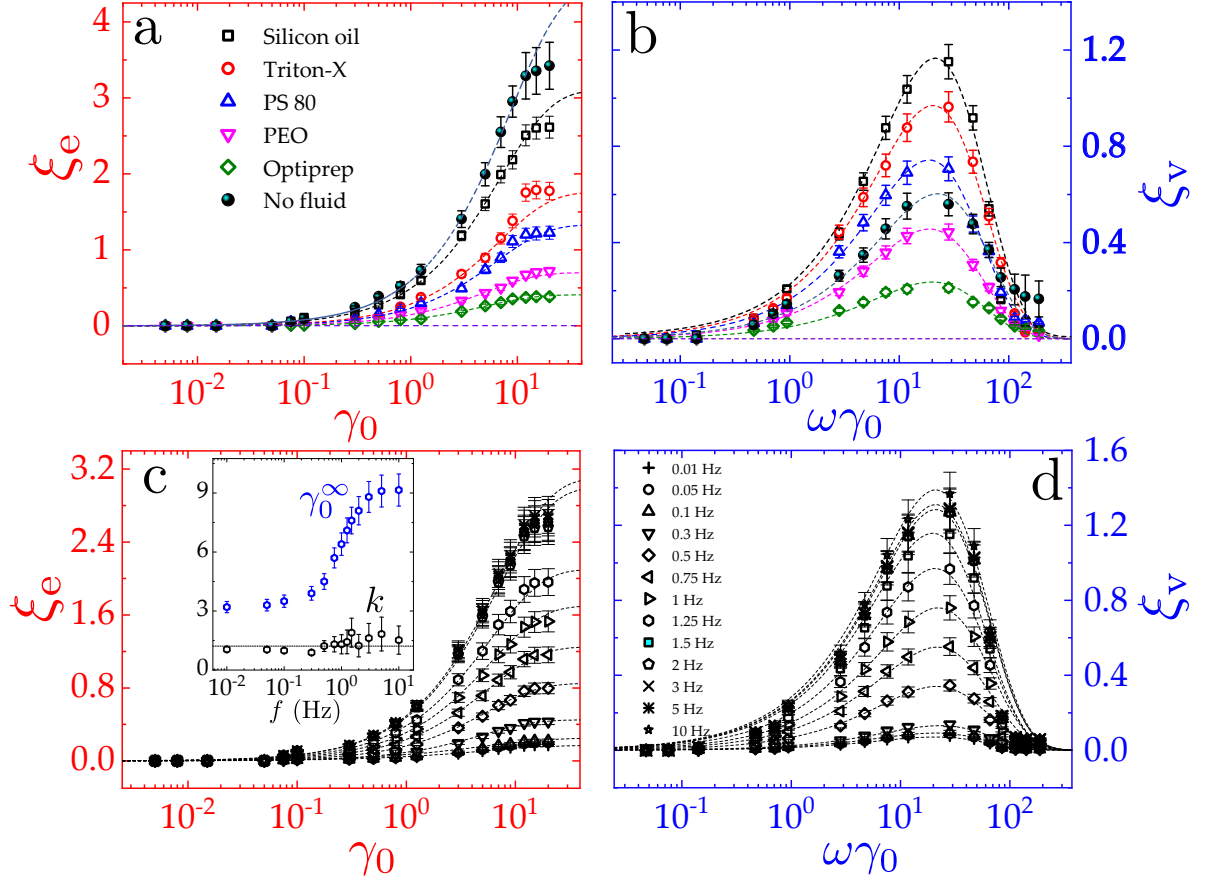


**Figure 4.5:** Semi-logarithmic representation of the characteristic degree of (a) elastic  $\zeta_e$  and (b) viscous  $\zeta_v$  nonlinearity as a function of strain amplitude and strain rate at  $f = 1.5$  Hz and  $N = 1$  N, respectively for Dynoseeds ( $d = 500$   $\mu\text{m}$ ) wet by fluids as shown in the legend. The dashed lines are the stretched exponential fits as described. Frequency dependence of (c) elastic  $\zeta_e$  and (d) viscous  $\zeta_v$  nonlinearity is shown for Dynoseeds ( $d = 500$   $\mu\text{m}$ ) wet with Silicon oil, to show the relevance of applied frequency in the rheology of wet grains. Inset captures the coupling dynamics between material response and the applied frequency.

**Table 4.1:** Stretched exponential fitting parameters for different surface tensions.

$\mu$ ( $\text{mN m}^{-1}$ )	$\gamma_0^\infty$	$1/k$	$\delta$	$\zeta_e^\infty : \zeta_v^\infty$
$10^{-3}$	8.7	0.45	0.9	4.5 : 2.3
21	7.0	0.46	0.9	3.1 : 4.2
33	6.8	0.54	0.9	1.7 : 3.7
43	6.3	0.54	0.9	1.3 : 2.8
55	5.0	0.69	0.9	0.7 : 1.7
79	5.0	0.72	0.9	0.4 : 0.9

scopic scales and the relative contribution of the surface tension of the interstitial fluid, we incorporate the role of capillary bridges (in terms of the rupture energy). Henceforth, in the

**Table 4.2:** Stretched exponential fitting parameters for different frequencies  $f$ .

$f(\text{Hz})$	$\gamma_0^\infty$	$1/k$	$\delta$	$\zeta_e^\infty : \zeta_v^\infty$
0.01	3.2	0.95	0.9	0.66 : 0.27
0.05	3.3	0.96	0.9	0.70 : 0.30
0.10	3.5	1.01	0.9	0.95 : 0.36
0.30	3.9	1.01	0.9	1.7 : 0.53
0.50	4.5	0.81	0.9	3.4 : 1.3
0.75	5.7	0.76	0.9	4.9 : 2.13
1.00	6.4	0.73	0.9	6.5 : 2.88
1.25	7.1	0.69	0.9	8.0 : 3.7
1.50	7.6	0.52	0.9	3.1 : 4.2
2.00	8.1	0.80	0.9	10.9 : 4.9
3.00	8.8	0.61	0.9	11 : 5.25
5.00	9.1	0.54	0.9	11.4 : 5.4
10.00	9.15	0.65	0.9	11 : 5.5

next section, the significance of surface tension in packing, dissipation and rearrangement dynamics of wet granular flows are studied.

## 4.2 Rearrangement Dynamics of Wet Grains and Powders

As found in chapter 3 in comparison to dry grains and the above section, that the non-linear stress-strain response of wet granular matter strongly depends on the breaking and regeneration dynamics of capillary bridges, that intrinsically stem from the surface tension governed cohesion. Thenceforth, we thoroughly study the role, the interstitial fluid's surface tension is playing in evoking such capillary profiles in a granular assembly. Primarily, the total force of cohesion  $F_{\text{tot}} = F_c + F_v$  is calculated for capillary bridges, followed by later use in estimating the total rupture energy  $\tilde{W}_{\text{tot}}$ . We integrate the ratio of these forces with capillary bridge volume  $\mu R$  from zero to the rupture length  $\tilde{H}$  for the capillary force  $F_c$  and from characteristic surface roughness length  $\tilde{d} \approx 0.005$  with respect to the length of the capillary bridge  $H$  for each strain amplitude. Where  $\tilde{H}$  is given as  $\simeq (1 + \frac{\theta_p}{2})\pi^{1/3} \frac{x+H}{2R}$ , allowing the total rupture energy required to break the liquid bridge in pendular regime is directly proportional to the surface tension  $\mu$  and viscosity  $\eta$  of the wetting fluid. Note: the values and definitions of additional parameters used for estimating  $\langle \tilde{W}_{\text{tot}} \rangle$  can be found in Chapter 2 and 3. The significance of surface tension on the rupture energy (as a measure of cohesion), the energy dissipated  $E_d$  by the system and the variation in the packing fraction per experiment, in governing slowly compacting or packing wet granular matter is shown in Fig. 4.6. Note: that the experimental strain defined here as  $\gamma_0^e$ , is a unidirectional strain (devoid of oscillations) applied on the parallel-plate setup of plexiglass under the microscope by a 2D moving stage (as described in Chapter 2). Moreover, the noise temperature obtained for different confinement pressure  $P$  for dry and wet grains ( $d = 500 \mu\text{m}$ ) in Chapter 3 is compared with grains wet with Optiprep in Fig. 4.6 (d). Whereas the packing of wet grains is depicted as a function of a qualitative strain defined as  $\gamma_0^*$ . This qualitative strain

$\gamma_0^*$  here represents the average of strain per number of oscillations and not the applied strain (i.e.  $\gamma$ ) at which the rheological measurements were made, such that for example,  $\phi^* \approx 0.01$  represents a measurement that is an average of  $\phi^*$  measured for 5 complete sinusoidal oscillations at  $\gamma_0 \approx 0.01$ . With all these unique variables, this figure is intended to describe the rearrangement dynamics from mesoscopic flow aspects.

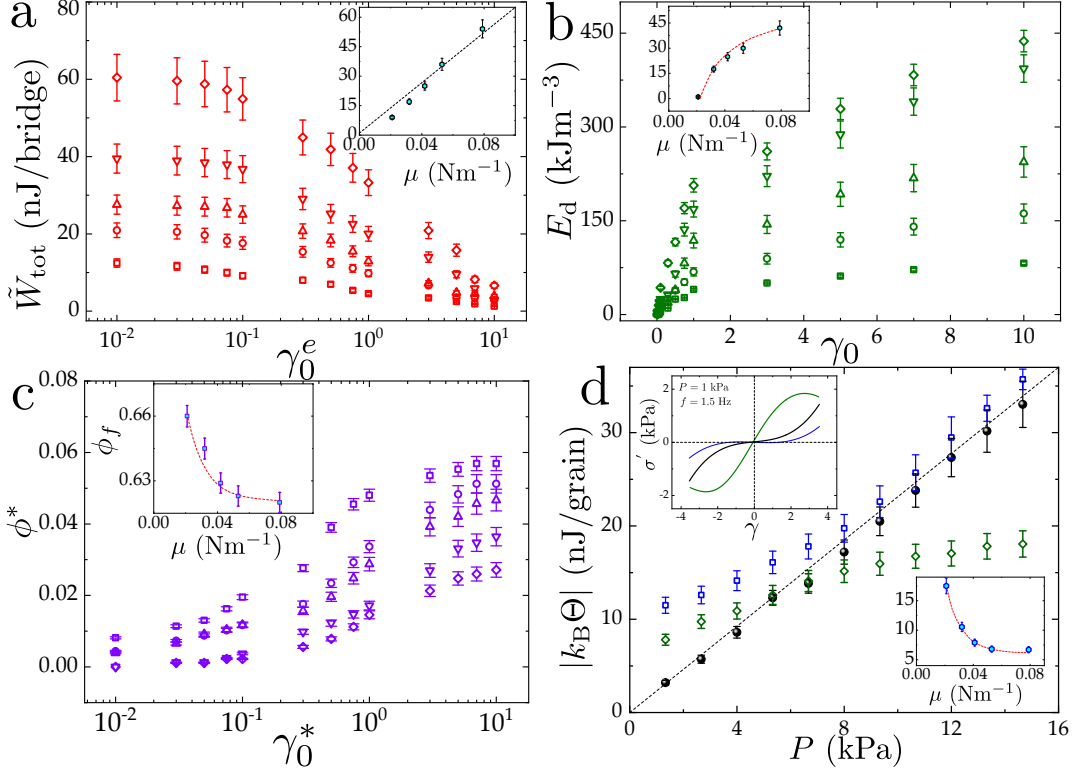


**Figure 4.6:** Fast to slow rearrangement dynamics of wet granular matter governed by the surface tension driven rupture energy ( $\tilde{W}_{\text{tot}}(\mu)$ ): a measure of *cohesion*). The dynamics are represented as a function of different forms of strains for (a)  $\tilde{W}_{\text{tot}}(\gamma_0^e)$ , (b)  $E_d(\gamma_0)$ , (c)  $\phi^*(\gamma_0^*)$ . (d) compares the  $k_B\Theta$  calculated in Chapter 3 for dry and wet grains with the grains wet with Optiprep as a function of confinement pressure  $P$ . The inset of (a), (b), (c) and (d) represents the surface tension ( $\mu$ ) dependence for the corresponding variables chosen at  $\gamma_0^{\text{onset}}$  or at the equivalent measurement specific strains, as defined here. The second inset of (d) corresponds to the elastic symmetry lines obtained at  $P = 1$  kPa for dry (in black), Silicon (in blue) and Optiprep (in green). Legends: Optiprep<sup>®</sup> (diamond); Polyethylene oxide (downward triangle); Polysorbitol 80 (upward triangle); Triton X (circle); Silicon oil (square); and dry grains (black spheres).

In Fig. 4.6 (a)  $\tilde{W}_{\text{tot}}$  is shown decaying for increasing  $\gamma_0^e$ , with a linear dependence on  $\mu$  shown in the inset [109, 119, 128, 132]. Packing (compaction-like) of grains is illustrated by the variation in the packing fraction per experiment  $\phi^* = \frac{\phi_f - \phi_i}{\phi_i}$  calculated for each strain cycle. All the insets illustrate surface tension dependence of the corresponding variables, roughly scaling as  $\tilde{W}_{\text{tot}} \sim \mu$  in (a),  $E_d \sim \log \mu$  in (b),  $\phi^* \sim \exp(-\mu)$  in (c) and  $k_B\Theta \sim \exp(-\mu)$  in (d). Fig. 4.6 (d) compares two systems composed of 500  $\mu\text{m}$  grains, the wet grains (low to high surface tension as 21  $\text{mNm}^{-1}$  and 79  $\text{mNm}^{-1}$ ) to dry grains. For accurate estimation of the noise temperature, we analysed the LB loops in accordance with our approach to SGR dynamics, as shown earlier in Chapter 3. Upon obtaining the elastic

symmetry lines, illustrated in Fig. 4.2(a) to (d), and fitting them with an equation of the form  $\sigma' = \sigma'_0 + A\gamma - B \sin\left(\frac{\gamma}{\gamma_0}\right)$  revealed the noise temperature as  $B = \ln\left(\frac{\gamma_0}{\gamma_0^{\text{onset}}}\right)k_B\Theta$ . Wherein, the parameter  $B$  for different surface tension and normal force  $N$  is depicted in Fig. 4.8 (a) and (b), as a function of strain amplitude  $\gamma_0$ , respectively. Note: the LB loops for the case of Optiprep at different normal forces is given in Appendix A Fig. .13.

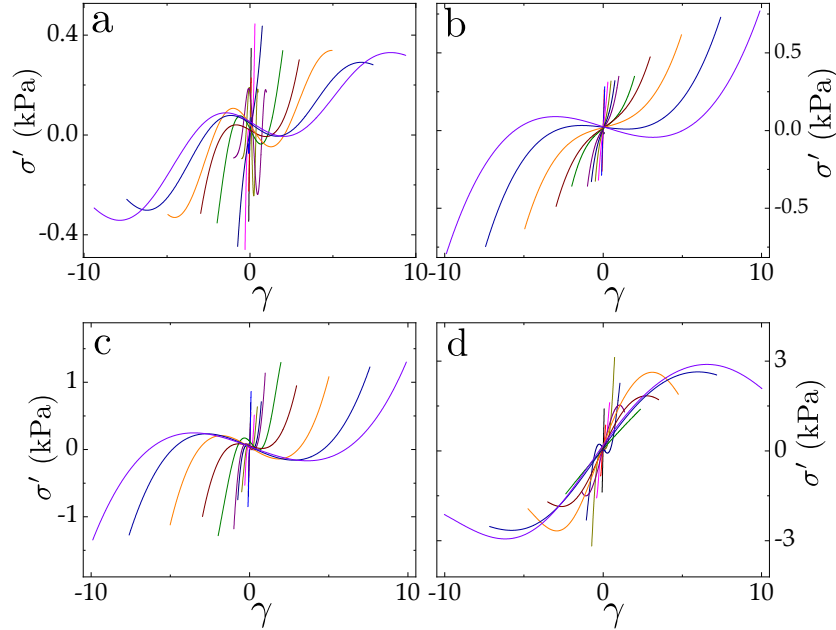


**Figure 4.7:** Elastic symmetry lines summarised for grains wet with (a) Optiprep<sup>®</sup>, (b) Polyethylene oxide, (c) Polysorbitol 80 and (d) Triton X. Note: the symmetry lines obtained for Silicon oil can be referred in Chapter 4.

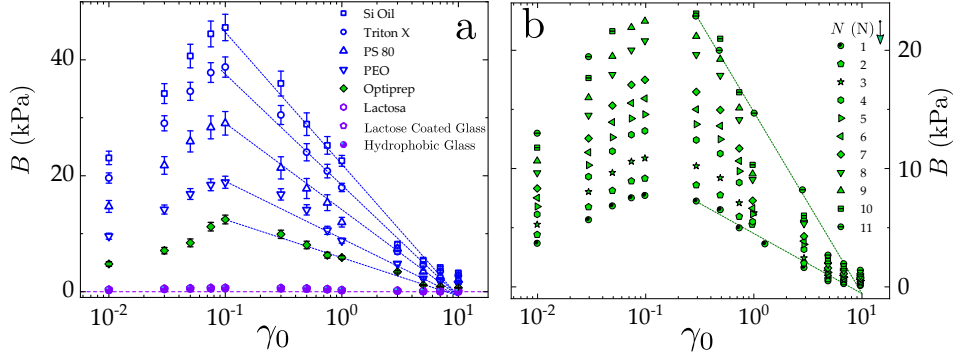


**Figure 4.8:** Calculations made for  $B$ –parameter as a function of strain amplitude for varying (a) surface tension and (b) normal force ( $N$ ) (see legends). Note: (b) only represents the case of Optiprep<sup>®</sup> at different  $N$ . The dashed lines are the fits with equation 3.2 to estimate the noise temperature  $k_B\Theta$ . Legend: Optiprep<sup>®</sup> (diamond); Polyethylene oxide (downward triangle); Polysorbitol 80 (upward triangle); Triton X (circle) and Silicon oil (square), cohesive powders in solid symbols involves: hydrophobic glass ( $d \approx 140 \mu\text{m}$ ), lactose coated glass ( $d \approx 140 \mu\text{m}$ ) and lactose monohydrate (lactosa<sup>®</sup>;  $d \approx 200 \mu\text{m}$ ).

### 4.3 Discussions and General Remarks

This study is a foremost demonstration of surface tension driven noise temperature in wet granular matter. We varied the *cohesiveness* of grains by wetting them with interstitial fluids of different surface tension in a pendular regime such that the system maintains effective capillarity, where the cohesive forces act exclusively via liquid bridges [59, 119, 120]. This allowed us to avoid pressure or suction effects that often arise in the funicular or capillary regime and ensure that the cohesive behaviour results from liquid bridges only [119, 120]. The non-linear dynamics are first addressed via FT-rheology combined with Chebyshev polynomials, as applied previously in Chapter 3. The nonlinear rheology clearly illustrated an elastic fluid-like to a viscous gel-like transition based on the first harmonic viscoelastic moduli and the corresponding noise temperature, which was found high at small surface tension, and approaching zero as  $\mu$  was increased, indicating the drop in the number of rearrangements (see Fig. 4.1). In addition, the vast differences in slopes of  $G_1''$  for highest and lowest surface tension cases (as shown in Fig. 4.1) strongly imply that the lower is the fluid surface tension, lower energy is required to break the capillary bridges and high energy is needed to break and move capillary bridges of wetting fluid with high surface tension. Besides, for an accurate estimation, the fact that the number of capillary bridges in a granular sample made by fluids of different surface tensions may also vary, and so the rupture energy. Furthermore, upon fitting the characteristic degree of nonlinearity  $\zeta$  with a stretched exponential function, the exponent  $\delta$  was found the same for all the cases of grains wet with different fluids as  $\delta \approx 0.9$ , despite the differences in their overall rheology and  $k$ –parameter values (Fig. 4.1; 4.1). This additionally compliments the question and proposition raised in [40, 86], that the fluid properties play an important role in governing material response in bulk as well as mesoscopic scales. The successful working of the stretched exponential model in fitting  $\zeta_e$  and  $\zeta_v$  was acknowledged by finding a constant proportionality between  $\zeta_e^\infty$  and  $\zeta_v^\infty$  by exactly of the order of  $\omega = 9.42 \text{ rad s}^{-1}$ , which might be more than just a correlation. This interdependence between viscoelastic nonlinearities strongly indicates

that irrespective of the stress-strain response, elastic or viscous, the behaviour of granular material stays viscoelastic, as the viscous flows at mesoscopic scales govern the bulk elasticity and *vice – versa*. Henceforth, to study the significance of wetting fluids in granular materials and powders, we followed the works [86, 119, 128, 129, 132] and calculated the viscous and capillary forces as a measure of cohesion. Followed by estimating the energy spent ( $\tilde{W}_{\text{tot}}$ ) and released  $E_d$  as grains began to rearrange at  $\gamma_0 \leq \gamma_0^{\text{onset}}$ . Upon applying the analytical approach hitherto illustrated in Chapter 4, we find  $\langle F_{\text{tot}} \rangle$  of a standard capillary bridge between two grains wet with (a) Silicon oil as  $7.4 \mu\text{N}$ , (b) Triton X as  $10.3 \mu\text{N}$ , (c) Polysorbitol 80 as  $21.5 \mu\text{N}$ , (d) Polyethylene oxide as  $33.7 \mu\text{N}$  and (e) Optiprep® as  $59.3 \mu\text{N}$ .

Therefore, to provide valuable insights on the intrinsic relationship between rearrangement dynamics and the physical properties of the wetting fluid, we made a comparative illustration by incorporating the role of cohesion  $\tilde{W}_{\text{tot}}$  compared to the dissipation  $E_d$ , and variation in the packing fraction per experiment  $\phi^*$  representing the compaction-like dynamics to the noise temperature  $k_B\Theta$ . Finding a linear dependence of  $\tilde{W}_{\text{tot}}$  on the surface tension validates our calculations of liquid forces and rupture energy to a reasonable degree of accuracy and in agreement with [3, 130]. As shown in Fig. 4.6 (b), the logarithmic growth of  $E_d$  over strain clearly acknowledges our aforesaid proposition, that the breaking and regeneration of liquid bridges in wet granular matter account for the energy dissipated. To capture a deeper view on the rearrangement dynamics in wet granular assemblies and how can they be controlled, we calculated the initial and final packing fraction as we illustrated earlier in Chapter 4, for every strain cycle per number of oscillations, and normalised in accordance with [133, 134, 151], denoted as  $\phi^*$ . The behaviour for granulates wet with the fluid of low surface tension  $\mu \approx 21 \text{ mN m}^{-1}$  and viscosity  $\eta \approx 0.018 \text{ mPa}$  showed compaction-like dynamics, which got slower as the surface tension and the viscosity of the wetting fluid was increased, with slowest at high  $\mu \approx 79 \text{ mN m}^{-1}$  and  $\eta \approx 0.9 \text{ mPa}$  (see Fig. 4.6 (c)). Wherein, the inset further corroborates the fact that at high surface tension, large energy input is needed to pack the grains via rearrangements, and *vice – versa*. Apparently, the slow packing of wet granulates, that gets slower with increasing  $\mu$  and the energy dissipated by wet grains due to breaking and regeneration of capillary bridges can be assumed interlinked with the surface tension of the fluid as such assumption has been already used for dry grains with emergent surface tension effects ( $\approx 1 \mu\text{N m}^{-1}$ ) by [121, 142, 148]. In that case, the structural rearrangements being the inherent origin of dissipation and compaction [7, 9, 22, 30, 34, 41, 116], must recognize these events of breaking and regeneration of capillary bridges by a temperature-like variable, the noise temperature, defined in this thesis as  $k_B\Theta$  in the units of J/grain [36].

Thenceforth, following with the SGR model-based analytical approach demonstrated in chapter 4, we decomposed the LB loops via stress-strain symmetry arguments and fitted the stress symmetry lines with a periodic series function to estimate the noise temperature. Moreover, to reveal a clear distinction between granular material types, we found cohesive powder systems, in contrast to wet granular matter, exhibited approximately a constant noise temperature, clearly indicating that the structural rearrangements are invariant to the applied deformation. Besides, the cohesive powder flow profile fits in a good agreement with gel-suspension like flows, as their monotonous dependence on noise temperature, suggests that *cohesivity* "prefers" an equal number of rearrangements regardless of the powder type. This implies that increasing the amount of energy required to rupture a capillary

bridge between grains can eventually collapse the rearrangements in a granular assembly, thereby shifting its phase from an elastic fluid-like to a solid or viscous gel-like state, which is analogous to the transient caging phenomena in thermal glasses [2, 3, 9, 22, 63]. Such rearrangement dynamics may result from caging by hindering the structural movements in wet granular materials, as the energy requirements to break and regenerate a capillary bridge exceeds the applied deformation. Thus, such a slow decay of rearrangements might be viewed as a reminiscence of the glass-like relaxation of wet granular systems. The afore-said findings presented heretofore have strong implications in industrial processes such as compaction, segregation, jamming and mixing of wet grains and cohesive powders.



## 5

# Conclusions and Outlook

Granular unrest (or jam), from food to earthquakes, ice floes, or torus belts of asteroids, serves as a model system to understand the governing dynamics of hard-sphere systems, hallmarked by their non-thermal motions [1, 4, 6]. Amid this endless pursuit to fully describe complex matter and establish a mean field theoretical framework (*vis-a-vis* thermodynamics) of granular matter, thermal glass formers are often exploited to draw analogies with granular dynamics [3, 5, 152]. Hereof, applications of trap and SGR models [2, 8, 9, 33–35, 153] have made staggering progress in describing slowly sheared granular matter, however, the presence of viscous effects at large deformation scales has earned it a notorious status of complex matter [3, 35, 106], a hard problem to address.

In this thesis, we have systematically studied the non-linear rheology of dry and wet granular matter at large deformations. By exploiting the stress-strain symmetry arguments via FT-rheology and Chebyshev polynomials, the material response is decomposed into elastic and viscous contributions (including the nonlinearities), providing a simplified means to make qualitative and quantitative analysis formulated in a characteristic degree of non-linearity  $\zeta$ . Subsequent to the identification of three dynamical regimes of granular flows in a shear cell; linear, non-linear and stick-slip via  $\zeta$ , we find that the deformation larger than the size of grain set the divergence from the linear response (at  $\gamma_0^{\text{onset}}$ ) representing nonlinear events as the reminiscence of rearrangements (as yield stress fluids, YSFs). In the SAOS regime, the logarithmic dependence for  $G'$  and  $G''$  for wet Dynoseeds strongly suggested the oscillating capillary bridges between grains before rearrangements begin. Contrastingly,  $G'$  and  $G''$  for dry grains scaled as  $\sim \gamma^{3/2}$  were found in good agreement with the formation of filamentary force-chain networks of polycrystalline quasilinear clusters driven by friction. Wherein, the viscoelastic non-linearities revealed a strong coupling between elasticity and viscosity in sheared granular systems. Supporting analysis of nonlinear viscoelastic moduli ( $G'_M$  and  $G'_L$ ) was done in accordance with [36], as a function of strain amplitude to compute the characteristic energy via a Boltzmann-like scaling parameter. Whence, the values of characteristic moduli ( $\tau_0, G_{0,j}$  and  $G_1^{0''}$ ) implied that the wet granular system can be assumed to be driven by a network of damped elastic oscillators, fluctuating around this characteristic energy while friction governed force chain networks in dry grains serving as the origin of their elasticity. These values were found to represent a non-thermal temperature, henceforth intended to provide a general view of these complex dynamics of grains.

Based on aforesaid findings, the underlying physics of dry and wet granular dynamics were recognized to be governed by similar concepts as of the SGR model. We followed

the works [7, 12, 30–32] to extend our understanding of this non-thermal temperature, "the noise temperature", in the vicinity of granular matter rheology. Thereupon, we began with the axiomatic description of the SGR formalism, where the granular assembly is viewed as a quenched-in distribution of mesoscopic regions in an elastic stress landscape. We first confirmed the  $\gamma_0^{\text{onset}}$  as an indicator of non-linearity, a transition point where oscillating grains begins to yield as mesoscopic regions (YSFs). In this part of the study, we found that the viscous flow at mesoscopic scale controls the macroscopic elastic response, complimenting the conjecture that the mesoscopic flow affects the macroscopic attributes in a more complicated manner than previously assumed. Note: viscous effects are not taken into account in SGR models, however, the model argues with a caveat that such effects must be considered as the system is deformed at larger scales. Favourably, the constitutive description of noise temperature comprises the viscoelastic moduli which allowed us to provide an experimental approach using basic measures of viscoelasticity to study the inherent dynamics (e.g. fluctuations, rearrangements and caging) of dry and wet grains, exhibiting shear induced compaction, dilatancy and jamming.

In this analytical strategy, the stress-strain symmetry was exploited to reveal the noise temperature as a periodic solution in a close resemblance to the constitutive equations of the SGR model. This finding additionally compliments the questions and propositions raised in the study [50] that reviewed how linear algebraic approaches conflate the information on the elastic and viscous processes whereas a periodic sequence can suffice the response of yield stress fluids. The complete rheological response of granular matter in terms of the noise temperature was additionally supported by scaling different flow aspects ( $\tau_a, E_d, G'_1, G'_M, B$ ) computing approximately the same noise temperature. Upon scaling with packing fraction, the noise temperature of different sized grains at constant confinement was found to follow bifurcation-like paths, where percolation of filamentary force chains in dry grains fails and grains jams by the epitaxial arrest of quasilinear clusters whereas wet granular samples begin to expand as dilatant fluid. The confinement pressure and the packing fraction at which these phenomena occur were found in good agreement with  $\sim$  Jamming point [2, 25, 35, 60].

Finding dilatant behaviour in wet grains under constant confinement and the associated rich dynamics of capillary bridges, provoked our interest to study the significance of wetting fluid in granular media. As we found that this interplay of breaking and regeneration of capillary bridges (elasticity) and the dissipation (viscous) are both intrinsically linked to a single parameter, the noise temperature, should therefore answer: whether wet granular flows are governed by the transient caging effects analogous to thermal glasses or not? Besides, our prime motivation for this study also stems from the inferences made on surface tension driven noise temperature in [30, 136].

Compared to the raw rheology data  $G'$  and  $G''$  for grains wet with different fluids, the nonlinear viscoelastic moduli showed an elastic fluid-like to a viscous gel-like transition at low to high surface tension, respectively, which is inherently related to the adjustment in local packing density (compaction-like). From the stretched exponential fits of  $\xi$  for grains wet with the fluids of different surface tension ( $\mu$ ) and viscosity ( $\eta$ ), showing the amount of nonlinearity is significantly small at high surface tension, complimented the idea proposed in [40, 86], conjecturing that at high  $\mu$  or  $\eta$ , it would take longer for a capillary bridge

to break. Herein, we calculated the total rupture energy of the possible capillary bridges present in a layer of grains deformed by a unidirectional strain  $\gamma_0^e$  under the microscope as  $\tilde{W}_{\text{tot}}$  to provide valuable insights on the wetting dynamics and fluid properties. A linear dependence of  $\tilde{W}_{\text{tot}}$  on  $\mu$  and  $\eta$  validated our analysis to a reasonable degree of accuracy and efficiency [3, 130]. As the slow compaction is taking place, the energy required to break and regenerate capillary bridges between grains decreases and simultaneously the energy dissipation of the system increases. This was illustrated by studying the packing dynamics, where a fast growth of  $\phi^*$  for grains wet with fluid of low  $\mu$  and  $\eta$  was found compared to the slowest at high  $\mu$  and  $\eta$ , corroborating that large energy input is required to pack the grains via rearrangements for a system wet with high surface tension fluid. As indicated by  $\phi^*$  and  $E_d$ , compaction-like dynamics are most likely governed by the action of breaking and regeneration of capillary bridges, which in fact are controlled by the surface tension of the fluid. Therefore, the structural rearrangements in the granular matter when viewed as a reminiscence of the noise temperature can be tuned by changing the surface tension alone.

In contrast to wet granular media, the cohesive powders showed a monotonous response to the noise temperature, indicating that their structural rearrangements are invariant to the applied deformation, and resembled the flow profile similar to a gel-suspension. In this regard, a stronger indication however alludes to the identification of the point of critical instability where rearrangements would collapse as the amount of energy required to rupture a capillary bridge between grains exceeds the applied deformation, corroborating to the transition from an elastic fluid-like to a solid or viscous gel-like state, analogous to the transient caging effects in thermal glasses. Furthermore, in contrast to the surface tension dependence of  $E_d \sim \log \mu$ ,  $\phi^* \sim \exp(-\mu)$ , and noise temperature as  $k_B \Theta \sim \exp(-\mu)$  supports the caging hindered structural rearrangements in wet granular materials. Because, since the dissipation is balanced by the energy spent in breaking and regenerating capillary bridges, slow decay of rearrangements is nevertheless, bound to the glass-like relaxation of the system.

These aforesaid findings provide valuable insights on the industrial processes such as compaction, segregation, jamming and mixing of wet grains and cohesive powders. The knowledge gained from this work offers an extensive experimental and analytical foreground to further develop and contribute to the *coarse-grained* description of non-linear dynamics of granular matter. We find our approach more general than it was intended to be and plan to apply this framework to describe the dynamical response of surface-treated powders, commodity polymers, electrical conductance and ferromagnetic dielectric discharge, provided that the response is nonlinear and satisfy symmetry arguments for analytical division.

This thesis captures a generic picture of nonlinear granular flows governed by the rearrangements viewed as a reminiscence of the noise temperature to describe compaction, dilatancy and jamming, particularly on the accounts of rheology.



## Bibliography

- [1] H. M. Jaeger, S. R. Nagel, and R. P. Behringer. “Granular solids, liquids, and gases”. *Rev. Mod. Phys.* 68 (4 1996), pp. 1259–1273.
- [2] R. P. Behringer, D. Bi, et al. “Why Do Granular Materials Stiffen with Shear Rate? Test of Novel Stress-Based Statistics”. *Physical Review Letters* 101 (26) (2008).
- [3] B. Kou, Y. Cao, et al. “Granular materials flow like complex fluids”. *Nature* 551 (7680) (2017), pp. 360–363.
- [4] R. A. Bagnold. “Experiments on a Gravity-Free Dispersion of Large Solid Spheres in a Newtonian Fluid under Shear”. *Proceedings of the Royal Society A: Mathematical, Physical and Engineering Sciences* 225 (1160) (1954), pp. 49–63.
- [5] A. Coniglio. *Unifying concepts in granular media and glasses*. Amsterdam Boston: Elsevier, 2004.
- [6] J. Duran. *Sands, Powders, and Grains*. Springer New York, 1999. 232 pp.
- [7] J. P. Bouchaud. “Weak ergodicity breaking and aging in disordered systems”. *Journal de Physique I* 2 (9) (1992), pp. 1705–1713.
- [8] S. Henkes, C. S. O’Hern, and B. Chakraborty. “Entropy and Temperature of a Static Granular Assembly: AnAb Initio Approach”. *Physical Review Letters* 99 (3) (2007).
- [9] D. Bi and B. Chakraborty. “Rheology of granular materials: dynamics in a stress landscape”. *Philosophical Transactions of the Royal Society A: Mathematical, Physical and Engineering Sciences* 367 (1909) (2009), pp. 5073–5090.
- [10] W. van Meegen, T. C. Mortensen, et al. “Measurement of the self-intermediate scattering function of suspensions of hard spherical particles near the glass transition”. *Physical Review E* 58 (5) (1998), pp. 6073–6085.
- [11] S. Chandran, R. Handa, et al. “Time Allowed for Equilibration Quantifies the Preparation Induced Nonequilibrium Behavior of Polymer Films”. *ACS Macro Letters* 6 (11) (2017), pp. 1296–1300.
- [12] S. M. Fielding, P. Sollich, and M. E. Cates. “Aging and rheology in soft materials”. *Journal of Rheology* 44 (2) (2000), pp. 323–369.
- [13] C. Monthus and J.-P. Bouchaud. “Models of traps and glass phenomenology”. *Journal of Physics A: Mathematical and General* 29 (14) (1996), pp. 3847–3869.
- [14] A. P. Young. *FRONT MATTER*. 1997.
- [15] A. B. Hart. “Motions in the Sun at the Photospheric Level: VI. Large-Scale Motions in the Equatorial Region”. *Monthly Notices of the Royal Astronomical Society* 116 (1) (1956), pp. 38–55.
- [16] Y. A. Gaponenko and V. E. Zakhvataev. *Journal of Applied Mechanics and Technical Physics* 43 (6) (2002), pp. 823–829.

- [17] J. Zirker. *Sunquakes : probing the interior of the sun*. Baltimore: Johns Hopkins University Press, 2003.
- [18] R. Freedman. *Universe*. New York, NY: W.H. Freeman and Co, 2008.
- [19] P. Bak, C. Tang, and K. Wiesenfeld. "Self-organized criticality". *Physical Review A* 38 (1) (1988), pp. 364–374.
- [20] P. Bak. *How Nature Works*. Springer New York, 1996.
- [21] A. Sornette and D. Sornette. "Self-Organized Criticality and Earthquakes". *Europhysics Letters (EPL)* 9 (3) (1989), pp. 197–202.
- [22] M. E. Cates, J. P. Wittmer, et al. "Jamming, Force Chains, and Fragile Matter". *Physical Review Letters* 81 (9) (1998), pp. 1841–1844.
- [23] M. E. Cates, J. P. Wittmer, et al. "Jamming and static stress transmission in granular materials". *Chaos: An Interdisciplinary Journal of Nonlinear Science* 9 (3) (1999), pp. 511–522.
- [24] A. J. Liu and S. R. Nagel. "Jamming is not just cool any more". *Nature* 396 (6706) (1998), pp. 21–22.
- [25] K. Lu, E. E. Brodsky, and H. P. Kavehpour. "A thermodynamic unification of jamming". *Nature Physics* 4 (5) (2008), pp. 404–407.
- [26] L. Papadopoulos, M. A. Porter, et al. "Network analysis of particles and grains". *Journal of Complex Networks* 6 (4) (2018), pp. 485–565.
- [27] M. Newman. *Networks*. Oxford University Press, 2018. 800 pp.
- [28] K. LU, E. E. BRODSKY, and H. P. KAVEHPOUR. "Shear-weakening of the transitional regime for granular flow". *Journal of Fluid Mechanics* 587 (2007), pp. 347–372.
- [29] M. E. Cates and P. Sollich. "Tensorial constitutive models for disordered foams, dense emulsions, and other soft nonergodic materials". *Journal of Rheology* 48 (1) (2004), pp. 193–207.
- [30] P. Sollich, F. ç. Lequeux, et al. "Rheology of Soft Glassy Materials". *Phys. Rev. Lett.* 78 (10 1997), pp. 2020–2023.
- [31] P. Sollich. "Rheological constitutive equation for a model of soft glassy materials". *Physical Review E* 58 (1) (1998), pp. 738–759.
- [32] J.-P. Bouchaud, M. E. Cates, et al. "Hysteresis and Metastability in a Continuum Sandpile Model". *Phys. Rev. Lett.* 74 (11 1995), pp. 1982–1985.
- [33] M. Kaushal and Y. M. Joshi. "Analyzing aging under oscillatory strain field through the soft glassy rheology model". *The Journal of Chemical Physics* 144 (24) (2016), p. 244504.
- [34] S. Henkes and B. Chakraborty. "Statistical mechanics framework for static granular matter". *Physical Review E* 79 (6) (2009).
- [35] K. LU, E. E. BRODSKY, and H. P. KAVEHPOUR. "Shear-weakening of the transitional regime for granular flow". *Journal of Fluid Mechanics* 587 (2007), pp. 347–372.
- [36] J. E. Fiscina, M. Pakpour, et al. "Dissipation in quasistatically sheared wet and dry sand under confinement". *Physical Review E* 86 (2) (2012).

- [37] C. Ness, Z. Xing, and E. Eiser. "Oscillatory rheology of dense, athermal suspensions of nearly hard spheres below the jamming point". *Soft Matter* 13 (19) (2017), pp. 3664–3674.
- [38] M. Bouzid, A. Izzet, et al. "Non-local rheology in dense granular flows". *The European Physical Journal E* 38 (11) (2015).
- [39] P. Y. Liu, R. Y. Yang, and A. B. Yu. "Self-diffusion of wet particles in rotating drums". *Physics of Fluids* 25 (6) (2013), p. 063301.
- [40] M. Badetti, A. Fall, and J.-N. Roux. "Rheology of wet granular materials under continuous shear: experiments and simulations". *EPJ Web of Conferences* 140 (2017). Ed. by F. Radjai, S. Nezamabadi, et al., p. 08019.
- [41] S. M. Fielding. "Elastoviscoplastic rheology and aging in a simplified soft glassy constitutive model". *Journal of Rheology* 64 (3) (2020), pp. 723–738.
- [42] E. Bouchbinder and J. S. Langer. "Nonequilibrium thermodynamics of driven amorphous materials. I. Internal degrees of freedom and volume deformation". *Physical Review E* 80 (3) (2009).
- [43] K. Kamrin and G. Koval. "Nonlocal Constitutive Relation for Steady Granular Flow". *Physical Review Letters* 108 (17) (2012).
- [44] Q. Zhang and K. Kamrin. "Microscopic Description of the Granular Fluidity Field in Nonlocal Flow Modeling". *Physical Review Letters* 118 (5) (2017).
- [45] "On dense granular flows". *The European Physical Journal E* 14 (4) (2004), pp. 341–365.
- [46] L. E. Silbert, J. W. Landry, and G. S. Grest. "Granular flow down a rough inclined plane: Transition between thin and thick piles". *Physics of Fluids* 15 (1) (2003), pp. 1–10.
- [47] F. D. Cruz, F. Chevoir, et al. "Viscosity bifurcation in granular materials, foams, and emulsions". *Physical Review E* 66 (5) (2002).
- [48] G. Koval, J.-N. Roux, et al. "Annular shear of cohesionless granular materials: From the inertial to quasistatic regime". *Physical Review E* 79 (2) (2009).
- [49] S. Kim and K. Kamrin. "Power-Law Scaling in Granular Rheology across Flow Geometries". *Physical Review Letters* 125 (8) (2020).
- [50] S. A. Rogers and M. P. Lettinga. "A sequence of physical processes determined and quantified in large-amplitude oscillatory shear (LAOS): Application to theoretical nonlinear models". *Journal of Rheology* 56 (1) (2012), pp. 1–25.
- [51] M. Wilhelm, D. Maring, and H.-W. Spiess. "Fourier-transform rheology". *Rheologica Acta* 37 (4) (1998), pp. 399–405.
- [52] K. S. Cho, K. Hyun, et al. "A geometrical interpretation of large amplitude oscillatory shear response". *Journal of Rheology* 49 (3) (2005), pp. 747–758.
- [53] K. Hyun, S. H. Kim, et al. "Large amplitude oscillatory shear as a way to classify the complex fluids". *Journal of Non-Newtonian Fluid Mechanics* 107 (1-3) (2002), pp. 51–65.
- [54] R. H. Ewoldt, A. E. Hosoi, et al. "An Ontology for Large Amplitude Oscillatory Shear Flow". *AIP Conference Proceedings*. AIP, 2008.
- [55] R. H. Ewoldt, M. T. Johnston, and L. M. Caretta. "Experimental Challenges of Shear Rheology: How to Avoid Bad Data". *Complex Fluids in Biological Systems*. Springer New York, 2014, pp. 207–241.

- [56] S. Sarkar, D. Bi, et al. "Origin of Rigidity in Dry Granular Solids". *Physical Review Letters* 111 (6) (2013).
- [57] T. Pöschel, C. Salueña, and T. Schwager. "Scaling properties of granular materials". *Physical Review E* 64 (1) (2001).
- [58] R. Ramirez, T. Pöschel, et al. "Coefficient of restitution of colliding viscoelastic spheres". *Physical Review E* 60 (4) (1999), pp. 4465–4472.
- [59] K. Krishnaraj and P. Nott. "Coherent Force Chains in Disordered Granular Materials Emerge from a Percolation of Quasilinear Clusters". *Physical Review Letters* 124 (19) (2020).
- [60] S. N. Pathak, V. Esposito, et al. "Force percolation transition of jammed granular systems". *Physical Review E* 96 (4) (2017).
- [61] E. Kuprian, T. D. Tuong, et al. "Persistent Supercooling of Reproductive Shoots Is Enabled by Structural Ice Barriers Being Active Despite an Intact Xylem Connection". *PLOS ONE* 11 (9) (2016). Ed. by M. Uemura, e0163160.
- [62] H. M. Princen. "Contact angles and transition regions in soap films". *The Journal of Physical Chemistry* 72 (9) (1968), pp. 3342–3345.
- [63] P. T. Metzger. "Htheorem for contact forces in granular materials". *Physical Review E* 77 (1) (2008).
- [64] H. Kramers. "Brownian motion in a field of force and the diffusion model of chemical reactions". *Physica* 7 (4) (1940), pp. 284–304.
- [65] P. Oswald. *Rheophysique : Ou comment coule la matiere*. Paris: Belin, 2005.
- [66] R. Larson. *The structure and rheology of complex fluids*. New York: Oxford University Press, 1999.
- [67] H. Bird Armstrong. *Liquids 2e V1*. John Wiley & Sons, 1987. 672 pp.
- [68] J. D. Ferry and H. S. Myers. "Viscoelastic Properties of Polymers". *Journal of The Electrochemical Society* 108 (7) (1961), p. 142C.
- [69] A. A. Collyer. *Techniques in Rheological Measurement*. Dordrecht: Springer Netherlands, 1993.
- [70] J. M. Dealy and K. F. Wissbrun. *Melt Rheology and Its Role in Plastics Processing*. Springer Netherlands, 1990.
- [71] Ferry. *Viscoelastic Properties 3e*. John Wiley Sons, 1980. 668 pp.
- [72] A. C. Pipkin. *Lectures on Viscoelasticity Theory*. Springer New York, 1986.
- [73] M. Stieger. "The Rheology Handbook - For users of rotational and oscillatory rheometers". *Applied Rheology* 12 (5) (2002), p. 232.
- [74] R. H. Ewoldt. "Defining nonlinear rheological material functions for oscillatory shear". *Journal of Rheology* 57 (1) (2013), pp. 177–195.
- [75] A. J. Giacomin and J. M. Dealy. "Large-Amplitude Oscillatory Shear". *Techniques in Rheological Measurement*. Springer Netherlands, 1993, pp. 99–121.
- [76] R. H. Ewoldt, P. Winter, et al. "Large amplitude oscillatory shear of pseudoplastic and elastoviscoplastic materials". *Rheologica Acta* 49 (2) (2009), pp. 191–212.

- [77] J. HARRIS. "Response of Time-dependent Materials to Oscillatory Motion". *Nature* 207(4998) (1965), pp. 744-744.
- [78] W. Philippoff. "Vibrational Measurements with Large Amplitudes". *Transactions of the Society of Rheology* 10(1) (1966), pp. 317-334.
- [79] S. Onogi, T. Masuda, and T. Matsumoto. "Non-Linear Behavior of Viscoelastic Materials. I. Disperse Systems of Polystyrene Solution and Carbon Black". *Transactions of the Society of Rheology* 14(2) (1970), pp. 275-294.
- [80] M. Wilhelm. "Fourier-Transform Rheology". *Macromolecular Materials and Engineering* 287(2) (2002), pp. 83-105.
- [81] S. N. Ganeriwala and C. A. Rotz. "Fourier transform mechanical analysis for determining the nonlinear viscoelastic properties of polymers". *Polymer Engineering and Science* 27(2) (1987), pp. 165-178.
- [82] K. Hyun, M. Wilhelm, et al. "A review of nonlinear oscillatory shear tests: Analysis and application of large amplitude oscillatory shear (LAOS)". *Progress in Polymer Science* 36(12) (2011), pp. 1697-1753.
- [83] K. Miyazaki, H. M. Wyss, et al. "Nonlinear viscoelasticity of metastable complex fluids". *Europhysics Letters (EPL)* 75(6) (2006), pp. 915-921.
- [84] H. M. Wyss, K. Miyazaki, et al. "Strain-Rate Frequency Superposition: A Rheological Probe of Structural Relaxation in Soft Materials". *Physical Review Letters* 98(23) (2007).
- [85] R. H. Ewoldt, A. E. Hosoi, and G. H. McKinley. "New measures for characterizing nonlinear viscoelasticity in large amplitude oscillatory shear". *Journal of Rheology* 52(6) (2008), pp. 1427-1458.
- [86] M. Badetti, A. Fall, et al. "Shear strength of wet granular materials: Macroscopic cohesion and effective stress". *The European Physical Journal E* 41(5) (2018), p. 68.
- [87] K. Atalik and R. Keunings. "On the occurrence of even harmonics in the shear stress response of viscoelastic fluids in large amplitude oscillatory shear". *Journal of Non-Newtonian Fluid Mechanics* 122(1-3) (2004), pp. 107-116.
- [88] M. D. Graham. "Wall slip and the nonlinear dynamics of large amplitude oscillatory shear flows". *Journal of Rheology* 39(4) (1995), pp. 697-712.
- [89] B. Debbaut and H. Burhin. "Large amplitude oscillatory shear and Fourier-transform rheology for a high-density polyethylene: Experiments and numerical simulation". *Journal of Rheology* 46(5) (2002), pp. 1155-1176.
- [90] T. D tsch, M. Pollard, and M. Wilhelm. "Kinetics of isothermal crystallization in isotactic polypropylene monitored with rheology and Fourier-transform rheology". *Journal of Physics: Condensed Matter* 15(11) (2003), S923-S931.
- [91] M. Abramowitz and I. A. Stegun. *Handbook of Mathematical Functions with Formulas, Graphs, and Mathematical Tables*. ninth Dover printing, tenth GPO printing. New York: Dover, 1964.
- [92] M. J. Reimers and J. M. Dealy. "Sliding plate rheometer studies of concentrated polystyrene solutions: Large amplitude oscillatory shear of a very high molecular weight polymer in diethyl phthalate". *Journal of Rheology* 40(1) (1996), pp. 167-186.
- [93] M. L. Gardel, F. Nakamura, et al. "Stress-Dependent Elasticity of Composite Actin Networks as a Model for Cell Behavior". *Physical Review Letters* 96(8) (2006).

- [94] C. Baravian and D. Quemada. "Using instrumental inertia in controlled stress rheometry". *Rheologica Acta* 37 (3) (1998), pp. 223–233.
- [95] L. C. E. Struik. "Free damped vibrations of linear viscoelastic materials". *Rheologica Acta* 6 (2) (1967), pp. 119–129.
- [96] M. L. Gardel. "Elastic Behavior of Cross-Linked and Bundled Actin Networks". *Science* 304 (5675) (2004), pp. 1301–1305.
- [97] U. Zolzer and H. -F. Eicke. "Free oscillatory shear measurements ?an interesting application of constant stress rheometers in the creep mode". *Rheologica Acta* 32 (1) (1993), pp. 104–107.
- [98] J. D. Berry, M. J. Neeson, et al. "Measurement of surface and interfacial tension using pendant drop tensiometry". *Journal of Colloid and Interface Science* 454 (2015), pp. 226–237.
- [99] R. B. Bird and C. F. Curtiss. "Fascinating polymeric liquids". *Physics Today* 37 (1) (1984), pp. 36–43.
- [100] T. G. Mezger. *The Rheology Handbook*. Vincentz Network, 2019.
- [101] S. Maccarrone, G. Brambilla, et al. "Ultra-long range correlations of the dynamics of jammed soft matter". *Soft Matter* 6 (21) (2010), p. 5514.
- [102] Y. Rahmani, K. van der Vaart, et al. "Dynamic heterogeneity in hard and soft sphere colloidal glasses". *Soft Matter* 8 (15) (2012), p. 4264.
- [103] J. F. James. *A student's guide to Fourier transforms : with applications in physics and engineering*. Cambridge, U.K. New York: Cambridge University Press, 2002.
- [104] F. C. MacKintosh, J. Käs, and P. A. Janmey. "Elasticity of Semiflexible Biopolymer Networks". *Physical Review Letters* 75 (24) (1995), pp. 4425–4428.
- [105] N. Y. Yao, R. J. Larsen, and D. A. Weitz. "Probing nonlinear rheology with inertio-elastic oscillations". *Journal of Rheology* 52 (4) (2008), pp. 1013–1025.
- [106] H. Shi, S. Roy, et al. "Steady state rheology of homogeneous and inhomogeneous cohesive granular materials". *Granular Matter* 22 (1) (2019).
- [107] D. M. Hanes and D. L. Inman. "Experimental evaluation of a dynamic yield criterion for granular fluid flows". *Journal of Geophysical Research* 90 (B5) (1985), p. 3670.
- [108] R. Ewoldt, A. Hosoi, and G. McKinley. "New measures for characterizing nonlinear viscoelasticity in large amplitude oscillatory shear". *Journal of Rheology* 52 (6) (2008), pp. 1427–1458.
- [109] S. Herminghaus. "Dynamics of wet granular matter". *Advances in Physics* 54 (2005), pp. 221–261.
- [110] M. B. Amar and D. Bonn. "Fingering instabilities in adhesive failure". *Physica D: Nonlinear Phenomena* 209 (1-4) (2005), pp. 1–16.
- [111] L. Benyahia, C. Verdier, and J.-M. Piau. "The Mechanisms of Peeling of Uncross-Linked Pressure Sensitive Adhesives". *The Journal of Adhesion* 62 (1-4) (1997), pp. 45–73.
- [112] C. Heussinger and J.-L. Barrat. "Jamming Transition as Probed by Quasistatic Shear Flow". *Physical Review Letters* 102 (21) (2009).

- [113] Gennes. *Capillarity and wetting phenomena : drops, bubbles, pearls, waves*. New York: Springer, 2004.
- [114] W. Alnoush, A. Sayed, and N. Alyafei. "Optimization of contact angle and interfacial tension measurements for fluid/rock systems at ambient conditions". *MethodsX* 6 (2019), pp. 1706–1715.
- [115] E. Y. Arashiro and N. R. Demarquette. "Use of the pendant drop method to measure interfacial tension between molten polymers". *Materials Research* 2 (1) (1999), pp. 23–32.
- [116] R. R. Hartley and R. P. Behringer. "Logarithmic rate dependence of force networks in sheared granular materials". *Nature* 421 (6926) (2003), pp. 928–931.
- [117] A. Lematre. "Origin of a Repose Angle: Kinetics of Rearrangement for Granular Materials". *Physical Review Letters* 89 (6) (2002).
- [118] C. Goldenberg and I. Goldhirsch. "Friction enhances elasticity in granular solids". *Nature* 435 (7039) (2005), pp. 188–191.
- [119] S. Mandal, M. Nicolas, and O. Pouliquen. "Insights into the rheology of cohesive granular media". *Proceedings of the National Academy of Sciences* 117 (15) (2020), pp. 8366–8373.
- [120] N. Mitarai and F. Nori. "Wet granular materials". *Advances in Physics* 55 (1-2) (2006), pp. 1–45.
- [121] J. P. D. Clewett, K. Roeller, et al. "Emergent Surface Tension in Vibrated, Noncohesive Granular Media". *Phys. Rev. Lett.* 109 (22 2012), p. 228002.
- [122] F. Fan, E. J. R. Parteli, and T. Pöschel. "Origin of Granular Capillarity Revealed by Particle-Based Simulations". *Phys. Rev. Lett.* 118 (21 2017), p. 218001.
- [123] L. Staron, A. Abramian, and P.-Y. Lagrée. "Capturing the failure of a cohesive granular step". *EPJ Web of Conferences* 249 (2021). Ed. by M. Aguirre, S. Luding, et al., p. 08006.
- [124] T. T. Vo, S. Nezamabadi, et al. "Additive rheology of complex granular flows". *Nature Communications* 11 (1) (2020).
- [125] J. Läger and H. Stettin. "Differences between stress and strain control in the non-linear behavior of complex fluids". *Rheologica Acta* 49 (9) (2010), pp. 909–930.
- [126] I. Goldhirsch and C. Goldenberg. "Elasticity and Force Chains". *Continuum Models and Discrete Systems*. Springer Netherlands, 2004, pp. 315–326.
- [127] P. C. F. Moller and D. Bonn. "The shear modulus of wet granular matter". *Europhysics Letters (EPL)* 80 (3) (2007), p. 38002.
- [128] Pitois, O., Moucheront, P., and Chateau, X. "Rupture energy of a pendular liquid bridge". *Eur. Phys. J. B* 23 (1) (2001), pp. 79–86.
- [129] Y. I. Rabinovich, M. S. Esayanur, and B. M. Moudgil. "Capillary Forces between Two Spheres with a Fixed Volume Liquid Bridge: Theory and Experiment". *Langmuir* 21 (24) (2005), pp. 10992–10997.
- [130] M. Scheel, R. Seemann, et al. "Liquid distribution and cohesion in wet granular assemblies beyond the capillary bridge regime". *Journal of Physics: Condensed Matter* 20 (49) (2008), p. 494236.

- [131] P. Lambert, A. Chau, et al. "Comparison between Two Capillary Forces Models". *Langmuir* 24 (7) (2008), pp. 3157–3163.
- [132] Z. Fournier, D. Geromichalos, et al. "Mechanical properties of wet granular materials". *Journal of Physics: Condensed Matter* 17 (9) (2005), S477–S502.
- [133] G. Lumay and N. Vandewalle. "Experimental Study of Granular Compaction Dynamics at Different Scales: Grain Mobility, Hexagonal Domains, and Packing Fraction". *Physical Review Letters* 95 (2) (2005).
- [134] J. E. Fiscina, G. Lumay, et al. "Compaction Dynamics of Wet Granular Assemblies". *Phys. Rev. Lett.* 105 (4 2010), p. 048001.
- [135] P. Sollich and M. E. Cates. "Thermodynamic interpretation of soft glassy rheology models". *Physical Review E* 85 (3) (2012).
- [136] P. Sollich. "Soft Glassy Rheology". *Molecular Gels*. Springer-Verlag, pp. 161–192.
- [137] P. G. de Gennes. "Granular Matter: A Tentative View". *More Things in Heaven and Earth*. Springer New York, 1999, pp. 629–643.
- [138] A. P. F. Atman, P. Brunet, et al. "From the stress response function (back) to the sand pile "dip"". *The European Physical Journal E* 17 (1) (2005), pp. 93–100.
- [139] N. Huang and D. Bonn. "Viscosity of a dense suspension in Couette flow". *Journal of Fluid Mechanics* 590 (2007).
- [140] L. Vanel, P. Claudin, et al. "Stresses in Silos: Comparison Between Theoretical Models and New Experiments". *Phys. Rev. Lett.* 84 (7 2000), pp. 1439–1442.
- [141] A. Kudrolli. "Sticky sand". *Nature Materials* 7 (3) (2008), pp. 174–175.
- [142] X. Cheng, L. Xu, et al. "Towards the zero-surface-tension limit in granular fingering instability". *Nature Physics* 4 (3) (2008), pp. 234–237.
- [143] J. P. D. Clewett, K. Roeller, et al. "Emergent Surface Tension in Vibrated, Noncohesive Granular Media". *Physical Review Letters* 109 (22) (2012).
- [144] J. R. Royer, D. J. Evans, et al. "High-speed tracking of rupture and clustering in freely falling granular streams". *Nature* 459 (7250) (2009), pp. 1110–1113.
- [145] T. Bhattacharjee, S. M. Zehnder, et al. "Writing in the granular gel medium". *Science Advances* 1 (8) (2015), e1500655.
- [146] A. Samadani and A. Kudrolli. "Angle of repose and segregation in cohesive granular matter". *Physical Review E* 64 (5) (2001).
- [147] C. Hanotin, S. K. de Richter, et al. "Vibration-induced Liquefaction of Granular Suspensions". *Physical Review Letters* 108 (19) (2012).
- [148] X. Cheng, G. Varas, et al. "Collective Behavior in a Granular Jet: Emergence of a Liquid with Zero Surface Tension". *Physical Review Letters* 99 (18) (2007).
- [149] P. G. ROGNON, J.-N. ROUX, et al. "Dense flows of cohesive granular materials". *Journal of Fluid Mechanics* 596 (2008), pp. 21–47.
- [150] J. E. Fiscina, G. Lumay, et al. "Compaction Dynamics of Wet Granular Assemblies". *Physical Review Letters* 105 (4) (2010).
- [151] S. J. Linz and A. Döhle. "Minimal relaxation law for compaction of tapped granular matter". *Physical Review E* 60 (5) (1999), pp. 5737–5741.

- [152] K. Binder and W. Kob. *Glassy Materials and Disordered Solids*. WORLD SCIENTIFIC, 2011.
- [153] P. Sollich, F. ç. Lequeux, et al. "Rheology of Soft Glassy Materials". *Phys. Rev. Lett.* 78 (10 1997), pp. 2020–2023.
- [154] S. Enferad, J. Petit, et al. "Effect of particle size and formulation on powder rheology". *Particulate Science and Technology* 39 (3) (2020), pp. 362–370.



# Appendix



# Appendix A

## A Supplementary Figures: LAOS and Soft Glassy Rheology

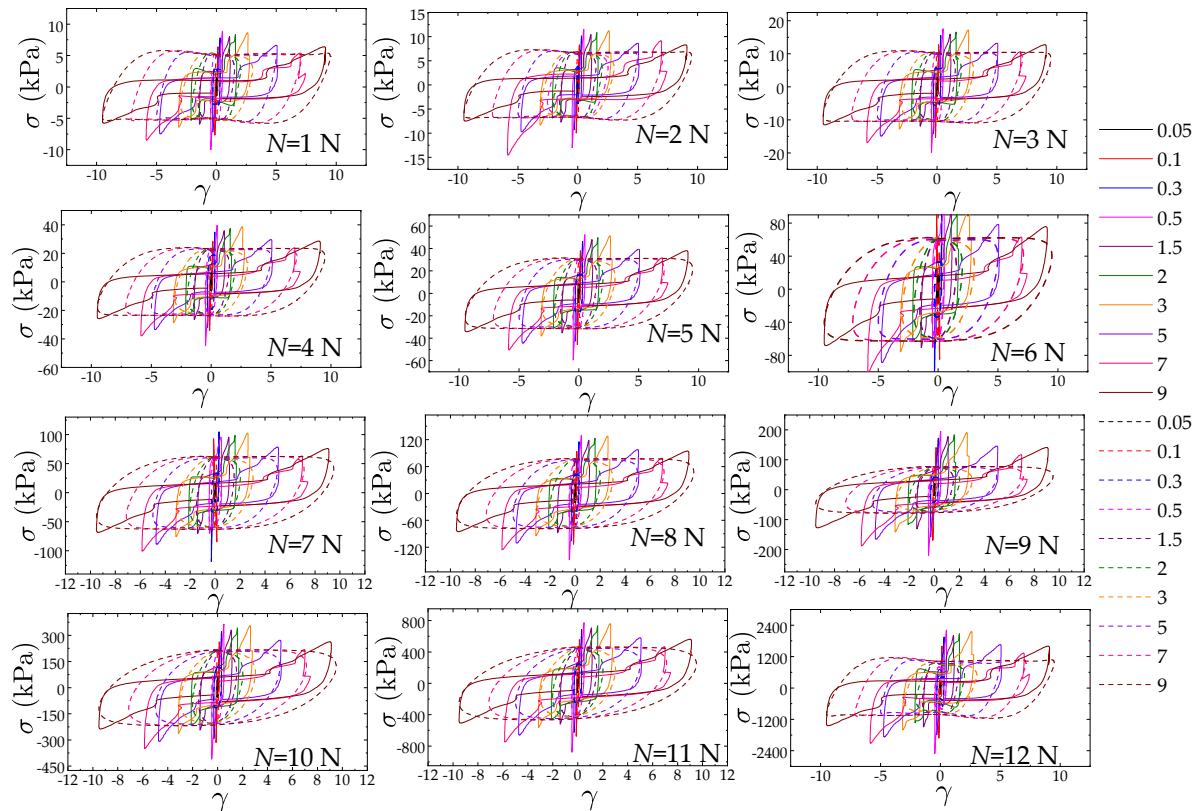


**Figure .1:** LB loops summarised for Dynoseeds beads of  $140\ \mu\text{m}$  diameter with (dashed lines) and without (solid lines) small additions of Silicon oil as a function of strain  $\gamma$  for each normal force cycle ( $N = 1\ \text{N} - 12\ \text{N}$ , top-left to bottom-right, respectively)

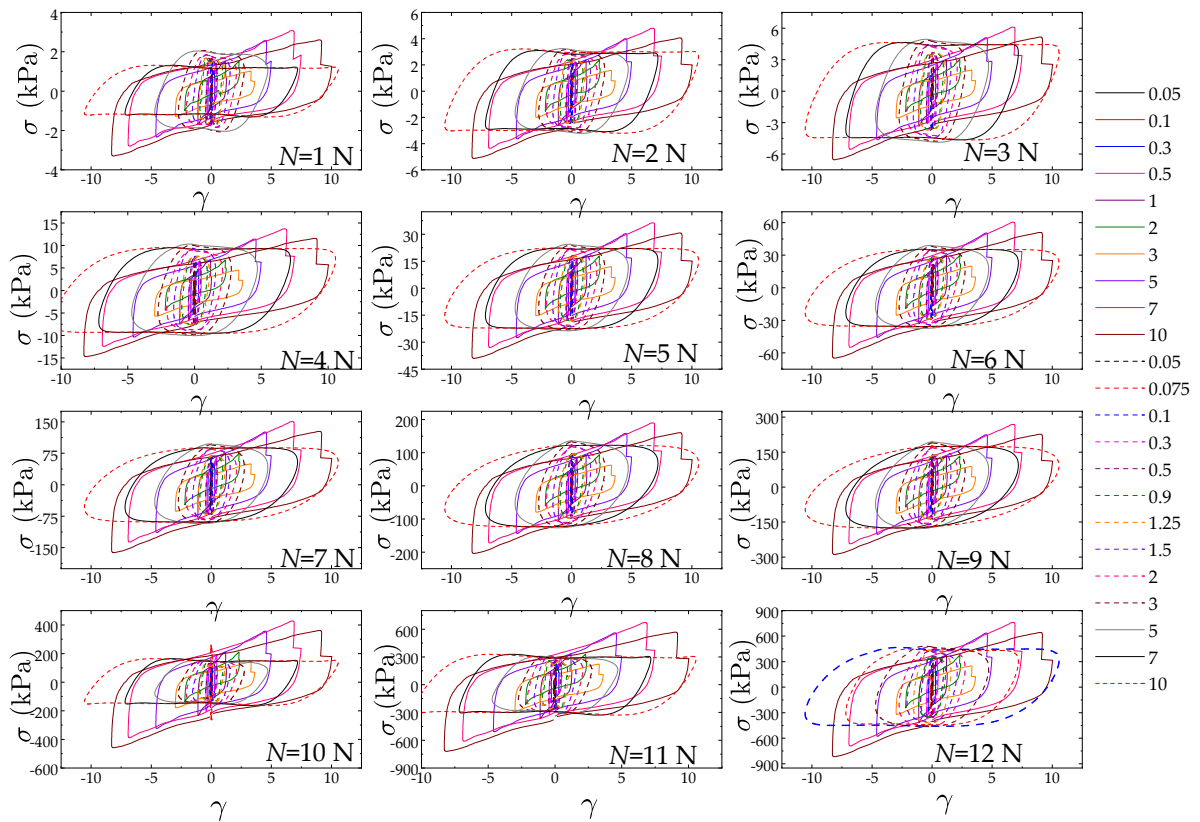


**Figure .2:** LB loops summarised for Dynoseeds beads of  $250\ \mu\text{m}$  diameter with (dashed lines) and without (solid lines) small additions of Silicon oil as a function of strain  $\gamma$  for each normal force cycle ( $N = 1\text{ N} - 12\text{ N}$ , top-left to bottom-right, respectively)

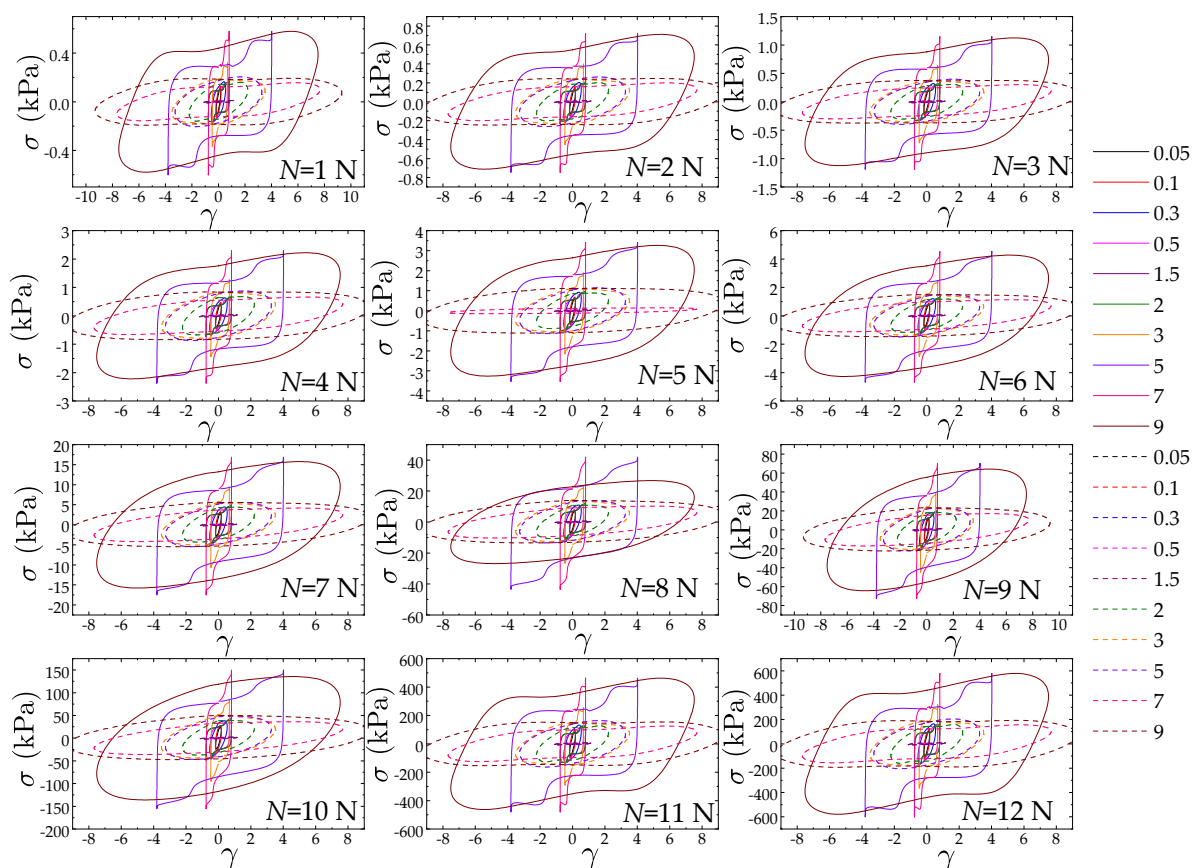


**Figure 3:** LB loops summarised for Dynoseeds beads of  $500\ \mu\text{m}$  diameter with (dashed lines) and without (solid lines) small additions of Silicon oil as a function of strain  $\gamma$  for each normal force cycle ( $N = 1\text{ N} - 12\text{ N}$ , top-left to bottom-right, respectively)

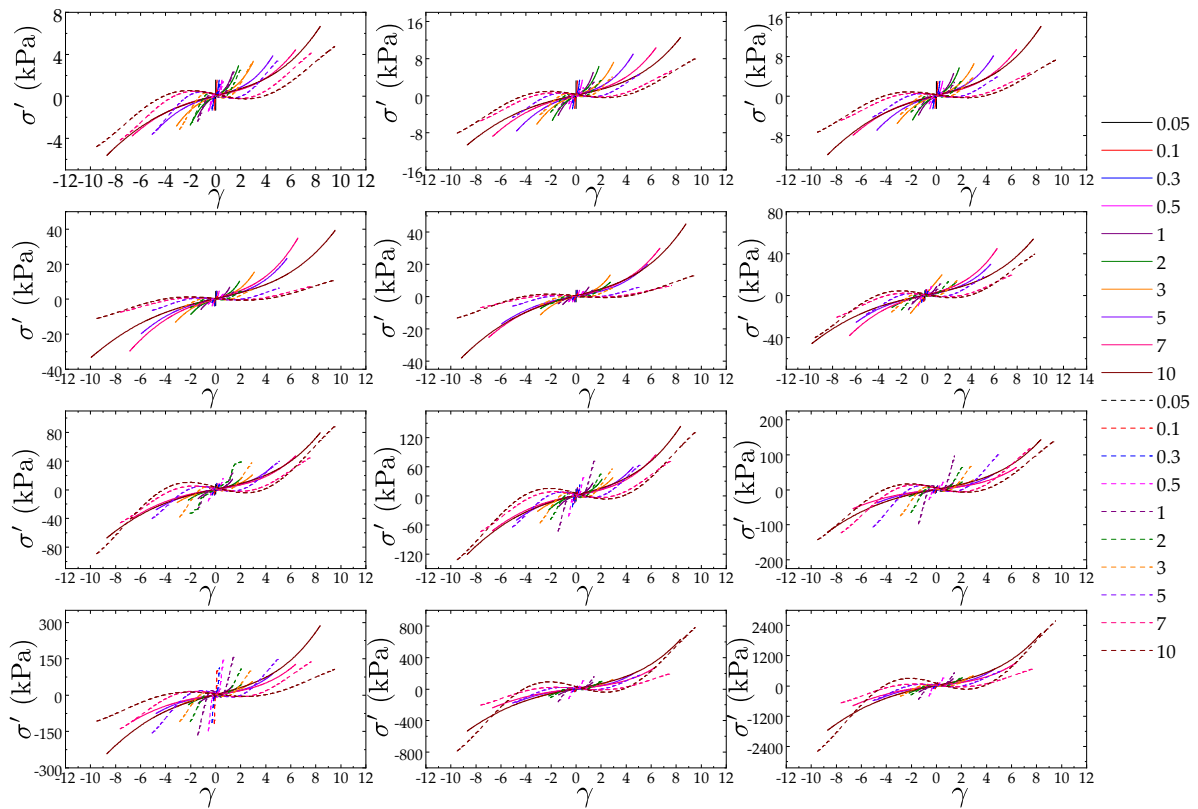


**Figure .4:** Corresponding elastic symmetry lines summarised for Dynoseeds beads of  $140\ \mu\text{m}$  diameter with (dashed lines) and without (solid lines) small additions of Silicon oil as a function of strain  $\gamma$  for each normal force cycle ( $N = 1\ \text{N} - 12\ \text{N}$ , top-left to bottom-right, respectively)

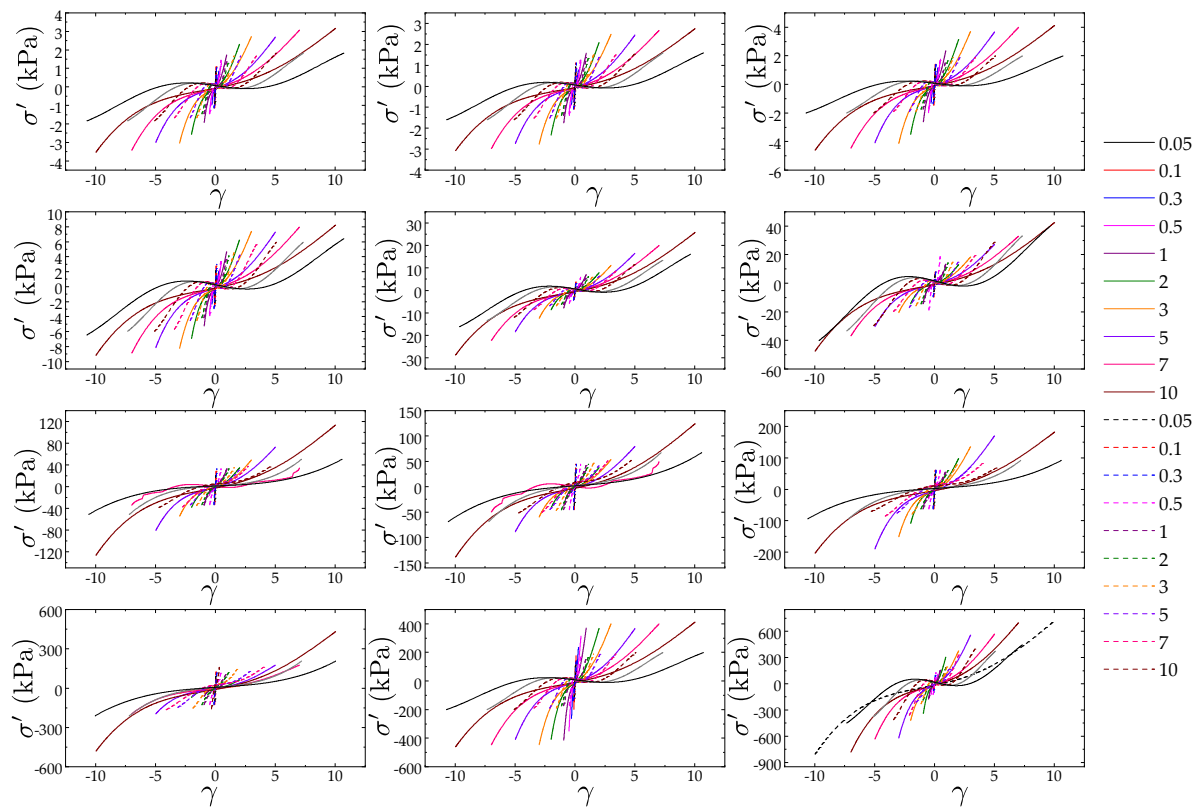


**Figure .5:** Corresponding elastic symmetry lines summarised for Dynoseeds beads of  $250\ \mu\text{m}$  diameter with (dashed lines) and without (solid lines) small additions of Silicon oil as a function of strain  $\gamma$  for each normal force cycle ( $N = 1\text{ N} - 12\text{ N}$ , top-left to bottom-right, respectively)

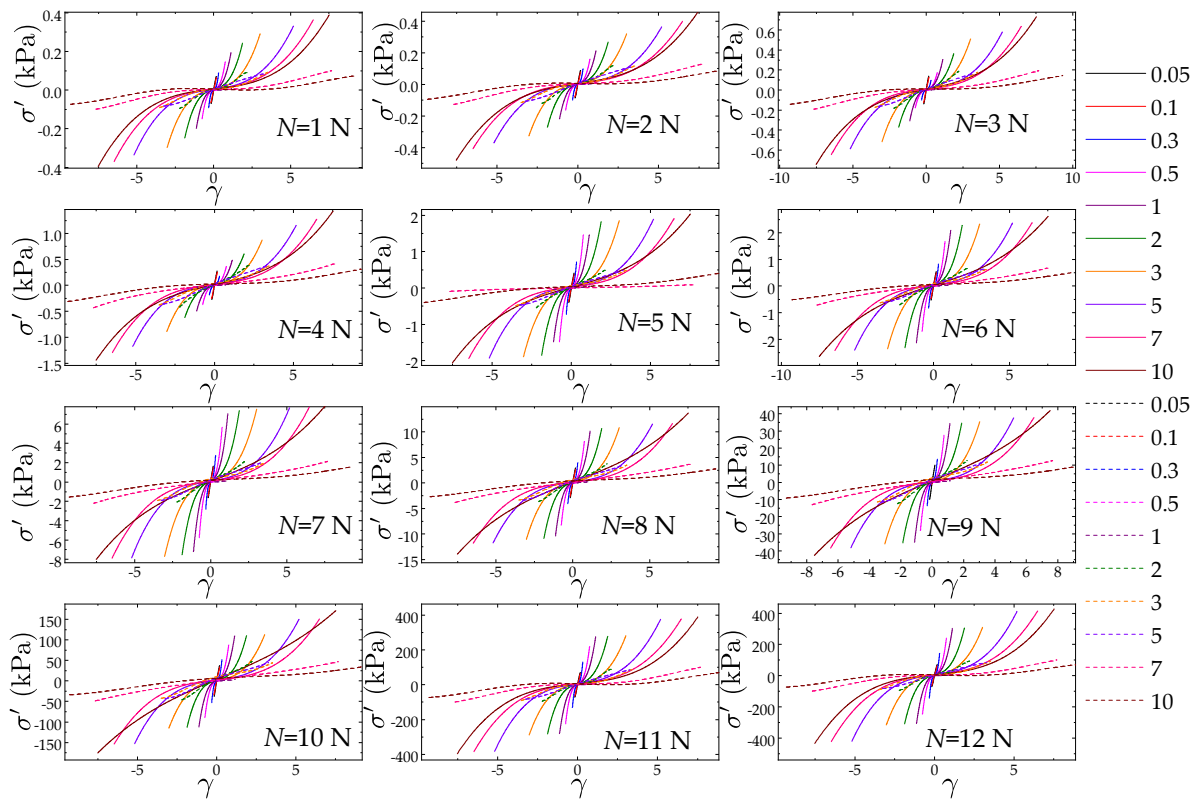


**Figure .6:** Corresponding elastic symmetry lines summarised for Dynoseeds beads of  $500\ \mu\text{m}$  diameter with (dashed lines) and without (solid lines) small additions of Silicon oil as a function of strain  $\gamma$  for each normal force cycle ( $N = 1\text{ N} - 12\text{ N}$ , top-left to bottom-right, respectively)

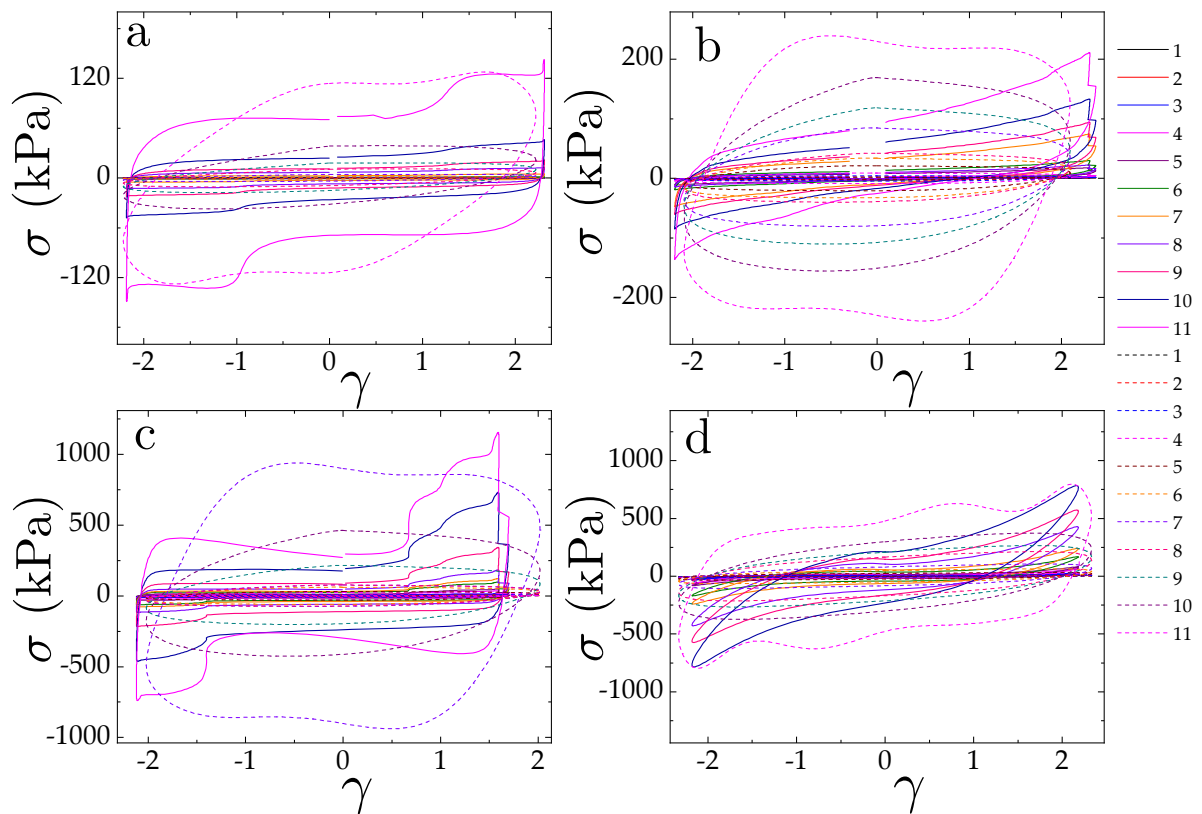


**Figure 7:** Lissajous-Bowditch loop from a LAOS experiment on Dynoseeds beads of (a)  $80\ \mu\text{m}$ , (b)  $140\ \mu\text{m}$ , (c)  $250\ \mu\text{m}$ , and (d)  $500\ \mu\text{m}$  diameter with (dashed lines) and without (solid lines) small additions of Silicon oil. The data is chosen at  $\gamma_0 \approx 2 > \gamma_0^{\text{onset}}$  for normal force  $N (= 0.5\ \text{N} - 12\ \text{N})$

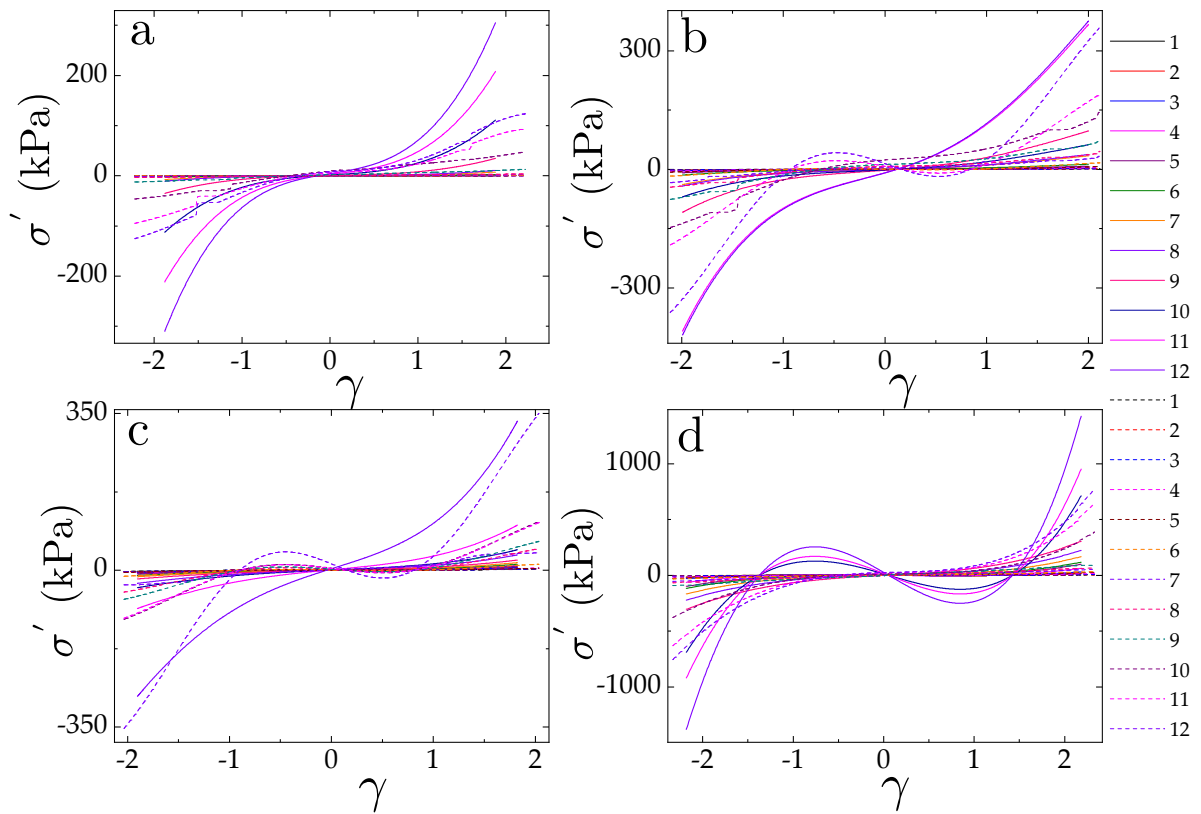


**Figure .8:** Corresponding symmetry lines for LB loops shown above depicted as (a) 80  $\mu\text{m}$ , (b) 140  $\mu\text{m}$ , (c) 250  $\mu\text{m}$ , and (d) 500  $\mu\text{m}$  diameter with (dashed lines) and without (solid lines) small additions of Silicon oil. The data is chosen at  $\gamma_0 \approx 2 > \gamma_0^{\text{onset}}$  for normal force  $N(= 0.5\text{N} - 12\text{N})$

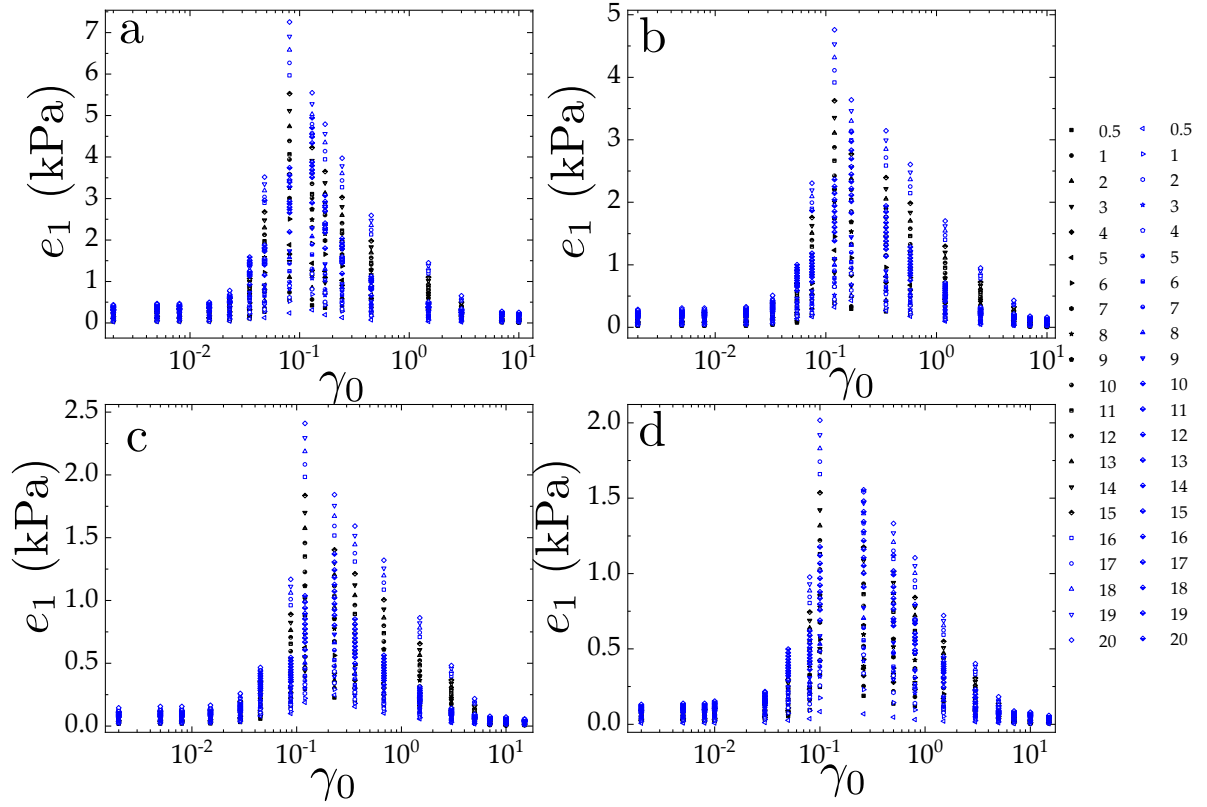


**Figure 9:** Summary of the first harmonic elasticity  $e_1$  in support to approximate the non-thermal motions of dry (solid black) and wet (open blue) granular matter as a function of strain amplitude for (a)  $500\ \mu\text{m}$  with  $|e_{1,\text{min}}^{\text{dry}}| \approx 3.5\ \text{nJ}/\text{grain}$ ,  $|e_{1,\text{min}}^{\text{wet}}| \approx 7\ \text{nJ}/\text{grain}$ ,  $|e_{1,\text{max}}^{\text{dry}}| \approx 49\ \text{nJ}/\text{grain}$ ,  $|e_{1,\text{max}}^{\text{wet}}| \approx 47\ \text{nJ}/\text{grain}$ , (b)  $250\ \mu\text{m}$  with  $|e_{1,\text{min}}^{\text{dry}}| \approx 10\ \text{nJ}/\text{grain}$ ,  $|e_{1,\text{min}}^{\text{wet}}| \approx 14\ \text{nJ}/\text{grain}$ ,  $|e_{1,\text{max}}^{\text{dry}}| \approx 97\ \text{nJ}/\text{grain}$ ,  $|e_{1,\text{max}}^{\text{wet}}| \approx 63\ \text{nJ}/\text{grain}$ , (c)  $140\ \mu\text{m}$  with  $|e_{1,\text{min}}^{\text{dry}}| \approx 15\ \text{nJ}/\text{grain}$ ,  $|e_{1,\text{min}}^{\text{wet}}| \approx 21\ \text{nJ}/\text{grain}$ ,  $|e_{1,\text{max}}^{\text{dry}}| \approx 120\ \text{nJ}/\text{grain}$ ,  $|e_{1,\text{max}}^{\text{wet}}| \approx 68\ \text{nJ}/\text{grain}$ , and (d)  $80\ \mu\text{m}$  with  $|e_{1,\text{min}}^{\text{dry}}| \approx 19\ \text{nJ}/\text{grain}$ ,  $|e_{1,\text{min}}^{\text{wet}}| \approx 24\ \text{nJ}/\text{grain}$ ,  $|e_{1,\text{max}}^{\text{dry}}| \approx 143\ \text{nJ}/\text{grain}$ ,  $|e_{1,\text{max}}^{\text{wet}}| \approx 93\ \text{nJ}/\text{grain}$ . The dashed lines are the fits of the characteristic scaling law described above with minimum and maximum values presented here. The legend follows up with the applied  $N$  in each experimental set.

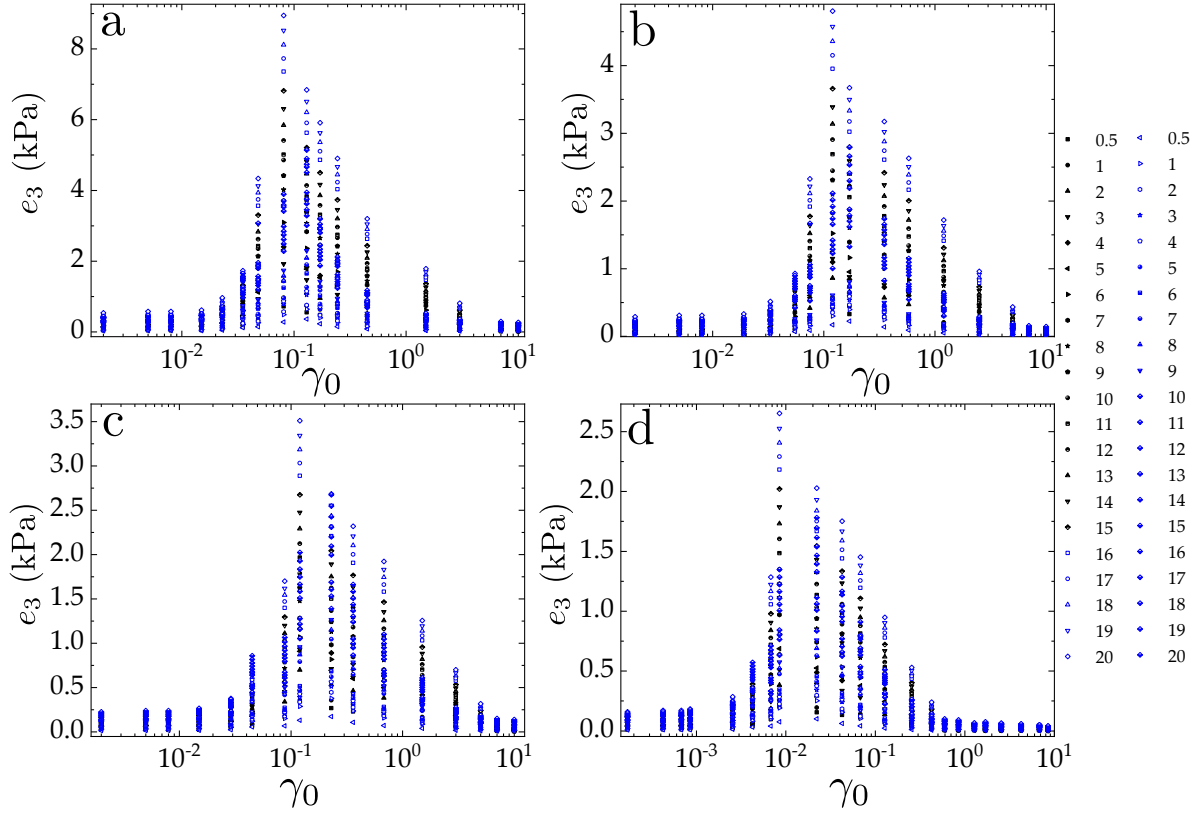


**Figure .10:** Summary of the third harmonic non-linear elasticity  $e_3$  in support to approximate the non-thermal motions of dry (solid black) and wet (open blue) granular matter as a function of strain amplitude for (a) 500  $\mu\text{m}$  with  $|e_{3,\text{min}}^{\text{dry}}| \approx 3.5 \text{ nJ/grain}$ ,  $|e_{3,\text{min}}^{\text{wet}}| \approx 7 \text{ nJ/grain}$ ,  $|e_{3,\text{max}}^{\text{dry}}| \approx 49 \text{ nJ/grain}$ ,  $|e_{3,\text{max}}^{\text{wet}}| \approx 47 \text{ nJ/grain}$ , (b) 250  $\mu\text{m}$  with  $|e_{3,\text{min}}^{\text{dry}}| \approx 10 \text{ nJ/grain}$ ,  $|e_{3,\text{min}}^{\text{wet}}| \approx 14 \text{ nJ/grain}$ ,  $|e_{3,\text{max}}^{\text{dry}}| \approx 97 \text{ nJ/grain}$ ,  $|e_{3,\text{max}}^{\text{wet}}| \approx 63 \text{ nJ/grain}$ , (c) 140  $\mu\text{m}$  with  $|e_{3,\text{min}}^{\text{dry}}| \approx 15 \text{ nJ/grain}$ ,  $|e_{3,\text{min}}^{\text{wet}}| \approx 21 \text{ nJ/grain}$ ,  $|e_{3,\text{max}}^{\text{dry}}| \approx 120 \text{ nJ/grain}$ ,  $|e_{3,\text{max}}^{\text{wet}}| \approx 68 \text{ nJ/grain}$ , and (d) 80  $\mu\text{m}$  with  $|e_{3,\text{min}}^{\text{dry}}| \approx 19 \text{ nJ/grain}$ ,  $|e_{3,\text{min}}^{\text{wet}}| \approx 24 \text{ nJ/grain}$ ,  $|e_{3,\text{max}}^{\text{dry}}| \approx 143 \text{ nJ/grain}$ ,  $|e_{3,\text{max}}^{\text{wet}}| \approx 93 \text{ nJ/grain}$ . The dashed lines are the fits of the characteristic scaling law described above with minimum and maximum values presented here. The legend follows up with the applied  $N$  in each experimental set.

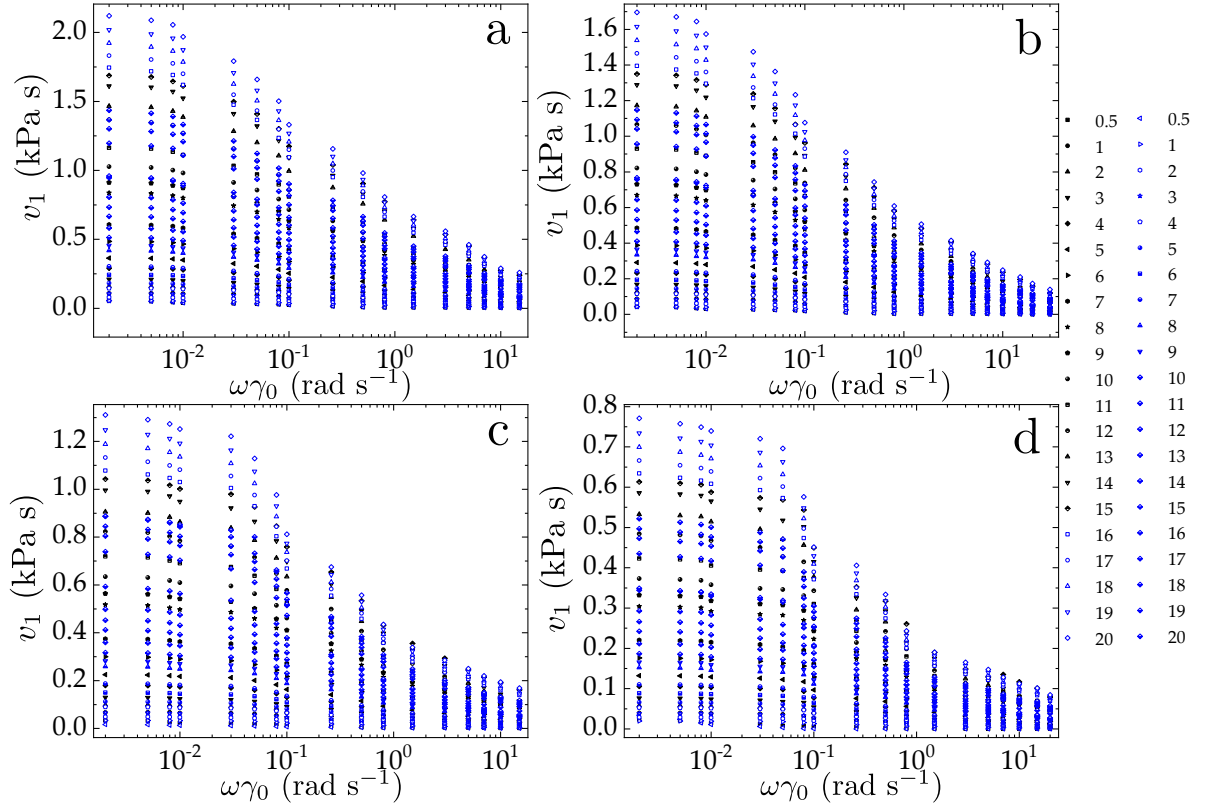


**Figure 11:** Summary of the first harmonic dynamic viscosity  $v_1$  in support to approximate the non-thermal motions of dry (solid black) and wet (open blue) granular matter as a function of strain amplitude for (a)  $500\ \mu\text{m}$  with  $|v_{1,\text{min}}^{\text{dry}}| \approx 3.5\ \text{nJ}/\text{grain}$ ,  $|v_{1,\text{min}}^{\text{wet}}| \approx 7\ \text{nJ}/\text{grain}$ ,  $|v_{1,\text{max}}^{\text{dry}}| \approx 49\ \text{nJ}/\text{grain}$ ,  $|v_{1,\text{max}}^{\text{wet}}| \approx 47\ \text{nJ}/\text{grain}$ , (b)  $250\ \mu\text{m}$  with  $|v_{1,\text{min}}^{\text{dry}}| \approx 10\ \text{nJ}/\text{grain}$ ,  $|v_{1,\text{min}}^{\text{wet}}| \approx 14\ \text{nJ}/\text{grain}$ ,  $|v_{1,\text{max}}^{\text{dry}}| \approx 97\ \text{nJ}/\text{grain}$ ,  $|v_{1,\text{max}}^{\text{wet}}| \approx 63\ \text{nJ}/\text{grain}$ , (c)  $140\ \mu\text{m}$  with  $|v_{1,\text{min}}^{\text{dry}}| \approx 15\ \text{nJ}/\text{grain}$ ,  $|v_{1,\text{min}}^{\text{wet}}| \approx 21\ \text{nJ}/\text{grain}$ ,  $|v_{1,\text{max}}^{\text{dry}}| \approx 120\ \text{nJ}/\text{grain}$ ,  $|v_{1,\text{max}}^{\text{wet}}| \approx 68\ \text{nJ}/\text{grain}$ , and (d)  $80\ \mu\text{m}$  with  $|v_{1,\text{min}}^{\text{dry}}| \approx 19\ \text{nJ}/\text{grain}$ ,  $|v_{1,\text{min}}^{\text{wet}}| \approx 24\ \text{nJ}/\text{grain}$ ,  $|v_{1,\text{max}}^{\text{dry}}| \approx 143\ \text{nJ}/\text{grain}$ ,  $|v_{1,\text{max}}^{\text{wet}}| \approx 93\ \text{nJ}/\text{grain}$ . The dashed lines are the fits of the characteristic scaling law described above with minimum and maximum set values presented here. The legend follows up with the applied  $N$  in each experimental set.

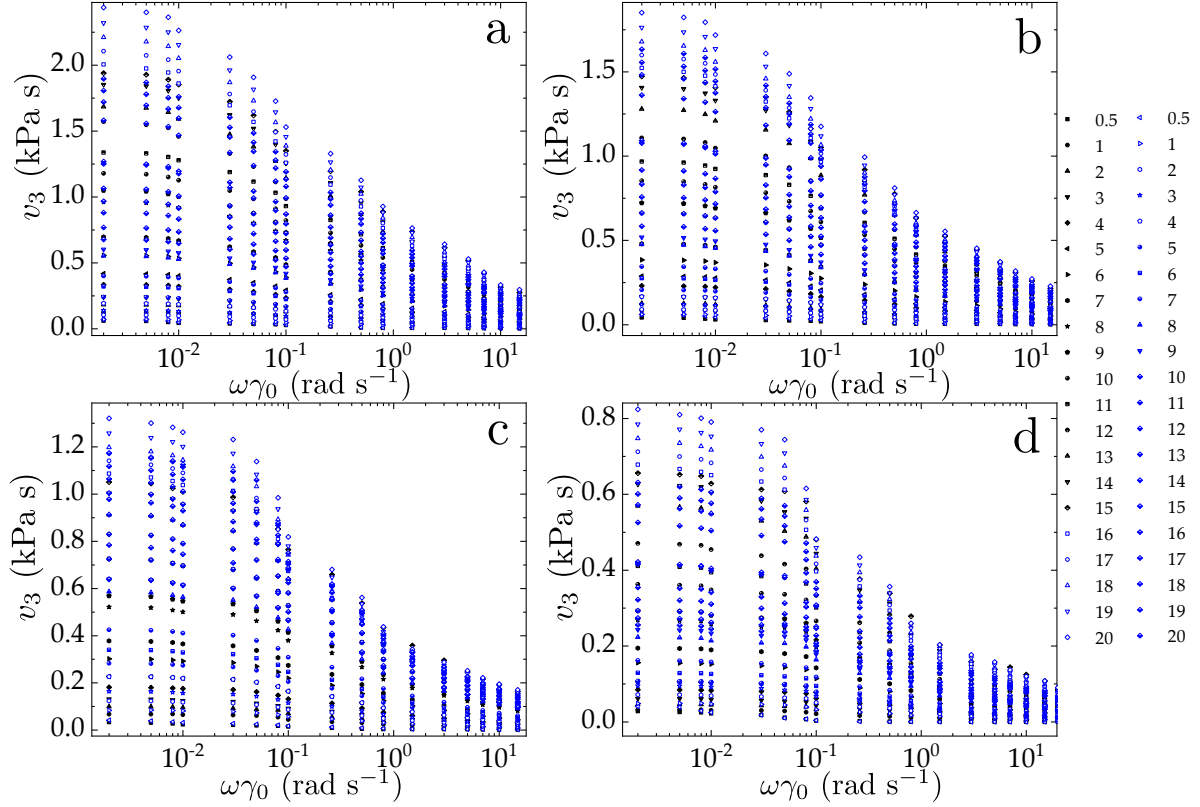


**Figure 12:** Summary of the third harmonic dynamic viscosity  $v_3$  in support to approximate the non-thermal motions of dry (solid black) and wet (open blue) granular matter as a function of strain amplitude for (a)  $500\ \mu\text{m}$  with  $|v_{3;\text{min}}^{\text{dry}}| \approx 3.5\ \text{nJ}/\text{grain}$ ,  $|v_{3;\text{min}}^{\text{wet}}| \approx 7\ \text{nJ}/\text{grain}$ ,  $|v_{3;\text{max}}^{\text{dry}}| \approx 49\ \text{nJ}/\text{grain}$ ,  $|v_{3;\text{max}}^{\text{wet}}| \approx 47\ \text{nJ}/\text{grain}$ , (b)  $250\ \mu\text{m}$  with  $|v_{3;\text{min}}^{\text{dry}}| \approx 10\ \text{nJ}/\text{grain}$ ,  $|v_{3;\text{min}}^{\text{wet}}| \approx 14\ \text{nJ}/\text{grain}$ ,  $|v_{3;\text{max}}^{\text{dry}}| \approx 97\ \text{nJ}/\text{grain}$ ,  $|v_{3;\text{max}}^{\text{wet}}| \approx 63\ \text{nJ}/\text{grain}$ , (c)  $140\ \mu\text{m}$  with  $|v_{3;\text{min}}^{\text{dry}}| \approx 15\ \text{nJ}/\text{grain}$ ,  $|v_{3;\text{min}}^{\text{wet}}| \approx 21\ \text{nJ}/\text{grain}$ ,  $|v_{3;\text{max}}^{\text{dry}}| \approx 120\ \text{nJ}/\text{grain}$ ,  $|v_{3;\text{max}}^{\text{wet}}| \approx 68\ \text{nJ}/\text{grain}$ , and (d)  $80\ \mu\text{m}$  with  $|v_{3;\text{min}}^{\text{dry}}| \approx 19\ \text{nJ}/\text{grain}$ ,  $|v_{3;\text{min}}^{\text{wet}}| \approx 24\ \text{nJ}/\text{grain}$ ,  $|v_{3;\text{max}}^{\text{dry}}| \approx 143\ \text{nJ}/\text{grain}$ ,  $|v_{3;\text{max}}^{\text{wet}}| \approx 93\ \text{nJ}/\text{grain}$ . The dashed lines are the fits of the characteristic scaling law described above with minimum and maximum values presented here. The legend follows up with the applied  $N$  in each experimental set.

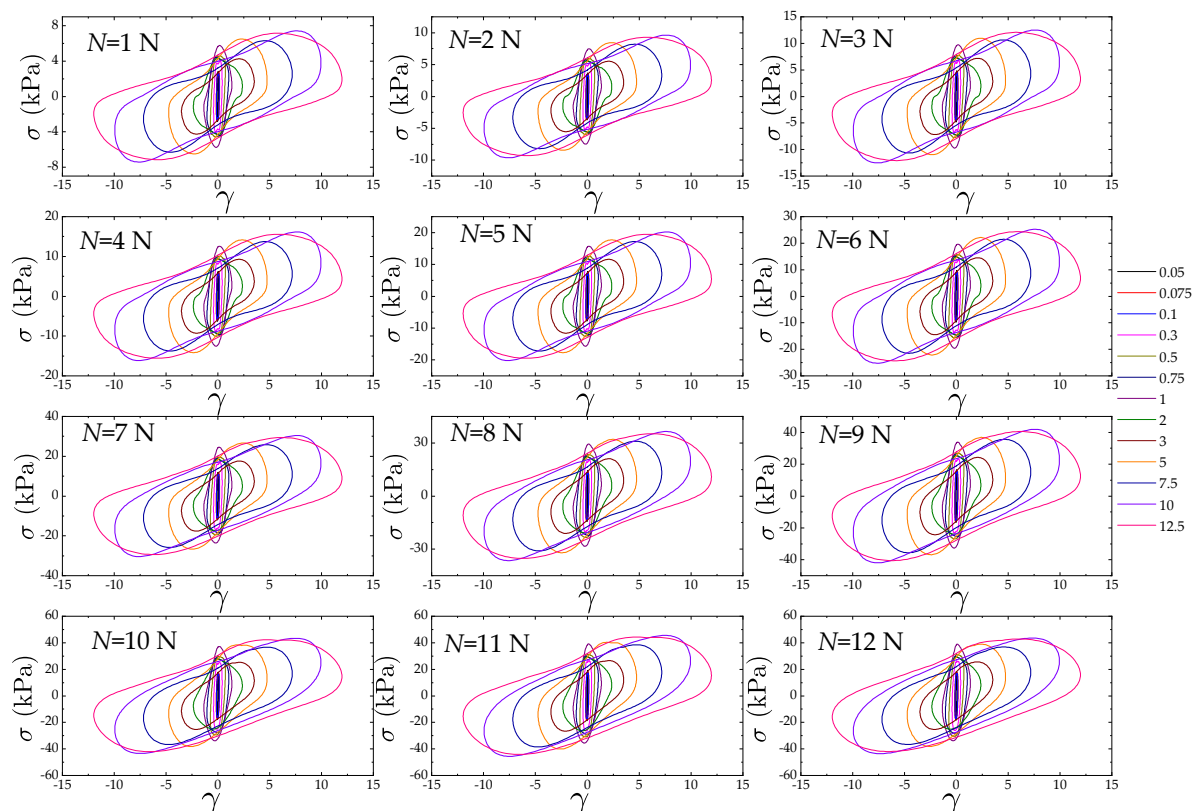


**Figure .13:** LB loops summarised for Dynoseeds beads of  $500\mu\text{m}$  diameter with small additions of Optiprep as a function of strain  $\gamma$  for each normal force cycle ( $N = 1\text{ N} - 12\text{ N}$  as indicated.)



# Appendix B

## B Powder Formulation for Glass Particles

In our attempt to achieve hydrophilic, hydrophobic and lactose coated features on glass grains of  $140\mu\text{m}$  diameter, we adopted the protocol optimised in [154] as a Powderreg Project initiative, and amended additional steps to ensure the desired properties. The step-wise instructions on the chemical treatment of raw powders are as follows.

### B.1 Hydrophilic and Hydrophobic Functionalization

We begin with adding sulphuric acid (95%-97% concentrated) and hydrogen peroxide (50% concentrated grade) in 3:1 ratio, primarily to remove organic impurities followed by introducing hydroxy (-OH) groups on the surface, thence hydrophilic nature as illustrated in Fig. .14. The beads were allowed to cool in the hood for 4 h under ambient conditions, then further washed with distilled water ( $\sim 5$  times) and oven-dried at  $70^\circ\text{C}$  for  $\sim 4$ h.

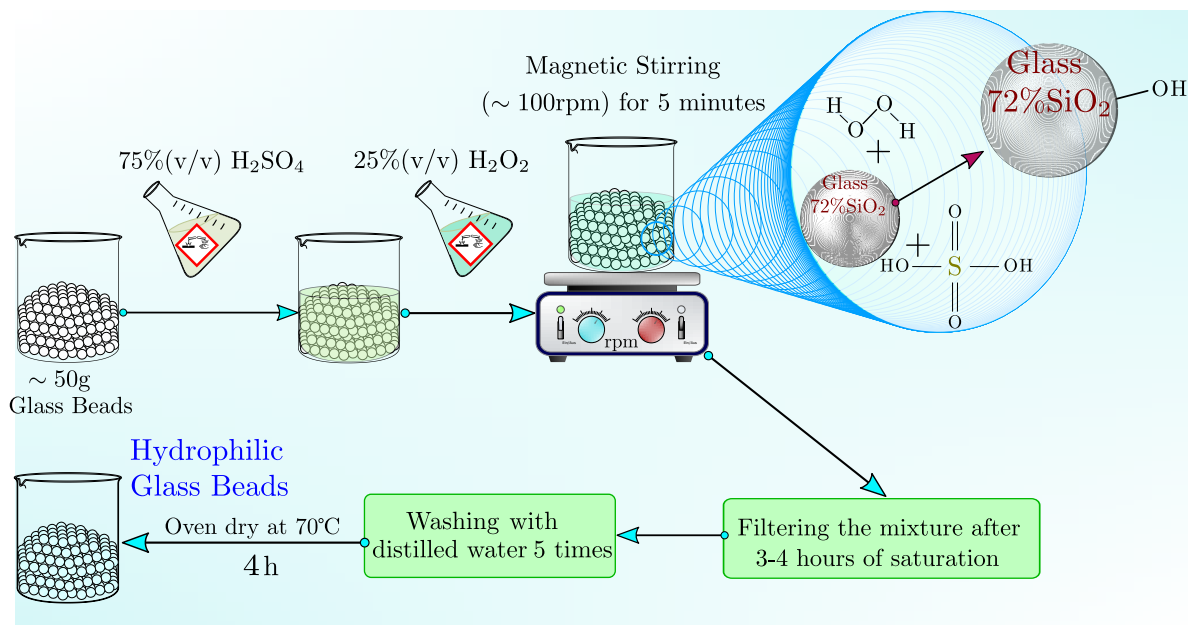


**Figure .14:** Corresponding elastic symmetry lines summarised for Dynoseeds beads of  $140\mu\text{m}$  diameter with (dashed lines) and without (solid lines) small additions of Silicon oil as a function of strain  $\gamma$  for each normal force cycle ( $N = 1\text{N} - 12\text{N}$ , top-left to bottom-right, respectively).

To add hydrophobic functionalities, we start with hydrophilic glass beads (note: not oven-dried, just washed), and add toluene with 2.5 g silane (1H,1H,2H,2H-perfluorooctyltriethoxysilane) purchased from Sigma-Aldrich GmbH. The beads were allowed to stay immersed in the aforesaid solution for 72h under ambient conditions. Hereafter, the beads were finally washed with toluene, then filtered to be dried at room temperature for 24 h, as sketched in the Fig. .15.

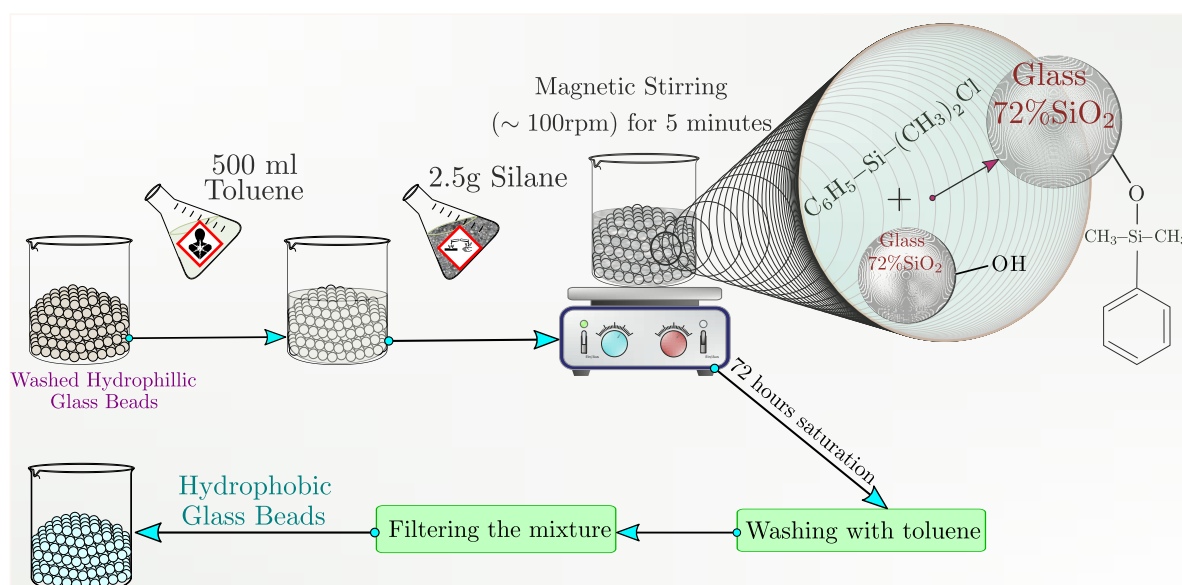


**Figure .15:** Corresponding elastic symmetry lines summarised for Dynoseeds beads of 140  $\mu\text{m}$  diameter with (dashed lines) and without (solid lines) small additions of Silicon oil as a function of strain  $\gamma$  for each normal force cycle ( $N = 1\text{ N} - 12\text{ N}$ , top-left to bottom-right, respectively)

# Acknowledgements

आध्यायान् दशाचार्य आचार्याणां शतं पिता । सहस्रं पितृन् माता गौरवेणातिरिच्यते ॥

This thesis is a child of love, beautiful people, all-nighters, thousands of cups of espresso, and a lot of whining.

Firstly, I would like to thank my advisor, Prof. Dr. Christian Wagner, for his constant flow of thought-provoking discussions, his unflagging moral support and a good sense of humour in the face of my confused ramblings. He did not only offered me care going far beyond what any other mentor would have done for their students, but also supported me through my personal life struggles. His mentorship has raised me as a researcher and as a person. Christian, I am really happy that I worked with you, and I learned a lot from you.

I would like to thank my supervisor, Dr. Jorge Fiscina. He devoted inordinate amounts of time helping me grow as a scientist. We have not only discussed forever about granular materials, quenched disorder, and the noise temperature (which you'll find plenty of in this thesis), but also about life, philosophy, and politics.

También, Jorge, estoy realmente muy feliz de haber trabajado contigo durante los últimos cuatro años y haber compartido tantos buenos recuerdos juntos. ¡Muchas gracias!.

I would like to give my sincere gratitude and thanks to my dissertation committee and their precious time, and I am particularly thankful to Prof. Dr. Rolf Pelster for his cordial acceptance to take over the responsibility as the second reviewer of this thesis. Your humble and friendly nature is truly admirable.

I am highly indebted to my mentors from Freiburg, Prof. Dr. Günter Reiter and Dr. Siva-surender Chandran. I would also like to thank Prof. Dr. Rolf Mülhaupt, Prof. Dr. Alexander N. Semenov, Prof. Dr. Jörg Baschnagel, Dr. Pascal Hebraud, and Dr. Falko Ziebert, I certainly would not have reached this far without your support.

I am grateful to Prof. Randy H. Ewoldt for his time and discussion on nonlinear rheology and for offering me the license to use his MATLAB code as MITLaos.

I would also like to thank Prof. Dr. Ralf Seemann and colleagues Dr. Martin Brinkmann and Dr. Michael Jung for consulting me as a rheologist and later permitting me to work in your group on surface tension measurements.

I would also like to thank and acknowledge all the members, partners and collaborators in the Powderreg project, for all those productive and wonderful times in conferences, expos, annual meetings and visits, especially, Prof. Nicolas Vandewalle, Dr. Sébastien Kiesgen de Richter, Prof. Sergiy Antonyuk, Diana Righi, Salvatore Pillitteri, Robert Hesse, Artur Pascot, and Shirin Enferad. I am grateful for the opportunity to carry out this research as a part of the action powder flow of powderreg project, supported by a cross-border cooperation program co-financed by the European Union / European Regional Development Fund.

Thanks are also due to Dr. Thomas John, for his useful tips, helping me with technical issues, troubleshooting experimental techniques, and for taking time out of his personal schedule teaching me analytical and mathematical concepts, whenever needed. Vielen Dank Thomas!

Weit weg von meiner Heimat, Elke Hüschen, meiner deutschen Mutter, reicht ein solches Dankeschön is gar nicht genug für alles, was Sie für mich getan haben. Je ne peux pas oublier ton mignon péché: "Ach du großer freck!"... Karin und Susannah, vielen Dank für alles und dafür, dass du bei Labor- und Verwaltungsaufgaben immer so hilfsbereit bist. Ich kann deinen bibbelschesbohnesupp mit quetschekuche nie vergessen! Nina Apfelbaum, ich bewundere deine Energie, Problemlösungskompetenz und die schnelle Hilfe, es ist wirklich toll und unkompliziert mit dir über jedes Problem zu sprechen. Danke für alles!

Herzliches danke Michael Schmidt! Muss man sahn! Die Kaffee laaft! Und vielen Dank an die gesamte Werkstattleitung, für die schnelle Herstellung der Artikel und das ungarische Gulasch von Titan.

It has been such a dynamic doctorate life that I will miss plenty, many thanks to all colleagues, members and friends I was fortunate to find in AG Wagner, Alexis Darras, Greta Simionato, Steffen Recktenwald, Stephan Quint, Thomas Fischer, Matthias Paulus, Franois Yaya, Oliver Köhn, Julie Martin-Wortham, Yazdan Rashidi, Revaz Chachanidze, Nanami Taketoshi, Christian Ruloff, Javad Najafi, Zakaria Boujja, Asena Abay, Nils Boussard, Lars Kaestner, Andreas Tschöpe, Felix Maurer, Daniel Flormann, Mohammed Nouaman, Mohammed Bendaoud.

I'm grateful for the beautiful discussions I had on complex systems with my small group of Indian mathematicians in Saarbruecken, Dr. Anurag Pandey, Dr. Bhaskar Chowdhury, Himanshu, and Dr. Kireeti Bodduna.

I would like to thank my co-authors with whom I share a mutual goal of developing and advancing the current state of biomaterials and green chemistry: Dr. Luis Valencia, Dr. Sugam Kumar, Dr. Héctor González, Ilse Magnana, Prof. Ramón Gómez, and Prof. Aji P Mathew.

Thinking about my greatest friends whom I treasure as my brothers, just one line of gratitude does not do any justice and would only dilute your role in my life: Sumit Majumdar, Alexander Kihm, Luis Valencia, Jakob Hörl, Shubham Surana and Kishore Atwal. Without your encouragement and support, I'd be lost. I would also like to express my deepest thanks to Lily Wang and Abhijna Das, who has supported me for the past six years.

Moni amada mia, cambiaste mi vida sin siquiera intentarlo, y no tengo palabras para expresar lo que significas para mí, pero pasaré toda mi vida buscándolas. No puedo imaginar cómo serían las cosas si no te hubiera conocido.